MULTINUCLEAR NMR STUDIES OF METAL – OXYGEN BATTERIES

CHARACTERIZATION OF REACTION PRODUCTS FORMED IN METAL - OXYGEN BATTERIES WITH MULTINUCLEAR SOLID-STATE NMR

BY

ZOË E.M. REEVE B.Sc.

A Thesis Submitted to the School of Graduate Studies in Partial Fulfillment of the

Requirement for the Degree Doctor of Philosophy

McMaster University

McMaster University DOCTOR OF PHILOSOPHY (2017) Hamilton, Ontario (Chemistry)

TITLE: Characterization of Metal – Oxygen Reaction Products with Multinuclear Solid-State NMR

AUTHOR: Zoë E.M. Reeve, B Sc. (University of Guelph)

SUPERVISOR: Professor G. R. Goward

NUMBER OF PAGES: *xx*, 213, w

ABSTRACT

This thesis has investigated electrolyte stability for the Li-O_2 and Na-O_2 batteries and the viability of applying multi-nuclear solid-state NMR to characterize their respective electrochemistries. Metal-oxygen batteries have extremely high energy densities, making them very attractive candidates for electric vehicle applications. However, the exact nature of the metal-oxygen battery chemistry is still not well understood. In this work, ^{7}Li nutation spectroscopy was demonstrated to be a diagnostic tool for distinguishing Li_2O_2 (desired product) from Li_2CO_3 (undesired species) in electrochemically-cycled electrodes. The TEGDME electrolyte was shown to display superior stability to the TMP electrolyte. With ^{17}O NMR, Li_2O_2 and evidence of electrolyte breakdown was observed in the TEGDME cell, whereas only electrolyte breakdown products were discovered within the TMP cell. A detailed breakdown mechanism for TMP was proposed, which accounts for the reaction products observed in the ^{1}H, ^{7}Li, ^{17}O and ^{31}P NMR spectra of the cycled electrodes. The expected Na-O_2 reaction products were establish to have unique ^{23}Na NMR signatures, allowing the desired Na_2O_2 and NaO_2 to be distinguished from the undesirable Na_2CO_3 using; 1D, 2D ^{23}Na-3QMAS, VT NMR and T_1 filtering experiments. ^{23}Na NMR of cycled Na-O_2 electrodes revealed a newly observed species, NaF in addition to the expected products; Na_2O_2 and Na_2CO_3. ^{23}Na NMR and PXRD of a mock electrode confirmed that NaO_2 degrades the carbon electrode (carbon C65 + PVDF), producing NaF and Na_2CO_3, in the absence of the electrolyte. This thesis highlights the value of solid-state NMR, which revealed the instability of NaO_2, and points to future research in topics of reagent stability and lifetimes for metal-air cells.

Acknowledgments

I would like to thank my thesis advisor, Prof. Gillian Goward, for her continuous support, patience, friendship and encouragement throughout my graduate degree. Furthermore, I'm very grateful to Prof. Goward for providing me with the opportunities to travel across North America and Europe, to attend scientific meetings.

I would also like to thank the late Prof. Alex Bain for his valuable advice as my committee member, as well as his assistance with my experimental work. I would also like to thank the rest of my committee members, Prof. Kruse and Prof. Melacini, for their insightful comments and thought provoking questions.

I am also very grateful to Jim Garrett (BIMR), Michal Leskes (WIS), Michael Palme (McMaster), Victoria Jarvis (MAX) and Dr. Glynis de Silveira (CCEM) for assistance with the experimental work. Thank-you to the NMR facility staff for their support and help with the NMR equipment and experiments. Additionally, I would like to thank Dr. Victor Terskikh, for his hospitality and mentorship during my time at the National Ultrahigh-field NMR facility for Solids.

A heart felt thanks to the past and present Goward group members for their expertise, friendship and stimulating discussions, which made the lab an enjoyable place to work and conduct research.

I dedicate this manuscript to my parents Dave and Ferne and my husband, Adam.

Table of Contents

Table of Tables

Table of Figures

List of Abbreviations and Symbols

ssNMR	Solid-State Nuclear Magnetic Resonance
M-O_2	Metal-oxygen
Li-O_2	Lithium-oxygen
Na-O_2	Sodium-oxygen
Z	Atomic number
I	Nuclear spin
m_I	Nuclear spin quantum number
μ_N	Magnetic moment
$\hbar$I	Spin angular moment vector
γ_N	Nuclear gyromagnetic ratio
g_N	Nuclear g factor
β_N	Nuclear magneton
B_0	External magnetic field strength
$\mathcal{H}$	Hamiltonian
ω_0	Larmor frequency
I_z	z-component of nuclear spin quantum number
m_α	High energy state in Zeeman splitting
m_β	Low energy state in Zeeman splitting
ΔE	Energy difference between α and β
k	Boltzmann constant
T	Temperature
K	Kelvin
FID	Free induction decay
β	Flip angle
t_p	Length of pulse
RF	Radio frequency
B_1	Applied magnetic field

T_1	Spin-lattice relaxation (longitudinal relaxation)
T_2	Spin-spin relaxation (transverse relaxation)
CSA	Chemical shielding anisotropy
M_z	Magnetization aligned along the z-axis
T_{1e}	Lifetime of the electronic spin state
FWHM	Full width half max
QCPMG	Quadrupole Carr-Purcell-Meiboom-Gill
MAS	Magic angle spinning
$\mathcal{H}_D$	Heteronuclear dipolar coupling Hamiltonian
θ	Angle between the spins and the external magnetic field
eQ	Electric quadrupole moment
C_q	Quadrupole coupling constant
EFG	Electric field gradient
η_q	Eta
CT	Central transition
ST	Satellite transition
δ_{iso}	Isotropic chemical shift
δ_{aniso}	Chemical shielding anisotropy
η_{CS}	Chemical shielding asymmetry
α, β, γ	Euler angles
P_2, P_4	Legendre polynomials
MQMAS	Multiple quantum magic angle spinning
3QMAS	Triple quantum magic angle spinning
MQ	Multiple quantum
SQ	Single quantum
Ω_{rf}, $\Omega_{nutation}$	Frequency of the applied RF field (also defined as γB_1)
DFS	Double frequency sweep
BIMR	Brockhouse Institute for Material Research
π_y	Refocusing pulse

PC / DMC	propylene carbonate/dimethyl carbonate
TEGDME	tetraethylene glycol dimethyl ether
TMP	trimethyl phosphate
FTIR	Fourier transformed infrared
PXRD	powder x-ray diffraction
TEM	transmission electron microscopy
SEM	scanning electron microscopy
SERS	surface enhanced Raman spectroscopy
DME	1,2-dimethoxyethane
DMDMB	2,3-dimethyl-2,3-dimethoxybutane
TTFP	tris(2,2,2 –trifluoroethyl) phosphite
TFP	tris(2,2,2-trifluoroethyl phosphate
TEP	Triethyl phosphate
XPS	X-ray photoelectron spectroscopy
PVDF	Polyvinylidene fluoride
LiTFSI	Lithium bis-trifluoromethanesulfonimide
XANES	X-Ray absorption near edge structure
VT	variable temperature
S	Electronic spin state
μ_e	Electron magnetic moment
$<S_z>$	Time averaged local electronic field
N_0	Avagadro's number
χ_M	Magnetic molar susceptibility
PPTA	Proton phase-transfer agent
SOP	Standard operating procedure
OCV	Open circuit voltage
HA	Weak acid
HO_2	soluble hydroperoxyl
SOP	Standard operating procedure

Chapter 1 : Introduction to Metal-Oxygen Battery Systems

1.1 Thesis Layout

This thesis describes the use of solid-state nuclear magnetic resonance (ssNMR) techniques to evaluate electrolyte materials for metal-oxygen (M-O_2) batteries. ssNMR is applied to determine the electrochemical reaction products formed in lithium-oxygen (Li-O_2) and sodium-oxygen (Na-O_2) cells. Particular attention is paid to the use of quadrupole nuclei to identifying the M-O_2 reaction products. Model materials were first examined to demonstrate that quadrupole NMR is an effective method to distinguished the desirable products from the unfavorable species, prior to evaluating electrochemically-cycled electrodes.

Chapter 1 provides the motivation for the work outlined throughout this thesis and a description of the current Li-O_2 and Na-O_2 battery technology. Chapter 2 introduces the fundamental principles of NMR spectroscopy and summarizes the techniques used within this thesis. The primary focus of Chapter 2 is on the study of quadrupole nuclei, highlighting the challenges associated with ^{17}O NMR spectroscopy and its application in the Li-O_2 battery studies. Chapter 3 presents the use of ^{7}Li quadrupole nutation spectroscopy to evaluate the stability of Li-O_2 electrolytes. The desired product, lithium peroxide (Li_2O_2), and the main electrolyte breakdown products, lithium carbonate (Li_2CO_3), have sufficiently dissimilar ^{7}Li quadrupole coupling constants such that the species can be separated using ^{7}Li nutation NMR. First the pristine materials were shown to have distinct nutation plots, and subsequently, this technique was applied to two model electrolytes systems; ethylene carbonate/dimethyl carbonate (PC/DMC) and tetraethylene

glycol dimethyl ether (TEGDME), and finally applied to a novel electrolyte; trimethyl phosphate (TMP). Chapter 4 describes a detailed multinuclear solid-state NMR investigation of the TMP electrolyte. TMP was determined to be an unsuitable Li-O_2 electrolyte based on the ^{1}H, ^{7}Li, ^{31}P and ^{17}O NMR spectra of cycled electrodes. A potential electrolyte breakdown mechanism was proposed that accounts for the formation of the observed reaction products. Chapter 5 is an in-depth ^{1}H and ^{17}O NMR study of the TEGDME electrolyte for the Li-O_2 battery. The first and second discharge processes where investigated, where ^{17}O NMR demonstrated that the amount of Li_2O_2 decreased on the second cycle. Chapter 6 introduces the use of solid-state ^{23}Na NMR to examine the Na-O_2 battery. Though a combination of direct 1D ^{23}Na NMR spectra, triple quantum magic angle spinning (3QMAS) filters, and relaxation studies the expected reaction products; sodium superoxide (NaO_2), sodium peroxide (Na_2O_2) and sodium carbonate (Na_2CO_3) are distinguished. In Chapter 7 these techniques are applied to electrochemically-cycled Na-O_2 electrodes. A new previously unobserved product, NaF was observed with ^{23}Na NMR, in addition to Na_2O_2 and Na_2CO_3. NaO_2 was not detected in the cathode NMR spectra. Instead NaO_2 was demonstrated to be reactive with the carbon electrode (carbon SuperC65 + PVDF). Chapter 8 provides a summary of the presented projects and proposes future work.

1.2 Motivation for Studying Non-Aqueous M-O_2 Batteries

Global warming represents a major threat to the planet, which can be combated by decreasing greenhouse gas (GHG) emissions. One approach is to develop alternative energies and energy storage devices for automotive applications. The transportation

section contributes ~ 13.1 % of GHG emission globally, corresponding to 5 billions tons of CO_2 produced per year.[1] By shifting way from the internal combustion engine towards electric vehicles, the goal of reducing GHG emissions becomes achievable. Within society this transition has already began, as hybrid and electric vehicles (HEV and EV, respectively) are commercially available. However the major obstacle that prevents the complete electrification of road transport is the insufficient storage capacity of batteries, which limits the driving range of EV.[2]

State-of-the-art Li-ion batteries (LIB) are based on intercalation electrodes.[3] Their development has revolutionized energy storage leading to advancements in small, portable electronic devices. The first rechargeable LIB was commercialized in 1991 by the SONY Corporation.[4] The battery consisted of a $LiCoO_2$ cathode and a graphite (C_6Li) anode.[4] Both electrodes operate via a redox reaction involving the insertion and extraction (intercalation and decalation respectively) of Li^+ ions into the host materials.[4] **Figure 1-1** shows a schematic diagram of a Li-ion battery during discharge, where the lithium is extracted from graphite anode and inserted in to the $LiCoO_2$ cathode.

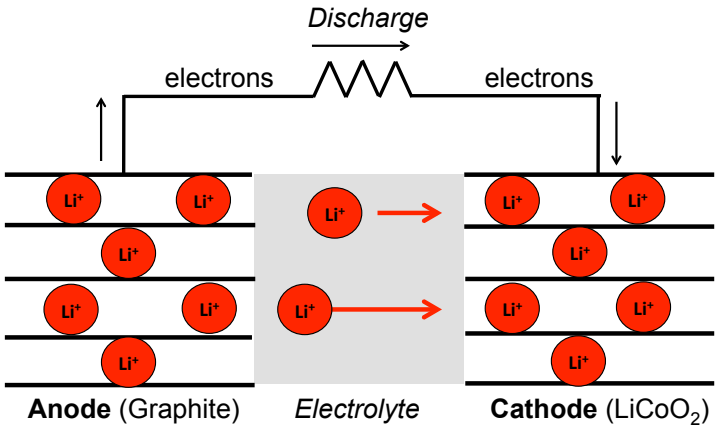

Figure 1-1 Schematic diagram of a Li-Ion battery during discharge where Li+ ions are extracted from the graphite anode, travel through the electrolyte and are inserted into the $LiCoO_2$ cathode. Simultaneously the electrons travel through an external circuit from the graphite anode to the $LiCoO_2$ cathode

Capacity is the ability of a material to store charge, the number of electrons transferred via an external circuit. For a cell the capacity is expressed in units of Ah, corresponding to the discharge current a battery can deliver over time. The specific capacity of an electrode material is the capacity per unit mass, reported in units of mAh/g.

The energy density of an electrode material is the ability of the material to store energy per unit volume (volumetric energy density with units of Wh/l) or per unit mass (gravimetric energy density with units of kWh/kg). For a battery to have a good energy density the operational voltage (average voltage of a cell during discharge), the capacity and the cell mass must be considered. The theoretical gravimetric energy density is calculated based on the number of charge transporters (Li^+ ions) that are incorporated into the electrode, by multiplying the capacity x voltage per unit mass ($Wh/kg = (Ah)(V)(kg)^{-1}$).

For intercalation electrodes there is an intrinsic limit to the reversible capacity, which is primarily based on the degree to which the active material's crystal structure will tolerate the presence of Li vacancies and changes to the oxidation state of the metal ion.[5] Even when LIBs are fully developed the highest energy storage will be too low to meet the demands of the transportation market.[6] The gravimetric energy density of commercially available Li-ion batteries is 0.387 kWh/kg[6] which is significantly lower than the gravimetric energy density of gasoline 13 kWh/kg[2]. With the aim of producing a battery that has a comparable energy density to gasoline, alternative chemistries such as the metal-air battery have been widely explored.

Metal-air batteries are promising candidates for use as energy storage devices in EVs due to their extremely high theoretical energy densities.[2, 7] The metal-air battery is more accurately described as the metal-oxygen battery as O_2 is the fuel source; hereafter the metal-air battery is referred to as the metal-oxygen (M-O_2) battery in this thesis. **Table 1-1** compares the cell potential and theoretical energy density of the commercially available LIB to various M-O_2 systems. The theoretical energy densities outlined are based on the discharge product. In the M-O_2 systems, O_2 is the active redox species at the cathode and the oxygen reduction reaction (ORR) occurs at the porous carbon support. The convention is to report the cell capacity as mAh per gram of carbon ($mAhg^{-1}_{carbon}$), based on a constant current assumption. This is because the end of the discharge capacity is reached when carbon electrode is choked by the deposition of the discharge products into the electrodes' pores. This convention assumes that the electrochemical products only deposits onto the carbon electrode.[8-9]

Frequently the theoretically energy density of the non-aqueous Li-O_2 battery is quoted as 11.586 kWh/kg, which is a comparable value to the energy density of gasoline.[2, 6] However the value, 11.586 kWh/kg is calculated based solely on the oxidation of lithium metal and does not account for the mass of O_2. Because all M-O_2 cells gain mass (O_2) during discharge, it is more accurate to include the mass of O_2 in the theoretical energy density calculations.[6] Therefore, the theoretical energy densities listed in **Table 1-1** include the weight of both reactants in the M-O_2 systems.

Table 1-1 Comparison of the theoretical energy density for various energy storage devices

Battery System (Cathode Reaction)	Cell Voltage (V)	Theoretical specific energy (kWh/kg)	Ref.
Li – ion $½C_6Li + Li_{0.5}CoO_2 \leftrightarrow 3C + LiCoO_2$	3.8	0.387	[6]
Li-O_2 (non-aqueous) $2Li + O_2 \leftrightarrow Li_2O_2$	2.96	3.505	[6]
Li-O_2 (aqueous) $2Li + ½O_2 + H_2O \leftrightarrow LiOH$	3.2	3.582	[6]
Na-O_2 (non-aqueous) $Na + ½O_2 \leftrightarrow NaO_2$	2.27	1.105	[7]
Na-O_2 (non-aqueous) $2Na + O_2 \leftrightarrow Na_2O_2$	2.33	1.602	[7]
Zn-O_2 $Zn + ½O_2 \leftrightarrow ZnO$	1.65	1.086	[6]

Table 1-1 demonstrates that even when we consider the mass of both reactants the Li-O_2 battery has the highest theoretical energy density, making the Li-O_2 battery the most promising candidate for EV applications. The substantial increase in the gravimetric energy density of Li-O_2 cells compared to the commercially available cell, arises as the Li-O_2 cathode stores more Li and hence more charge, than the Li_2CoO_2 cathodes on a per mass basis.[6]

Two Li-O_2 battery architectures are outlined in **Table 1-1** which have fundamentally different chemistries based to the choice of electrolyte.[2] The aqueous design has a higher operating voltage and a slightly larger theoretical energy density than the non-aqueous design. Based solely on **Table 1-1**, the aqueous Li-O_2 design appears more promising than the non-aqueous design. However, in practice the aqueous cell design is more challenging to fabricate, because lithium reacts violent with water. Therefore the lithium metal anode must be coated with an artificial solid electrolyte interference (SEI) to prevent it from reacting with the aqueous electrolyte.[10]

In electrochemical cells, the SEI is a layer, which forms on the electrode as a result of a reaction between the surface of the electrode and the electrolyte.[11] The SEI is formed on the initial discharge/charge of the battery. Once the SEI is created it remains in place and is believed to protect the electrode from further reactions with electrolyte.[12].

In the non-aqueous cell design, the SEI forms naturally during the first discharge, without modifying the Li anode. Additionally, Li metal is less reactive with the organic electrolytes (used in non-aqueous cells), than with water. Thus the non-aqueous Li-O_2 cell design is preferred for automotive applications,[2] and is the primary focus of this thesis.

The non-aqueous Na-O_2 battery should also be considered for EV applications, despite Na-O_2 cells' having a lower theoretical energy density than the Li-O_2 battery. Sodium is a competitive battery material with a comparable redox potential to lithium (**Table 1-2**) coupled with the fact that sodium is highly abundant in nature and an inexpensive material.[13-15] This is unlike lithium, which is becoming a globally limited resource.[15] Moreover, the Na-O_2 system has demonstrated rechargeability[16] and early

reports of this system suggest that the battery chemistry is cleaner (fewer undesirable side reactions are reported compared to Li-O_2 cells). [17] Hence, the Na-O_2 battery is explored in the later portion of this thesis.

The remainder of this chapter outlines the current state of Li-O_2 and Na-O_2 battery technology.

Table 1-2 Comparison of Lithium and Sodium Characteristics[15]

Property	Lithium	Sodium
Potential vs. Standard Hydrogen Electrode (V)	-3.045	-2.714
Cost (per metal carbonate)	$ 5 000 / ton	$ 150 / ton
Atomic Weight (g/mol)	6.90	23.00
Cation Radius (Å)	0.76	1.06
Melting Point (^{0}C)	180.50	97.70

1.3 Description of a Non-Aqueous M-O_2 Battery

The non-aqueous M-O_2 battery is composed of a porous carbon support, a non-aqueous electrolyte and a metal foil, which acts as an anode. The active cathode material, molecular oxygen (O_2), is accessed from the atmosphere and enters the cell through the porous carbon membrane. Large quantities of CO_2 and H_2O negatively affect the cell performance resulting in the formation of Li_2CO_3 and lithium hydroxide (LiOH) respectively.[6] Thus these gases must be prevented from entering the cell. In a research setting this is achieved by cycling the M-O_2 cells in pure oxygen environment such as the glass chamber shown in **Figure 1-2**.

Figure 1-2 (Left) Glass cell chamber which is flooded with pure O_2 gas and housed the M-O_2 cells during electrochemical cycling and (right) a coin cell used to cycle the M-O_2 batteries which had holes drilled in the top to allow O_2 gas to enter the electrochemical system

1.3.1 Description of the Ideal M-O_2 Electrochemistry

At the cathode during discharge, dissolved oxygen is reduced to the superoxide radical ($O_2^{-\cdot}$) on the carbon support. The $O_2^{-\cdot}$ then combines with M^+ ions from the electrolyte, producing a solid discharge product (metal oxide (M_2O), metal superoxide (MO_2) or metal peroxide (M_2O_2)) layer on the carbon membrane. The supply of M^+ ions in the electrolyte is replenished by oxidation of the metal anode during discharge. Simultaneously the electrons travel from the anode to the cathode via an external circuit to powering a device. A schematic representation of a M-O_2 cell during discharge is shown in **Figure 1-3**. During charging, the discharge products decompose regenerating O_2 and M^+ ions and the electrons travel from the cathode to the anode through the external circuit.

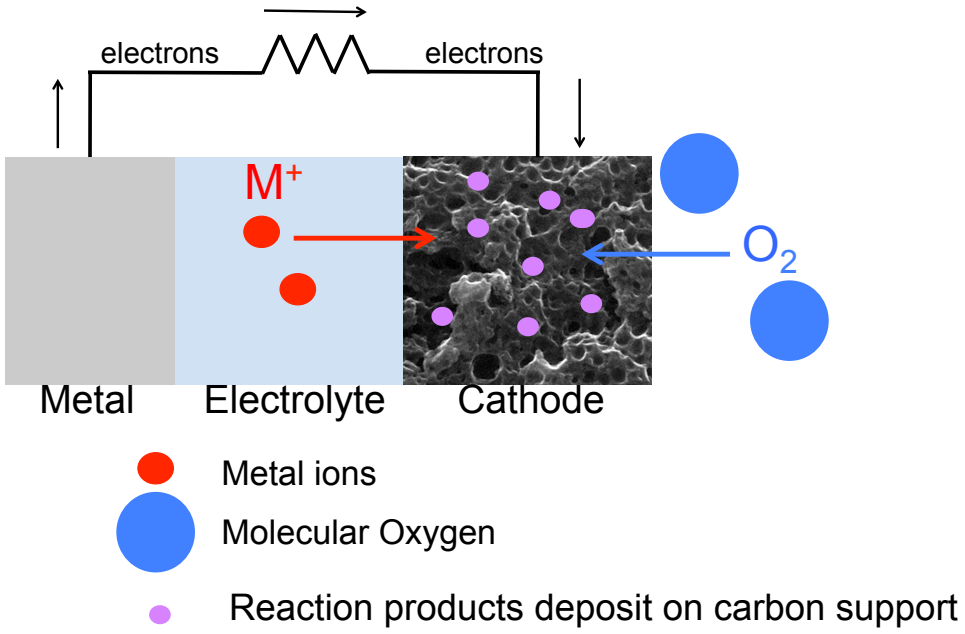

Figure 1-3 Schematic diagram of a metal-oxygen battery during discharge where dissolved O_2 is reduced to the superoxide radical on the carbon support. The superoxide then combines with M^+ ions from the solution to form a solid discharge product layer on the carbon membrane. Simultaneously the electrons travel through an external circuit from the metallic anode to the air cathode

1.3.2 Ideal Features of a Non-Aqueous Electrolyte for the M-O_2 Battery

A battery electrolyte is a solution in which the conducting salt is dissolved into a solvent. Both the salt and solvent must be electrochemically stable over the operational window of the battery. The electrolyte solvent is chosen to favor ionic conductivity, and the solvent must be able to wet the electrode and the separator.

Extra requirements are placed on M-O_2 electrolytes. An ideal M-O_2 electrolyte would be chemically stable in the presence of O_2, its reduced intermediate species, the electrochemical discharge products and the metal anode. The electrolyte must exhibit O_2 solubility and O_2 diffusion. As M-O_2 cells operate as open device, the electrolyte should

be a low volatility liquid to prevent it from evaporating during the operation of the cell. All of these physical and chemical properties must be simultaneously considered when selecting and evaluating potential electrolyte formulations.

1.3.3 Electrolyte Instability in the M-O_2 Battery

Electrolyte instability is a serious challenge that is preventing the further development of the alkali metal-oxygen battery.[18-19] It is well accepted that the choice of electrolyte influences the oxygen reduction reaction, oxygen evolution reaction, the reversibility of the cell and the chemical composition of the discharge products.[18-20]

The highly reactive superoxide radical can undergo many different types of reactions in an aprotic medium. The superoxide can behave as a nucleophile (**equations 1.1** and **1.2**), as a base (**equation 1.3**) or as an electron transfer agent (**equation 1.4**). [19]

$$RX + O_2^{\cdot -} \rightarrow X^- + ROO^{\cdot} \quad (1.1)$$

$$RCOX + O_2^{\cdot -} \rightarrow XO^- + ROO^{\cdot} \quad (1.2)$$

$$RCH_2CH_2X + O_2^{\cdot -} \rightarrow HO_2^- + RCH{=}CH_2X \quad (1.3)$$

$$A + O_2^{\cdot -} \rightarrow A^- + O_2 \quad (1.4)$$

Polar aprotic solvents (those typically used in non-aqueous Li-O_2 and Na-O_2 batteries) contain heteroatoms and therefore have polarized bonds. The polarized bonds can react with the superoxide radical. This was observed in the initial Li-O_2 electrolyte stability investigations. [19-20] Carbonate-based electrolyte undergo nucleophillic attack[21] and ether-based electrolyte experience proton abstractions by the superoxide[22]. Both process result in parasitic side reactions.[21-22] More recently degradation of ether-based electrolytes has also been observed in the Na-O_2 battery.[23-24] Further details outlining the Li-O_2 and Na-O_2 electrolyte stabilities are presented in section 1.4.

The degree of electrolyte breakdown and the Li-O_2 / Na-O_2 discharge products can be controlled by solvating the MO_2 species. This in turn influences the cell's electrochemical performance.[19, 25-26] The cathode has a dual role in M-O_2 cells. As noted in the previous section, the porous cathode allows for O_2 diffusion into the electrolyte. Additionally, the products are also deposited on the surface of the cathode. Once the cathode is coated in the reaction species, new O_2 molecules can not be reduced at the electrode's surface, ending the discharge process.[27] If the electrochemical reaction species are grown in solution then large discharge capacities can be realized without clogging the electrode's pores. The solution mechanism for lithium peroxide (Li_2O_2) formation is proposed by Johnson et al.[25] utilizing Pearson theory of hard and soft, acid and base (HSAB) chemistry[28]. In the Na-O_2 battery, sodium superoxide (NaO_2) is proposed to be solubilized and formed in solution with the aid of a proton phase-transfer agent (PPTA). [24, 26] The solution formation mechanisms are elaborated on below.

1.3.3.1 Solution Mechanism of Li_2O_2 Formation in Li-O_2 Cells

In Li-O_2 cells, the morphology of the discharge product is strongly influenced by the solubility of the lithium superoxide (LiO_2) intermediate in the non-aqueous electrolyte.[25] LiO_2 is generated from the one electron reduction of O_2 at the cathode. The LiO_2 is then partitioned between LiO_2 that is dissolved in the electrolyte and LiO_2^* that is absorbed to the electrode's surface, as outlined in **equation 1.5**. [25]

$$LiO_2^* \leftrightarrow Li^+_{(sol)} + O_2^-{}_{(sol)} + \text{ion pairs} + \text{higher aggregates} \quad (1.5)$$

For aprotic solvents, the solubility of a salt is primarily determined by the solvation of the cation by the solvent molecule. The ability of the solvent to solubilize a cation is discussed in terms of a donor number (DN). The DN of a solvent is related to the Lewis basicity of a liquid.[29] From Pearson's theory of HSAB chemistry, Li^+ ions are hard acid, which prefer to bind with hard bases.[28] The hard acid are better stabilized by a high DN solvent, such as dimethyl sulfoxide (DMSO, DN = 30). With a high DN solvent, LiO_2 remains dissolved in solution. In solution LiO_2 spontaneously disproportions to Li_2O_2 (**equation 1.6**), which precipitate onto the electrode as large toroidal particles.[19, 25]

$$2LiO_2 \rightarrow Li_2O_2 + O_2 \quad (1.6)$$

Li^+ ions (and Li^+ ion containing materials) are poorly solvated in solvents that have a low DN (ie. acetonitrile, DN = 14). In that case the equilibrium outlined in **equation 1.5**, lies to the left and surface absorbed LiO_2^* is the dominant species. On the surface LiO_2 either undergoes a second electron reduction (**equation 1.7**) or disproportionation (**equation 1.6**) to form a Li_2O_2 film.[19, 25]

$$LiO_2 + Li^+ + e^- \rightarrow Li_2O_2 \qquad (1.7)$$

When the electrolyte solvent has an intermediate DN (i.e. dimethoxyethane (DME), DN = 20) there is not a strong preference for whether LiO_2 is solvated or remains

absorbed to the surface. Thus both the solution and surface pathways will contribute, resulting in a combination of crystalline Li_2O_2 structures and thin films.[25]

1.3.3.2 Solution Mechanism of NaO_2 Formation in Na-O_2 Cells

At low concentrations H_2O or other weak acids (HA), are thought to act as PPTA, stabilizing NaO_2 in Na-O_2 cells.[26] The PPTA reacts with the superoxide at the cathode via **equations 1.8**. The soluble hydroperoxyl (HO_2) intermediate then transports it away from electrode. NaO_2 is generated in solution, as outlined in **equations 1.9**. [24, 26] Once a supersaturated solution is achieved the cubic NaO_2 crystals precipitate out of solution [24]

$$HA + O_2^- \leftrightarrow HO_2 + A^- \qquad (1.8)$$

$$HO_2 + Na^+ \leftrightarrow NaO_2(s) + H^+ \qquad (1.9)$$

The protons act as carrier, continually removing the superoxide from the cathode surface,[26] allowing large discharge capacities to be achieved without clogging the electrode's pore. However, water has the potential to also induce other parasitic reactions, thus other weak acid additives are under investigation.[19] The use of PPTA is one approach for controlling the formation of NaO_2 in Na-O_2 cells.

1.4 M-O_2 Battery Systems and Electrolyte Materials Studied in this Thesis

The selection of a stable electrolyte, that facilitates reversible cycling is not the only problem facing M-O_2 batteries, but it is considered to be the most important challenge that must be overcome to further develop the Li-O_2 technology[6, 20] and to a

lesser extent the Na-O_2 system[23, 30-31] (where the Na-O_2 cell chemistry is still not well understood).[30-31] In both M-O_2 systems it is not readily apparent if the desired electrochemistry, electrolyte breakdown or a combination of the two has occurred, based solely on the discharge profiles. The nature of the electrochemistry can be revealed through careful characterization of electrochemically-cycled electrodes.

The M-O_2 reaction products are expected to be a combination of amorphous and crystalline phases.[30, 32-33] Powder X-ray diffraction (PXRD) provides valuable structural information about the discharge products. However, PXRD is limited by the degree of crystallinity and is insensitive to amorphous materials. Solid-state nuclear magnetic resonance (ssNMR), on other hand, is not restricted to the surface or by the degree of crystallinity of the electrochemical particles. It delivers structural information about the local chemical environment at the nucleus of interest, offering an element-specific approach for monitoring the cell chemistry.

Within this thesis ^{7}Li, ^{17}O and ^{23}Na ssNMR are used to track the formation of the metal-oxygen reaction products as a function of the electrochemical-cycling conditions. ^{1}H and ^{31}P ssNMR were utilized to probe electrolyte decomposition. As the desirable products do not contain protonated or phosphorus-based species, evidence of ^{1}H or ^{31}P NMR signals in the NMR spectra of the cycled cathodes is expected to indicate the occurrence of chemical side reactions.

The electrolyte materials investigated by this thesis are outlined in **Table 1-3**. Chapter 2 discusses the solid-state NMR techniques that are applied, to uncover the complex reactions that occur within Li-O_2 and Na-O_2 cells.

Table 1-3 Summary of Electrolyte Materials Investigated by this thesis

Battery System	Class of Electrolyte Material	Specific Electrolyte
Li-O_2	Carbonate	PC/DMC
	Ether	TEGDME
	Phosphate Ester	TMP
Na-O_2	Ether	DEGDME

1.4.1 The Li-O_2 Battery

The pioneering work on the rechargeable, room temperature Li-O_2 battery was performed by *Abraham et al.* in 1996.[8] The original cell design employed a polymer electrolyte membrane sandwiched between a porous carbon support and a Li metal foil anode. The cell was re-charged for at least three cycles and exhibited a overpotential of 1.4 V.[8] An overpotential occurs when the charging voltage is at a higher potential than the discharge voltage.

The Li-O_2 cell design was further developed, primarily by *Read et al.*[9] and *Bruce et al.*[34], resulting in the cell configuration discussed in **section 1.3**. *Read et al*[9] examined liquid electrolytes and was the first to characterize the cell components in terms of the discharge products. His findings illustrated that the cell performance and the identity of the reaction products was influenced by the electrolyte.[9] *Bruce et al.* introduced catalytic agents to the cathode reaction and demonstrated that despite a fading capacity, capacities of at least 600 mAh/g could be reached for the 50th cycle.[34] The results of *Bruce et al.*[34] work initiated the strong interest in Li-O_2 batteries, that is still persists today.[2]

Based on the Li/O_2 electrochemical couple, there are three possible electrochemically products that could be formed during discharge; lithium oxide (Li_2O), lithium superoxide (LiO_2) and lithium peroxide (Li_2O_2), outlined in **Table 1-4**. However, only lithium peroxide is observed as a solid phase discharge product using Fourier transformed IR (FTIR), powder X-ray diffraction (PXRD), surface enhanced Raman spectroscopy [35], solution state nuclear magnetic resonance (NMR),[22] and ^{17}O solid-state NMR (ssNMR).[36] The four-electron transfer reaction, associated with Li_2O formation, is believed to be unfavourable compared to the two-electron transfer process, associated with lithium peroxide formation. Thus Li_2O is not produced. Lithium superoxide is detected as a transient species in cyclic voltammetry (CV) studies.[37] LiO_2 is initially formed and rapidly disproportions into Li_2O_2, via **equation 1.6** or LiO_2 undergoes a 2nd reduction to Li_2O_2 as outlined in **equation 1.7** .[37] Theses experimental results are consistent with computations studies, which predict LiO_2 to be unstable under the normal cell operating conditions (1 atm, 300 K). [38-39]

Table 1-4 Potential Discharge Reactions that Could Occur at the O_2 Electrode in the Li-O_2 Cell

Discharge Reaction	Potential (V vs. Li/Li^+)	Ref.
$4Li^+ + 4e + O_2 \rightarrow 4Li_2O$	2.91	[40]
$2Li^+ + 2e + O_2 \rightarrow Li_2O_2$	2.96	[40]

The electrolyte plays a critical role it the Li-O_2 electrochemistry.[20] Throughout this thesis, the stability of three electrolytes; PC/DMC, TEGDME and TMP, was evaluated using ssNMR. A summary of the electrochemical performance for each compound is provided below.

1.4.1.1 PC/DMC Electrolyte

Carbonate-based electrolytes were the first class of electrolyte solvents studied for the Li-O_2 battery. Initially in 2006, Bruce et al.[41] reported that an 1M electrolyte solution of lithium hexafluorophosphate ($LiPF_6$) in propylene carbonate (PC) facilitated the reversible formation of Li_2O_2. The cells could be cycled to a capacity of 1000 mAh/g for at least 10 times before the capacity began to fade. With PXRD the discharge product were shown to completely decompose during charging and in-situ mass spectra suggested that the O_2 was the dominant gas released during charging.[41]

It wasn't until 2011 that PC was shown to be an unsuitable Li-O_2 electrolyte.[21] Using differential electrochemical mass spectrometry (DEMS), solution state ^1H and ^{13}C NMR, PXRD, surface enhanced Raman [35] and Fourier transformed infrared spectroscopy (FTIR), Li_2O_2 was not detected.[21] Instead the discharge products were found to be Li_2CO_3, lithium formate (HCO_2Li), lithium acetate (CH_3CO_2Li), H_2O and alkyl carbonates, from electrolyte decomposition.[21] The reaction products decomposed upon charging[21] giving the appearance that the electrochemistry was reversible. The observed electrolyte instability is not exclusive to PC but will occur whenever carbonate-based electrolytes are used in Li-O_2 cells.[21]

In this thesis, a 1M solution of $LiPF_6$ in propylene carbonate / dimethyl carbonate (PC / DMC, 1:1 mixture by volume) was selected to model electrolyte breakdown in the Li-O_2 battery. The structures of PC and DMC are illustrated in **Figure 1-4**. In Chapter 3, ^7Li nutation spectroscopy is applied to identifying the Li-O_2 discharge products. An important component of the study is demonstrating that ^7Li nutation spectroscopy is

sensitive to the presence of electrochemically generated Li_2CO_3. Thus ^7Li nutation experiments were performed on electrodes extracted from Li-O_2 cells that had been cycled with the PC/DMC electrolyte. All of the electrochemical cycling and NMR measurements, utilizing the PC/DMC electrolyte system were performed in the Goward research group at McMaster Unversity

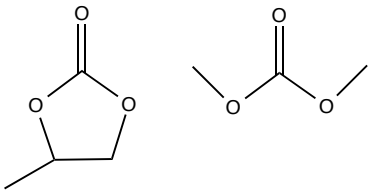

Figure 1-4 The molecular structures of the carbonate-based electrolyte studied in this thesis, a 1:1 mixture by volume of PC / DMC, left : propylene carbonate (PC) and right : dimethyl carbonate (DMC)

1.4.1.2 TEGDME Electrolyte

Ether-based electrolytes are considered the most promising electrolyte solvent for Li-O_2 cells.[20] Ethers are non-flammable, have a wide electrochemical window and display substantial stability against nucleophilic substitution by the superoxide radical.[42] This is evident from the fact that Li_2O_2 is the main discharge product.[43-44] Ether-based materials are not a perfect Li-O_2 electrolyte as Li_2CO_3 and electrolyte breakdown species (Li_2CO_3, LiOH, CH_3CO_2Li, HCO_2Li) are simultaneously formed during the operation of the cell. An additional issues is that ethers do not exhibit long-term stability.[20] The percentage of Li_2O_2 diminishes and the quantity of undesirable species grows as the number of cycles increases.[45-46] In the case of ether electrolytes, the primary

decomposition mechanism is thought to be abstraction of hydrogen by the superoxide radical.[22, 47]

Tetraethylene glycol dimethyl ether (TEGDME) is a very popular ether electrolyte owing to its low vapour pressure and high molecular weight.[20] In Chapters 3 and 4 of this thesis, TEGDME was treated as the benchmark compound for electrolyte stability as Li_2O_2 production is confirmed to occur on the first discharge.[46, 48-49] The structure of TEGDME is shown in **Figure 1-5**.

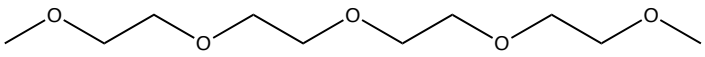

Figure 1-5 The molecular structure of tetraethylene glycol dimethyl ether (TEGDME)

In Chapter 3, the TEGDME electrolyte was selected to generate electrochemical Li_2O_2, to demonstrate that ^{7}Li nutation spectroscopy is sensitive to Li_2O_2 in cycled electrodes. In Chapter 4, the ^{17}O NMR spectrum of an extract cathode (cycled with the TEGDME electrolytes) illustrates the distinct ^{17}O signature of Li_2O_2. Chapter 5 outlines an in-depth ^{1}H and ^{17}O NMR study of cycled electrodes, which explores the first and second discharge.

All electrochemically cycling and ^{17}O enrichment was performed in the Goward research group, at McMaster University. The ^{7}Li and ^{17}O NMR spectra collected at 11.7 T (Chapters 3 and 4), were acquired at McMaster University under the supervision of Prof. Gillian Goward. The high field (21.1 T) ^{17}O NMR spectra discussed in Chapter 5, were collected at the National Ultra-high Field Facility for Solids at the National

Research Council in Ottawa. The experiments collected at this facility were completed by or under the supervision of Dr. Victor V. Terskikh. All NMR spectra were processed at McMaster University under the supervision of Prof. Gillian Goward.

1.4.1.3 TMP Electrolyte

Phosphate esters have not been widely investigated as potential Li-O_2 electrolytes. One phosphate ester, triethyl phosphate (TEP), has demonstrated some promise as potential electrolyte solvent. Li_2CO_3 was reported as the main discharge product with some evidence of Li_2O_2 based on an X-ray photoelectron spectroscopy (XPS) investigation.[50] In both the XRD and FTIR studies low signal intensity was observed, implying that the discharge species may be amorphous.[50] This suggests that phosphate esters warrant further investigation using a technique that is sensitive to the bulk material and independent of the degree of crystallinity, such as ssNMR.

In this thesis an analogous material, trimethyl phosphate (TMP) was investigated as a potential Li-O_2 electrolyte via multinuclear ssNMR. TMP was selected, as it has many desirable chemical and physical properties; a low viscosity (2 mPa/s), high boiling point (197 ^{o}C) and TMP has a low-flammability.[51-52] This safe electrolyte is expected to allow sufficient Li^+ conduction without worrying that the electrolyte will evaporate during the operation of the cell.

Additionally the central phosphorusatom in TMP is expected to be stable against nucleophilic attack. The phosphorusis found in its highest oxidation state of + 5, thus the phosphorus cannot be further oxidized by the superoxide species. TMP is expected to be a safe and stable electrolyte. The structure of TMP is shown in **Figure 1-6.**

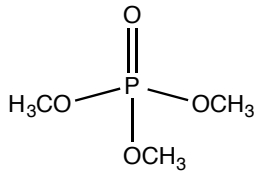

Figure 1-6 The molecular structure of trimethyl phosphate (TMP)

Chapters 3 and 4 of this thesis focus on characterizing the discharge products formed when the TMP electrolyte was used in Li-O_2 cells. In Chapter 3, ^{7}Li nutation spectroscopy and ^{17}O NMR demonstrate that TMP is an unsuitable electrolyte as Li_2CO_3 is found to be the main product. Chapter 4 explores the origin of the electrolyte instability and proposes a mechanism that accounts for the formation of reaction products, observed in the ^{1}H, ^{7}Li, ^{17}O and ^{31}P NMR spectra of the cycled electrodes. All of the electrochemical cycling and NMR measurements were performed in the Goward research group at McMaster University.

1.4.2 The Na-O_2 Battery

The non-aqueous, room temperature Na-O_2 battery was first reported by *Sun et al.*[16] in 2011. The design of the Na-O_2 battery is analogous to the Li-O_2 cell, where the Li anode is replaced by metallic Na and the electrolyte contains Na^+ ions. In spite of the similar characteristics between Li and Na, different discharge products are produced in Li-O_2 and Na-O_2 cells.[16-17, 21] This implies that each system has a unique underlying mechanism.[17]

The key difference in the Li-O_2 and Na-O_2 battery chemistries is thought to be stability of the metal superoxide.[38, 53] As discussed in **section 1.4.1**, lithium superoxide is

not stable in Li-O_2 cells. However, initial experimental studies[17, 54] and theoretical calculations[38, 53] proposed that NaO_2 has an increased stability compared to LiO_2. The increased stability is attributed to Na^+ being a softer Lewis acid, with a higher polarizability, which more effectively stabilizes the superoxide. As noted in **section 1.4.1**, there are three potential oxide species that may be created during the discharge process; sodium oxide (Na_2O), NaO_2 and sodium peroxide (Na_2O_2). The discharge reactions and the theoretical formation potentials for each product is outline in **Table 1-5.** It should be noted that sodium oxide is not experimentally observed. This is attributed to the fact that the theoretical formation potential of Na_2O (1.94 V) is lower than the experimentally observed discharge plateau voltage ($\geq$ 2.0 V).[7, 16]

Table 1-5 Potential Discharge Reactions that Could Occur at the O_2 Electrode in the Na-O_2 Cell

Discharge Reaction	Potential (V vs. Na/Na^+)	Ref.
$4Na^+ + 4e + O_2 \rightarrow 4Na_2O$	1.94	[16]
$Na^+ + e + O_2 \rightarrow NaO_2$	2.26	[16]
$2Na^+ + 2e + O_2 \rightarrow Na_2O_2$	2.33	[16]

NaO_2 and Na_2O_2 have similar theoretical formation potentials to each other and are within error of each other, with respect to the experimental discharge plateau value.[16] Thus the electrochemical product cannot be directly elucidated by only considering the discharge profile. Na_2O_2 is the thermodynamically preferred product, whereas NaO_2 is the kinetically favored species produced via a single electron transfer.[16] There is a likely a competition between the formation of the two products during discharge.[55] Experimentally this has been observed, where the distribution of NaO_2 and Na_2O_2 is

correlated to the applied current density. High current densities favor the formation of the kinetic product NaO_2, whereas lower current densities resulted in the thermodynamically favored product, Na_2O_2.[55]

In a similar fashion to the Li-O_2 battery, the choice of electrolyte influences the discharge products produce in Na-O_2 cells. Carbonate-based electrolytes were the first class of organic electrolytes tested for the Na-O_2 battery.[16] Both Na_2O_2 and Na_2CO_3, (an electrolyte breakdown species), were observed in TEM and FTIR studies of cycled-electrodes.[16] Evidence of Na_2O_2 with a carbonate-based electrolyte suggests that the Na-O_2 cells operate as a cleaner battery system with fewer parasitic side reactions.[17] The promise of a more stable M-O_2 battery system, with better reversibility is the main motivation for examining the sodium-oxygen chemistry.

In an attempt to decrease the degree of electrolyte breakdown, the electrochemical community has changed its focus to ether-based organic solvents, which have displayed increased stability against nucleophilic attack in the Li-O_2 system.[22]

1.4.2.1 DEGDME Electrolyte

The focus to date has been on the use of linear ether molecules such as; DME[56], diethylene glycol dimethyl ether (DEGDME)[23-24, 30-31, 54-55] and TEGDME,[57] with the majority of the studies concentrating on the popular electrolyte, DEGDME. When NaO_2 is exclusively formed, a very low overpotential on charging (<200 mV) is observed, [54, 58] as illustrated in **Figure 1-7**. When the cell exhibits a low charge overpotential the battery is able to operate within an electrochemical window that minimizes the oxidation of side products during charge.[54] This also offers the benefit of increased round-trip efficiency

of charge and discharge. Thus resulting in a battery with good reversibility and cleaner chemistry.[17]

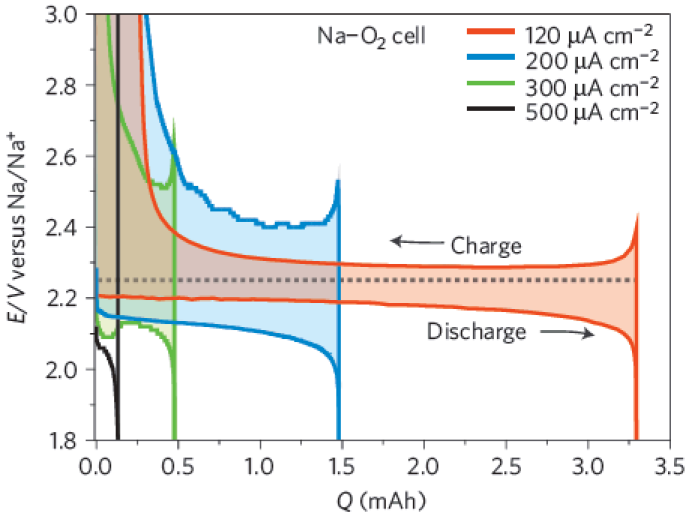

Figure 1-7 Discharge-charge cycles of Na-O_2 cells at various current densities, cutoff potentials were set to 1.8 V for discharge and 3.6 V for charge. Dotted line: $E^0(NaO_2)$ – 2.27 V[54], reproduced with permission. Copyright 2012, Nature Publishing Group

The exclusive formation of NaO_2 has been reported with ether-based electrolytes.[54, 58] However, sodium superoxide is an elusive and potentially unstable[31] component. The electrochemical formation of pure NaO_2 has not yet been reproduced. [18, 30-31, 55, 59] Instead sodium peroxide (Na_2O_2)[56], sodium peroxide dihydrate ($Na_2O_2 \cdot 2H_2O$)[57] and a mixture thereof[30-31, 55] have been reported as the main discharge products by; PXRD[30, 55, 57], Raman[30, 55], IR[55], TEM[31, 56], SEM[30-31, 55] X-Ray absorption near edge structure (XANES)[31] and X-Ray photoelectron spectroscopy (XPS)[55]. The reason for the variation in the discharge species is not yet understood but may be related to differences in the experimental conditions.[40] The electrochemical performance of the Na-O_2 cell is also found to vary depending on the particular reaction product produced.

When Na_2O_2 is detected, poor reversibility and higher overpotentials ranging from 0.3 V to > 1.0 V, are observed.[60] The Na-O_2 electrochemical curve associated with Na_2O_2 formation (**Figure 1-8**), takes on a similar appearance to typical Li-O_2 curves (**Figure 1-9**), which have large overpotentials.

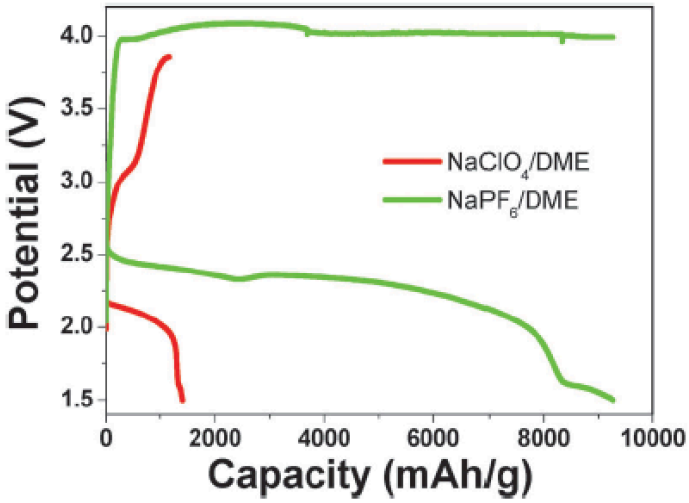

Figure 1-8 First galvanostatic curves of (graphene nanosheets) Na-O_2 cells in $NaClO_4$/DME and $NaPF_6$/DME electrolytes at 200 mA/g[60], reproduced with permission. Copyright 2013, Royal Society of Chemistry.

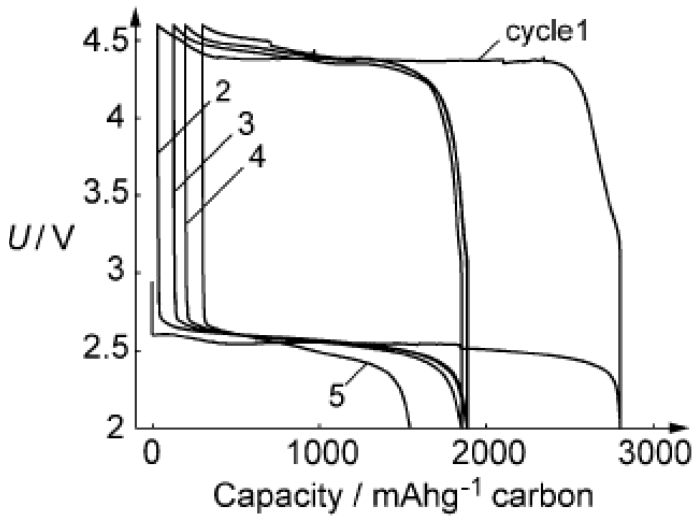

Figure 1-9 Electrochemical Li-O_2 curves of a super P/Kynar cathode cycled in 1 M $LiPF_6$ in TEGDME under 1 atm O_2 between 2 and 4.6 V vs. Li/Li^+ [22], reproduced with permission. Copyright 2011, American Chemical Society

Recent studies have further brought into question the stability of NaO_2. The decomposition products produced do not fully decompose on charge[23] and NaO_2 has been observed to undergo side reactions.[30-31] This illustrates that the Na-O_2 battery chemistry may be more problematic[30] than originally believed. It is critical to the ongoing developmental of the Na-O_2 technology, that there is a clear understanding of the electrochemical reactions.

In Chapter 6 of this thesis, solid-state ^{23}Na NMR techniques are applied for the first time, to examine the expected pristine Na-O_2 reaction products. The ^{23}Na NMR study is expanded in Chapter 7 to include electrochemically-cycled electrodes. In Chapter 7, the widely studied DEGDME electrolyte was selected. The molecular structure of

DEGDME is shown in **Figure 1-10**. The electrochemically cycling was performed both in the Goward research group at McMaster University and by our collaborators at Western University. All ^{23}Na NMR spectra were collected and processes at McMaster University under the supervision of Prof. Gillian Goward.

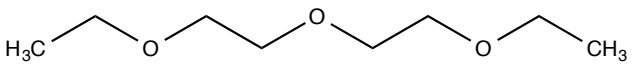

Figure 1-10 The molecular structure of diethylene glycol diethyl ether (DEGDME)

1.5 Summary

Multinuclear solid-state NMR is a sensitive tool for investigating metal-oxygen batteries. The following chapters demonstrate the use of solid-state NMR to characterize the Li-O_2 and Na-O_2 discharge products; particular its application in evaluating Li-O_2 electrolyte materials and in untangling the Na-O_2 battery chemistry. Overall a deeper understanding of the Li-O_2 and Na-O_2 electrochemistries will aid in the selection of stable materials for M-O_2 cells. This is expected to enhance the electrochemical performance of the batteries and contribute to improving this emerging class of energy storage devices.

1.6 References

[1] B. G. Pollet;I. Staffell;J. L. Shang, *Electrochimica Acta* **2012**, *84*, 235.
[2] G. Girishkumar, McCloskey, B., Luntz, C., Swanson, S. and Wilcke, W. , *J. Phys. Chem. Lett.* **2010**, *1*, 2193.
[3] J. B. Goodenough;K.-S. Park, *J. Am. Chem. Soc.* **2013**, *135*, 1167.
[4] Y. Nishi, *The Chemical Record* **2001**, *1*, 406.
[5] J. B. Goodenough;Y. Kim, *Chem. Mater.* **2010**, *22*, 587.
[6] P. G. Bruce;A. Freunberger Stefan;L. J. Hardwick;J.-M. Tarascon, *Nat Mater* **2012**, *11*, 172.
[7] S. K. Das;S. Lau;L. A. Archer, *J. Mater. Chem. A* **2014**, *2*, 12623.
[8] K. Abraham;Z. Jiang, *J. Electrochem. Soc.* **1996**, *143*, 1.
[9] J. Read, *J. Electrochem. Soc.* **2002**, *149*, A1190.
[10] I. Kowalczk;J. Read;M. Salomon, *Pure Appl. Chem.* **2007**, *79*, 851.
[11] E. Peled, *J. Electrochem. Soc.* **1979**, *126*, 2047.
[12] K. Xu, *Chem. Rev.* **2004**, *104*, 4303.
[13] N. Yabuuchi;K. Kubota;M. Dahbi;S. Komaba, *Chem. Rev.* **2014**, *114*, 11636.
[14] B. L. Ellis;L. F. Nazar, *Curr. Opin. Solid State Mater. Sci.* **2012**, *16*, 168.
[15] M. D. Slater;D. Kim;E. Lee;C. S. Johnson, *Adv. Funct. Mater.* **2013**, *23*, 947.
[16] Q. Sun;Y. Yang;Z.-W. Fu, *Electrochem. Commun.* **2012**, *16*, 22.
[17] B. D. McCloskey;J. M. Garcia;A. C. Luntz, *J. Phys. Chem. Lett.* **2014**, *5*, 1230.
[18] H. Yadegari;Q. Sun;X. Sun, *Adv. Mater.* **2016**, *28*, 7065.
[19] D. Aurbach;B. D. McCloskey;L. F. Nazar;P. G. Bruce, *Nature Energy* **2016**, *1*, 16128.
[20] M. Balaish;A. Kraytsberg;Y. Ein-Eli, *Phys. Chem. Chem. Phys.* **2014**, *16*, 2801.
[21] S. A. Freunberger;Y. Chen;Z. Peng;J. M. Griffin;L. J. Hardwick;F. Barde;P. Novak;P. G. Bruce, *J. Am. Chem. Soc.* **2011**, *133*, 8040.
[22] S. A. Freunberger;Y. Chen;N. E. Drewett;L. J. Hardwick;F. Bardé;P. G. Bruce, *Angew. Chem. Int. Ed.* **2011**, *50*, 8609.
[23] R. Black;A. Shyamsunder;P. Adeli;D. Kundu;G. K. Murphy;L. F. Nazar, *ChemSusChem* **2016**, *9*, 1795.
[24] C. Xia;R. Fernandes;F. H. Cho;N. Sudhakar;B. Buonacorsi;S. Walker;M. Xu;J. Baugh;L. F. Nazar, *J. Am. Chem. Soc.* **2016**, *138*, 11219.
[25] L. Johnson;C. Li;Z. Liu;Y. Chen;S. A. Freunberger;P. C. Ashok;B. B. Praveen;K. Dholakia;J.-M. Tarascon;P. G. Bruce, *Nat. Chem.* **2014**, *6*, 1091.
[26] C. Xia;R. Black;R. Fernandes;B. Adams;L. F. Nazar, *Nat Chem* **2015**, *7*, 496.
[27] D. Geng;N. Ding;T. Hor;S. W. Chien;Z. Liu;D. Wuu;X. Sun;Y. Zong, *Adv. Energy. Mater.* **2016**.
[28] R. G. Pearson, *J. Am. Chem. Soc.* **1963**, *85*, 3533.
[29] V. Gutmann, *Coord. Chem. Rev.* **1976**, *18*, 225.
[30] J. Kim;H. Park;B. Lee;W. M. Seong;H.-D. Lim;Y. Bae;H. Kim;W. K. Kim;K. H. Ryu;K. Kang, *Nat. Commun.* **2016**, *7*.
[31] H. Yadegari;M. N. Banis;B. Xiao;Q. Sun;X. Li;A. Lushington;B. Wang;R. Li;T.-K. Sham;X. Cui;X. Sun, *Chem. Mater.* **2015**, *27*, 3040.

[32] R. R. Mitchell;B. M. Gallant;Y. Shao-Horn;C. V. Thompson, *J. Phys. Chem. Lett.* **2013**, *4*, 1060.
[33] J. Wang;Y. Li;X. Sun, *Nano Energy* **2013**, *2*, 443.
[34] T. Ogasawara;A. Debart;M. Holzapfel;P. Novak;P. G. Bruce, *J. Am. Chem. Soc.* **2006**, *128*, 1390.
[35] I. Belharouak;W. Lu;D. Vissers;K. Amine, *Electrochem. Commun.* **2006**, *8*, 329.
[36] M. Leskes;N. E. Drewett;L. J. Hardwick;P. G. Bruce;G. R. Goward;C. P. Grey, *Angew. Chem. Int. Ed.* **2012**, *51*, 8560.
[37] Z. Peng;S. A. Freunberger;L. J. Hardwick;Y. Chen;V. Giordani;F. Bardé;P. Novák;D. Graham;J. M. Tarascon;P. G. Bruce, *Angew. Chem.* **2011**, *123*, 6475.
[38] B. Lee;D.-H. Seo;H.-D. Lim;I. Park;K.-Y. Park;J. Kim;K. Kang, *Chem. Mater.* **2014**, *26*, 1048.
[39] J. Sangster;A. D. Pelton, *J. Phase Equilib.*, *13*, 296.
[40] P. Adelhelm;P. Hartmann;C. L. Bender;M. Busche;C. Eufinger;J. Janek, *Beilstein L. Nanotechnol.* **2015**, *6*, 1016.
[41] T. Ogasawara;A. Debart;M. Holzapfel;P. Novak;P. G. Bruce, *J. Am. Chem. SOC.* **2006**, *128*, 1390.
[42] V. S. Bryantsev;V. Giordani;W. Walker;M. Blanco;S. Zecevic;K. Sasaki;J. Uddin;D. Addison;G. V. Chase, *J. Phys. Chem. A* **2011**, *115*, 12399.
[43] S. A. Freunberger;Y. Chen;N. E. Drewett;L. J. ardwick;F. Bard;P. G. Bruce, *Angewandte Chemie* **2011**, *50*, 8609.
[44] M. Leskes;A. J. Moore;G. R. Goward;C. P. Grey, *J. Phys. Chem. C* **2013**, *117*, 26929.
[45] B. D. McCloskey;D. S. Bethune;R. M. Shelby;G. Girishkumar;A. C. Luntz, *J. Phys. Chem. Lett.* **2011**, *2*, 1161.
[46] A. Freunberger Stefan;Y. Chen;N. E. Drewett;L. J. Hardwick;F. Bardé;P. G. Bruce, *Angew. Chem. Int. Ed.* **2011**, *50*, 8609.
[47] B. D. Adams;R. Black;Z. Williams;R. Fernandes;M. Cuisinier;E. J. Berg;P. Novak;G. K. Murphy;L. F. Nazar, *Adv. Energy. Mater.* **2015**, *5*.
[48] H.-G. Jung;J. Hassoun;J.-B. Park;Y.-K. Sun;B. Scrosati, *Nat Chem* **2012**, *4*, 579.
[49] J. Hassoun;H.-G. Jung;D.-J. Lee;J.-B. Park;K. Amine;Y.-K. Sun;B. Scrosati, *Nano Lett.* **2012**, *12*, 5775.
[50] W. Xu;J. Hu;M. H. Engelhard;S. A. Towne;J. S. Hardy;J. Xiao;J. Feng;M. Y. Hu;J. Zhang;F. Ding;M. E. Gross;J.-G. Zhang, *J. Power Sources* **2012**, *215*, 240.
[51] X. Wang;E. Yasukawa;S. Kasuya *J. Electrochem. Soc.* **2001**, *148*, A1066.
[52] J. K. Feng;X. P. Ai;Y. L. Cao;H. X. Yang, *J. Power Sources*, *177*, 194.
[53] S. Kang;Y. Mo;S. P. Ong;G. Ceder, *Nano letters* **2014**, *14*, 1016.
[54] P. Hartmann;C. L. Bender;M. Vračar;A. K. Dürr;A. Garsuch;J. Janek;P. Adelhelm, *Nat. Mater.* **2013**, *12*, 228.
[55] H. Yadegari;Y. Li;M. N. Banis;X. Li;B. Wang;Q. Sun;R. Li;T.-K. Sham;X. Cui;X. Sun, *Energy Environ. Sci.* **2014**, *7*, 3747.
[56] W. Liu;Q. Sun;Y. Yang;J.-Y. Xie;Z.-W. Fu, *Chem. Commun.* **2013**, *49*, 1951.
[57] J. Kim;H.-D. Lim;H. Gwon;K. Kang, *Phys. Chem. Chem. Phys.* **2013**, *15*, 3623.

[58] C. L. Bender;P. Hartmann;M. Vračar;P. Adelhelm;J. Janek, *Adv. Energy. Mater.* **2014**, *4*, 1301863.
[59] N. Ortiz-Vitoriano;T. P. Batcho;D. G. Kwabi;B. Han;N. Pour;K. P. C. Yao;C. V. Thompson;Y. Shao-Horn, *J. Phys. Chem. Lett.* **2015**, *6*, 2636.
[60] W. Liu;Q. Sun;Y. Yang;J.-Y. Xie;Z.-W. Fu, *Chem. Commun.* **2013**, *49*, 1951.

Chapter 2 : Introduction to Solid-State NMR Spectroscopy

2.1 Introduction

Solid-state nuclear magnetic resonance (ssNMR) is the main technique applied to examine electrolyte stability and characterize the metal-oxygen reaction products, presented in Chapter 1. Prior to this thesis, there had only been a limited number of studies utilizing ssNMR spectroscopy to investigating the Li-O_2 battery,[1-2] and no studies had been performed on Na-O_2 cells. Throughout this thesis, quadrupolar nuclei play an important role in the investigation of the lithium–oxygen and sodium-oxygen battery chemistries.

This chapter presents the theoretical background, describing the interactions that govern the behavior of a nuclear spin in an applied magnetic field. Since quadrupolar nuclei are a critical component of this thesis, a description of the quadrupole interaction is included. Despite ^{17}O being a challenging NMR nucleus, ^{17}O NMR is the main spectroscopic handle available to uncover the Li-O_2 electrochemistry.[1] The strategies applied to overcome the difficulties associated with ^{17}O NMR are also highlighted.

2.2 Nuclear Spins in a Magnetic Field

2.2.1 Behavior of a Nuclear Spin in an Applied Magnetic Field

A nucleus is identified by the atomic number (Z), mass number and nuclear spin quantum number (I). If the atomic number and the mass number of the nucleus are both even then I = 0 and the nucleus is magnetically inactive. If on the other hand, the nucleus possesses either an odd mass, odd atomic number or both, then the nucleus has a non-zero spin, is magnetically active and possesses a non-zero magnetic moment (μ_N).[3] The μ_N is defined by **equation 2.1**[4]:

$$\boldsymbol{\mu_N} = \gamma_N \hbar \boldsymbol{I} = g_N \beta_N \boldsymbol{I} \quad (2.1)$$

The nuclear spin, I, is an intrinsic form of angular momentum, $\hbar I$ is the spin angular momentum vector and γ_N is the gyromagnetic ratio of the nucleus, where the units are reported in term of $\text{radians} \cdot \sec^{-1} \cdot \text{gauss}^{-1}$.[4] Alternatively the magnetic moment may also be expressed in terms of the nuclear g factor (g_N) and the nuclear magneton (β_N).[4] Together the values of g_N and I distinguish one nucleus from the next.[4]

The nuclear spin angular momentum is quantized into discrete nuclear spin states, whose values ranging from $+I$ to $-I$, filling in the sequence outlined in **equation 2.2**, where m_I is the nuclear spin quantum number. [3-4]

$$m_I = +I, (I-1), \ldots, (-I-1), -I \quad (2.2)$$

Protons (hydrogen nuclei) are the most commonly studied NMR nucleus. In the case of ^{1}H, I = ½ thus there are two allowed spin states m_I = + ½ and m_I = -½. In the presence of an external static magnetic field B_0, there will be an interaction between the magnetic moment μ_N, B_0 and the Hamiltonian ($\mathcal{H}$, the energy operator). The interaction is described in **equation 2.3**:[4]

$$\mathcal{H} = -\boldsymbol{\mu_N} \cdot \mathbf{B_0} \quad (2.3)$$

When a nucleus (that possess a I > 0) is in the presence of an applied magnetic field, the nuclear spins will move around the applied field, keeping a constant angle between the μ_N and B_0. This type of motion is called precession.[5] The rate at which the precession occurs is the Larmor frequency (ω_0). The Larmor frequency, **equation 2.4**, is governed by both, the magnetic field strength and the gyromagnetic ratio.[4]

$$\omega_0 = \gamma \boldsymbol{B}_0 \qquad (2.4)$$

In NMR literature, the magnetic field strength is often reported in terms of the proton Larmor frequency. The fields described as 200 MHz, 500 MHz and 900 MHz correspond to the respective magnetic fields strengths of 4.70 T, 11.7 T and 21.1 T.

2.2.2 Zeeman Splitting in an Applied Magnetic Field

For a given nucleus with a spin, *I*, there are *2I + 1* allowed spin states. In the absence of an applied magnetic field, the energy of all of the spin states are equivalent.[3-5] The introduction of an applied magnetic field (B_0) breaks the degeneracy and the energy levels split. This separation of the energy levels is the Zeeman splitting.[5]

By convention, the applied static magnetic field is along the z-direction. There is an interaction between the nuclear spins' magnetic moment and B_0 (**equation 2.3**) which may be rewritten in terms of I_z, in **equation 2.5**, where I_z is to the component of the nuclear spins along the z direction.[4]

$$\mathcal{H} = -\gamma \mathbf{B_0} \hbar \boldsymbol{I_z} \qquad (2.5)$$

For the ^{1}H nucleus, the spins will occupy either the + ½ or the -½ spin state as illustrated in the energy level diagram, **Figure 2-1**. The magnetic moment of m_I = + ½ aligns with B_0, whereas the magnetic moment of the m_I = - ½ spin state are antiparallel to

B_0. Thus the $m_I = + ½$ spin state is a lower energy, than the $m_I = - ½$ spin state. The lower energy spin state ($m_I = + ½$) is denoted α and the higher energy spin ($m_I = - ½$) is denoted β. [4]

The distribution of the spins between the two possible spin states is governed by the Boltzmann distribution (**equation 2.6**), where ΔE is the energy difference between α and β (**equation 2.7**), k is the Blotzmann constant 1.38 x10-^{23}J/K·mole, T is the temperature (K) and $\frac{N_\beta}{N_\alpha}$ is the population ratio between m_α and m_β.[5]

$$\frac{N_\beta}{N_\alpha} = e^{-\Delta E/kT} \quad (2.6)$$

$$\Delta E = -\gamma B_0(m_\beta - m_\alpha) = h\omega_0 \quad (2.7)$$

A schematic representation of the Zeeman interaction for a ^{1}H nucleus is illustrated in **Figure 2-1**.[3-4]

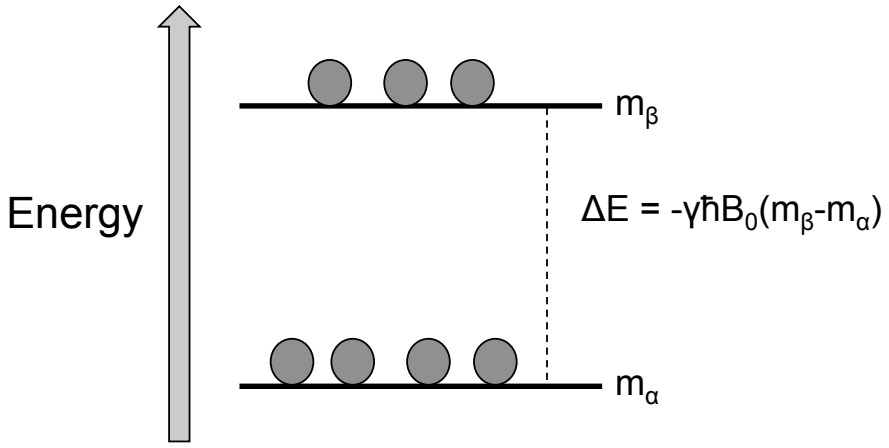

Figure 2-1 A Schematic illustration of the Zeeman interaction for a spin ½ nucleus

2.2.3 Radiofrequency Pulses

In the presence of an external magnetic field (B_0), the bulk magnetization of the spin system is aligned along the z-axes. The free induction decay (FID) is the observable NMR signal, which arises from the precession of the magnetization in the xy plane. The bulk magnetization is rotated from the z-axes into the xy plane through the application of an oscillating radio frequency (RF) field (a magnetic field denoted B_1). The RF field has a similar frequency to the Larmor frequency of the nucleus. The application of the B_1 field causes a rotation about either the x- or y-axes through the flip angle, β, **equation 2.8**[5], where ω_1 is the Larmor frequency, and t_p is the length of time for which the RF pulse is applied. The flip angle can be controlled by varying t_p.[6-7]

$$\beta = \omega_1 t_p \qquad (2.8)$$

Equation 2.9 is the Hamiltonian that describes the interaction of the nuclear spins with the external static field and the interaction of the nuclear spins with a pulse applied along

the x-axis, oscillating at ω_{RF}.[8] $B_0\boldsymbol{I_Z}$ is the interaction of the spins with the external static B_0 field and the $2B_1\boldsymbol{I_X}\cos\omega_{RF}\tau$ term describes the interaction of the spins with the oscillating B_1 field.[8]

$$\mathcal{H} = -\gamma(B_0\boldsymbol{I_Z} + 2B_1\boldsymbol{I_X}\cos\omega_{RF}\tau) \quad (2.9)$$

The presence of the quadrupole interaction further complicates the interaction between the RF field and spin system, and is further discussed in Section 2.3.5.

2.2.4 Nuclear Spin Relaxation

The application of the B_1 field perturbs the distribution of the populations (between the spin states) away from the thermal equilibrium governed by the Boltzmann distribution. The populations are restored to their original configuration though a process called relaxation. Nuclear relaxation is not spontaneous but requires simulation from a fluctuating local magnetic field.[5] There are two modes of nuclear spin relaxation, spin-lattice relaxation also known as longitudinal relaxation, or T_1 relaxation and, spin-spin relaxation, which is also called transverse relaxation or T_2 relaxation. Chemical shielding anisotropy (CSA), dipolar coupling, the paramagnetic interactions and the quadrupole interaction are the main contributions to relaxation mechanisms in solids where applicable.[5]

2.2.4.1 Spin-Lattice Relaxation

The spin-lattice time constant (T_1) is the time period required for the spins to relax from the xy-plane to the z-plane, after the application of a RF pulse (**Figure 2-2**).

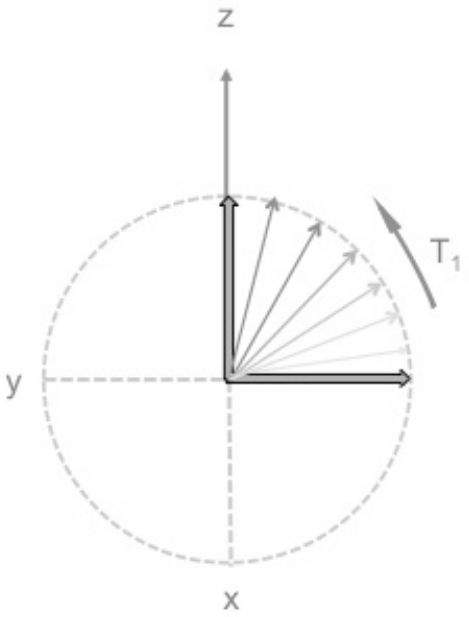

Figure 2-2 Spin-lattice relaxation after a pulse places the imagination in the xy-plane

During T_1, the spins relax to the thermal equilibrium conditions, by releasing excess energy to the surrounding crystal lattice in the form of thermal energy. Recovery of the magnetization along the z-axis (M_z), from 0 to the original equilibrium value M_z^{eq}, is described mathematically by the exponential **equation 2.10** [5].

$$M_z = M_z^{eq}\left(1 - e^{-\frac{t}{T_1}}\right) \qquad (2.10)$$

The spin-lattice relaxation time is influenced by the surrounding crystallographic environment at the nucleus and provides insight into the chemical structure. For a spin ½ nucleus the dipolar coupling and CSA interactions are the main contributors to T_1. If the nuclear spin is greater than ½, then the T_1 is governed by the quadrupole interaction, unless unpaired electrons are present. In that case, the paramagnetic interaction is the main factor influencing the nucleus' T_1.[5]

T_1 is an important experimental parameter. It is measured either with inversion recovery or by saturation recovery experiments. To obtain NMR spectra where the integrated resonances are representative of the actual amounts of materials present for each site, the wait period between each experiment must be five times T_1. For some materials this is possible. However, for diamagnetic Li- and Na-containing materials this will result in extremely long experimental times, especially if the nucleus is in a high symmetry site (i.e. CSA and quadrupole interactions are not present). For diamagnetic materials the T_1 can range from several seconds to tens of seconds.[5] Conversely, the T_1 is dramatically reduced to the microsecond-millisecond timescale, if the material is paramagnetic. The decrease in the T_1 occurs because the electronic state (T_{1e}), of the unpaired electron, that participates in the electron-nuclear paramagnetic interaction has a very short lifetime.[9]

In a complex mixture, containing both diamagnetic and paramagnetic materials, it is possible to separate the fast and slow relaxing materials via T_1 filtering experiments. This simple and effect approach is utilized in Chapter 6, to detect the presence of the paramagnetic sodium superoxide in a multi-component mixture.

2.2.4.2 Spin-Spin Relaxation

After the application of an RF pulse, the spins are aligned together in the xy-plane, the same plane where the NMR signal is detected. Over time the spins spread out, (dephasing) until the net magnetization is zero, **Figure 2-3**. The rate at which the spins diphase in the xy-plane is the spin-spin time constant (T_2) and the dephasing spins generate the detectable NMR signal.[5]

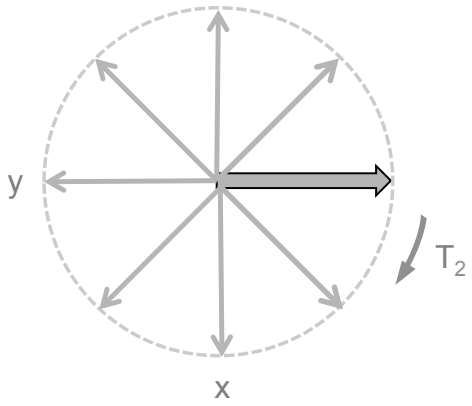

Figure 2-3 Spin-spin relaxation after the application of a pulse, which puts the magnetization in the xy-plane (the z direction is coming out of the page)

The magnitude of T_2 influences the appearance of the NMR spectrum. A long T_2 (slow relaxation in the xy-plane) results in a sharp NMR resonance, whereas a short T_2 (fast relaxation in the xy-plane) corresponds to a broad lineshape. T_2 may be directly determined from the line width of the NMR resonance. First the full width at half max (FWHM) is determined (in Hz) for the peak of interest. Next the T_2 is calculated by taking the inverse of FWHM.[5]

$$\text{FWHM} = \frac{1}{T_2} \quad (2.11)$$

Alternatively T_2 may also be measured using QCPMG[10] (which is further discussed in section 2.5) or with a Hanh echo[11] experiment where the delay time is systemically increased.

2.2.5 Magic Angle Spinning (MAS)

Magic angle spinning (MAS) is a technique, which is routinely applied in ssNMR to mimic the narrow line widths found in solution-state NMR spectra. Solid-state spectra are inherently broader because the affects from CSA, dipolar coupling and the quadrupole interaction are observable. The Hamiltonian, for each interaction, contains an angular dependent term ($3\cos^2\theta - 1$), illustrated by the heteronuclear dipolar coupling Hamiltonian for two nuclear spins; *i* and *j*:[8]

$$\mathcal{H}_D = -\frac{\mu_0}{4\pi}\frac{\gamma_i\gamma_j\hbar}{r_{ij}^3}(3\cos^2\theta - 1) \qquad (2.12)$$

In solution-state, the nuclei are constantly tumbling and the orientation of the CSA, the dipolar coupling and quadrupole tensors are rapidly averaged over all values, effectively averaging the $(3\cos^2\theta - 1)$ term to zero on the NMR timescale,[8] and the anisotropic interactions are not observed.

MAS achieves a similar result for solid-state samples, by physically spinning the samples at the magic angle with respect to the magnetic field. The magic angle, $54.74°$, is the θ value which causes the angular dependence term, $(3\cos^2\theta - 1)$, to drop to zero.[8] For the interaction to be completely eliminated from the solid-state spectra, the (i.e. only the isotropic chemical shift is observed) the spinning rate must be at least three times greater than the value of the interaction in Hz.[8] When sufficiently fast spinning is not achieved, the signal is divided into frequency bands, called spinning side bands, which are separated by the spinning speed. **Figure 2-4** compares the ^{7}Li spectra of lithium acetate under static and MAS conditions.

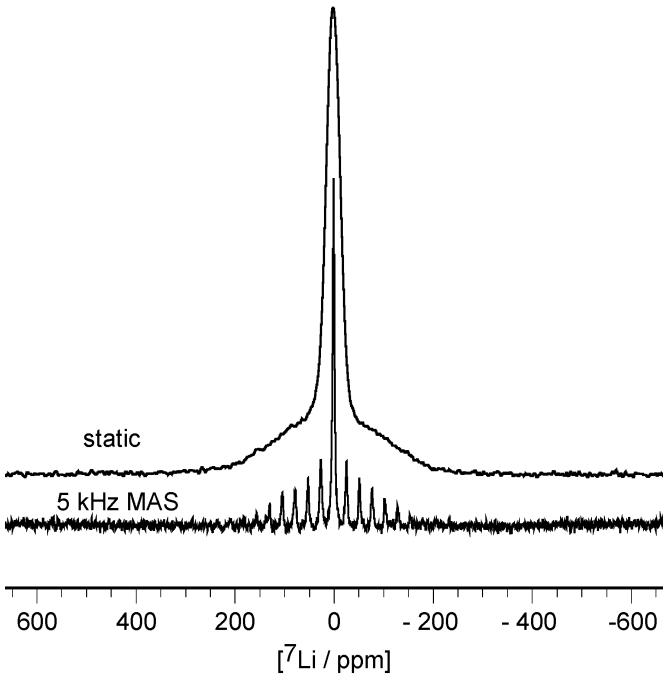

Figure 2-4 Comparison of the static and MAS ^{7}Li NMR spectra of lithium acetate, collected at 11.7 T, where the most intense resonance in the MAS spectrum corresponds to the isotropic peak

MAS is effective at removing the broadening due to CSA and dipolar interactions. However, the quadrupole lineshape is only partially narrowed under MAS. The second-order quadrupole interaction contains two terms angular dependent terms and there is no single axis spinning technique, that completely eliminates both terms.[8] The behavior of quadrupolar nuclei under MAS conditions is further discussed in section 2.3.3.

2.3 Solid-State NMR of Quadrupole Nuclei

Quadrupolar nuclei have a spin > ½ and possess electric quadrupole moments (eQ). Q is a nuclear property, which is measured in terms of m^2 and is independent of the nucleus' chemical environment. The values of Q for the presented half-integer

quadrupolar nuclei (^{7}Li, ^{17}O and ^{23}Na) are listed later in **Table 2.1**. The quadrupole coupling constant (C_q) arises from the interaction of the eQ with the electric field gradient (EFG), which is reflective of the distribution of charge around the nucleus. The C_q may range from 0 kHz to several MHz depending on the magnitude of Q and the degree of symmetry at the crystallographic site. The local geometry of the quadrupolar nucleus greatly influences NMR lineshape, allowing quadrupolar NMR to be a sensitive probe of molecular structure. Throughout this thesis, quadrupolar nuclei were heavily relied on to identify the metal-oxygen reaction products.

2.3.1 Quadrupole Parameters

The quadrupole interaction is described by the quadrupole coupling constant C_q, and eta (η_q). C_q (**equation 2.13**)[12] is a measure of the interaction between the nuclear electric quadrupole moment (eQ) and e_q, where e_q is the largest component of the electric field gradient tensor (**V**). The electric field gradient tensor (EFG) has three principal axes; V_{xx}, V_{yy} and V_{zz}, and by convention $V_{zz} \geq V_{xx} \geq V_{yy}$, thus $e_q = V_{zz}$.[12] The EFG is determined by the distribution of charge (which arises from electrons and other nuclei) surrounding the nucleus. η_q (**equation 2.14**)[12] is a dimensionless parameter, which reflects the asymmetry of the EFG. The values of C_q and η_q greatly influence the lineshape of both the central transition and the satellite transitions since both are affected by the quadrupole interaction. The influence of the quadrupole interaction on the NMR lineshape is further addressed in section 2.3.3. [12-13]

$$C_q = \frac{e^2 qQ}{h} \qquad (2.12)$$

$$\eta_q = \frac{V_{xx} - V_{yy}}{V_{zz}} \quad (2.13)$$

The electric quadrupole moments for the studied nuclei are outlined in **Table 2-1**. Given that the quadrupole coupling involves a molecular property (the EFG created by the electrons at the site of the nucleus) and a nuclear property (eQ), the listed values of the quadrupole moments do not accurately reflect the typical magnitudes of the quadrupole interaction.[5] Nuclei with a large quadrupole moment can still have small C_q values when the EFG is highly symmetric. This is observed in Chapters 3 and 6, where ^{7}Li and ^{23}Na nuclei are predominantly in symmetric ionic environments resulting in small C_q values.

Oxygen atoms on the other hand, participate in a wide range of molecular bonds. This results in a large variation in the magnitude of C_q despite the seemingly small electric quadrupole moment.[14-15] The dependence of the quadrupole interaction on the bonding arrangements is taken advantage of in Chapters 3, 4 and 5 of this thesis, where ^{17}O NMR spectroscopy is applied to detect Li_2O_2.[1]

Table 2-1 Quadrupole Moments of Studied Quadrupolar Nuclei

Nucleus	Spin	Electric Quadrupole Moment, Q ($10^{-28}m^2$)
^{7}Li	3/2	-4.01
^{17}O	5/2	-2.558
^{23}Na	3/2	10.4

2.3.2 Energy Level Splitting in a Magnetic Field

The energy levels of quadrupolar nuclei are affected by the Zeeman interaction (**Figure 2-1**) and the quadrupole interaction. An example of the energy level diagram for

a spin 3/2 nucleus is illustrated in **Figure 2-5**. There are four spin states resulting from the Zeeman interaction that produce three single-quantum transitions.[3] The quadrupole interaction perturbs the frequency of each transition differently. The frequencies of the satellite transitions (ST), ($m_I = +3/2 \leftrightarrow m_I = +1/2$ and $m_I = -1/2 \leftrightarrow m_I = -3/2$) are affected by the first-order quadrupole interaction, whereas the central transition (CT, $m_I = +1/2 \leftrightarrow m_I = -1/2$) is unaltered. When the quadrupole interaction is large (comparable to the Zeeman interaction), the second-order quadrupole interaction must be considered. The second-order quadrupole interaction affects all transitions, resulting in broad powder patterns for the central transition.

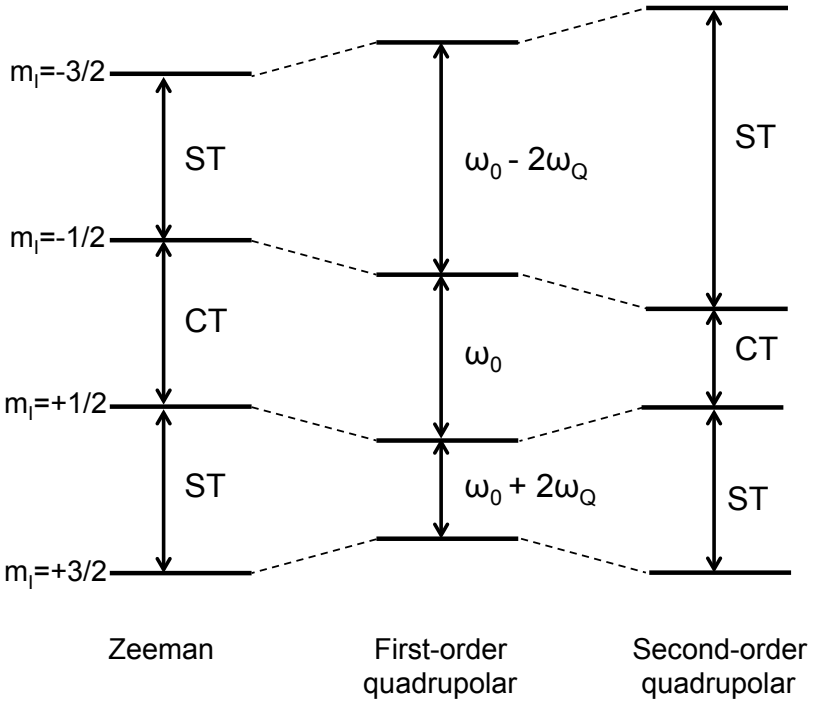

Figure 2-5 The energy level diagram for a spin 3/2 nucleus in a strong magnetic field, illustrating the effects of the Zeeman interaction, the first-order quadrupole interaction and the second-order quadrupole interaction. [16]

The energy level diagram for a spin 1 quadrupolar nucleus (ie. ^{2}H, ^{6}Li) is different than the half-integer quadrupole nucleus. In the spin 1 system, there are three energy levels (m_I = 1,0,-1) resulting in two satellite transitions and no central transition. This produces unique spectra, where the STs are often sensitive to molecular motion, allowing molecular dynamics to be probed.[8]

2.3.3 Quadrupolar Lineshapes

The central transition lineshape provides insight into the chemical environment and bonding arrangement at the nucleus, due to the dependence of the quadrupole

interaction on the nucleus' crystallographic symmetry. In the NMR experiment, the central transition is observed because it is only broadened by the second-order quadrupole interaction. This is unlike the satellite transitions, which are broadened by both the first-order and second-order quadrupole interactions. The STs have low intensity signals and typically are too far off resonance to observe. When chemical shielding isn't considered, the appearance of the central transition is dominated by the quadrupole interaction (C_q and η_q).

The breadth of the CT powder pattern depends on the magnitude of the C_q (**Figure 2-6a**). If the quadrupolar nucleus has perfect cubic symmetry ($V_{xx}=V_{yy}=V_{zz}$), then the quadrupole interaction drops to zero. Evidence of the quadrupole interaction in the NMR spectrum, indicates non-cubic symmetry at the nucleus, with larger C_q values associated with lower site symmetry. The position of the singularities is controlled by η_q (**Figure 2-6b**), where η_q ranges from 0 to 1. η_q reflects the symmetry at the EFG. When the nucleus has axial symmetry η_q equals 0.[13]

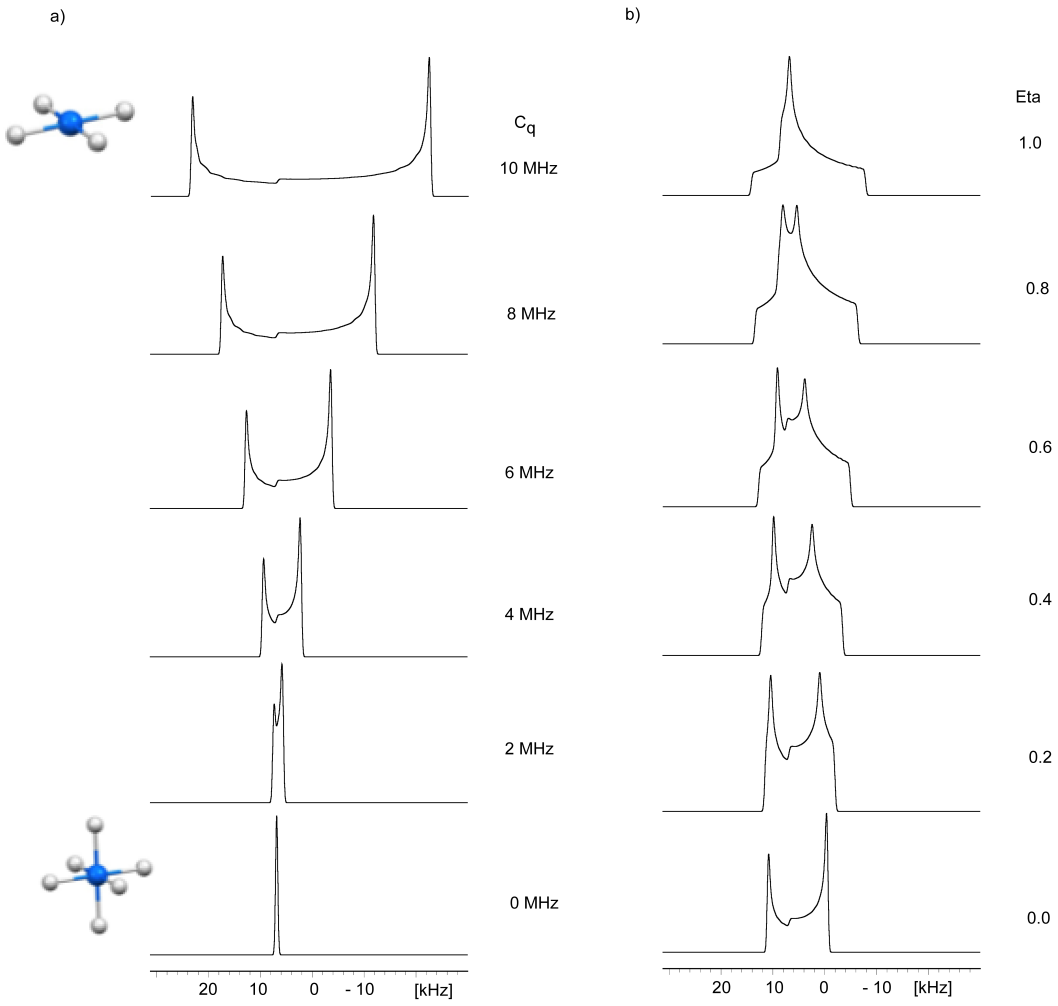

Figure 2-6 Simulated central transition for a spin 5/2 system, at a 11.7 T magnetic field (a) under axial symmetry (η_q= 0), where the C_q ranges from 0 MHz to 10 MHz. (b) for a C_q value of 5 MHz, where the eta value was varied from 0.0 to 1.0

When considering chemical shielding, in combination with the quadrupole interaction, there are now eight parameters that contribute to the NMR lineshape; $\delta_{iso}, \delta_{aniso}, \eta_{CS}, C_q, \eta_q, \alpha, \beta$ and γ. The chemical shielding influences the central transition lineshape depending on the values of the isotropic chemical shift δ_{iso} (in ppm), the chemical shift anisotropy δ_{aniso} (in ppm) and the chemical shift asymmetry η_{CS}

(dimensionless).[8] Additionally, the orientation of the CSA tensor with respect to the EFG tensor, contributes to the shape of the NMR resonance and is described by three Euler angles (α, β and γ), [8]

The value of the C_q (in Hz) remains constant with the external magnetic field. However the second-order quadrupole interaction is inversely proportional to the magnetic field strength and the spectral width (in ppm) decreases with increasing field strength. The CSA interaction on the other hand, scales linearly with applied magnetic field. To accurately determine the parameters that describe the NMR lineshape, it is beneficial to measure the quadrupole spectra at multiple magnetic field strengths. The resulting spectra are fit to the same set of parameters, producing a more accurate description of the quadrupole interaction.

MAS is widely applied in ssNMR to obtain high-resolution spectra (section 2.2.5). However, MAS does not completely average the quadrupole interaction. Nevertheless, the line width is still reduced for a quadrupolar nucleus by averaging the CSA, dipolar coupling and first-order quadrupole interaction. This is illustrated in **Figure 2-7**, where a spin 5/2 nucleus has axial symmetry.

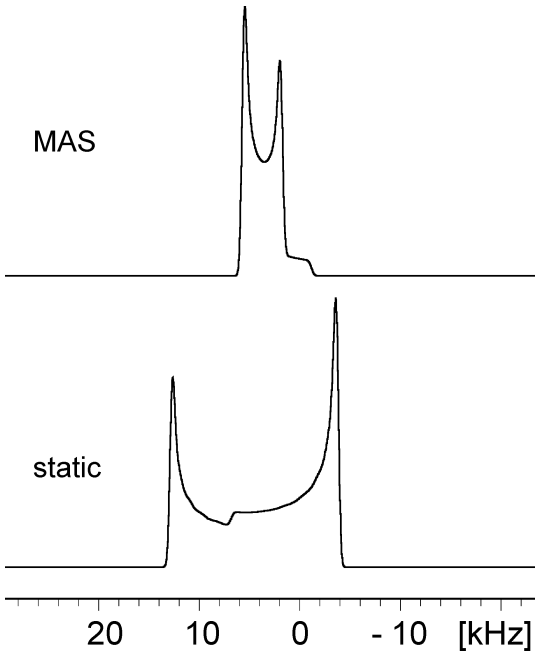

Figure 2-7 A comparison of the simulated static and MAS quadrupole lineshapes for a spin 5/2 nucleus with η_q= 0, a C_q value of 5 MHz at a magnetic field of 11.7 T

The spectral frequency of the second-order central transition powder pattern under MAS is described by **equation 2.15**, where ν_{iso} is the frequency from the chemical shielding, $C_0\nu_{QIS}$ is the zero order quadrupole term and α and β are the Euler angles. **Equation 2.15** contains two angle-dependent terms; $P_2(\cos(\theta))$ and $P_4(\cos(\theta))$, which are the second-order Legendre polynomials (**equation 2.16)** and the fourth-order Legendre polynomials (**equation 2.17**) respectively.[13] MAS only averages the $P_2(\cos(\theta))$ term to zero, thus the residual broadening in the MAS quadrupole spectrum results from $P_4(\cos(\theta))$.[13]

$$\nu = \nu_{iso} + C_0\nu_{QIS} + C_2 \cdot P_2(\cos(\theta)) \cdot \nu_2(\alpha,\beta) + C_4 \cdot P_4(\cos(\theta)) \cdot \nu_4(\alpha,\beta) \quad (2.15)$$

$$P_2(\cos(\theta)) = \frac{1}{2}[3\cos^2\theta - 1] \qquad (2.16)$$

$$P_4(\cos(\theta)) = \frac{1}{28}[35\cos^4\theta - 30\cos^2\theta + 3] \qquad (2.17)$$

The $P_4(\cos(\theta))$ term may be averaged to zero when θ is either 30.56° or 70.12°.[13] To completely average the second-order quadrupole interaction, the sample must simultaneously be spun around two angles. While this is possible, it is challenging to implement and requires the use of highly specialized equipment. An alternative approach is to apply the multiple quantum magic angle spinning (MQMAS).[17-18] Triple quantum magic angle spinning (3QMAS) is applied as part of the Na-O_2 investigation outlined in Chapters 6 and 7. The theoretical background behind MQMAS is discussed below.[17-19]

2.3.4 Multiple Quantum Magic Angle Spinning (MQMAS)

Multiple quantum magic angle spinning (MQMAS) is a two-dimensional (2D) NMR technique that produces high-resolution quadrupolar spectra, by refocusing the second-order quadrupolar interaction through a multiple quantum (MQ) excitation in combination with spinning at the magic angle.

For powder samples under MAS, the residual broadening in the CT lineshape is contributed by the fourth-order Legendre polynomial **(equation 2.17**) from the second-order quadrupole interaction. The resonance frequency for a symmetric multiple quantum transition (+m → -m) can be expressed using Legendre polynomials and also contains the $P_4(\cos(\theta))$ term.

$$\nu_{+m\rightarrow -m} = -\frac{C_q^2}{\omega_0[2I(2I-I)]^2}[A_0C_0 + A_2C_2P_2 + A_4C_4P_4] \qquad (2.18)$$

In **equation 2.18** the A_i term describes the orientation dependence of the quadrupole interaction and the C_j term is a coefficients. The coefficient depends on the spin quantum number I and the order of the transition:

$$C_0(I,m) = 2m[I(I+1) - 3m^2] \quad (2.19)$$

$$C_2(I,m) = 2m[8I(I+1) - 12m^2] \quad (2.20)$$

$$C_4(I,m) = 2m[18I(I+1) - 34m^2] \quad (2.21)$$

The second-order quadrupole interaction may be eliminated if **equation 2.22** is satisfied. This occurs when the spin (I) evolves under the effects of transitions m_1 and m_2 during two consecutive time periods t_1 and t_2. In practice the CT signal is detected where $m_2 = ½$. A pure isotropic echo is formed when $t_2 = kt_1$ (**equation 2.23**)

$$C_4(I,m_1)t_1 + C_4(I,m_2)t_2 = 0 \quad (2.22)$$

$$t_2 = \left(\frac{C_4(I,m_1)}{C_4\left(I,\frac{1}{2}\right)}\right)t_1 = kt_1 \quad (2.23)$$

The simplest MQMAS experiment (**Figure 2-8**) has two hard (non-selective pulse) pulses with a delay t_1 between them. The first pulse excites a higher-order coherence (m_1), which evolves during t_1. The second pulse converts the MQ coherence into the observable single quantum (SQ) coherence ($m_2 = ½$). The isotropic echo is observed during t_2. The desired MQ coherence pathway is selected by phase cycling. A

full 2D spectrum is generated by systematically incrementing t_1. In the resulting 2D NMR spectrum, the individual chemical shifts are resolved in the indirect (isotropic) dimension and the quadrupole lineshapes are separated for each site in the direct (isotropic + anisotropic) dimension. The value of t_2 is determined by **equation 2.23** and the values of K for various I and m_I combinations are listed in **Table 2-2**.

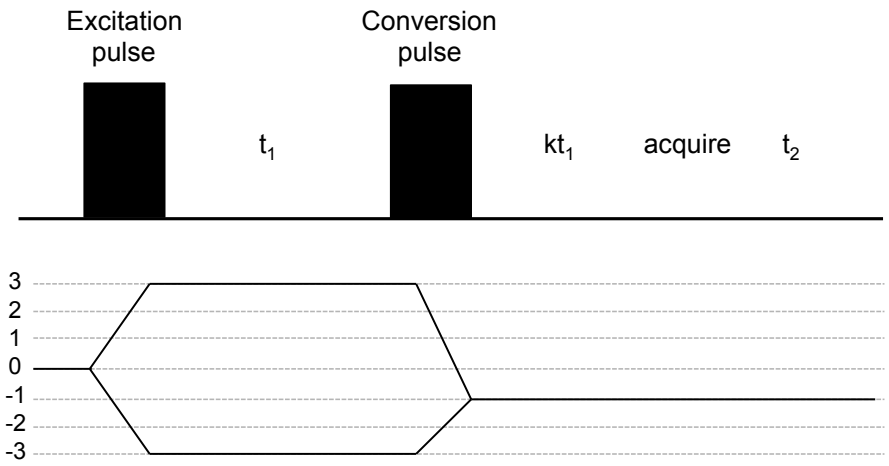

Figure 2-8 Schematic representation of the basic two pulse MQMAS pulse sequence, for when I = 3/2, where the triple quantum coherence is initially excited[8]

Table 2-2 The Values of K (equation 2.23) in MQMAS Spectroscopy[19]

m	3Q	5Q	7Q	9Q
I				
3/2	7/9			
5/2	19/12	25/12		
7/2	101/45	11/9	161/45	
9/2	91/36	95/36	7/18	31/6

In this thesis a more sophisticated version of the MQMAS pulse sequence was utilized (**Figure 2-9**). The MQMAS sequence used has three pulses and a z-storage step.

The z-storage produces pure absorption lineshapes, by eliminating residual transverse coherence. The first two pulses are hard pulses, which follow the coherences pathway; $\pm p \rightarrow 0 \rightarrow -1$. Next there is an intermediate step, where the magnetization is stored along z, removing the phase memory from the crystallites. The final pulse is a selective CT pulse. The observed signal that survives the MQ filter, originated from the selected MQ transition. Furthermore there if the quadrupole coupling is zero, the there will be no signal in the MQMAS spectrum.

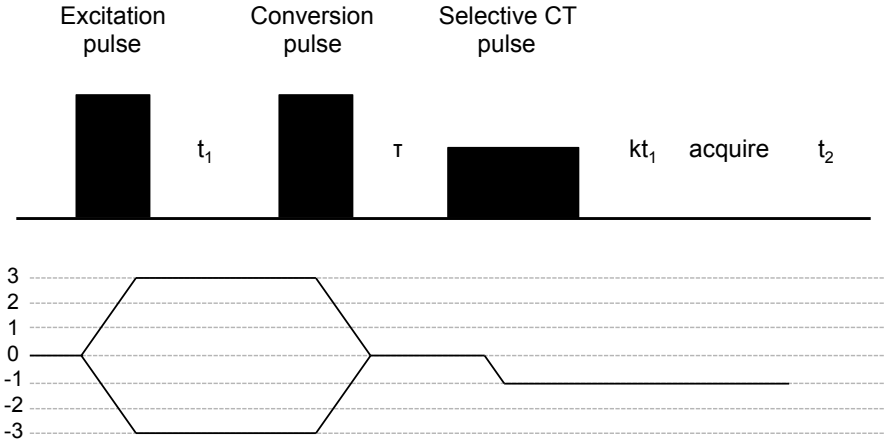

Figure 2-9 Schematic representation of the three pulse MQMAS sequence, which includes a z-storage step for the nuclear spin I=3/2, where the triple quantum coherence is initially excited [8]

^{23}Na-3QMAS is applied in Chapter 6 and 7, as part of the sodium-oxygen battery investigation. With ^{23}Na-3QMAS overlapping Na sites are separated, allowing the individual components in multi-component mixtures to be identified.

2.3.5 Pulse Response of Quadrupolar Nuclei

In a spin ½ system the applied RF field is presumed to be the dominant interaction. This is equivalent to assuming that no other evolutions occur during the pulse. For a quadrupole system this is not necessarily true, as typical RF field strengths range from 40 to 60 kHz, and the quadrupole interaction can vary from several kHz to several MHz. Thus the quadrupole interaction is often the largest interaction. The implication for the spin system is that the RF pulse is no longer considered instantaneous, instead the quadrupole interaction evolves during the RF pulse. This phenomenon may be probed through nutation spectroscopy.[20-22]

During a nutation experiment the flip angle (**equation 2.8**) is systematically varied and the resulting signal intensity is monitored. A nutation plot is generated by mapping the signal intensity as a function of the flip angle or pulse width.[5, 7-8] For a spin ½ nucleus the nutation plot will be sinusoidal, and the nutation frequency is equivalent to the frequency of the applied RF field:[5, 8, 23]

$$\Omega_{rf} = \gamma B_1 \qquad (2.23)$$

Quadrupole nuclei respond differently to RF pulses depending on the relative magnitude of the C_q with respect to the RF field strength. When performing nutation spectroscopy on a quadrupolar nucleus, three situations that must be considered;

(i) *the non-selective pulse* ($\gamma B_1 >> C_q$): When the γB_1 field dominates the quadrupole interaction, the RF pulse simultaneously affects both the central

transition and satellites. The resulting nutation plot will be sinusoidal and the pulse response of the CT will be comparable to that of a spin ½ nucleus. The nutation frequency is defined as $\Omega_{nutation} = \gamma B_1$.

(ii) the selective excitation of the central transition ($\gamma B_1 << C_q$): When the quadrupole interaction dominates the γB_1 field, the RF pulse will only excite the central transition. The nutation plot will still be sinusoidal, but the nutation frequency is compressed by a factor of I + ½. For a spin 3/2 system the nutation frequency becomes $\Omega_{nutation} = 2\gamma B_1$.[23-25]

(iii) the intermediate case ($\gamma B_1 \sim C_q$): In the intermediate case the nutation frequency is influenced by both the γB_1 field and the quadrupole interaction. The resulting nutation plot will be non-sinusoidal. [23]

Knowledge of the nutation frequency provides qualitative information about the size of the quadrupole interaction. [20, 22, 26] In the intermediate case, when a constant γB_1 field is applied, the nutation plots of two materials is expected to differ depending on the magnitude of the quadrupole interaction. This is the basis of the method developed in Chapter 3, where a ^{7}Li nutation study explores the stability of three Li-O_2 electrolytes.

2.4 Choice of Nuclei Studied in This Thesis

This thesis focuses on studying metal-oxygen reaction products. ^{6,7}Li and ^{17}O are the obvious NMR nuclei to select, for investigating the Li-O_2 electrochemistry. Correspondingly, the Na-O_2 electrochemistry may be revealed with ^{23}Na and ^{17}O NMR. The nuclei studied within this thesis are summarized in **Table 2-3**, along with their respective Larmor frequencies at 11.7 T, 19.9 T and 21.1 T, as these are the most

commonly used magnetic fields. **Table 2-1** outlines the value of the quadrupole moments for the quadrupole nuclei.

Table 2-3 Table of nuclei considered in this thesis

Nucleus	Larmor Frequency at 11.7 T (MHz)	Larmor Frequency at 19.9 T (MHz)	Larmor Frequency at 21.1 T (MHz)	Nuclear Spin	Natural Abundance (%)
^{1}H	500.130	850	900.130	1/2	99.98
^{7}Li	194.370	330.393	349.825	3/2	92.41
^{17}O	67.800	115.248	122.026	5/2	0.038
^{23}Na	132.294	224.876	238.101	3/2	100
^{31}P	202.456	344.139	364.379	1/2	100

The Li-O_2 materials of interest are diamagnetic ionic compounds, where the ^{6,7}Li chemical shifts are very similar.[2, 27] Thus, the electrochemical reaction products, cannot be elucidated based solely on chemical shifts.[28] However, the ^{7}Li quadrupole coupling constants of Li_2O_2 and Li_2CO_3 are dissimilar enough to differentiate the two species.[1] This avenue is further explored in Chapter 3, utilizing ^{7}Li nutation spectroscopy. The nutation experiments are performed directly on the cycled electrodes, taking advantage of the high natural abundance of ^{7}Li (**Table 2-3**). This is unlike the ^{17}O NMR experiments, where isotopic enrichment is necessary.

^{17}O is a very difficult NMR nucleus. The spectra are nontrivial to acquire, as they often exhibit significant line broadening from the quadrupole interaction,[12] combined with the low natural abundance and low Larmor frequency (**Table 2-3**). In spite of these challenges, ^{17}O NMR is the main spectroscopic tool employed in the Li-O_2 battery investigation. Li_2O_2 (the desired product) has a very broad, diagnostic lineshape from the

extremely large ^{17}O C_q of 18 MHz.[1] The Li_2O_2 spectrum is distinct from the spectra of the electrolyte breakdown products, (**Figure 2-10)** all of which have a ^{17}O C_q of approximately 7 MHz.[1, 29] To overcome the above outlined challenges associated with ^{17}O NMR, the electrochemically-cycled Li-O_2 electrodes were isotopically enriched and two signal enhancement techniques; double frequency sweep (DFS)[30] and quadrupole Carr-Purcell-Meiboom-Gill (QCPMG)[10, 31], are applied throughout this work (Chapters 3, 4 and 5). Details of the enrichment process and the signal enhancement techniques are further discussed in Section 2.5.

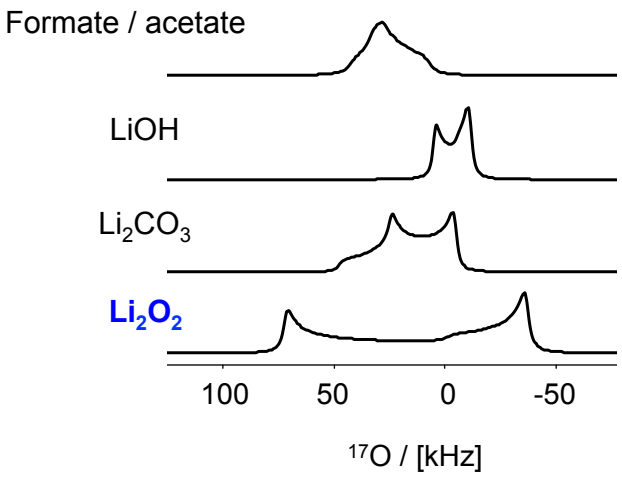

Figure 2-10 Simulations of the ^{17}O central transition lineshapes of the relevant Li-O_2 discharge products at 21.1 T under static conditions using reported ^{17}O quadrupole parameters[1, 29]

To the best of our knowledge, this is the first time that solid-state NMR spectroscopy is applied to explore the sodium-oxygen cell chemistry. Prior to beginning the experimental work, simulations were performed which predicts that both ^{23}Na and ^{17}O will be informative spectroscopic probes (see *appendices A1 and A2*). The simulations were performed using Simpson software.[32-33] Sample Simpson input files are provided in

appendix A3. The NMR parameters used in the simulations were calculated with the CASTEP[34] software. Owning to the expensive nature of ^{17}O-enrichment and the rapid acquisition times associated with ^{23}Na NMR experiments, this works focuses on the application of ^{23}Na NMR (Chapter 6 and 7).

Electrolyte decomposition products are monitored with ^{1}H and ^{31}P NMR in Chapters 4 and 5. Since the desirable products in the Li-O_2 do not contain proton or phosphorus atoms, evidence of protonated or phosphorus signals in the electrode NMR spectra are expected to indicate evidence of electrolyte decomposition.

2.5 Use of ^{17}O NMR Spectroscopy to Study the Li-O_2 Battery

^{17}O NMR of electrochemically-cycled electrodes provides values insight into the Li-O_2 electrochemistry in Chapters 3, 4 and 5. Isotropic enrichment, signal enhancement techniques and the acquisition of the spectra at ultrahigh magnetic fields (i.e. 21.1 T) are applied, to aid in the acquisition of the extracted cathode spectra.

2.5.1 ^{17}O-Enrichment Protocol Used in This Thesis

It can be difficult to incorporate ^{17}O-enriched atoms into a synthetic scheme, as the two readily available ^{17}O-labelled sources are O_2 gas and H_2O. This requires the enrichment process to include either a hydrolysis or a gas exchange reaction.[14] ^{17}O-enrichment of M-O_2 cells is relatively simple, as molecular oxygen is the redox active cathode material.

To generate ^{17}O-enriched discharge products, the cell is cycled under a ^{17}O-enriched O_2 gas environment. The resulting ^{17}O NMR spectrum of the extracted cathode

then contains a record of all possible products produced from the enriched molecular oxygen starting material.

All ^{17}O NMR enrichment was performed at McMaster University by Zoe Reeve, the current author, using a specially built gas manifold (**Figure 2-11).** The enrichment manifold was designed and constructed by Jim Garret, with the Brockhouse Institiute for Materials Research (BIMR), in collaboration with Zoe Reeve and Prof. Gillian R. Goward. Details pertaining to the gas line manifold are provided in the *appendix, A4* and the standard operating procedure (SOP) for ^{17}O-enriching a M-O_2 cell is outlined in *appendix A5*.

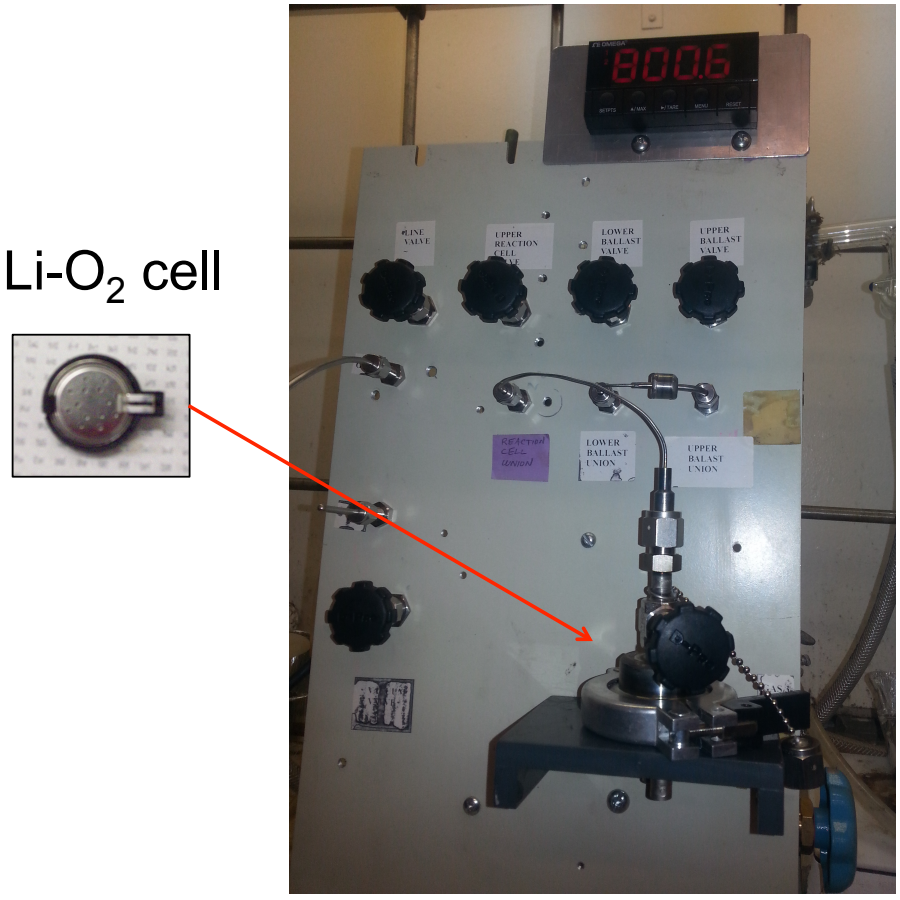

Figure 2-11 A photo of the specially built ^{17}O enrichment gas manifold, where a Li-O_2 cell is inside the silver reaction chamber and the system is under ^{17}O-enriched gas

2.5.2 Signal Enhancement Techniques

Sensitivity is a significant challenge for NMR spectroscopy,[35] especially for nuclei with a low natural abundance and low Larmor frequency, such as ^{17}O (**Table 2-3**). One of the main approaches to enhance the S/N for quadrupolar nuclei is to borrow or transfer magnetization from the ST to boost the CT signal.[35] Typically population transfer methods, like DFS, are applied as a preparation step before the NMR

experiment.[35] QCPMG is an alternative approach to improve the S/N, where the spectra may be collected in less time.

A discussion of both DFS and QCPMG is provided below. In Chapter 3, DFS was the only signal enhancement technique applied, whereas in Chapter 4, DFS and QCMPG are used in combination.

2.5.2.1 Double Frequency Sweep (DFS)

DFS increases the signal in the CT, by modifying the populations of the satellite transitions by a population transfer.[30] (**Figure 2-12**). Under normal circumstances, the populations of the energy levels are governed by the Boltzmann distribution (Section 2.2.2). During DFS, an adiabatic pulse simultaneously sweeps over the high- and low-frequency satellite transitions, altering the energy level populations; either through saturating the energy levels (**Figure 2-12b)** or by inverting the energy levels (**Figure 2-12c)**. Saturation equalizes the population of the upper and lower energy levels resulting in an theoretical enhancement factor of I + ½ for the CT.[36] A greater theoretical enhancement factor, of 2I, is possible for the CT if a full inversion of the populations occurs.[36]

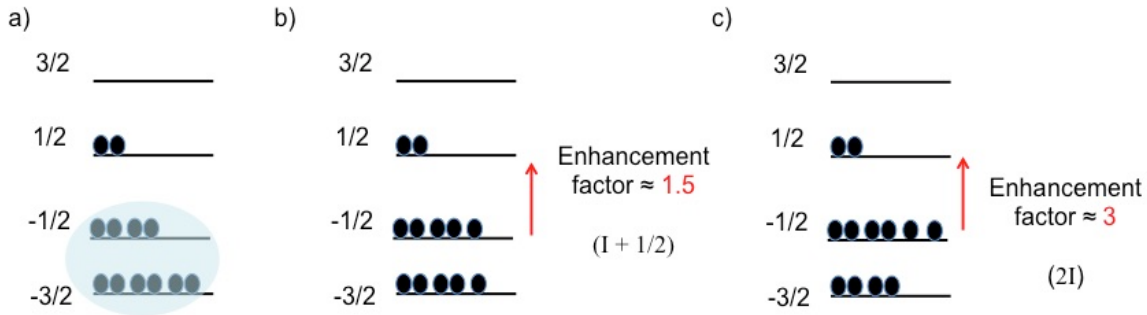

Figure 2-12 Energy level diagram for a spin 3/2 nucleus (a) at thermal equilibrium population based on the Boltzmann distribution (b) the population arrangement after saturation of the energy levels and (c) the population arrangement after the inversion of the +3/2 ↔ +1/2 transition[36]

The signal enhancement effects of DFS may be demonstrated with a $NaNO_3$ single crystal (**Figure 2-13**). In the static ^{23}Na NMR spectrum, (I = 3/2) both satellite transitions and the central transition are observed, in the absence of DFS. When DFS is applied the signal intensity of the CT in enhanced by a factor of ~3, indicating full inversion has occurred. This is confirmed by the disappearance of the ST in the spectrum.

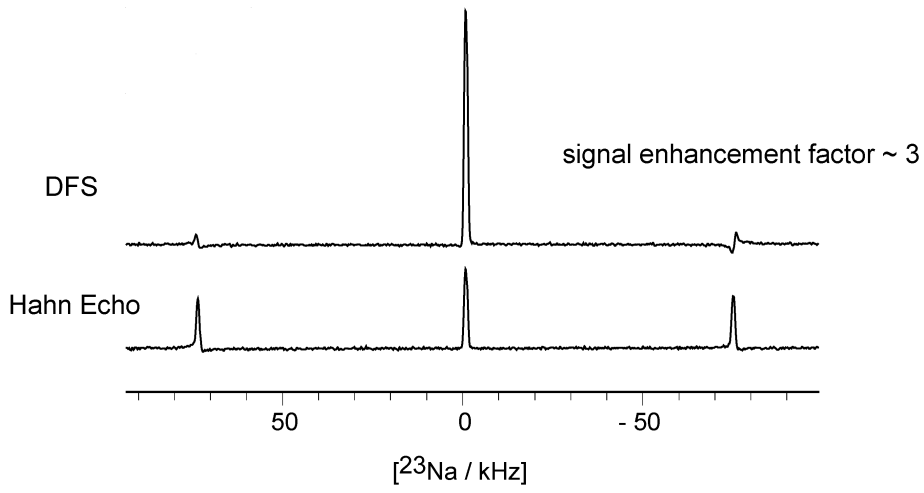

Figure 2-13 Static ^{23}Na NMR spectrum of a $NaNO_3$ single crystal, collected at 11.7 T, illustrating the signal enhancement effects of DFS

In this thesis, DFS is applied to ^{17}O-enriched cathodes, to aid in acquiring the ^{17}O NMR spectra at a moderate magnetic field strength (11.7 T). ^{17}O is a spin 5/2 nucleus, where there are two sets of STs. To achieve the maximum enhancement of the CT, first the outer STs are inverted, prior to inverting the inner STs.[36] This process is illustrated in **Figure 2-14**.

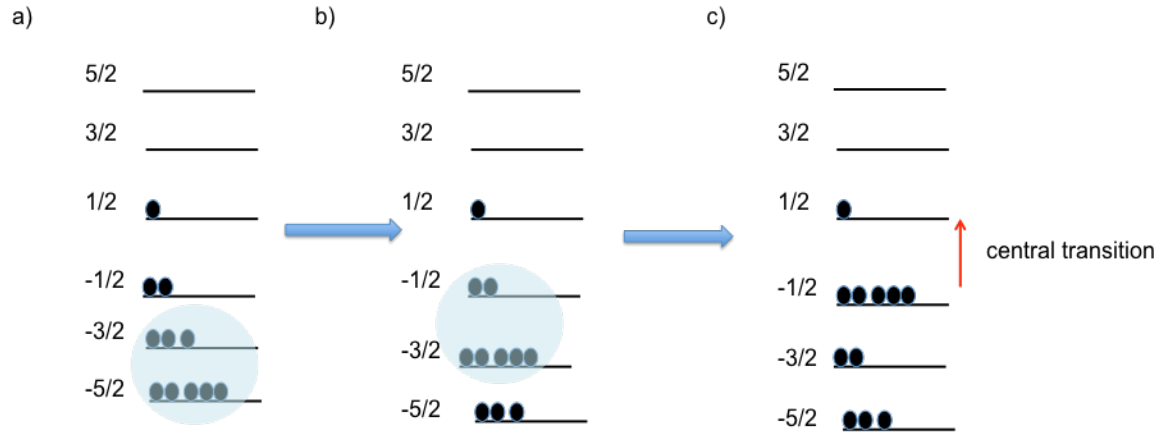

Figure 2-14 Energy level diagram for a spin 5/2 nucleus (a) at thermal equilibrium population based on the Boltzmann distribution (b) the population arrangement after the inversion of the + 5/2 ↔ + 3/2 transition and (c) the population arrangement after the inversion of the +3/2 ↔ +1/2 transition[36]

DFS was tested on a model material; a 10% ^{17}O-enriched lithium hydroxide (LiOH) sample, prior to being applied to the extracted Li-O_2 electrodes. The enriched LiOH was fabricated by adding Li metal to 10% ^{17}O-enriched H_2O. Once a saturation solution was created, the precipitate was dried under vacuum for several hours to remove any waters of hydration from the enriched sample. The LiOH ^{17}O signal is enhanced by a factor of ~5 (**Figure 2-15**) from the application of DFS. Thus DFS is expected to be beneficial in collecting the ^{17}O spectra of the ^{17}O-enriched Li-O_2 electrodes.

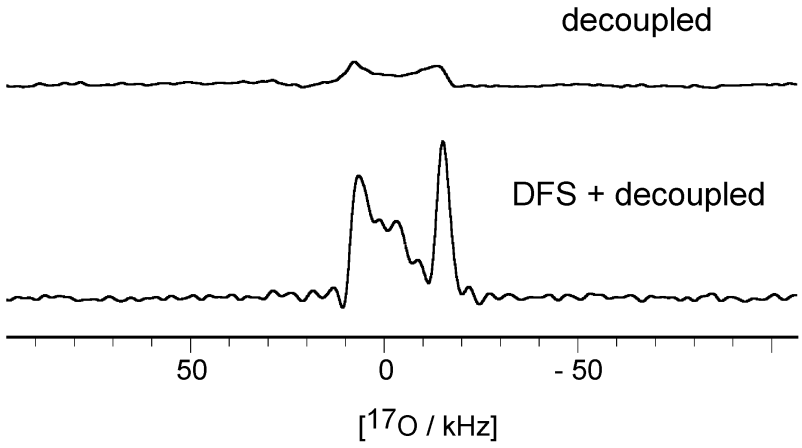

Figure 2-15 Static ^{17}O NMR spectrum of $^{7}Li^{17}OH$ (10 % ^{17}O-enriched) collected at 11.7 T, where the application of DFS produced an enhancement factor of 5 fold.

2.5.2.2 Quadrupole-Carr-Purcell-Meiboom-Gill (QCPMG)

The QCPMG pulse sequence[10, 31] is a variation of the Hahn-echo experiment,[11] where multiple echo are collected, thus increasing the total acquired signal. The pulse sequence is illustrated in **Figure 2-16**. The first part of the sequence corresponds to a standard Hahn echo, and the second part, in brackets, is repeated N times till the signal decays. This results is an echo train, where refocusing π_y pulses are applied every τ. In the time domain, a series of decaying echoes are observed.[35]

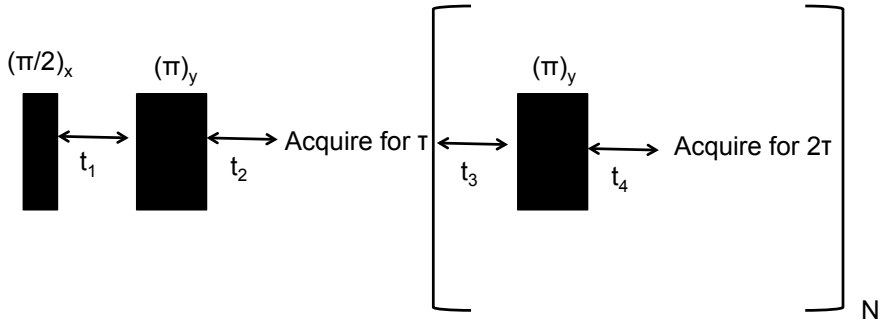

Figure 2-16 A Schematic representation of the QCPMG pulse sequence[37]

There are two sources that contribute to the signal enhancement effects of QCPMG (compared to an echo). The first is that several echoes are collected with every FID, and the second is that in the QCPMG spectrum, the signal is concentrated into spikelet rather than the dispersed over a broad pattern.[35] The spacing between the spikelet in the spectrum depends on 2τ.[37] Thus is it possible to miss important features and singularities. This is not a major concern for the ^{17}O cathode spectra because ^{17}O NMR is being used here to screen for the presence or absence of the extremely broad ^{17}O Li_2O_2 signal in the discharged cathodes. Additionally the ^{17}O NMR parameters for the various Li-O_2 reactions species are already known.

QCMPG may be combined with the population transfer technique DFS. The sensitivity is reported to increases by two orders of magnitude.[37] The combined DFS-QCMPG experiment was tested on the same model compound, the 10% ^{17}O-enriched LiOH sample, discussed above. Through the application of DFS-QCMPG an enhancement factor of ~11 was observed (**Figure 2-17**). Thus, the DFS-QCMPG

experiment is expected to ensure that the ^{17}O spectra of the extracted Li-O_2 cathodes are collected in a timely manner, in Chapter 4.

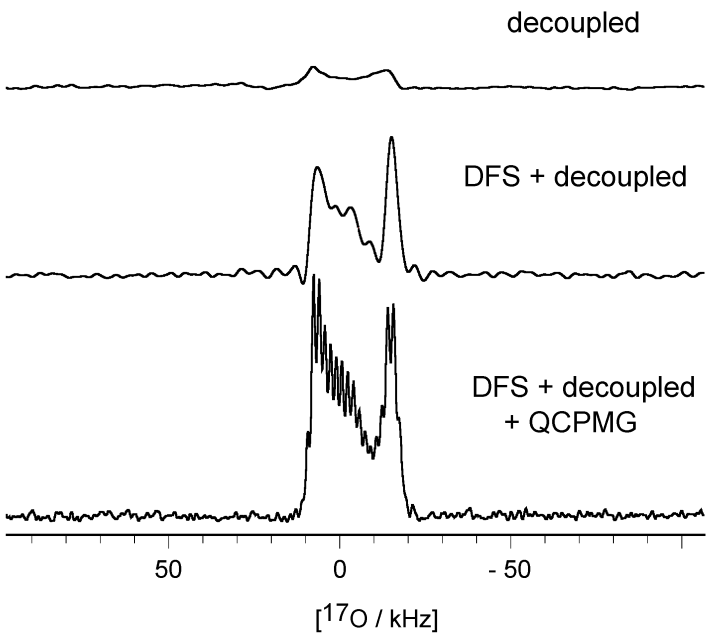

Figure 2-17 Static ^{17}O NMR spectrum of $^{7}Li^{17}OH$ (10 % ^{17}O-enriched) collected at 11.7 T, where the application of DFS-QCMP produced an enhancement factor of 11 fold.

2.6 Summary

ssNMR is the main spectroscopic tool applied to characterize the Li-O_2 and Na-O_2 battery chemistry in this thesis in this thesis. This chapter outlines the fundamental nuclear properties that give rise to the observed spectral features, and details specific experiments that are applied in the subsequent chapters. Additionally the use of ^{17}O NMR to investigate the Li-O_2 battery is highlighted including the; isotropic enrichment process and the application of signal enhancement techniques.

The use of quadrupolar nuclei has been vital in providing a deeper understanding of the Li-O_2 and Na-O_2 electrochemistry. The techniques discussed in this chapter have been essential in obtaining high-resolution spectra of quadrupolar nuclei. This ensures the accurate characterization of the metal-oxygen reaction products. The findings from the multinuclear NMR studies are discussed in Chapters 3 through 7.

2.7 References

[1] M. Leskes;N. E. Drewett;L. J. Hardwick;P. G. Bruce;G. R. Goward;C. P. Grey, *Angew. Chem. Int. Ed.* **2012**, *51*, 8560.

[2] J. Xiao;J. Hu;D. Wang;D. Hu;W. Xu;G. L. Graff;Z. Nie;J. Liu;J.-G. Zhang, *J. Power Sources* **2011**, *196*, 5674.

[3] D. L. Pavia;G. M. Lampman;G. S. Kriz;J. A. Vyvyan, *Introduction to spectroscopy*, Cengage Learning, **2008**.

[4] A. Carrington;A. D. McLachlan, **1967**.

[5] M. H. Levitt, *Spin Dynamics: Basics of Nuclear Magnetic Resonance*, John Wiley & Sons, Chichester, Uk, **2001**.

[6] P. Hore;J. Jones;S. Wimperis, *NMR: The Toolkit: how Pulse Sequences Work*, Oxford University Press, USA, **2015**.

[7] J. Keeler, *Understanding NMR Spectroscopy*, John Wiley and Sons, New York **2005**.

[8] M. J. Duer, *Introduction to Solid-Sate NMR Spectroscopy*, Blackwell Publishing Ltd, Oxford, UK **2004**.

[9] J. Cabana;C. P. Grey, in *Encyclopedia of Inorganic Chemistry*, John Wiley & Sons, Ltd, **2006**.

[10] S. Meiboom;D. Gill, *Review of Scientific Instruments* **1958**, *29*, 688.

[11] E. L. Hahn, *Physical review* **1950**, *80*, 580.

[12] R. E. Wasylishen;S. E. Ashbrook;S. Wimperis, *NMR of Quadrupolar Nuclei in Solid Materials*, John Wiley & Sons, **2012**.

[13] A. P. M. Kentgens, *Geoderma* **1997**, *80*, 271.

[14] S. E. A. a. M. E. Smith, *Chemical Society Reviews* **2006**, *35*, 718.

[15] G. Wu, *Progress in Nuclear Magnetic Resonance Spectroscopy* **2008**, *52*, 118.

[16] S. E. Ashbrook, *Phys. Chem. Chem. Phys.* **2009**, *11*, 6892.

[17] A. Medek;J. S. Harwood;L. Frydman, *J. Am. Chem. Soc.* **1995**, *117*, 12779.

[18] L. Frydman;J. S. Harwood, *J. Am. Chem. Soc.* **1995**, *117*, 5367.

[19] T. Bräuniger;M. Jansen, *Z. Anorg. Allg. Chem.* **2013**, *639*, 857.

[20] T. L. Spencer;G. R. Goward;A. D. Bain, *Solid State Nuclear Magnetic Resonance* **2013**, *53*, 20.

[21] A. Samoson;E. Lippmaa, *Physical Review B* **1983**, *28*, 6567.

[22] T. L. Spencer;G. R. Goward;A. D. Bain, *Can. J. Chem.* **2011**, *89*, 764.

[23] W. S. Veeman, *Zeitschrift für Naturforschung Section A-A Journal of Physical Sciences* **1992**, *47*, 353.

[24] L. Pandey;S. Towta;D. G. Hughes, *The Journal of Chemical Physics* **1986**, *85*, 6923.

[25] A. P. M. Kentgens;J. J. M. Lemmens;F. M. M. Geurts;W. S. Veeman, *Journal of Magnetic Resonance (1969)* **1987**, *71*, 62.

[26] R. Janssen;W. S. Veeman, *Journal of the Chemical Society, Faraday Transactions 1: Physical Chemistry in Condensed Phases* **1988**, *84*, 3747.

[27] L. A. Huff;J. L. Rapp;L. Zhu;A. A. Gewirth, *J. Power Sources* **2013**, *235*, 87.

[28] Z. Xu;J. F. Stebbins, *Solid State Nuclear Magnetic Resonance* **1995**, *5*, 103.

[29] M. Leskes;A. J. Moore;G. R. Goward;C. P. Grey, *J. Phys. Chem. C* **2013**, *117*, 26929.
[30] D. Iuga;H. Schäfer;R. Verhagen;A. P. M. Kentgens, *Journal of Magnetic Resonance* **2000**, *147*, 192.
[31] H. Y. Carr;E. M. Purcell, *Physical Review* **1954**, *94*, 630.
[32] M. Bak;J. T. Rasmussen;N. C. Nielsen, *Journal of Magnetic Resonance* **2011**, *213*, 366.
[33] M. Bak;J. T. Rasmussen;N. C. Nielsen, *Journal of Magnetic Resonance* **2000**, *147*, 296.
[34] S. J. Clark;M. D. Segall;C. J. Pickard;P. J. Hasnip;M. I. Probert;K. Refson;M. C. Payne, *Zeitschrift für Kristallographie* **2005**, *220*, 567.
[35] F. A. Perras;J. Viger-Gravel;K. M. N. Burgess;D. L. Bryce, *Solid State Nuclear Magnetic Resonance* **2013**, *51–52*, 1.
[36] R. Siegel;T. T. Nakashima;R. E. Wasylishen, *Concepts in Magnetic Resonance Part A* **2005**, *26A*, 62.
[37] R. Siegel;T. T. Nakashima;R. E. Wasylishen, *Concepts in Magnetic Resonance Part A* **2005**, *26A*, 47.

Chapter 3 : Identification of Electrochemical Reaction Products in Lithium-Oxygen Cells with ^{7}Li Nutation Spectroscopy

3.1 Introduction

This chapter demonstrates that ^{7}Li nutation spectroscopy is an effective method to identify Li_2O_2 in cycled Li-O_2 electrodes. The ^{7}Li quadrupole interaction of Li_2O_2 and Li_2CO_3 is a similar magnitude to typical radiofrequency fields, thus the ^{7}Li nutation frequency is simultaneously influenced by both interactions. The discharge products were determined via ^{7}Li nutation spectroscopy for two model electrolyte systems; TEGDME and PC/DMC. The ^{7}Li nutation frequencies of the cycled electrodes were compared to the nutation frequencies of pristine Li_2O_2 (30 kHz) and pristine Li_2CO_3 (40 kHz). Li_2CO_3 was found to be the main reaction product formed in the PC/DMC electrolyte, as the PC/DMC electrode had a fast ^{7}Li nutation frequency (41 kHz), similar to the nutation frequency of pristine Li_2CO_3. It was concluded that both Li_2O_2 and Li_2CO_3 were produced in the TEGDME electrode, since the ^{7}Li nutation frequency of the TEGDME electrode was an intermediate values (38 kHz) between the nutation frequencies of the pristine materials. Based on the fast ^{7}Li nutation frequency of the TMP cycled electrode (45 kHz), a novel electrolyte material, Li_2O_2 was determined not to be present. Instead the Li_2CO_3 was shown to be the main reaction product. This was confirmed with ^{17}O NMR spectroscopy.

This work was published in the *Canadian Journal of Chemistry*. Initial manuscripts were prepared by the current author, Z. E. M. Reeve. The content was reproduced with the permissions of: *The Canadian Journal of Chemistry (**93**, 976-982, 2015) with co-authors G. R. Goward and A. D. Bain. © 2015 NRC.* All electrochemically cycling and ^{17}O-enrichment was performed at McMaster. The ^{7}Li and ^{17}O NMR spectra

were collected and processes at McMaster University under the supervision of Prof. Gillian R. Goward and Prof. Alex D. Bain.

With automotive applications in mind there has been a search for lighter and higher energy density batteries. The lithium-oxygen (Li-O_2) battery is an attractive battery design as the theoretical energy density is equivalent to gasoline. The high energy density results from the electrochemical formation of Li_2O_2 from the reaction of molecular oxygen and metallic lithium. [1-2] This has made the Li-O_2 battery a promising potential energy storage candidate for hybrid and electric vehicles. [1, 3-7]

Currently the electrolyte instability is considered to be a crucial issue that must be resolved to allow for further development of the Li-O_2 technology.[3-6] Almost all non-aqueous electrolytes tested have been shown to be unstable in the Li-O_2 environment. Instead of the desired electrochemistry occurring, the reduced oxygen species, the intermediate superoxide radical, attacks and decomposes the electrolyte. [1, 5-6, 8-11] The resulting discharge products are electrolyte breakdown species, rather than Li_2O_2.

The Li-O_2 discharge products are being investigated with Raman[12], Fourier transformed infrared (FTIR)[10, 13], powder x-ray diffraction (PXRD)[13] and in situ gas chromatography/mass spectroscopy (GC/MS)[10]. From transmission and scanning electron microscopy (TEM and SEM) studies the discharge species are thought to be a mixture of both amorphous and crystalline phases[3, 14]. Another powerful technique is solid-state nuclear magnetic resonance (ssNMR). ssNMR offers a nucleus-specific approach to study the local structure of materials even when the system is amorphous or highly disordered.

In particular, ^{17}O ssNMR has been shown to be a valuable tool in the identification of Li_2O_2.[15-16] Li_2O_2 has a unique ^{17}O signature in the NMR spectrum from the large quadrupole coupling constant (C_q) of 18 MHz.[15-16] This allows for Li_2O_2 to be easily differentiated from other electrolyte breakdown species, such as Li_2CO_3, LiOH, CH_3CO_2Li and HCO_2Li [10, 13] all of which have ^{17}O C_q of approximately 7 MHz. [15-16] In order to perform ^{17}O NMR of cycled electrodes expensive ^{17}O-enrichment is necessary, due to its very low natural abundance (0.04%). An alternative approach is to take advantage of the higher natural abundance of ^{6}Li (7.6%) or ^{7}Li (92.4%).

The Li-O_2 battery species of interest are diamagnetic salts, which are primarily ionically bonded. Thus, the isotropic $^{6,7}Li$ chemical shift range is very small and insensitive to differences in the lithium environments. [17-18] Attempts have been made within the literature to distinguish Li_2O_2 from the electrolyte breakdown species with ^{6}Li NMR[19-20] the lower natural abundance nucleus, since ^{6}Li NMR spectra are inherently higher resolution than the ^{7}Li NMR spectra. This is not a robust approach as the ^{6}Li chemical shifts of Li_2O_2 and the electrolyte breakdown species are still too similar to allow for the Li-O_2 discharge products to be accurately identified. [19-20]

Recently the ^{7}Li quadrupole interaction has been shown to be a diagnostic tool for the differentiation of Li_2O_2 from Li_2CO_3[15], a main electrolyte breakdown species[10, 13]. The ^{7}Li quadrupole interaction was shown to be sensitive to differences in the ^{7}Li chemical environments of Li_2O_2 and Li_2CO_3. [15] The previously reported ^{7}Li quadrupole parameters were estimated with CASTEP[21-22] code based on the known crystal structures. [23-24] The experimental values of 35 kHz and 120 kHz for Li_2O_2 and Li_2CO_3,

respectively were in good agreement with the calculated values.[15] Unfortunately, because of the amorphous and heterogeneous nature of the discharge products formed via electrochemical cycling, characteristic quadrupole features were not present in the ^{7}Li spectra of cycled electrodes; instead broad, featureless resonances centered around 0 ppm were observed. If ^{7}Li quadrupole parameters can be extracted from the NMR spectra of cycled electrodes then we propose here that it becomes possible to differentiate Li_2O_2 from Li_2CO_3 in the cathode samples, taking advantage of the high sensitivity of ^{7}Li.

Nutation spectroscopy was applied as a method to probe the ^{7}Li C_q of the discharge products. Three electrolyte systems were studied: propylene carbonate/dimethyl carbonate (PC/DMC), tetraethylene glycol dimethyl ether (TEGDME) and a novel electrolyte, trimethyl phosphate (TMP). By identifying whether Li_2O_2 was a discharge product in the chosen electrolyte systems, the relativity stability of the electrolytes systems can be inferred.

3.1.2 Nutation Spectroscopy

During a nutation experiment the flip angle is systematically varied and the resulting signal intensity is monitored. A nutation plot is generated by mapping the signal intensity as a function of flip angle or pulse width.[25-27] In a spin ½ system the applied RF field is presumed to be the dominant interaction in the spin system and the resulting nutation plot will be sinusoidal. In a quadrupole system the RF field is not necessarily the dominant interaction. Depending on the system the quadrupole interaction can vary from several kHz to several MHz.[28] The quadrupole interaction is often larger than typical RF field strengths (40 to 60 kHz). When performing nutation spectroscopy on a quadrupole

nucleus, three situations must be considered: the $\gamma B_1 >> C_q$, $\gamma B_1 << C_q$ and the intermediate case where $\gamma B_1 \sim C_q$. When the γB_1 field dominates the quadrupole interaction, the RF pulse simultaneously affects both the central transition and satellites. The nutation plot will be sinusoidal. When the quadrupole interaction dominates the γB_1 field the RF pulse will only excite the central transition. The nutation plot will still be sinusoidal and the nutation frequency becomes compressed by a factor of I + 1/2, where I is the nuclear spin.[29-31] For the intermediate case the nutation frequency is influenced by both the γB_1 field and the quadrupole interaction. The nutation plot will be non-sinusoidal[29-31] and sensitive to the size of the quadrupole interaction. For a given γB_1 field the nutation plots are expected to be distinct for two species that have dissimilar Cq's.

3.2 Experimental

3.2.1 Li-O_2 Electrochemistry

The cathode slurries were prepared in a weight ratio of 0.625:1: 1 by mixing Super C65 carbon black (Timcal), Polyvinylidene fluoride (ATOFINA Canada Inc) and dibutyl phthalate (DBP, Sigma Aldrich). The cathodes were washed in dry diethyl ether and dried at room temperatures for several hours. The ethylene carbonate/dimethyl carbonate (PC/DMC, Novolyte Technologies) electrolyte was a 1M $LiPF_6$ solution in a 50/50 by volume mixture of ethylene carbonate/dimethyl carbonate. The TEGDME electrolyte was a 1M LiTFSI solution in tetraethylene glycol dimethyl ether (Sigma Aldrich). The TMP electrolyte was a 0.5M LiTFSI solution in trimethyl phosphate (TMP, Sigma Aldrich). The Li-O_2 batteries were assembled in an argon atmosphere versus

metallic Li with Celgard separators. The Li-O_2 cells were galvanostatic cycled at a rate of 70 mA/g of carbon in a pure oxygen environment. The TEGDME cathode, TMP cathode and PC/DMC cathodes were cycled to the following respective capacities 1000 mAh/g, 1150 mAh/g and 900 mAh/g. The Li-O_2 cells are disassembled in an argon atmosphere. The discharged cathodes were washed in dry acetonitrile and then dried for several hours under vacuum prior to NMR analysis.

3.2.1.1 ^{17}O-enrichment of Li-O_2 Cells

The TMP cathode was enriched with 70 % oxygen gas (CortecNet Corp). The cell was assembled under argon and sealed in an airtight container. The cell was then connected to a specially built gas line manifold. A digital manometer is a part of the manifold line allowing for the pressure within the cell to be accurately monitored during the evacuation and refilling periods. Once the cell was attached to the manifold the pressure within the cell was reduced to approximately 100 mmHg, refilled to a pressure of 760 mmHg of pure natural abundance air. After an open circuit voltage of 2.8 V was observed the atmosphere within the airtight container was removed, where the pressure was reduced to approximately 100 mmHg. The airtight container was then filled with ^{17}O-enriched gas to a pressure of approximately 760 mmHg. The cell rested for 12 hours, then was cycled and prepared for NMR analysis as outlined above. Further details about the ^{17}O gas line manifold are provided in the *appendices A4* and *A5*.

3.2.2 Solid-State NMR Spectroscopy

3.2.2.1 1D ^{7}Li NMR and ^{7}Li Nutation Spectroscopy

Static solid-state ^{7}Li NMR was performed on a Bruker Avance I AV500 spectrometer using a standard 2.5 mm MAS probe. A reference solution of 1 M LiCl in water was used to calibrate the RF fields for the nutation experiments. The RF field was on resonance for all experiments performed. A nutation plot was collected for each material at the following RF fields; 10kHz, 30kHz, 52 kHz, 57 kHz and 62.5 kHz. For each RF field the flip angle was varied from 45^{0} to 1400^{0} in increments of 45^{0} to create the nutation data set, with a total of 30 points. For the pristine Li_2O_2 (Sigma Aldrich) and Li_2CO_3 (Sigma Aldrich), each point was collected in 8 scans with a delay time of 234 s and 300 s respectively. The ^{7}Li T_1 of Li_2O_2 and Li_2CO_3 were determined to be 78 ± 10 s and 98 ± 10 s from saturation recovery. For the nutation experiments delay times of $3xT_1$ was used. For the cycled cathodes, relaxation was much faster, so each point was collected with 1024 scans with a delay time of 1 s.

3.2.2.2 ^{17}O NMR Spectroscopy

The ^{17}O NMR measurements were performed on a Bruker 500 MHZ Avance I spectrometer using a 2.5 mm diameter rotors at a spinning rate of 25 kHz. The rotor was center packed using a spacer of dry alumina powder because the sample size was less than the rotor volume. The ^{17}O ssNMR measurements were made using a delay time of 1.5 s and referenced to H_2O at 0 ppm. A rotor synchronized double frequency sweep (DFS) echo was collected with a nutation frequency of 100 kHz and 12.5 kHz for the RF pulse and DFS pulse respectively.

3.3 Results and Discussion

3.3.1 Determination of Discharge Species with ^{7}Li NMR

Pristine Li_2O_2 and Li_2CO_3 have distinct static ^{7}Li NMR spectra since the ^{7}Li C_q of Li_2O_2 and Li_2CO_3 are different. [15] The ^{7}Li spectrum of Li_2CO_3 has a characteristic quadrupole lineshape where satellites are observed. The Li_2O_2 spectrum shows no quadrupole features; instead the spectrum is a broad Gaussian lineshape. The broadening has been attributed to homonuclear ^{7}Li-^{7}Li dipolar interactions.[15]

The TMP cathode ^{7}Li spectrum was compared to the ^{7}Li spectra of pristine Li_2O_2 and Li_2CO_3 to determine if Li_2O_2 was formed with the TMP electrolyte shown in **Figure 3-1**. The TMP cathode ^{7}Li spectrum consisted of a broad featureless peak. Neither quadrupole features which would indicate Li_2CO_3 or the Gaussian lineshape associated with Li_2O_2, were observed. Hence it was not possible to identify the discharge products. Nutation NMR was introduced as an alternative method to measure the ^{7}Li quadrupole interaction of the discharge species.

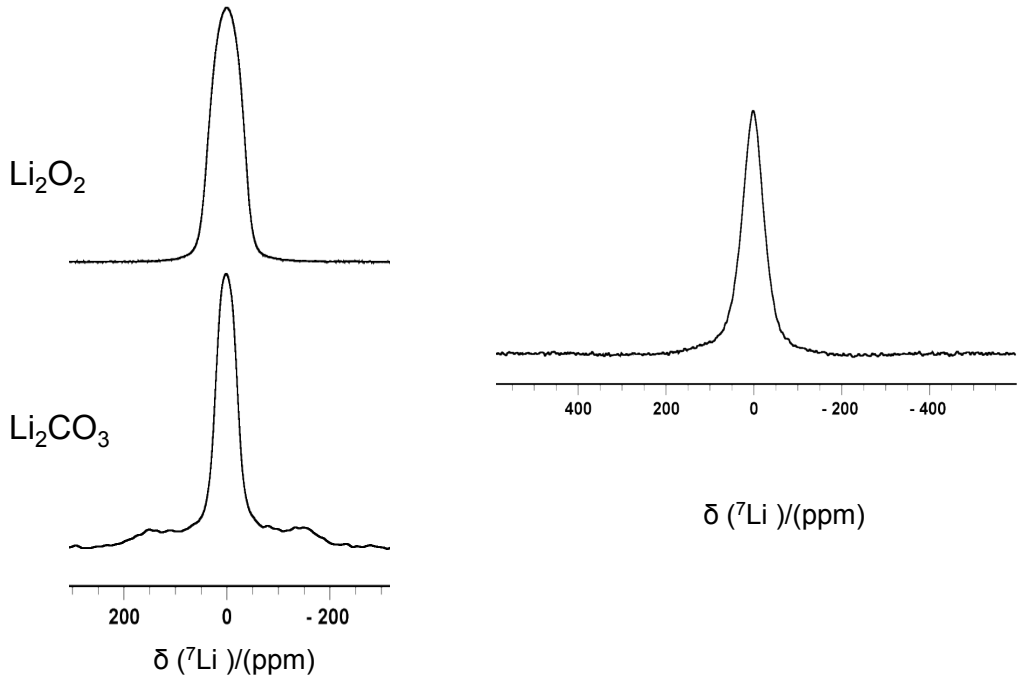

Figure 3-1 The distinct static ^{7}Li spectra of pristine, crystalline Li_2O_2 and pristine Li_2CO_3 (left) and the static ^{7}Li spectra of the cycled TMP cathode, where a single cathode was centered packed between dry alumina (right)

3.3.2 Simulated ^{7}Li Nutation Plots

First, preliminary ^{7}Li nutation plots of crystalline Li_2O_2 and Li_2CO_3 were simulated, shown in **Figure 3-2**. The simulations were performed using a modified version of the spin 3/2 nutation single crystal code[32], where a powder average was superimposed. The nutation plots were modeled with a homogeneous, on resonance γB_1 field, at the following RF fields; 10 kHz, 30 kHz, 50 kHz and 70 kHz. The ^{7}Li quadrupole parameters used in the nutation simulations were previously reported, where the ^{7}Li C_q of Li_2O_2 is 35 kHz with an eta (η) value of 0. The ^{7}Li C_q of Li_2CO_3 is 120 kHz and the η value is 0. Based on the crystal structures Li_2CO_3 has a single Li site[33] and

Li_2O_2 has two crystallographic Li sites[23] that appear as a single Li site in the ^7Li NMR spectrum.

From the simulated nutation plots, at a weak γB_1 field, ≤ 50 kHz Li_2O_2, the smaller ^7Li quadrupole species, was expected to have a slower nutation frequency than Li_2CO_3 the larger ^7Li quadrupole coupling constant species. The observed difference in the simulated nutation plots suggested that Li_2O_2 and Li_2CO_3 could be identified if the applied γB_1 field was less than 50 kHz. The most pronounced difference in the simulated nutation frequencies of crystalline Li_2O_2 and Li_2CO_3 was expected to occur when a 30 kHz γB_1 field was applied with pulse widths greater than 12 μs but less than 70 μs.

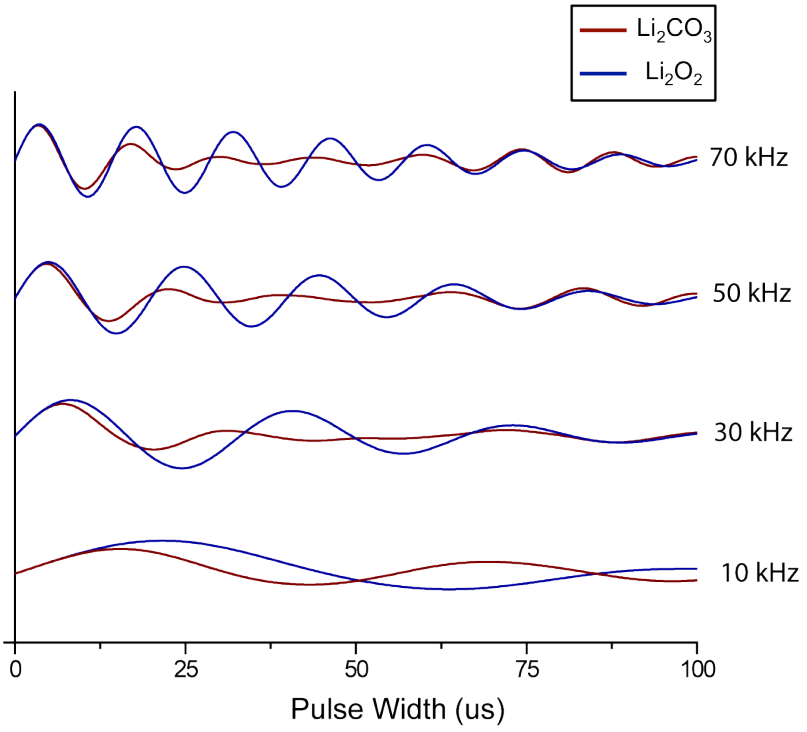

Figure 3-2 A comparison of the simulated ^{7}Li nutation plots of pristine Li_2CO_3 and pristine Li_2O_2 for various applied γB_1 field, where the applied γB_1 field was incremented from 10 kHz to 70 kHz by 20 kHz

3.3.3 Experimental ^{7}Li Nutation Plots of Pristine Li_2O_2 and Li_2CO_3

The nutation frequency for the intermediate case is composed of many sinusoids. A definable parameter, a quantifiable term is needed to compare the nutation frequencies between materials at a given RF field. Typically the raw data, the time domain data, is examined. As observed in **Figure 3-3**, there is a dominant frequency in the nutation plots of the pristine materials, which we call the pseudo nutation frequency. Since the quadrupole couplings are different, the dominant frequency of pristine Li_2O_2 is different than the dominant frequency of pristine Li_2CO_3. To extract the dominant frequency from

the time domain data a Fourier transformation was applied. Since a small number of time domain data points were collected the Fourier transformed data set is not ideal but was adequate to identify the pseudo nutation frequency. The frequency domain nutation data sets are supplied in the *appendix A6*.

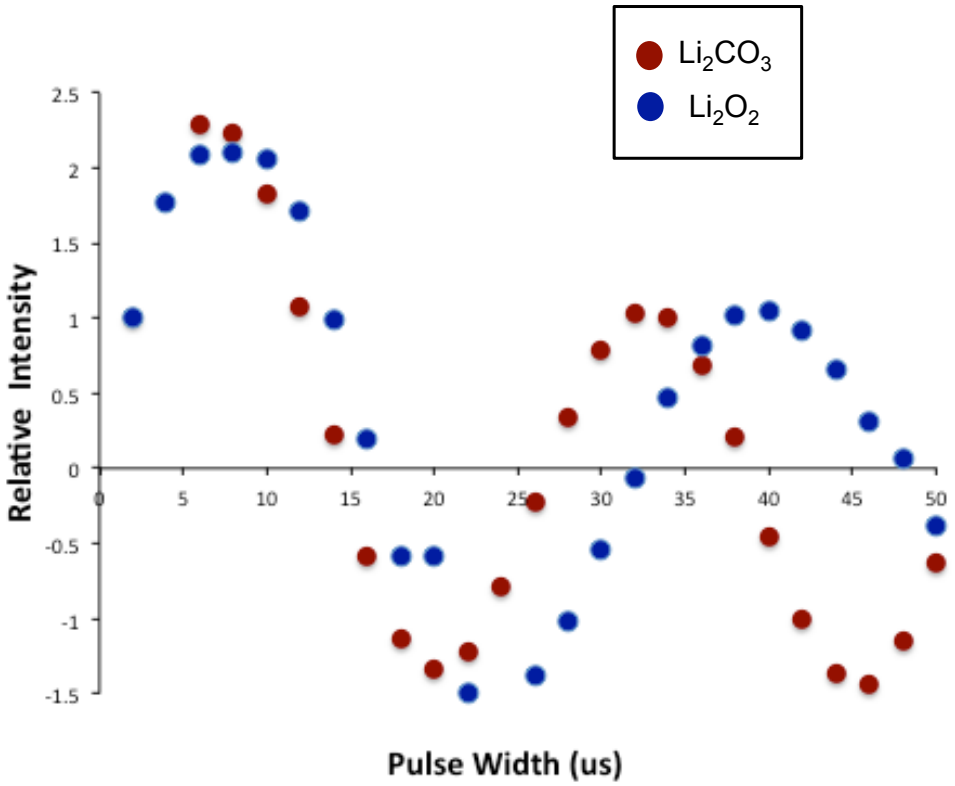

Figure 3-3 A comparison of the ^{7}Li nutation plots of the pristine Li_2O_2 and pristine Li_2CO_3 collected with a 30 kHz γB_1 field where the smaller ^{7}Li quadrupole species (Li_2O_2) has a slower nutation frequency than the larger ^{7}Li quadrupole species (Li_2CO_3)

The pseudo nutation frequencies of the pristine materials can also be compared qualitatively. The nutation frequencies were qualitatively monitored in the time domain, by examining the pulse widths required for the sample to reach the nominal flip angles (for a sample with no quadrupole interaction) of 360^{o} and 540^{o}. The values were determined from the nutation plots.

The ^{7}Li nutation plots of the pristine materials are shown in **Figure 3-3** where the applied RF field was 30 kHz. The nutation plots are measurably different, allowing Li_2CO_3 and Li_2O_2 to be distinguished when the pulse width was greater than 15 ± 1 μs. **Figure 3-3,** demonstrates that longer pulse widths were required for pristine Li_2O_2 to reach the same nominal flip angles as pristine Li_2CO_3. The nominal flip angles of 360^{o} and 540^{o} were obtained by the application of 32 ± 1 μs and 48 ± 1 μs pulses respectively for pristine Li_2O_2. This is in contrast to pristine Li_2CO_3 where pulse widths of 25 ± 1 μs and 39 ± 1 μs were needed to achieve the same flip angles. From the frequency domain nutation plots pristine Li_2O_2 was determined to have a slower pseudo nutation frequency than pristine Li_2CO_3. The pseudo nutation frequencies of pristine Li_2O_2 and Li_2CO_3 were found to be 33 kHz and 40 kHz respectively. The difference in the pseudo nutation frequency observed in **Figure 3-3** confirms that ^{7}Li nutation NMR can be used to differentiate pristine Li_2O_2 from pristine Li_2CO_3.

3.3.4 Electrochemical Materials

With the aim to determine the stability of the TMP electrolyte, first two popular electrolyte systems (namely TEGDME and PC/DMC) were investigated with ^{7}Li nutation NMR, as electrochemically produced Li_2O_2 and Li_2CO_3 have different structural and NMR properties than the pristine phases studied above. TEGDME and PC/DMC electrolytes were chosen as the model electrolyte systems since the discharge products and the electrolyte stability for these systems have been well documented. TEGDME is considered moderately stable as Li_2O_2 and Li_2CO_3 have been observed by PXRD and FTIR[9] whereas Li_2CO_3 was found to be the main discharge product for the PC/DMC

electrolyte with FTIR, Raman[10], ^{7}Li and ^{17}O NMR[15] studies. For each electrolyte system studied the Li-O_2 cell was discharged at constant current. Discharge capacities of 1000 mAh/g, 900 mAh/g and 1150 mAh/g were obtained for the TEGDME, PC/DMC and TMP electrolytes systems respectively. The electrochemical discharge profiles are shown in **Figure 3-4.**

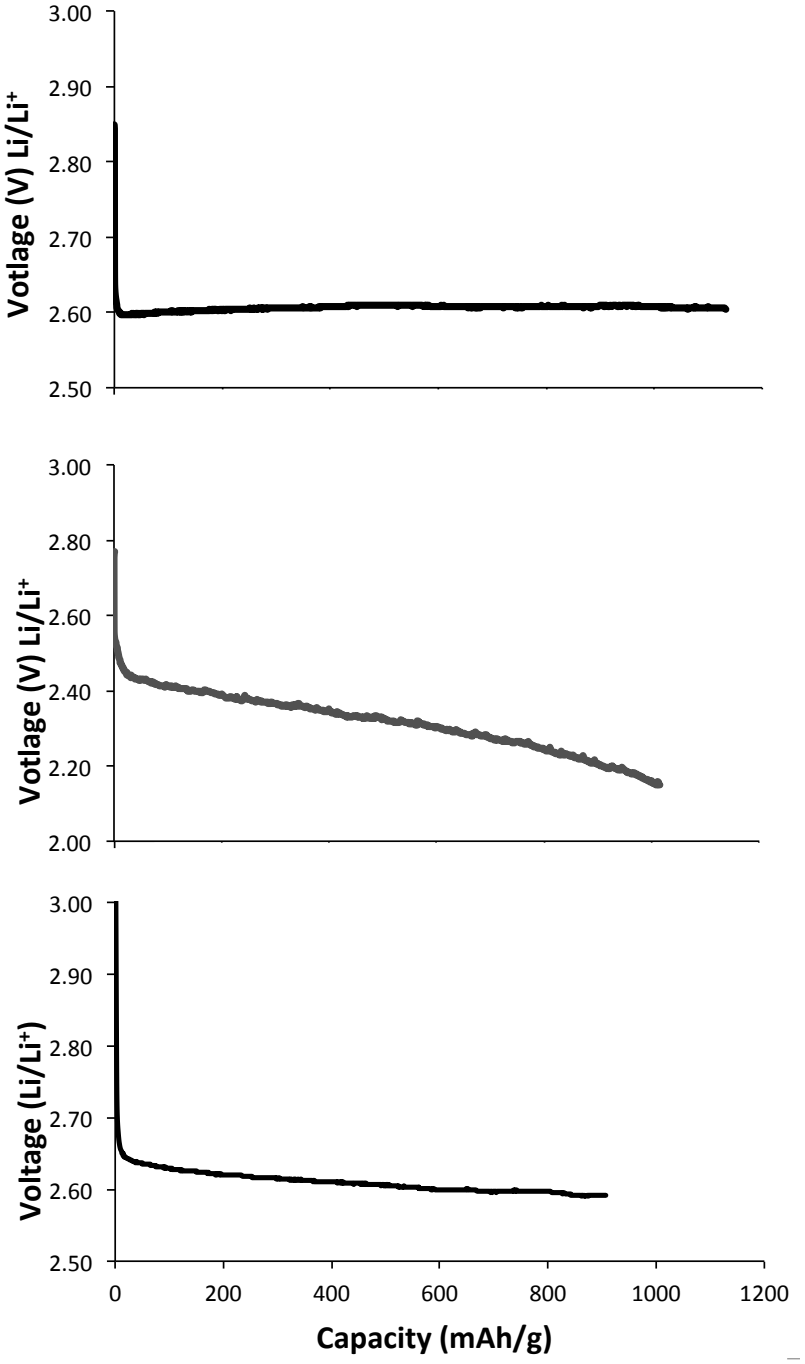

Figure 3-4 The galvanostatic electrochemical cycling profiles of the Li-O_2 cells where the following electrolyte systems were used PC/DMC (upper), TEGDME (middle) and TMP (bottom) where all cells were cycled at a rate of 70 mAh/g carbon

3.3.5 Experimental ^{7}Li Nutation Plots of Model Electrolyte Systems

The ^{7}Li nutation plots of the cycled cathodes are shown in **Figure 3-5** where the applied γB_1 field was 30 kHz. For each cathode sample the nutation experiments were performed on a single cathode. The TMP, TEGDME and PC/DMC cathode had the following respective masses; 4.8 mg. 4.3 mg and 4.5 mg and approximately 1% of the cathode's mass is expected to be the discharge product. The remaining material is the carbon cathode host.

As observed in the nutation plots of the pristine materials, **Figure 3-4**, the nutation plots of the TEGDME and PC/DMC cathodes are measurably different when the pulse width was greater than 15 ± 1 μs. The TEGDME cathode was observed to have a slower nutation frequency than the PC/DMC cathode. In other words, longer pulse widths were required for the TEGDME cathode to achieve the same nominal flip angles as the PC/DMC cathode. The nominal flip angles of 360^{o} and 540^{o} were obtained by the application of 30 ± 1 μs and 42 ± 1 μs pulses respectively. These are comparable to the pulse widths required for pristine Li_2O_2 to reach the nominal flip angles shown in **Table 3-1.** From the frequency domain data the pseudo nutation frequency of the TEGDME cathode was determined to be 38 kHz. This value is between the pseudo nutation frequencies of the pristine Li_2O_2, 33 kHz, and the pristine Li_2CO_3, 40 kHz. Suggesting that both Li_2O_2 and Li_2CO_3 are formed during discharge and that both species influence the TEGDME ^{7}Li pseudo nutation frequency. The identification of the TEGDME discharge species by nutation NMR is consistent with the discharge products reported in the literature. [13, 34]

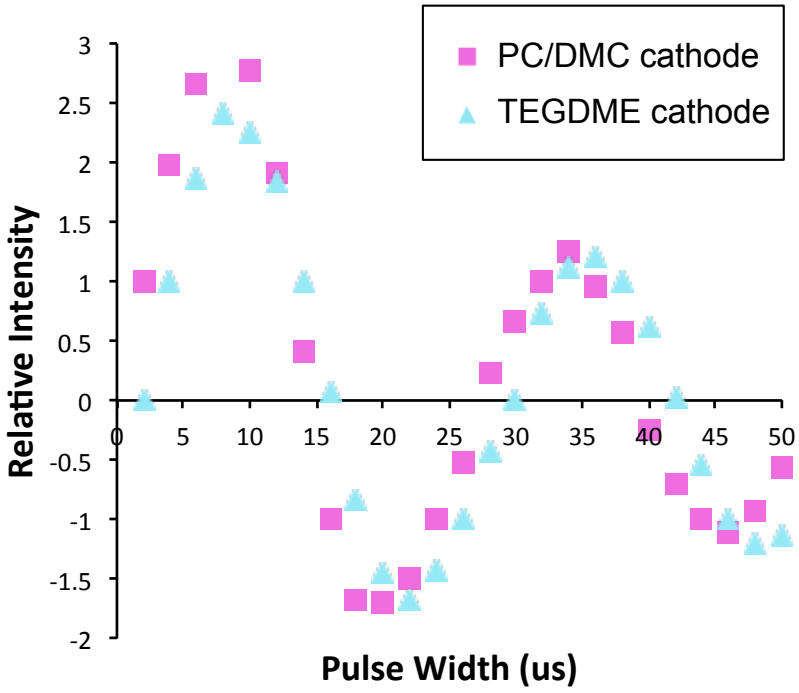

Figure 3-5 A comparison of the ^{7}Li nutation plots of the cycled electrodes when a 30 kHz γB_1 field was applied showing the slower nutation frequency of the TEGDME cathode from the presence of Li_2O_2 and the faster nutation frequencies of the PC/DMC cathode from the absence of Li_2O_2

Short pulse widths, 27 ± 1 μs and 39 ± 1 μ, were needed for the PC/DMC cathode to reach the respectively 360° and 540° flip angles. The pulse widths associated with the 360° and 540° flip angles for pristine Li_2CO_3 are comparable values to the required pulse widths for the PC/DMC cathode as outlined in **Table 3-1**.The pseudo nutation frequency of the PC/DMC cathode is 41 kHz, and is very similar to the pseudo nutation frequency of pristine Li_2CO_3, 40 kHz. This suggests that that Li_2CO_3 is present in the PC/DMC cycled cathode and that Li_2O_2 is absent. The conclusions drawn from the ^{7}Li nutation analysis of the PC/DMC discharge species is consistent with previous characterizations of the PC/DMC electrolyte. [10, 15, 35]

Table 3-1 The Pseudo ^{7}Li Nutation Frequencies and Pulse Widths for the Nominal 360^{0} and 540^{0} Flip Angles of the Li-O_2 Materials when the Applied γB_1 Field was 30 kHz

	Pristine Li_2O_2	Pristine Li_2CO_3	TEGDME cathode	PC/DMC cathode
Pseudo Nutation Frequency (kHz)	33	40	38	41
360^{0} pulse width (± 1 μs)	32	25	30	27
540^{0} pulse width (± 1 μs)	48	39	42	39

3.3.6 Experimental ^{7}Li Nutation Plots of the TMP Electrolyte

^{7}Li nutation NMR was applied to determine if Li_2O_2 was formed during discharge with the TMP electrolyte. The nutation plot of the TMP cathode is shown in **Figure 3-6** where the applied γB_1 field was 30 kHz. The pseudo ^{7}Li nutation frequency of the TMP cathode was found to be 45 kHz from the frequency domain nutation data. The pulse widths required for the TMP cathode to reach the nominal flip angles of 360^{o} and 540^{o} were 24 ± 1 μs and 38 ± 1 μs respectively. Both the ^{7}Li pseudo nutation frequency and the nominal flip angles of the TMP cathode corresponded to the pristine Li_2CO_3 values, indicating that Li_2CO_3 is a main discharge product. Because of the fast pseudo nutation frequency it is unlikely that Li_2O_2 is also formed in the TMP cathode. This suggests that TMP is not suitable Li-O_2 electrolyte. Additionally, the reversible capacity of TMP cells was found to be low.

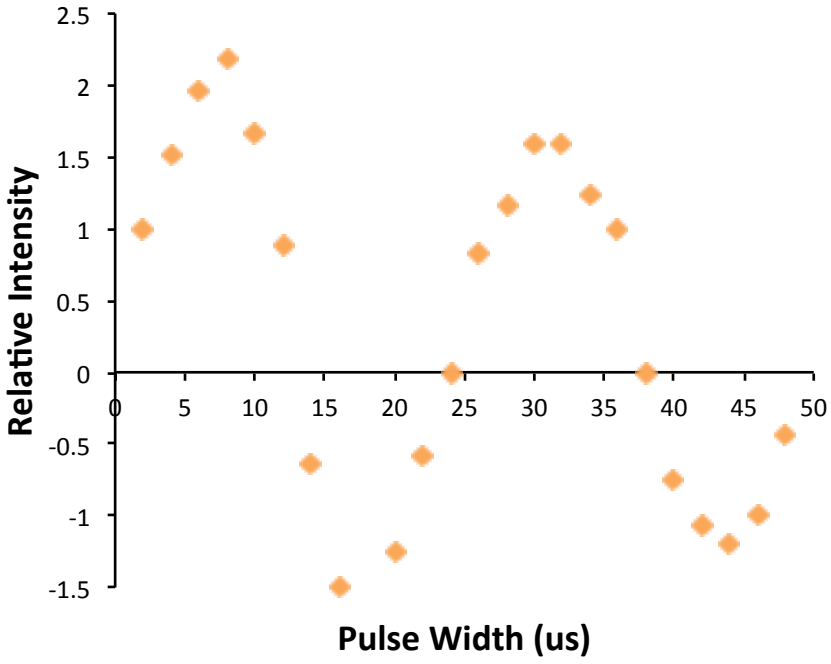

Figure 3-6 The ^{7}Li nutation plot of the cycled TMP electrodes when a 30 kHz γB_1 field where the fast nutation frequency indicates an absence of Li_2O_2

The results obtained from the ^{7}Li nutation analysis of the TMP electrolyte discussed here are consistent with related work currently being done within our research lab. When a Li-O_2 cell with TMP electrolyte, was cycled to a capacity of 1000 mAh/g using 70% ^{17}O-enriched oxygen gas Li_2O_2 was not observed in the ^{17}O NMR spectrum of the cycled cathode. Instead Li_2CO_3 was determined to be the main discharge product. This is observed in **Figure 3-7**, where the simulated ^{17}O spectrum of Li_2CO_3 fits a portion of the experimental ^{17}O cathode spectrum. The simulated Li_2O_2 spectrum does not correspond to the features observed in the experimental spectrum, indicating that Li_2O_2 is

not present in a measurable quantity. The simulations were performed using reported ^{17}O quadrupole parameters.[15-16]

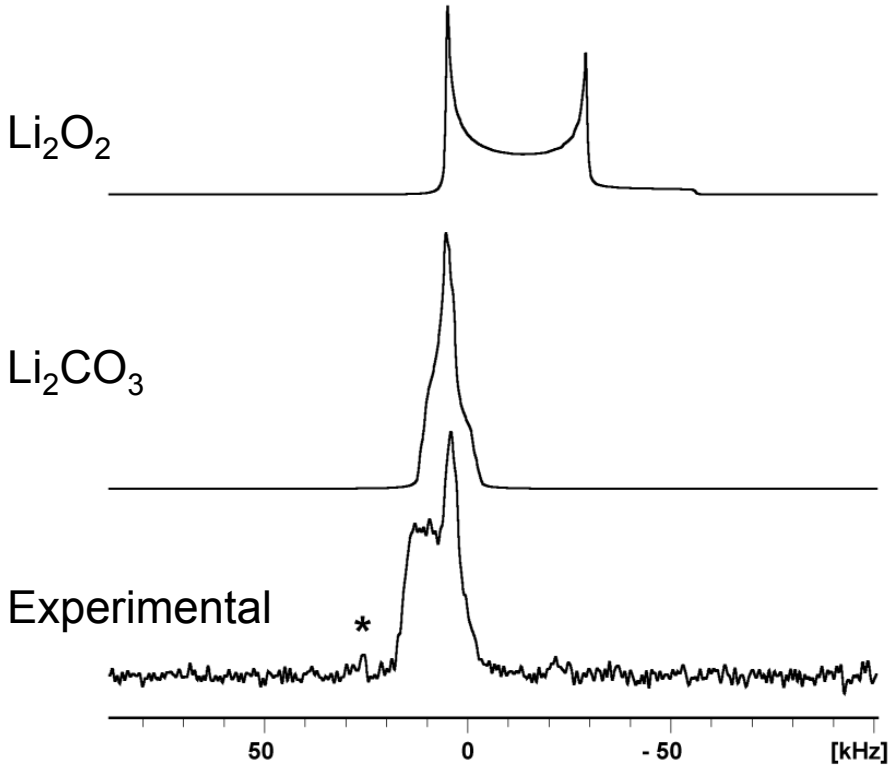

Figure 3-7 25 kHz MAS ^{17}O DFS spectrum of a 70% ^{17}O-enriched TMP cathode that was discharged to a capacity of 1000 mAh/g, compared to the simulated ^{17}O lineshapes corresponding to Li_2CO_3 (middle, where the overall simulation was shown which is composed of two oxygen sites; O1: δ_{iso}= 154 ppm, C_q = 7.22 MHz, η_q= 0.9 and O2: δ_{iso}= 166 ppm, C_q = 7.40 MHz, η_q= 0.8) and Li_2O_2 (top, δ_{iso}= 227 ppm, C_q = 18 MHz and η_q= 0), with * corresponds to the natural abundance ^{17}O signal from the ZrO_2 rotor

3.3.7 ^{7}Li Nutation Frequencies of Li-O_2 Materials

In the nutation experiment the applied γB_1 field is a controllable variable. To confirm that the greatest difference in the nutation frequency of Li_2O_2 and Li_2CO_3

occurred with an applied γB_1 field of 30 kHz, nutation experiments were performed on pristine Li_2O_2, pristine Li_2CO_3, the TEGDME cathode and the PC/DMC cathode at the following γB_1 fields; 10 kHz, 30kHz, 52 kHz, 57 kHz and 62.5 kHz. The pseudo nutation frequencies were calculated and plotted as a function of applied γB_1 field shown in **Figure 3-8**. Additionally the expected nutation frequencies for the two extreme cases, $\gamma B_1 >> C_q$, $\gamma B_1 << C_q$, were labeled on **Figure 3-8**. All experimental nutation frequencies were between the two extremes confirming that the Li-O_2 materials satisfies the $C_q \sim RF$ condition. This demonstrates that the Li-O_2 materials of interest can be classified as the intermediate case (for quadrupole nutation) and that both the γB_1 field and the ^{7}Li quadrupole interaction should influence the nutation plots. For a given γB_1 field the observed variations in the nutation frequencies of two materials should reflect differences in the size of the ^{7}Li quadrupole interaction.

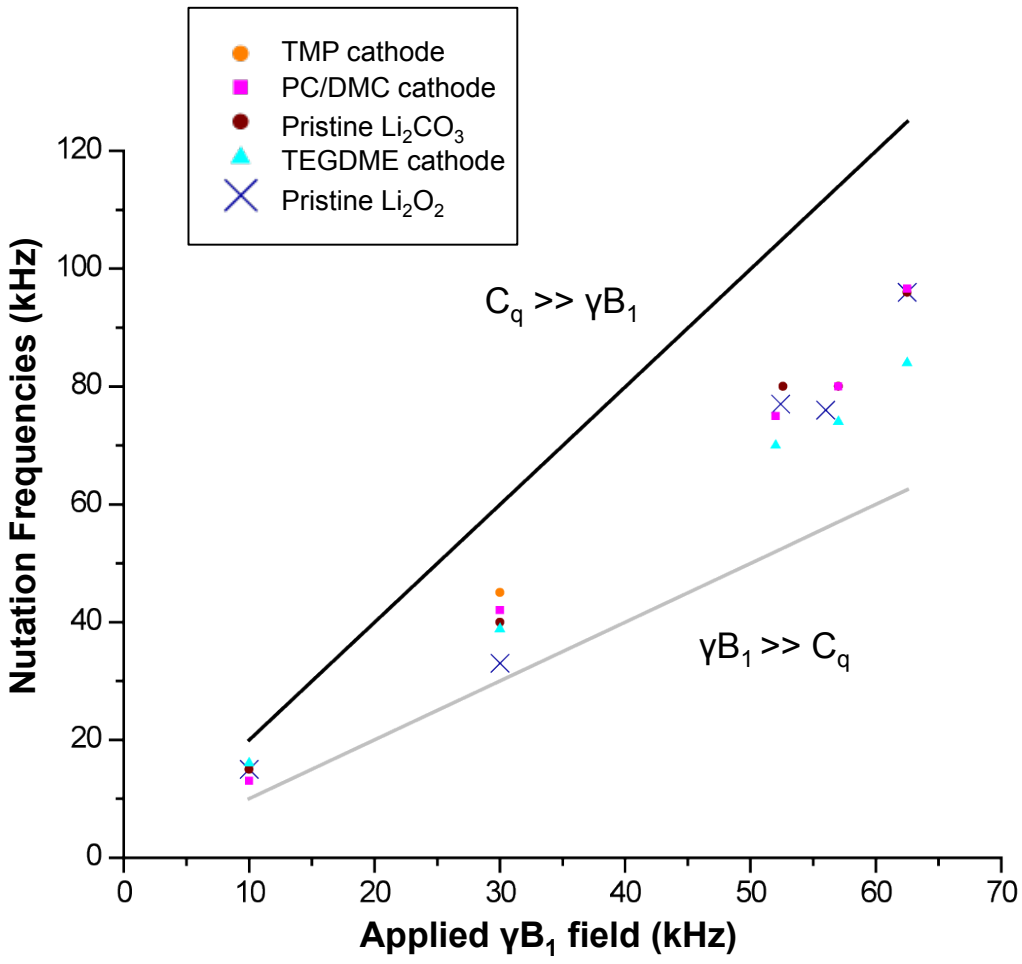

Figure 3-8 A comparison of pristine Li_2O_2, pristine Li_2CO_3, TMP cathode, TEGDME cathode and PC/DMC cathode pseudo nutation frequencies as a function of applied γB1 field, where the expected nutation frequencies for the two extreme cases were also outlined

Figure 3-8 confirms that the greatest differences in the nutation frequencies of pristine Li_2O_2 and Li_2CO_3 occurred when the γB_1 field was 30 kHz. For all other γB_1 fields the nutation frequencies of the pristine materials were too similar to allow for Li_2O_2 to be distinguished from the Li_2CO_3. The 30 kHz γB_1 field was the only γB_1 field where the nutation frequency of the TEGDME cathode was an intermediate value between the nutation frequencies of the pristine Li_2O_2 and Li_2CO_3. From this we infer that both Li_2O_2

and Li_2CO_3 are discharge species for the TEGMDE cathode, which is consistent with the known discharge products for the TEGDME electrolyte.[9] **Figure 3-8** also demonstrates that the nutation behaviour of the PC/DMC cathode closely matches that of pristine Li_2CO_3. This further suggests that Li_2CO_3 is the main discharge species form with the PC/DMC cathode. This is also consistent with the literature for the PC/DMC electrolyte system. [10, 15, 35] As the 30 kHz γB_1 field was observed to be the most sensitive to differentiating Li_2O_2 and Li_2CO_3 in the pristine materials and the cycled cathodes, the nutation plot of the novel electrolyte TMP was only determined for a 30 kHz γB_1 field.

3.4 Summary

^{7}Li nutation NMR was shown to been an effective tool for the identification of electrochemically generated Li_2O_2 in cycled cathodes. First ^{7}Li nutation NMR accurately predicted the discharge products for two model electrolyte systems, PC/DMC and TEDGME, and subsequently was applied to the TMP electrolyte. Li_2CO_3 was determined to be a main discharge species of the PC/DMC electrolyte as the ^{7}Li nutation frequency of the PC/DMC cathode (41 kHz) was comparable to the ^{7}Li nutation of pristine Li_2CO_3 (40 kHz). Both Li_2O_2 and Li_2CO_3 were determined to be discharge species in the TEGDME electrolyte since the TEGDME cathode ^{7}Li nutation frequency (38 kHz) was an intermediate value between the nutation frequency of both pristine Li_2O_2 (33 kHz) and pristine Li_2CO_3. Li_2CO_3 was determined to be the main discharge species formed with the TMP electrolyte. The TMP cathode nutation frequency (45 kHz) was comparable to the nutation frequency of pristine Li_2CO_3. The fast nutation frequency of the TMP cathode indicated that Li_2O_2 was not a discharge product and that TMP is not a suitable Li-O_2

electrolyte. The nutation NMR results of the TMP electrolyte were consistent with results from a ^{17}O NMR experiment performed on a TMP cathode. This work has demonstrated that ^{7}Li nutation NMR is an effective tool to determine the stability of Li-O_2 electrolytes.

3.5 References

[1] G. Girishkumar, McCloskey, B., Luntz, C., Swanson, S. and Wilcke, W. , *Journal of Physical Chemistry Letters* **2010**, *1*, 2193.

[2] J. K. Z. Abraham K. M. , *Journal of Electrochemical Society* **1996**, *143*, 1.

[3] J. Wang, Y. Li, X. Sun, *Nano Energy* **2013**, *2*, 443.

[4] G. BrucePeter, A. FreunbergerStefan, J. HardwickLaurence, M. TarasconJean, *Nat Mater* **2012**, *11*, 172.

[5] M. Balaish, A. Kraytsberg, Y. Ein-Eli, *Phys. Chem. Chem. Phys.* **2014**, *16*, 2801.

[6] J. Christensen, P. Albertus, R. S. Sanchez-Carrera, T. Lohmann, B. Kozinsky, R. Liedtke, J. Ahmed, A. Kojic, *J. Electrochem. Soc.* **2012**, *159*, R1.

[7] B. Dunn, H. Kamath, J.-M. Tarascon, *Science* **2011**, *334*, 928.

[8] V. S. Bryantsev, J. Uddin, V. Giordani, W. Walker, D. Addison, G. V. Chase, *Journal of Electrochemical Society* **2013**, *160*, A160.

[9] S. A. Freunberger, Y. Chen, N. E. Drewett, L. J. ardwick, F. Bard, P. G. Bruce, *Angewandte Chemie* **2011**, *50*, 8609.

[10] S. A. Freunberger, Y. Chen, Z. Peng, J. M. Griffin, L. J. Hardwick, F. Barde, P. Novak, P. G. Bruce, *J. Am. Chem. Soc.* **2011**, *133*, 8040.

[11] V. S. Bryantsev, V. Giordani, W. Walker, M. Blanco, S. Zecevic, K. Sasaki, J. Uddin, D. Addison, G. V. Chase, *J. Phys. Chem. A* **2011**, *115*, 12399.

[12] I. Gunasekara, S. Mukerjee, E. J. Plichta, M. A. Hendrickson, K. M. Abraham, *J. Electrochem. Soc.* **2014**, *161*, A381.

[13] P. Bruce, G., Freunberger, Stefan, A, Nicholas, Drewett, E., Hardwick, Laurence, J., Barde, Fanny, *Angewandte Chemie* **2011**, *50*, 8609.

[14] R. R. Mitchell, B. M. Gallant, Y. Shao-Horn, C. V. Thompson, *J. Phys. Chem. Lett.* **2013**, *4*, 1060.

[15] M. Leskes, N. E. Drewett, L. J. Hardwick, P. G. Bruce, G. R. Goward, C. P. Grey, *Angew. Chem. Int. Ed.* **2012**, *51*, 8560.

[16] M. Leskes, A. J. Moore, G. R. Goward, C. P. Grey, *J. Phys. Chem. C* **2013**, *117*, 26929.

[17] Z. Xu, J. F. Stebbins, *Solid State Nuclear Magnetic Resonance* **1995**, *5*, 103.

[18] K. J. D. Mackenzie, M. E. Smith, *Multinuclear Solid-State NMR of Inorganic Materials Vol. 6*, Elsevier Science Ltd., Cambridge, UK, **2002**.

[19] L. A. Huff, J. L. Rapp, L. Zhu, A. A. Gewirth, *journal of power Sources* **2013**, *235*, 87.

[20] J. Xiao, J. Hu, D. Wang, D. Hu, W. Xu, G. L. Graff, Z. Nie, J. Liu, J.-G. Zhang, *J. Power Sources* **2011**, *196*, 5674.

[21] S. J. Clark, M. D. Segall, C. J. Pickard, P. J. Hasnip, M. I. Probert, K. Refson, M. C. Payne, *Zeitschrift für Kristallographie* **2005**, *220*, 567.

[22] M. Segall, P. J. Lindan, M. a. Probert, C. Pickard, P. Hasnip, S. Clark, M. Payne, *Journal of Physics: Condensed Matter* **2002**, *14*, 2717.

[23] L. G. Cota, P. de la Mora, *Acta Crystallographica Section B* **2005**, *B61*, 133.

[24] W. Honle, H. Schnering, *Acta Crystallogr. A* **1978**, *34*.

[25] M. H. Levitt, *Spin Dynamics: Basics of Nuclear Magnetic Resonance*, John Wiley & Sons, Chichester, Uk, **2001**.

[26] J. Keeler, *Understanding NMR Spectroscopy*, John Wiley and Sons, New York **2005**.
[27] M. J. Duer, *Introduction to Solid-Sate NMR Spectroscopy*, Blackwell Publishing Ltd, Oxford, UK **2004**.
[28] A. P. M. Kentgens, *Geoderma* **1997**, *80*, 271.
[29] L. Pandey, S. Towta, D. G. Hughes, *The Journal of Chemical Physics* **1986**, *85*, 6923.
[30] W. Veeman, *ZEITSCHRIFT FUR NATURFORSCHUNG SECTION AA JOURNAL OF PHYSICAL SCIENCES* **1992**, *47*, 353.
[31] A. P. M. Kentgens, J. J. M. Lemmens, F. M. M. Geurts, W. S. Veeman, *Journal of Magnetic Resonance (1969)* **1987**, *71*, 62.
[32] T. L. Spencer, G. R. Goward, A. D. Bain, *Solid State Nuclear Magnetic Resonance* **2013**, *53*, 20.
[33] Y. Idemoto, J. W. Richardson Jr, N. Koura, S. Kohara, C.-K. Loong, *Journal of Physics and Chemistry of Solids* **1998**, *59*, 363.
[34] C. Laoire, S. Mukerjee, E. J. Plichta, M. A. Hendrickson, K. M. Abraham, *J. Electrochem. Soc.* **2011**, *158*, A302.
[35] B. D. McCloskey, D. S. Bethune, R. M. Shelby, G. Girishkumar, A. C. Luntz, *The Journal of Physical Chemistry Letters* **2011**, *2*, 1161.

Chapter 4 : Evaluation of the Stability of TMP as a Lithium-Oxygen Battery Electrolyte via Multinuclear Solid-State NMR

4.1 Introduction

This chapter discusses the work done towards understanding the stability of the TMP electrolyte in the Li-O_2 battery. Using ^{17}O NMR, the stability of two potential Li-O_2 electrolytes; TEDGME and TMP, are compared. The TEGDME electrolyte displayed superior stability as Li_2O_2 was observed in combination with electrolyte breakdown products. In the TMP cell, only electrolyte breakdown species are found. A potential electrolyte decomposition mechanism is proposed for TMP, that accounts for the formation of the reaction products observed in the ^{1}H, ^{7}Li, ^{31}P and ^{17}O ssNMR spectra of the electrochemically-cycled cathodes.

This work was published in the *Journal of Physical Chemistry C*. Initial drafts of the manuscript were prepared by the current author, Z. E. M. Reeve. The content was reproduced with the permissions of *The Journal of Physical Chemistry C* ***(119),*** *48, 26840-26848, 2015) with co-authors A. D. Pauric, K. J. Harris and G. R. Goward. Copyright (2015) American Chemical Society.* All electrochemically cycling and ^{17}O-enrichment was performed at McMaster. All NMR spectra were collected and processed at McMaster University under the supervision of Prof. Gillian R. Goward.

The lithium-oxygen (Li-O_2) battery is a promising, rechargeable, high-energy-density storage device for hybrid and electric vehicles as the theoretical energy density is comparable to gasoline.[2] The theoretical energy density has not been achieved and there are many challenges still associated with the Li-O_2 battery, with perhaps the most important one being poor electrolyte stability.[3-5]

The Li-O_2 cell operates as an open device where the active cathode material, O_2, is accessed from the atmosphere. The anode is Li metal and lithium ions migrate between electrodes *via* a non-aqueous electrolyte.[6] When the cell is operational, molecular oxygen is reduced to the superoxide radical on a porous carbon support. Ideally the superoxide combines with Li^+ ions from the electrolyte solution, forming an insulating layer of solid lithium peroxide (Li_2O_2) on the carbon membrane. In addition to the desired electrochemistry, the superoxide also attacks the electrolyte, resulting in undesirable electrolyte breakdown products.

Many classes of non-aqueous compounds have been investigated as potential electrolyte solvents. A stable electrolyte that facilitates reversible formation of Li_2O_2 has yet to be realized.[5] Propylene carbonate (PC), the electrolyte originally investigated, was found to be highly unstable. Lithium carbonate (Li_2CO_3) is the primary discharge product with no evidence of Li_2O_2.[7] The instability was determined based on several spectroscopic and structural investigations including; Fourier transformed IR (FTIR), powder X-ray diffraction (PXRD), surface enhanced Raman spectroscopy (SERS), solution state nuclear magnetic resonance (NMR),[7] and ^{17}O solid-state NMR (ssNMR).[8]

Superior stability has been observed with ether-based electrolytes such as 1,2-dimethoxyethane (DME) and tetraethylene glycol dimethyl ether (TEGDME), though both Li_2O_2 and Li_2CO_3 are detectable on first discharge.[1, 8-10] In spite of their favorable initial performance, ether electrolytes do not exhibit long-term stability.[5] The percentage of Li_2O_2 diminishes and the quantity of undesirable species grows as the number of cycles increases.[9, 11] The primary decomposition mechanism is thought to be the abstraction of

the β hydrogen by the superoxide radical. To overcome this limitation *Nazar, L. F. et al.* [12] investigated a DME derivative, 2,3-dimethyl-2,3-dimethoxybutane (DMDMB). In DMDMB the backbone protons of DME were substituted with methyl groups. The DMDMB electrolyte displayed lower reactivity and improved cycling compared to DME.[12] Unfortunately, low molecular weight ethers have vapour pressures that are too high to be practical for the Li-O_2 battery.[5] These observations highlight the fact that the physical properties of potential electrolyte solvents, the electrochemical stability window, and the chemical stability against the superoxide radical must all be considered simultaneously when evaluating possible electrolyte formulations.

Low vapour pressure, high boiling point solvents are often quite viscous, hindering electrochemical performance by impeding ionic motion. Exceptions to this rule have been observed for partially fluorinated phosphate esters, partially fluorinated phosphites, and phosphate estesr.[13] The partially fluorinated phosphorus compounds tris(2,2,2 –trifluoroethyl) phosphite (TTFP) and tris(2,2,2-trifluoroethyl phosphate (TFP) were previously considered in a co-solvent mixture, where PC was the secondary solvent in both cases.[13] Both co-solvent mixtures showed improved performance with respect to pure PC. TTFP was found to display superior conductivity, attributed to the lower viscosity of TTFP (1.45 cP) compared to TFP (3.59 cP).[13] However, TTFP is not expected to be a suitable Li-O_2 electrolyte, since the valence of the phosphorus in TTFP is +3, which could easily be oxidized to +5 by the superoxide radical.[13] Materials that are already in their highest oxidation state are preferred and expected to be resistant to attack by the superoxide radical.

Triethyl phosphate (TEP), is a non-fluorinated phosphate ester which has demonstrated some promise as a potential Li-O_2 electrolyte. Li_2CO_3 with some Li_2O_2 was reported as the main discharge products based on an X-ray photoelectron spectroscopy (XPS) investigation.[14] Low signal intensity was observed in both XRD and FTIR studies, suggesting that the discharge species may be amphorous.[14] Phosphate esters warrant further study with a technique that is sensitive to the bulk material and independent of crystallinity.

Here trimethyl phosphate (TMP), an analogous material to TEP, was investigated as a potential Li-O_2 electrolyte. TMP was selected based on its low-flammability, low cost, and high boiling point (197 ^{o}C).[15-16] TMP was therefore investigated as a possible safe, stable Li-O_2 electrolyte. The suitability of TMP was determined by examining the electrochemical behaviour and stability of TMP in the presence of the superoxide radical with ex-situ ssNMR experiments of extracted cathode materials following electrochemical cycling.

ssNMR is a nucleus specific approach that probes the chemical environments of nuclei in both crystalline and highly disordered systems. Li_2O_2 and Li_2CO_3 have different ^{7}Li quadrupole coupling constant (C_q) which could be used to identify discharge species in cycled cathodes.[8] However, the ^{7}Li NMR spectra of the cathode materials share a narrow chemical shift range centered at 0 ppm for the diamagnetic reaction products, and comparably broad featureless spectra.[8, 17] Instead, ^{7}Li nutation spectroscopy has been used to indirectly determine the ^{7}Li C_q of the discharge products. With this approach Li_2CO_3 and Li_2O_2 have been distinguished in cycled Li-O_2 electrodes.[18] Quantification

of the relative amounts of lithiated species is difficult in that case. An alternative approach was taken here utilizing ^{17}O NMR spectroscopy to directly determine the species formed.

^{17}O NMR is an extremely valuable tool to determine whether Li_2O_2 is formed within a Li-O_2 cell.[1, 8] Li_2O_2 has a ^{17}O C_q of 18 MHz[8] which is significantly larger than the ^{17}O C_q for most oxygen-containing materials.[19-20] For this reason, Leskes et al. have proposed the use of ^{17}O NMR as a screening tool for Li-O_2 electrolytes.[1, 8] The undesirable electrolyte breakdown species, Li_2CO_3, LiOH, HCO_2Li, and CH_3CO_2Li, all have ^{17}O C_q values of approximately 7 MHz, allowing Li_2O_2 to be readily identified from the undesirable electrolyte breakdown species *via* ^{17}O NMR.[1, 8]

^{1}H and ^{31}P NMR were also investigated here for their sensitivity as probes of TMP decomposition. As Li_2O_2 does not contain H or P atoms, spectroscopic evidence of protonated or phosphorous-based discharge products in the cycled cathode spectra would be indicative of electrolyte breakdown. Through this multinuclear NMR investigation, the electrochemical processes that occurred within the Li-O_2 battery were examined and the suitability of the TMP electrolyte was determined.

4.2 Experimental

4.2.1 Li-O_2 Electrochemistry

The cathode slurries and Li-O_2 batteries were assembled following a previously published procedure[21] outlined in Chapter 3, section 3.2.1. The TMP and TEGDME electrolytes solutions used in this study were a 0.5 M LiTFSI (lithium bis-trifluoromethanesulfonimide) solution in trimethyl phosphate (Sigma Alridch) and a 1 M

LiTFSI solution in tetraglyme (Sigma Alridch). The cells rested at equilibrium for 12 hours prior to galvanostatic cycling at a rate of 70 mA/g of carbon in a pure oxygen environment. The Li-O_2 cells were disassembled under argon. The discharged cathodes were extracted, washed in dry acetonitrile and dried for several hours under vacuum prior to NMR analysis.

4.2.1.1 Linear Voltammetry Study of TMP

Linear voltammetry experiments were performed using a three-electrode set up. The working electrode was a glassy carbon electrode. Both the counter and reference electrodes were constructed from lithium foil. The linear sweep voltammetry curves were collected at a scan rate of 100 mV/s with a step size of 2 mV.

4.2.1.2 ^{17}O-enrichment of Li-O_2 Cells

The TMP and TEGDME cathodes were cycled in the presence of 70 % $^{17}O_2$ enriched oxygen gas, purchased from CortecNet Corp. The ^{17}O-enrichment of the Li-O_2 cells follows a previously published procedure, which is outlined in Chapter 3, section 3.2.1.1. The ^{17}O-enrichment process employed here, involving a specially built gas manifold line. Details about the gas line manifold are provided in *appendices A4* and *A5*.

The cell cycling and NMR preparation for the ^{17}O-enriched cells was identical to the non-enriched cells outline above. The dried electrode material had a mass of ~ 5 mg, of which 20 % corresponds to the mass of lithium-oxygen discharge products. Thus, in spite of the seemingly high level of isotopic enrichment, the data sets required more than five hours of acquisition time, and produced spectra with S/N ratios of about five for the cycled cathodes.

4.2.2 Solid-State NMR Spectroscopy

All solid-state NMR (ssNMR) measurements were performed on a Bruker 500 MHz Avance I spectrometer using 2.5 mm diameter rotors, which were centered packed with dry alumina powder in cases where the volume of the electrode material was less than the rotor volume.

4.2.2.1 ^{1}H NMR Spectroscopy

The ^{1}H ssNMR spectra were acquired using a 5 s recycle delay time and were referenced to adamantane at 1.86 ppm. The spectra were collected using a background-suppressing, rotor-synchronized echo with a 25 kHz sample-spinning rate and an rf nutation frequency of 83 kHz.

4.2.2.2 ^{7}Li NMR Spectroscopy

The ^{7}Li ssNMR spectra were acquired using a recycle delay time of 1 s and were referenced to a 1 M solution of LiCl in H_2O at 0 ppm. The static ^{7}Li NMR spectra were collected with a solid echo with a nutation frequency was 60 kHz.

4.2.2.3 ^{17}O NMR Spectroscopy

The ^{17}O ssNMR measurements of the cycled cathodes were made using a 1.5 s delay time and referenced to natural abundance H_2O at 0 ppm. The ^{17}O signal from water was observed in 128 scans using a 0.1 s delay time. The static cathode spectra were collected utilizing a double frequency sweep (DFS)[22] echo and the Carr-Purcell/Meiboom-Gill (CPMG) acquisition method,[23-26] where the excitation and refocusing pulses had 100 kHz nutation rate and the DFS waveform was swept from

1.2 MHz to 0.2 MHz over 1 ms at a power level of 15 kHz. Because acquisition times were too long for experimental optimization, parameters for the DFS sweep were first optimized *in silico*, using the SIMPSON[27] software package to model the spin system with its known quadrupole parameters.[1, 8]

4.2.2.4 ^{31}P NMR Spectroscopy

The ^{31}P ssNMR spectra were referenced to 85 % H_3PO_4 at 0 ppm. The cathode spectra were acquired using a rotor-synchronized echo with a 100 s recycle delay, a 42 kHz nutation frequency, and 10 - 15 kHz sample rotation rates.

4.3 Results and Discussion

4.3.1 Electrochemical Analysis

Figure 4-1 shows a linear sweep voltammogram of a 0.5 M solution of LiTFSI in TMP collected under argon. The voltammogram demonstrates that TMP is electrochemically stable from 1.5 V to 4.5 V (vs. Li/Li^+) as minimal electrochemical activity was detected. This voltage range encompasses previously reported discharge plateaus for Li-O_2 cells,[2, 5] and illustrates that TMP is on the edge of the oxidative stability needed for the charging process as there is a high over potential associated with the Li-O_2 cell.

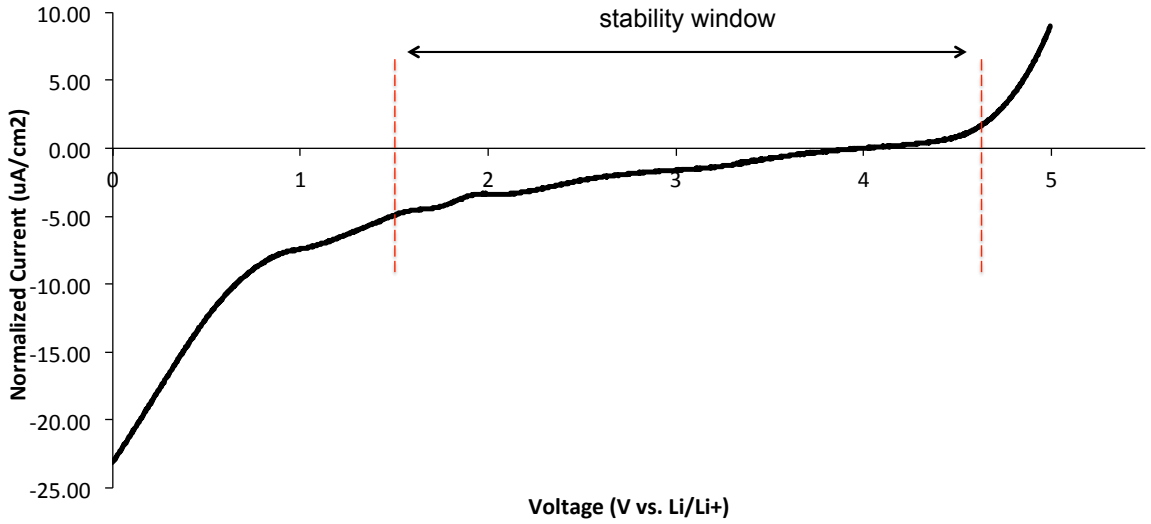

Figure 4-1 Linear sweep voltammogram of a 0.5 M LiTFSI solution in TMP at a scan rate of 100 mV/s in an argon atmosphere

The galvanostatic cycling curve of the TMP cell is shown in **Figure 4-2a**. The discharge plateau occurs at 2.5 V with a discharge capacity exceeding 1000 mAh/g and the charging plateau is observed to occur at 4.6 V. The cycling curve of the TMP cell in **Figure 4-2a** demonstrates similar electrochemical behaviour to the cycling curve of the TEGDME cell shown in **Figure 4-2b**. In this study, TEGDME was treated as the benchmark for electrolyte stability because TEDGME is a moderately stable electrolyte where Li_2O_2 formation is known to occur.[9-10, 28] The discharge plateau for the TEGDME cell occurs at 2.55 V and the charging plateau occurs at 4.4 V. In both electrolyte systems a large hysteresis is observed. For the Li-O_2 battery the hysteresis is believed to result from the insulating nature of the discharge product, Li_2O_2.[29] The observed hysteresis in the cycling curve of the TMP cell, combined with the similarities between the TMP and TEGDME discharge behaviour suggests that Li_2O_2 may be the electrochemical reaction

product formed in the presence of the TMP electrolyte. This hypothesis is based solely on the electrochemical stability window of TMP, and the electrochemical performance of the Li-O_2 cell upon galvanostatic cycling. Further details of the electrochemical reaction products are elucidated using ssNMR. The samples selected for the ex-situ NMR study were limited by the specific capacities outlined in **Figures 4-2a and 4-2b**. For both electrolytes only the D_{1000} cathode was ^{17}O-enriched.

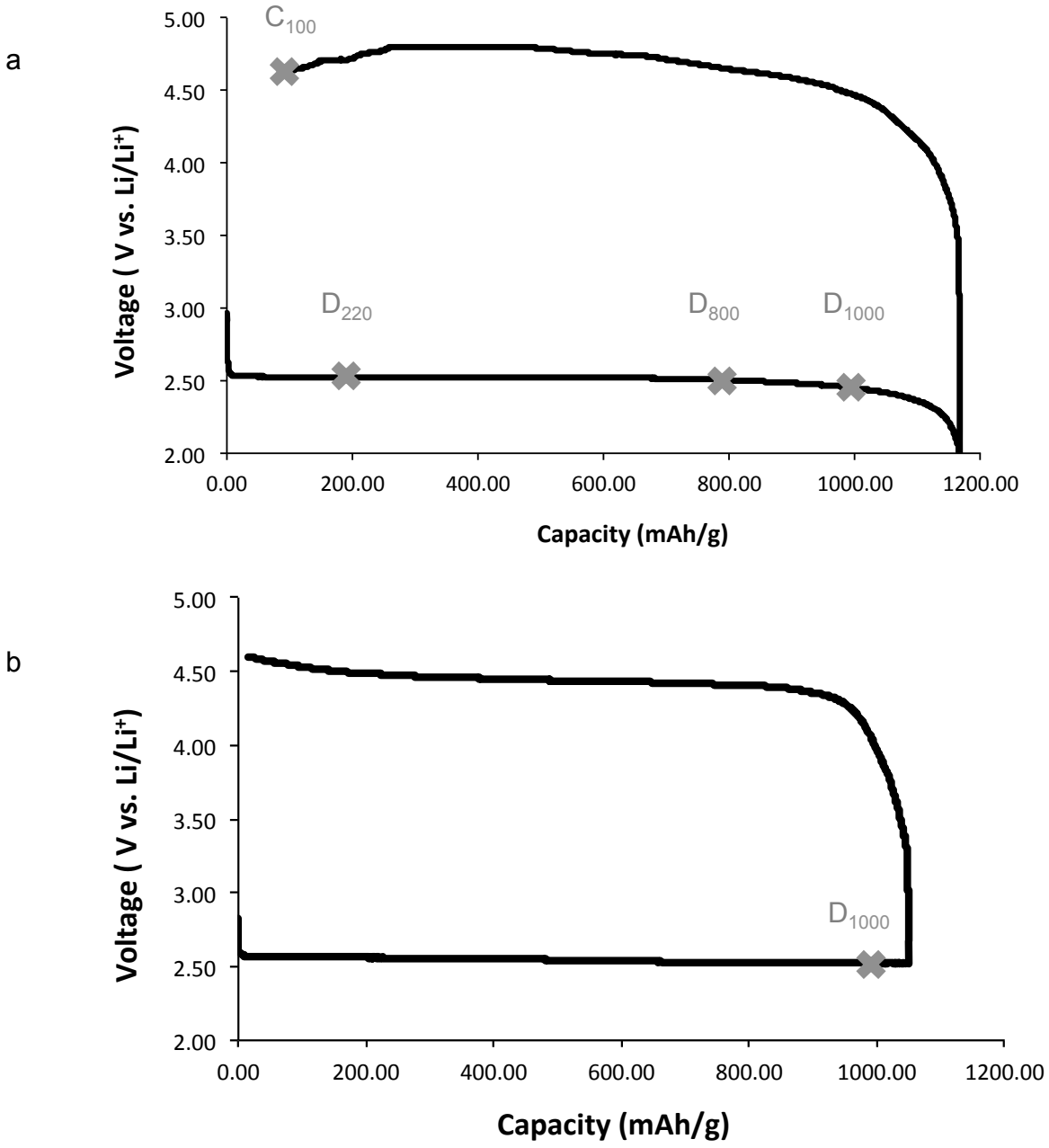

Figure 4-2 Galvanostatic cycling plots of Li-O_2 cells cycled at a rate of 70 mA/g where the first cycled is shown when the electrolyte was a 0.5 M solution of LiTFSI in TMP (2a) and the electrolyte was a 1 M solution of LiTFSI in TEGDME (2b)

4.3.2 ^{17}O NMR of Cycled Cathodes

The main discharge products produced in Li-O_2 cells were determined by performing ^{17}O NMR on cycled cathodes. The ^{17}O NMR spectra of the cathodes cycled in either the TMP or TEGDME electrolyte are shown in **Figure 4-3**. For both electrolyte systems, the electrochemistry was carried out under 70 % ^{17}O-enriched oxygen gas, generating cathodes loaded with ^{17}O-enriched products, which precipitate onto the porous carbon support.[1, 8] The molecular oxygen is reduced to the superoxide anion, which then further reacts to generate the electrochemical products. Thus the ^{17}O spectrum of the extracted cathode material contains a record of all possible precipitates formed from the enriched molecular oxygen starting material. The cathode spectra were collected using two signal-enhancement techniques: double-frequency sweeps (DFS)[22] and quadrupolar Carr-Purcell/Meiboom-Gill (QCPMG) echo trains.[23-26]

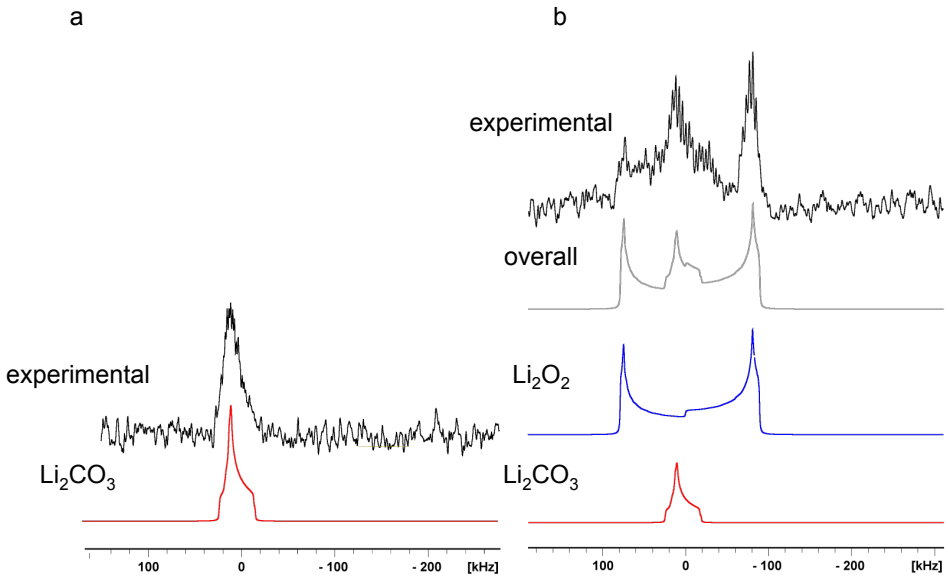

Figure 4-3 Static DFS-QCMP ^{17}O NMR spectra (a) TMP discharged cathode and (b) TEGDME discharge cathode, where both cells were cycled to a capacity of 1015 mAh/g. The experimental spectra (black lines) were simulated by using the relevant ^{17}O quadrupole parameters for Li_2O_2 (blue) and Li_2CO_3 (red)

For comparison to the ^{17}O-enriched electrochemical samples, the ^{17}O central transition NMR lineshapes of the relevant Li-O_2 species were modeled. The simulations were performed using the SIMPSON[27, 30] software package at 11.7 T under static conditions with the reported ^{17}O quadrupole parameters.[1, 8] (Sample SIMPSON input files are provided in the *appendix A3*). **Figure 4-4** demonstrates that even at moderate fields Li_2O_2 has a distinct ^{17}O spectrum from the ^{17}O C_q of 18 MHz, combined with the axial symmetry that results in the double-horn shaped pattern. The Li_2O_2 lineshape is readily distinguished from the undesirable breakdown species lineshapes, all of which have a ^{17}O C_q of approximately 7 MHz.[1, 8] It should be noted that the electrochemical reaction products are unlikely to be crystalline, or even locally ordered. Nevertheless, the

quadrupolar parameters of the ^{17}O nuclei are not expected to be sufficiently different between the pristine and electrochemical reaction products; and therefore, the simulated lineshape parameters will provide a robust diagnostic tool. The Li_2CO_3 lineshape was represented in **Figure 4-4** as a single oxygen site despite Li_2CO_3 having two crystallographic oxygen sites, as the two sites cannot be distinguished at this field strength. The ^{17}O NMR parameters applied to model the experimental spectra in **Figure 4-3** are consistent with previously determined values from high field studies[1, 8] and CASTEP simulations.[31-32]

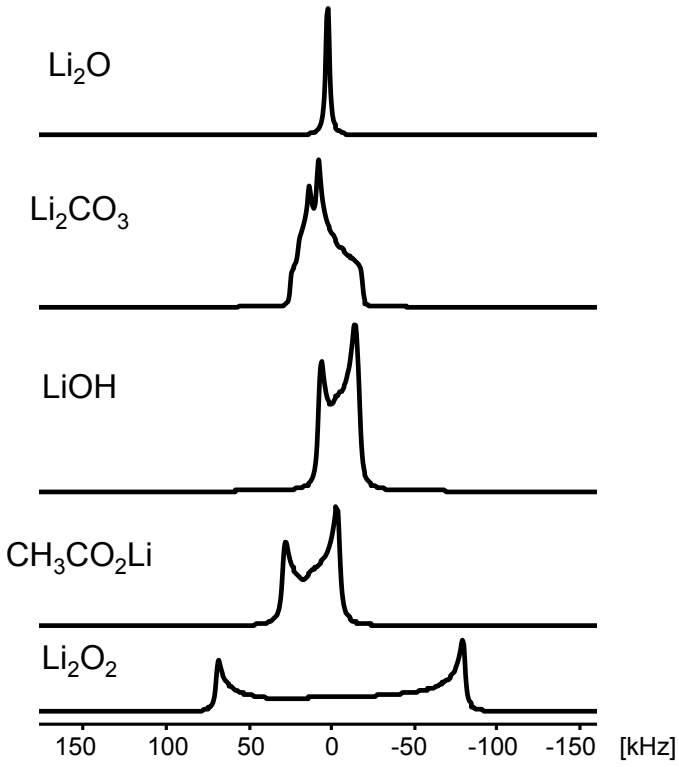

Figure 4-4 Simulations of the ^{17}O central transition lineshapes of the relevant Li-O_2 discharge species at 11.7 T under static conditions using reported ^{17}O quadrupole parameters[1]

The ^{17}O NMR spectrum of the TMP cathode, **Figure 4-3a,** is substantially narrower than the distinct Li_2O_2 line shape, indicating that Li_2O_2 is not formed as a significant electrochemical product during discharge. The Li_2CO_3 ^{17}O parameters (red lineshape) fit well with the experimental spectrum, demonstrating that lithium carbonate is a key discharge product. Considering the ^{17}O NMR spectra of other possible electrolyte by-products, which are simulated in **Figure 4-4**, it is observed that the acetate lineshape is similar to the carbonate in breadth, as they have comparable quadrupole coupling constants. The lineshape of lithium acetate is distinct from carbonate in the positions of the singularities, but, given the signal to noise limitations of the spectra, we

cannot unequivocally distinguish the two. In the ^{1}H spectroscopy below, we provide further evidence for the presence of acetate, but note that carbonate would not be visible in that case. Most significantly, the absence of a measureable quantity of Li_2O_2 indicates that TMP is highly unstable in the presence of the superoxide radical.

The ^{17}O NMR spectrum of the TEGDME cathode, **Figure 4-3b,** can be modeled as a sum of the Li_2O_2 ^{17}O parameters (blue lineshape) and the Li_2CO_3 ^{17}O parameters (red lineshape). The central region of the experimental spectrum may contain contributions for other undesirable side products in addition to Li_2CO_3. The ^{17}O spectrum demonstrates that TEGMDE is a moderately stable electrolyte because a large percentage of the discharge products are Li_2O_2. However TEGDME is not an ideal electrolyte as there is evidence of parasitic side reactions, which have been reported previously. [9]

The ^{17}O NMR spectra of the cycled cathodes indicate that TEGMDE is a more stable electrolyte than TMP in the Li-O_2 battery. This refutes the original hypothesis, that TMP would be a viable electrolyte for Li-O_2 cells, in spite of the promising electrochemical window, and competitive reversible capacity on the first cycle. Given that there was no evidence of the distinctive Li_2O_2 signal, we conclude that further investigation using ^{17}O-enrichment would not provide greater insight into the TMP electrochemical reactions within the Li-O_2 cell. Beyond this we rely on multinuclear NMR studies to identify other possible reaction products.

4.3.3 ^{1}H NMR of TMP Cells

^{1}H NMR spectroscopy was performed on the cycled TMP cathodes to determine which protonated discharge products were formed. The spectra, **Figure 4-5**, were normalized to the intensity of the 2.5 ppm polyvinylidene fluoride (PVDF) binder peak, i.e., to the constant amount of binder used in all cells. Here we are assuming negligible breakdown of the PVDF binder following a single electrochemical cycle. [33] All ^{1}H NMR spectra of cycled cathodes show intensity at 3.5 ppm, which is the same region as the TMP's methoxy group. Residual TMP is observed in the NMR spectrum of the electrolyte soaked, uncycled cathode **Figure 4-5.** In addition to TMP ($P{=}O(OMe)_3$), two other structures were expected to contain methoxy functional groups; a TMP derivative species ($^{-}OP{=}O(OMe)_2$) and free LiOMe. Both LiOMe and the TMP derivative species are hypothesized to be byproducts from TMP decomposition, where the TMP derivative structure is proposed to result from the loss of a methyl group.

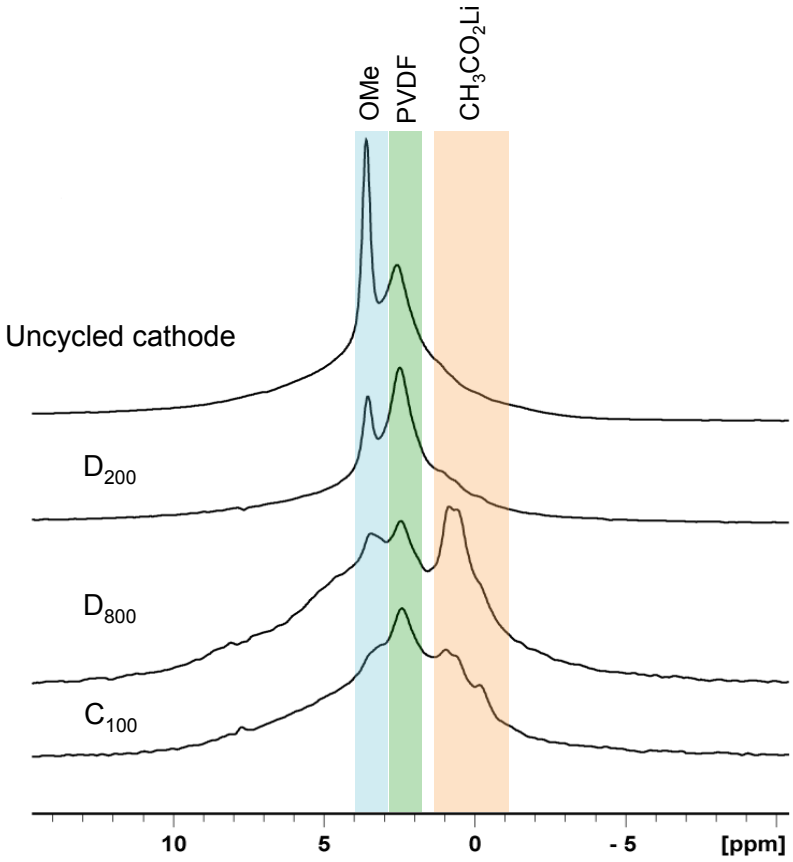

Figure 4-5 25 kHz background suppressed MAS ^{1}H NMR spectra of cycled cathodes, where the OME functional group is highlighted in blue, the PVDF resonance is highlighted with green and CH_3CO_2Li is highlighted with orange respectively

When the ^{1}H NMR spectra of the uncycled electrode and the cycled cathodes are compared, three new resonances are observable in the NMR spectra, which are not present in the uncycled electrode, indicating that protonated electrolyte breakdown species are formed during the operation of the cell. Three ^{1}H resonances were observed are at 1 ppm, 0.6 ppm and - 0.3 ppm. The three sites were attributed to the formation of three lithium acetate phases, which only differed in their degrees of crystallinity. This is

consistent with a previous report where a single Li-O_2 discharge product corresponded to multiple ^{1}H signals due to the formation of disordered phases.[1]

In preparation for the solid-state NMR measurements, the cathodes are washed with dry acetonitrile and dried under vacuum. The washing solution from a cycled cathode was retained and a solution state ^{1}H NMR spectrum was acquired (shown in *appendix A7*). In the solution state spectra there was no evidence of additional soluble species, confirming that the ssNMR spectra represent all protonated discharge species formed within the cell. The intensity of the lithium acetate ^{1}H signals greatly increased as the discharge capacity increased from D_{200} to D_{800}. This suggests that lithium acetate is present in measurable quantities after the cell has been operational for several hours.

4.3.4 ^{7}Li NMR of TMP Cells

Lithiated discharge species were observed in the ^{7}Li NMR spectra of all the cathodes cycled in TMP electrolyte, **Figure 4-6.** In this case the spectra were normalized to the mass of the electrode. The static ^{7}Li spectra are composed of a broad featureless resonance and a sharp resonance. The sharp peak is attributed to residual LiTSFI salt and the broad peak corresponds to lithiated discharge products. ^{17}O NMR showed that Li_2CO_3 is the main discharge product and ^{1}H NMR demonstrated that there is minimal lithium acetate present at D_{200}, thus the lithiated material observed in **Figure 4-6** is assigned as Li_2CO_3.

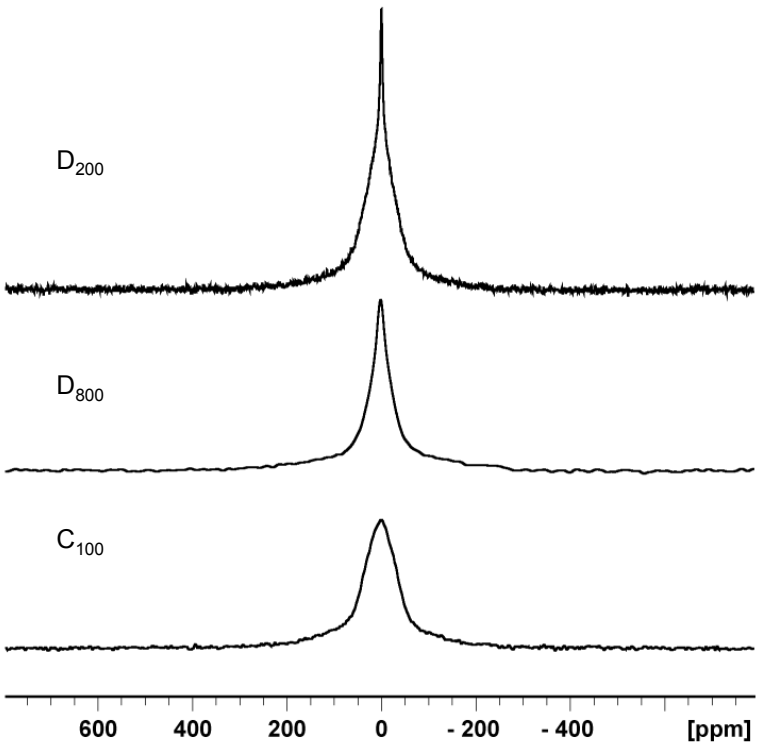

Figure 4-6 Normalized static ^{7}Li NMR spectra of the cycled TMP cathodes at different points on the electrochemical curve

4.3.5 ^{31}P NMR of TMP Cells

^{31}P NMR was used to directly examine TMP's chemical stability in the presence of the superoxide radical. All cathodes show residual electrolyte solvent at 1 ppm in **Figure 4-7**. In the spectra of the cycled cathodes, a second peak of varying intensity is observed at – 12 ppm. Signals are not observed outside of the chemical shift window for P (+5) centers, suggesting that electrolyte breakdown does not involve a direct attack on the phosphoruscenter but rather at other regions of the molecular structure. Additionally, no species other than the TMP electrolyte, were observed in the solution state ^{31}P NMR

spectrum, collected of the waste washing solution, shown in *appendix A7*. This demonstrates that the ^{31}P spectrum shown in **Figure 4-7** reflects all phosphorus discharge products formed within the cell.

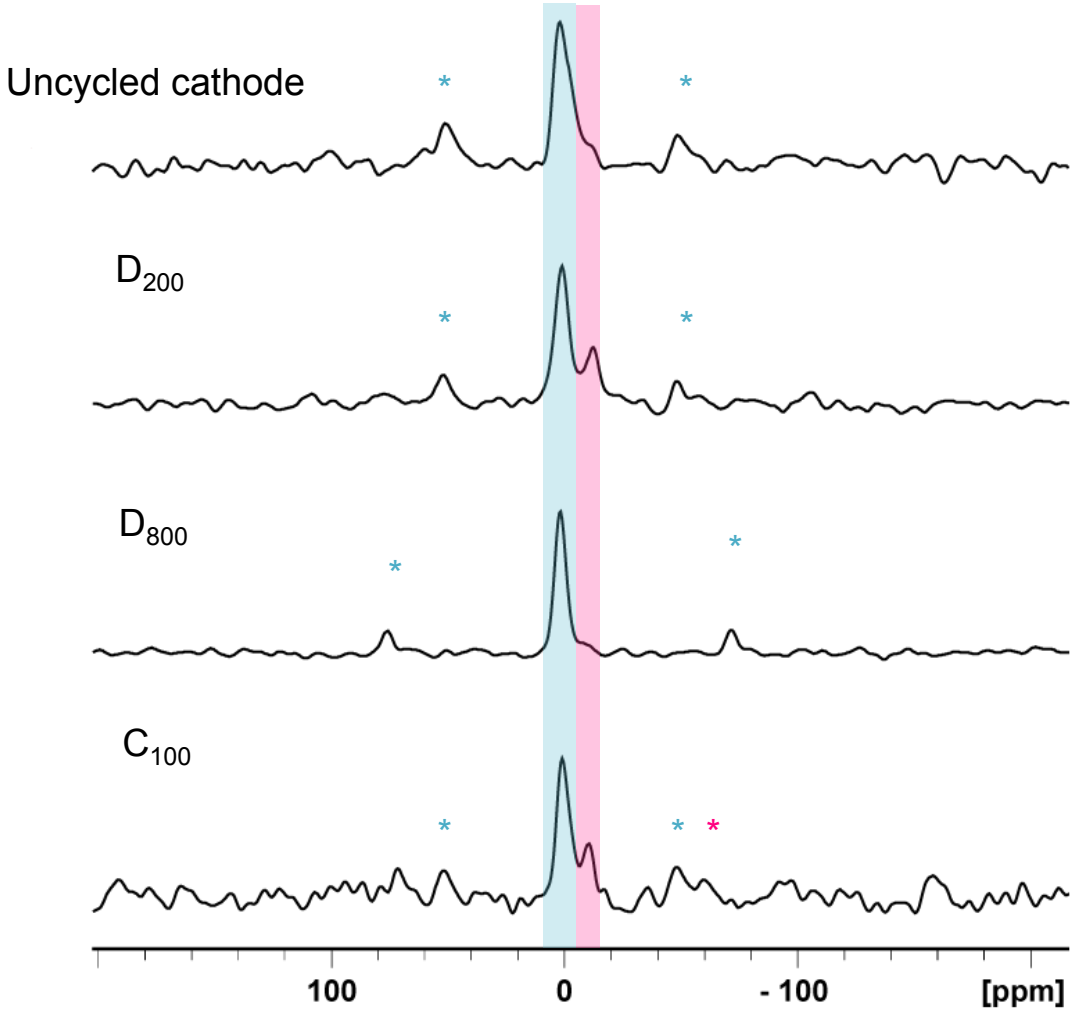

Figure 4-7 10 kHz MAS ^{31}P NMR spectra of the cycled cathodes except D_{800} which was collected at a 15 kHz MAS. Blue identifies the phosphorus in TMP and TMP derivate, the pink represents the polyphosphate species. Asterisks indicate spinning side bands, and are colour-coded to match the isotropic peaks to which they correlate

This supports our original hypothesis, that the phosphorus atom, with a formal charge of +5, would be stable against nucleophilic attack by the superoxide. The two peaks observed, in **Figure 4-7**, are consistent with a TMP derivative species $-OP=O(OMe)_2$ and polyphosphates; two of the breakdown species hypothesized in the following section. It is also possible that the signal at -12 ppm is a contribution from absorbed TMP molecules as the uncycled cathode spectrum shows a small shoulder of intensity at that position.

4.3.5 Charging Process of TMP Cells

The spectra acquired for the C_{100} electrode, shown in **Figures 4-5, 4-6, and 4-7,** demonstrate that the electrochemical process is not fully reversible upon charging. The substantial ^{1}H, ^{7}Li, and ^{31}P signals detectable at the top of the charging cycle indicate that discharge products remain on the electrode in measurable quantities at C_{100}. This is surprising, given that the electrochemistry appears to be fully reversible when only considering the electrochemical profile of the TMP cell, **Figure 4-2a**.

4.3.6 Overview of Proposed TMP Decomposition Mechanism

Multinuclear ssNMR was used to probe the electrochemical processes that occurred within the Li-O_2 battery. Despite the unfavorable electrochemistry we were able to develop a mechanism that accounts for the formation of the discharge products observed in the ^{1}H, ^{7}Li, ^{17}O and ^{31}P NMR spectra of the cycled cathodes. Such a mechanism is valuable to the ongoing development of electrolytes in metal-air cells.

Within the Li-O_2 cell the superoxide radical initiates electrolyte degradation by either nucleophilic attack or by proton abstraction. Here, we propose that TMP

decomposes via the proton abstraction mechanism. The ^{31}P NMR spectra of the uncycled and cycled electrodes suggest that the TMP's central phosphorus atom is stable against nucleophilic attack. This was expected as the phosphorus atom is found in its highest oxidation state of + 5. Additionally the proton abstraction mechanism is supported by a computational study, which predicts that the TMP methoxy group is the most probable site of attack by the superoxide radical.[34]

The proposed mechanism is divided into three reaction pathways; the proton abstraction reaction, the lithium formate pathways and the self-reaction of the TMP derivative. ^{17}O-enriched lithium formate and the TMP derivative species result from parasitic reactions that are initiated by the proton abstraction step, **Figure 4-8**. Li_2CO_3 and CH_3CO_2Li are produced via the lithium formate pathway, **Figure 4-9** and the polyphosphate results from the self-reaction of TMP outlined in **Figure 4-10**.

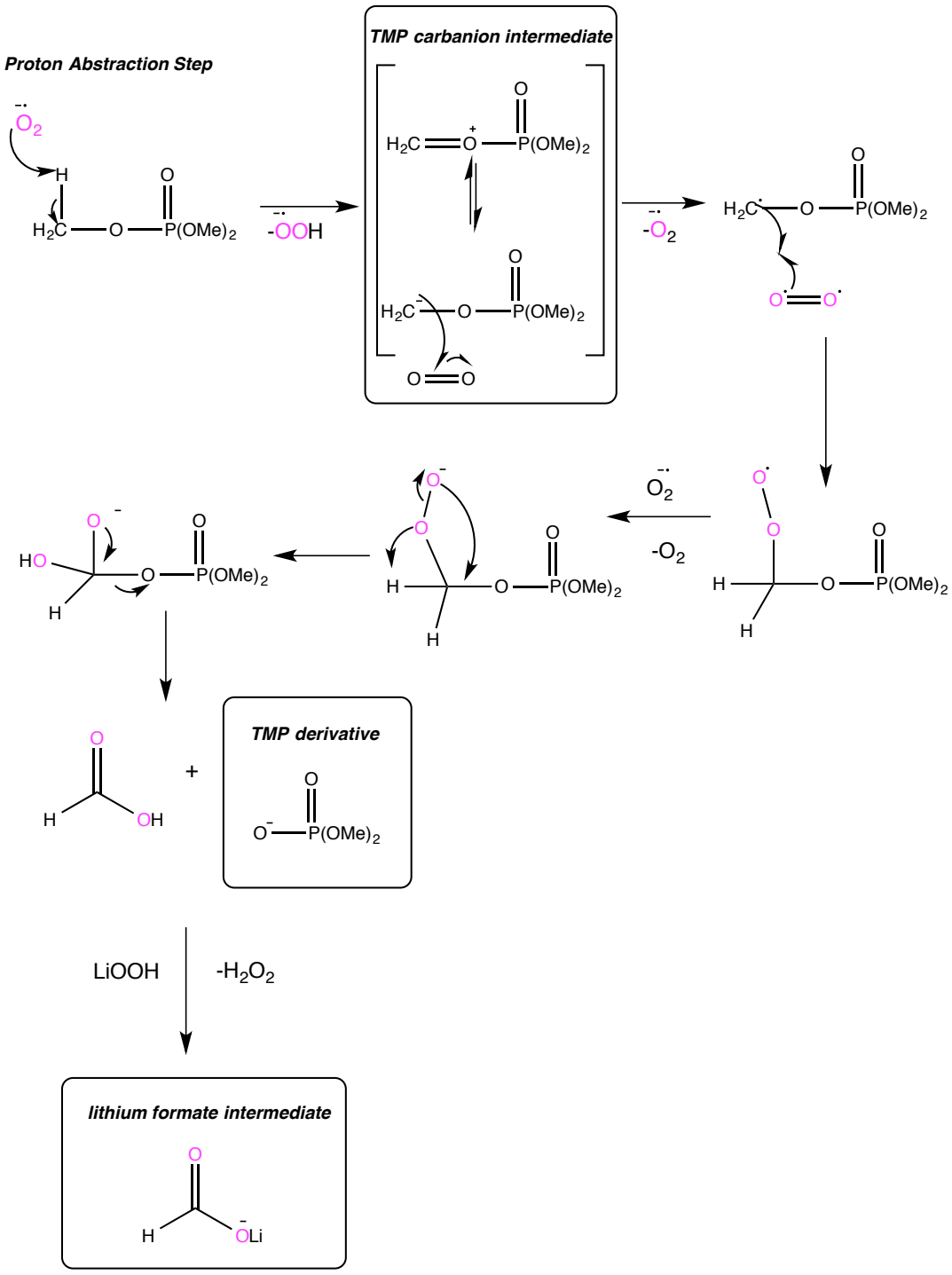

Figure 4-8 In the proposed mechanism the 17O-enriched oxygen atoms have been highlighted in pink. The first part of the proposed mechanism the proton abstraction steps are outlined

There are two proposed lithium formate pathways. In the first pathway, peroxide ions attack lithium formate resulting in lithium carbonate. In the second proposed pathway the TMP carbanion intermediate, created in **Figure 4-8**, attacks lithium formate resulting in lithium acetate and the TMP derivative. The peroxide pathway is expected to be more favorable because HO^-_2 ions are expected to be more abundant within the cell than the TMP carbanion intermediate. HO^-_2 ions are generated as a by-product of the initial proton abstraction step and the TMP carbanion intermediate is predicted to participate in the parasitic reactions outlined in **Figure 4-8**. Thus lithium acetate will be observed only after a large quantity of the carbanion has accumulated. This is expected to occur at long discharge times. Thus at early discharge times Li_2CO_3 is the primary product formed while at long discharge times both Li_2CO_3 and acetate are detected. The proposed mechanism accounts for why a significant amount of lithiated material, Li_2CO_3, is observed at D_{200} while there is limited evidence of protonated discharge products, in particular lithium acetate, at the same discharge capacity observed in the ^1H NMR spectrum.

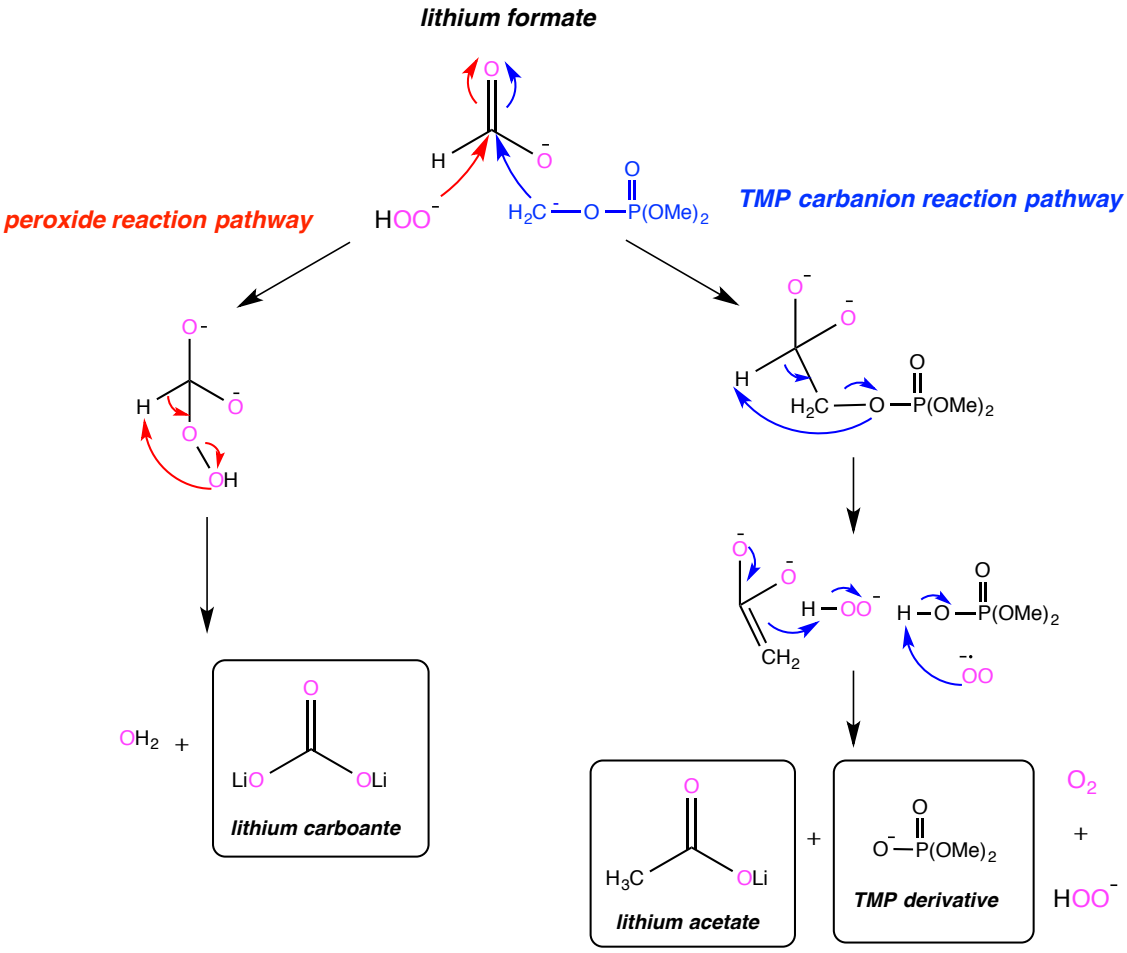

Figure 4-9 The following describes the potential reaction pathways involving lithium formate

In the ^{31}P NMR spectra of the cycled cathodes a polyphosphate structure was observed in small quantities. Polyphosphate is proposed to be formed by the self-reaction of the TMP derivative outlined in **Figure 4-10**.

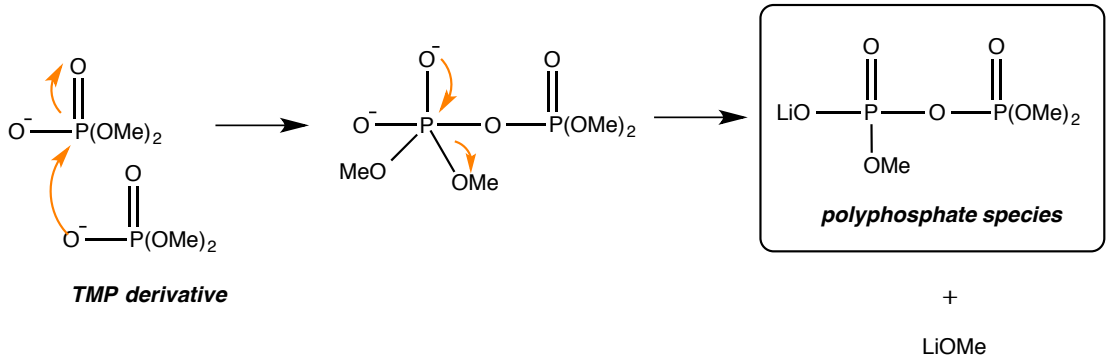

Figure 4-10 Self Reaction of TMP derivative

4.4 Summary

TEGDME was found to be a more stable Li-O_2 electrolyte than TMP based on an ^{17}O NMR investigation. Both Li_2O_2 and Li_2CO_3 were observed at the end of discharge with the TEDGME electrolyte, whereas Li_2CO_3 was determined to be the primary discharge product formed during discharge with the TMP electrolyte. By comparing the ^{1}H and ^{7}Li NMR spectra of the cycled cathodes lithium carbonate and lithium acetate were determined to be produced via different consecutive electrolyte breakdown pathways. A mechanism was proposed that accounts for the formation of the discharge species observed in the ^{1}H, ^{7}Li, ^{17}O and ^{31}P NMR spectra of the cycled cathodes. The inherent instability of TMP prevents TMP from being a suitable Li-O_2 electrolyte despite

the promising electrochemical performance. This work highlights the importance of characterizing the discharge products in electrolyte stability studies. Both electrolytes studied here display evidence of electrolyte decomposition thus alternative electrolytes continue to be explored. Multinuclear NMR is expected to be an informative method to assess new metal-air battery components for future development.

4.5 References

[1] M. Leskes, A. J. Moore, G. R. Goward, C. P. Grey, *J. Phys. Chem. C* **2013**, *117*, 26929.
[2] G. Girishkumar, B. McCloskey, C. Luntz, S. Swanson, W. Wilcke, *J. Phys. Chem. Lett.* **2010**, *1*, 2193.
[3] P. G. Bruce, A. Freunberger Stefan, L. J. Hardwick, J.-M. Tarascon, *Nat. Mater.* **2012**, *11*, 172.
[4] M. A. Rahman, X. Wang, C. Wen, *J. Appl. Electrochem.* **2013**, *44*, 5.
[5] M. Balaish, A. Kraytsberg, Y. Ein-Eli, *Phys. Chem. Chem. Phys.* **2014**, *16*, 2801.
[6] K. M. Abraham, K. Z. Jiang, *J. Electrochem. Soc.* **1996**, *143*, 1.
[7] S. A. Freunberger, Y. Chen, Z. Peng, J. M. Griffin, L. J. Hardwick, F. Barde, P. Novak, P. G. Bruce, *J. Am. Chem. Soc.* **2011**, *133*, 8040.
[8] M. Leskes, N. E. Drewett, L. J. Hardwick, P. G. Bruce, G. R. Goward, C. P. Grey, *Angew. Chem. Int. Ed.* **2012**, *51*, 8560.
[9] A. Freunberger Stefan, Y. Chen, N. E. Drewett, L. J. Hardwick, F. Bardé, P. G. Bruce, *Angew. Chem. Int. Ed.* **2011**, *50*, 8609.
[10] H.-G. Jung, J. Hassoun, J.-B. Park, Y.-K. Sun, B. Scrosati, *Nat Chem* **2012**, *4*, 579.
[11] B. D. McCloskey, D. S. Bethune, R. M. Shelby, G. Girishkumar, A. C. Luntz, *J. Phys. Chem. Lett.* **2011**, *2*, 1161.
[12] B. D. Adams, R. Black, Z. Williams, R. Fernandes, M. Cuisinier, E. J. Berg, P. Novak, G. K. Murphy, L. F. Nazar, *Adv. Energy. Mater.* **2015**, *5*, 1400867
[13] S. S. Zhang, K. Xu, J. Read, *J. Power Sources* **2011**, *196*, 3906.
[14] W. Xu, J. Hu, M. H. Engelhard, S. A. Towne, J. S. Hardy, J. Xiao, J. Feng, M. Y. Hu, J. Zhang, F. Ding, M. E. Gross, J.-G. Zhang, *J. Power Sources* **2012**, *215*, 240.
[15] X. Wang, E. Yasukawa, S. Kasuya *J. Electrochem. Soc.* **2001**, *148*, A1066.
[16] J. K. Feng, X. P. Ai, Y. L. Cao, H. X. Yang, *J. Power Sources*, *177*, 194.
[17] L. A. Huff, J. L. Rapp, L. Zhu, A. A. Gewirth, *J. Power Sources* **2013**, *235*, 87.
[18] Z. E. M. Reeve, G. R. Goward, A. D. Bain, *Can. J. Chem.* **2015**.
[19] V. Lemaitre, M. E. Smith, A. Watts, *Solid State Nucl. Magn. Reson.* **2004**, *26*, 215.
[20] G. Wu, *Progress in Nuclear Magnetic Resonance Spectroscopy* **2008**, *52*, 118.
[21] Z. E. M. Reeve, G. R. Goward, A. D. Bain, *Can. J. Chem.* **2015**, 1.
[22] D. Iuga, H. Schafer, R. Verhagen, A. P. M. Kentgens, *J. Magn. Reson.* **2000**, *147*, 192.
[23] S. Meiboom, D. Gill, *Rev. Sci. Instrum.* **1958**, *29*, 688.
[24] H. Y. Carr, E. M. Purcell, *Physical Review* **1954**, *94*, 630.
[25] M. Bloom, E. Sternin, *Biochemistry* **1987**, *26*, 2101.
[26] J. T. Cheng, P. D. Ellis, *J. Phys. Chem.* **1989**, *93*, 2549.
[27] M. Bak, J. T. Rasmussen, N. C. Nielsen, *J. Magn. Reson.* **2000**, *147*, 296.
[28] J. Hassoun, H.-G. Jung, D.-J. Lee, J.-B. Park, K. Amine, Y.-K. Sun, B. Scrosati, *Nano Lett.* **2012**, *12*, 5775.

[29] J. Wang, Y. Li, X. Sun, *Nano Energy* **2013**, *2*, 443.
[30] M. Bak, J. T. Rasmussen, N. C. Nielsen, *J. Magn. Reson.* **2011**, *213*, 366.
[31] S. J. Clark, M. D. Segall, C. J. Pickard, P. J. Hasnip, M. I. Probert, K. Refson, M. C. Payne, *Z. Kristallogr.* **2005**, *220*, 567.
[32] M. D. Segall, P. J. D. Lindan, M. I. J. Probert, C. Pickard, P. J. Hasnip, S. J. Clark, M. C. Payne, *J. Phys. Condens. Matter* **2002**, *14*, 2717.
[33] R. Black, S. H. Oh, J.-H. Lee, T. Yim, B. Adams, L. F. Nazar, *J. Am. Chem. Soc.* **2012**, *134*, 2902.
[34] V. S. Bryantsev, J. Uddin, V. Giordani, W. Walker, D. Addison, G. V. Chase, *J. Electrochem. Soc.* **2013**, *160*, A160.

Chapter 5 : Evaluation of TEGDME as a Lithium-Oxygen Electrolyte with Solid-State ^{17}O NMR

5.1 Introduction

In Chapters 3 and 4 of this thesis, tetraethylene glycol dimethyl ether (TEGDME) was treated as a moderately stable Li-O_2 electrolyte. With ^{7}Li nutation and ^{17}O NMR[1-2] Li_2O_2 and Li_2CO_3 were found to be the main electrochemical products, in accordance with previous reports.[3-4] Based on the ^{17}O NMR spectrum of the TEGDME electrode (**Figure 4-3b**) in Chapter 4, it was suspected that additional degradation species were present. However, under static conditions at a magnetic field strength of 11.7 T, it was not possible to confirm this. Here, a detailed ^{1}H and ^{17}O NMR investigation was performed to identify all the reaction products produced over the first and second discharge. High-resolution ^{17}O spectra were collected through the use of ultrafast MAS (62.5 kHz) at an ultra-high magnetic field strength (21.1 T).

The reversible formation of Li_2O_2 was observed in the ^{17}O NMR spectra of the cycled electrodes, where less Li_2O_2 was found at the end of the second discharge compared to the first discharge. Additionally, the electrolyte breakdown species were determined to be; lithium carbonate, lithium hydroxide (LiOH) and lithium acetate (CH_3CO_2Li), with ^{1}H and ^{17}O NMR of the cycled electrodes.

With ^{17}O MAS NMR, lithium carbonate and lithium acetate was demonstrated to only partially decompose upon charging, suggesting that the parasitic undesirable species will accumulate over multiple charging cycles. This was confirmed with the ^{1}H NMR of the cycled electrodes. Interestingly, lithium formate (HCO_2Li) was only observed in an electrode that was stopped on the seventeenth discharge.

All electrochemically cycling and ^{17}O enrichment was performed at McMaster. All NMR experiments performed at the magnetic field strength of 11.7 T were collected at McMaster Unversity, under the supervision of Prof. Gillian R. Goward. The ^{17}O NMR performed at 21.1 T was collected at the National Ultra-high Field Facility for Solids at the National Research Council in Ottawa either under the supervision of Dr. Victor V. Terskikh or by Dr Victor V. Terskikh. All NMR spectra were processed at McMaster University under the supervision of Prof. Gillian R. Goward. The SEM image of the cycled electrode was collected by Dr. Glynis de Silveira at the Canadian Centre for Electron Microscopy, at McMaster University.

5.2 Experimental

5.2.1 Li-O_2 Electrochemistry

The cathode slurries and Li-O_2 batteries were assembled following a previously published procedure[1] outlined in Chapter 3, section 3.2.1. The TEGDME electrolyte solutions was a 1 M LiTFSI solution in tetraethylene glycol dimethyl ether (Sigma Alridch). The cells rested at equilibrium for 12 hours prior to galvanostatic cycling at a rate of 70 mA/g of carbon in a pure oxygen environment. The Li-O_2 cells were disassembled under argon. The discharged cathodes were extracted, washed in pure TEGDME solvent and dried for several hours under vacuum prior to NMR analysis.

5.2.1.2 ^{17}O Enrichment of Li-O_2 Cells

The ^{17}O enriched electrodes were cycled in the presence of 70 % $^{17}O_2$ enriched oxygen gas, purchased from CortecNet Corp. The ^{17}O enrichment of the Li-O_2 cells follows a previously published procedure[1], which is outlined in Chapter 3, section

3.2.1.1. The ^{17}O enrichment process used in this thesis involving a specially built gas manifold line. (See *appendices A4* and *A5* for further detail the ^{17}O-enrichment process).

5.2.2 Solid-State NMR Spectroscopy

All NMR measurements that were performed using 2.5 mm diameter rotors, which were centered packed with dry alumina power when the electrode material sample volume was less than the rotor volume.

5.2.2.1 ^{1}H NMR Spectroscopy

The ^{1}H NMR measurements were performed on a Bruker 500 MHz Avance I spectrometer using 2.5 mm diameter rotors. The ^{1}H ssNMR spectra were acquired using a 5 s recycle delay time and were referenced to adamantane at 1.86 ppm. The spectra were collected using a background-suppressing, rotor-synchronized echo with a 25 kHz sample-spinning rate and an rf nutation frequency of 63 kHz.

5.2.2.2 ^{17}O NMR Spectroscopy

All ^{17}O NMR spectra of the cycled cathodes were acquired using a 2 s delay and were referenced to the natural abundance ^{17}O signal in H_2O at 0 ppm. The ^{17}O signal from water was observed in 128 scans using a 0.5 s delay time.

Static ^{17}O NMR at 11.7 T was collected on a Bruker 500 MHz Avance I spectrometer using 2.5 mm diameter rotors. The spectra were acquired using a solid echo, with a ^{17}O nutation frequency of 80 kHz and 40 kHz of ^{1}H decoupling.

The ^{17}O NMR spectra collected at 21.1 T was performed on a Bruker 900 MHz Avance II spectrometer at the National Ultrahigh-Field NMR Facility for Solids. The

static spectra were collected using 2.5 mm rotors, with a Hahn echo experiment and ^{1}H decoupling. The ^{17}O nutation frequency and ^{1}H decoupling powers were 45 kHz and 50 kHz respectively. The 62.5 kHz MAS spectra were collected using a Hahn echo, with a ^{17}O nutation frequency of 45 kHz.

5.2.3 SEM Images of Cycled Electrodes

The SEM images were collected using a FEI Magellan 400, using a 2.00 kV beam. The electrode sample was not coated prior to SEM analysis. Great care was taken during the imaging to avoid damaging the sample, as the electrode was very sensitive to the energy of the beam.

5.3 Results and Discussion

Based on the previous two chapters[1-2] and literature reports[3-4], it is well established that both Li_2O_2 and electrolyte breakdown products are formed in Li-O_2 cells with the TEGDME electrolyte. The most commonly reported degradation species are; Li_2CO_3, LiOH, CH_3CO_2Li and HCO_2Li.[3]

The aim of this chapter is to determine when the TEGDME degradation occurs and to monitor the behavior of the electrochemical reaction products over multiple discharge cycles. These objectives are accomplished though a ^{1}H and ^{17}O NMR investigation of Li-O_2 electrodes that were cycled with a TEGDME electrolyte.

In regards to when the degradation occurs, we have proposed two possible hypotheses. In hypothesis A, all of the Li_2O_2 is initially produced and then the breakdown species are formed. Alternatively, hypothesis B proposes that Li_2O_2 and the breakdown products are produced at the same rate. This would occur if there is a continually

competition between the superoxide radical species reacting with the Li^+ ions in solution or directly attacking the electrolyte. The answer to this objective has practical implications. If hypothesis A is found to be true, then the discharge capacity of the cells may be limited such that only Li_2O_2 is produced. Theoretically this could prevent the accumulation of parasitic species on the electrodes surface, which should facilitate reversible electrochemical cycling.

5.3.1 Li-O_2 Electrochemistry

Figure 5-1 is a representative electrochemical curve illustrating the first and second discharge profile for a Li-O_2 cell, with the TEGDME electrolyte. The cathode samples selected for the ^{17}O NMR study were ^{17}O-enriched, thereby produced electrochemical reaction products, which are also ^{17}O-enriched. The isotopic enrichment was carried out by cycling the cells under a 70 % ^{17}O enriched oxygen gas environment, using a specially designed gas line manifold. The cells were then stopped at the specific capacities outlined in **Figure 5-1**. The discharge process was limited to a capacity of 1000 mAh/g and the charging process was limited to 4.6 V, as TEGDME decomposes at higher potentials.[5]

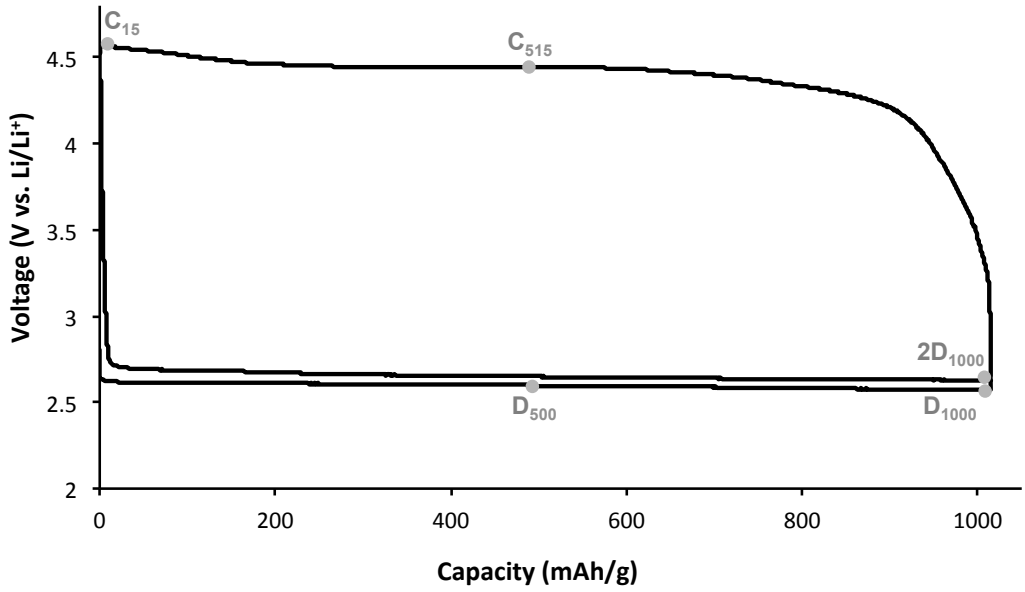

Figure 5-1 Representative electrochemical profile of a Li-O_2 cell where the discharge capacity was limited to 1000 mAh/g, with the a 1M LiTFSI in TEGDME electrolyte with the specific capacities highlighted for the studied ^{17}O enriched electrodes

The long-term stability of TEGDME, over multiple cycles was also investigated in this chapter. The electrochemical curves that illustrate the long-term cycling behavior of TEGDME are provided in **Figure 5-2**. Here the cell was stopped on the seventeen discharge cycles, at a capacity of 400 mAh/g ($17D_{400}$) for analysis with ^{1}H NMR. A capacity fade is observed in **Figure 5-2**, where the capacity decreases from 550 mAh/g on the first cycle to 400 mAh/g on the seventeenth cycle. A similar capacity fade was also reported by *Lim et al.*[6] for the TEGDME electrolyte. Initially the cell reached a discharge capacity of 500 mAh/g, however reversible cycling was not maintained and the capacity gradually decreases to 400 mAh/g by the twenty cycle.[6] The capacity fade is attributed to the accumulation of undesirable species on the electrode.

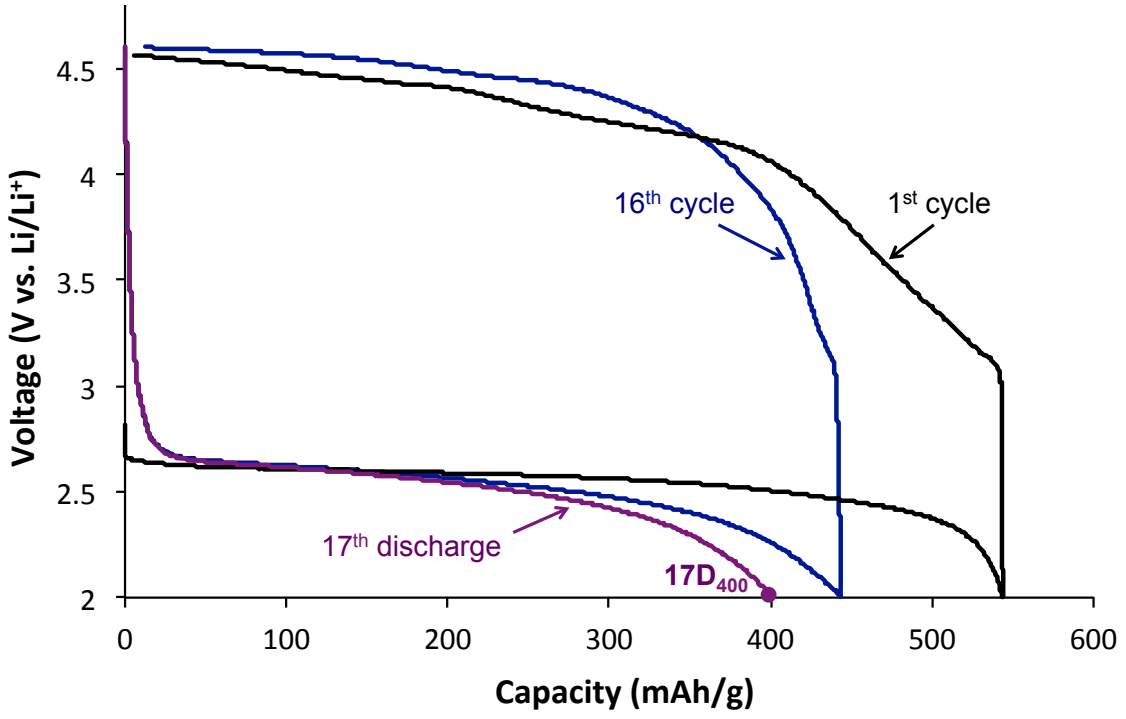

Figure 5-2 Representative electrochemical profile of a Li-O_2 cell that was cycled over multiple charging events, where the first, sixteenth and seventeen discharge cycles are shown

5.3.2 ^{17}O NMR of Cycled Electrodes

^{17}O NMR is the primary tool used in the TEGDME investigation. Li_2O_2 has a uniquely broad, axial lineshape from the large ^{17}O C_q of 18 MHz.[7-8] This makes the Li_2O_2 spectrum distinct from the ^{17}O spectra of the undesirable electrolyte breakdown species. The degradation products all cluster around 0 kHz and have a much smaller ^{17}O C_q of approximately 7 MHz.[7-8] The unique Li_2O_2 signature is readily detected under static conditions, even at a moderate magnetic field strength of 11.7 T, as demonstrated in Chapter 4 (**Figures 4-2** and **4-3**). However, under those conditions it is not possible to accurately identify the breakdown products. Even at an ultrahigh magnetic field of 21.1 T (**Figure 5-3**), the degradation products still partially overlap under static conditions. To

overcome this limitation, we turned to ultrafast MAS (at a rate of 62.5 kHz) at a 21.1 T, to resolve the degradation products, illustrated in **Figure 5-3.**

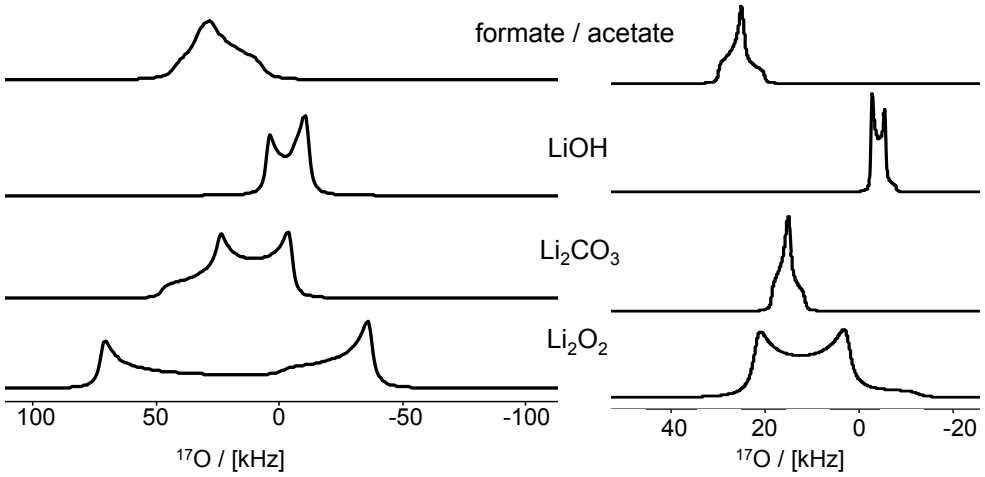

Figure 5-3 Simulations of the ^{17}O central transition lineshapes of the relevant Li-O_2 reaction species at 21.1 T under (left) static conditions and (right) a MAS speed of 60 kHz, using the reported ^{17}O NMR parameters[7]

The ^{17}O central transition lineshapes, shown in **Figure 5-3**, were modeled with the SIMPSON[9] software, using the reported ^{17}O quadrupole parameters.[8] (Sample SIMPSON input files are provided in *appendix A3*). As noted in Chapter 4, lithium acetate and lithium formate have very similar ^{17}O NMR parameters (δ_{iso} ~ 265 ppm and C_q ~ 7 MHz).[8] Therefore a single simulation is provided in **Figure 5-3**, representing the expected ^{17}O lineshape of both species. Lithium acetate and lithium formate are readily distinguished with ^{1}H NMR further. This is further addressed in section 5.3.4**.**

5.3.2.1 Determining the Relative Amount of Li_2O_2 with static ^{17}O NMR

As noted above, the ^{17}O NMR parameters have previously been reported for Li_2O_2[7] and are listed in **Table 5-1**. Using the literature values, it was not possible to accurately model the experimental lithium peroxide lineshape observed in the ^{17}O NMR spectrum of the cycled electrode, D_{1000}. A good fit of the lineshape was only obtained after the chemical shift anisotropic terms (δ_{aniso} and η_{aniso}) were modified and the Euler angles were considered. The values of the Euler angles applied in the modeling were calculated by Dr. Victor V. Terskikh at the National Ultra-high Field Facility for Solids at the National Research Council in Ottawa, using the EFGShield software[10] and are reported in **Table 5-1**.

In this study, the Li_2O_2 ^{17}O NMR parameters were determined by fitting the singularities, the horns in the axial lineshape, observed in an electrochemical sample (D_{1000}), under static conditions at two magnetic fields strengths (11.7 T and 21.1 T), and at two MAS spinning speeds (31.25 kHz and 62.5 kHz) at a 21.1 T (**Figure 5-4**). The experimentally determined ^{17}O isotropic chemical shift and quadrupole coupling constant were found to be in good agreement with the reported literature and CASTEP values. The experimentally determined δ_{aniso} term had the same sign but a smaller magnitude than the previously reported literature and CASTEP values (**Table 5-1**). [7-8, 11-12]

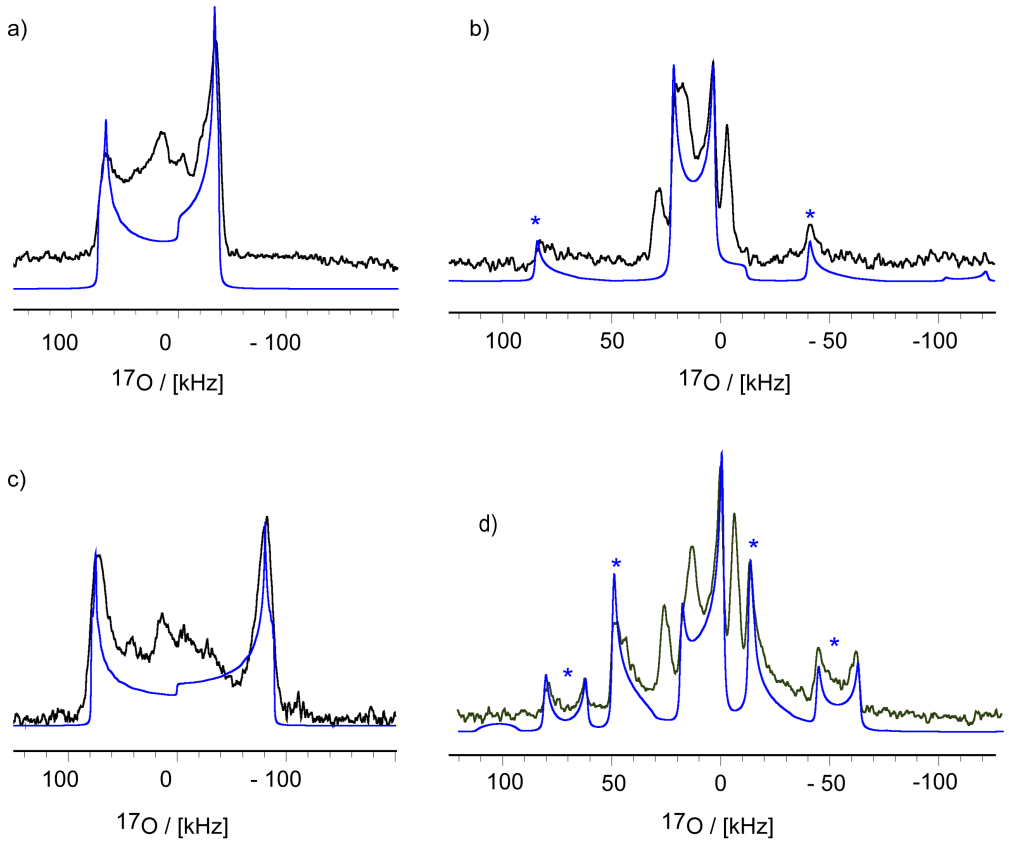

Figure 5-4 ^{17}O NMR spectra of D_{1000} collected under (a) static conditions at 21.1 T, (b) under static conditions at 11.7 T, (c) at a MAS rate of 62.5 kHz at 21.1 T and (d) at a MAS rate of 31.25 kHz at 21.1 T, where the Li_2O_2 lineshape in simulated in blue under the various experimental conditions with the spinning side bands labeled with *

Table 5-1 Comparison of the experimentally determined ^{17}O NMR parameters with literature values

	Experimental	CASTEP (DFT) [7]	Literature Values [7]
δ_{iso}	227	222 ± 3	227
δ_{aniso}	-225 ± 5	-469 ± 7	-327
η_{aniso}	0.3 ± 0.05	0	0
C_Q (MHz)	18 ± 0.1	18.68	18
η_Q	0.05 ± 0.05	0	0
α	30	-	-
B	0	-	-
γ	0	-	-

The large CSA contribution to the Li_2O_2 lineshape is most evident in **Figure 5-4d**, the NMR spectrum collected at 21.1 T, with a moderate spinning speed of 31.25 kHz. The asymmetry of the CT lineshape and the spinning side band manifold features, labeled as * in **Figure 5-4**, are characteristic of the CSA contribution. When ultrafast MAS at a rate of 62.5 kHz is applied, the CSA contribution to the Li_2O_2 lineshape becomes negligible. This is observed in **Figure 5-4b**, where the horns in the central transition lineshape display equal intensity, because the ultrafast MAS completely (or almost completely) averages the CSA interactions zero. Additionally the 62.5 kHz MAS spectrum (**Figure 5-4b**) is much simpler than the 31.25 kHz spectrum (**Figure 5-4d**), as the faster spinning speed results in fewer ssb, making the site assignment significantly easier. Therefore, the identity and the relative amounts of the Li-O_2 reaction species were determined based on the 62.5 kHz MAS ^{17}O spectra of the cycled electrodes. This is further discussed in section 5.3.3.2.

The static ^{17}O NMR spectra (**Figure 5-5**) of the cycled electrodes were collected at two magnetic field strengths; 11.7 T and 21.1 T. The cathode spectra are normalized to account for the number of scans used in the acquisition and for the mass of each electrode. In **Figure 5-5** at D_{500}, the diagnostic Li_2O_2 lineshape is observable at both magnetic field strengths. There is also evidence of electrolyte breakdown, at both fields, from the signal intensity centered around 0 kHz. This finding refuses hypothesis A, as a pure Li_2O_2 phase is not observed at D_{500}. Instead both the desired and parasitic reaction species are found, suggesting that the desired electrochemistry and the degradation reactions occur simultaneously.

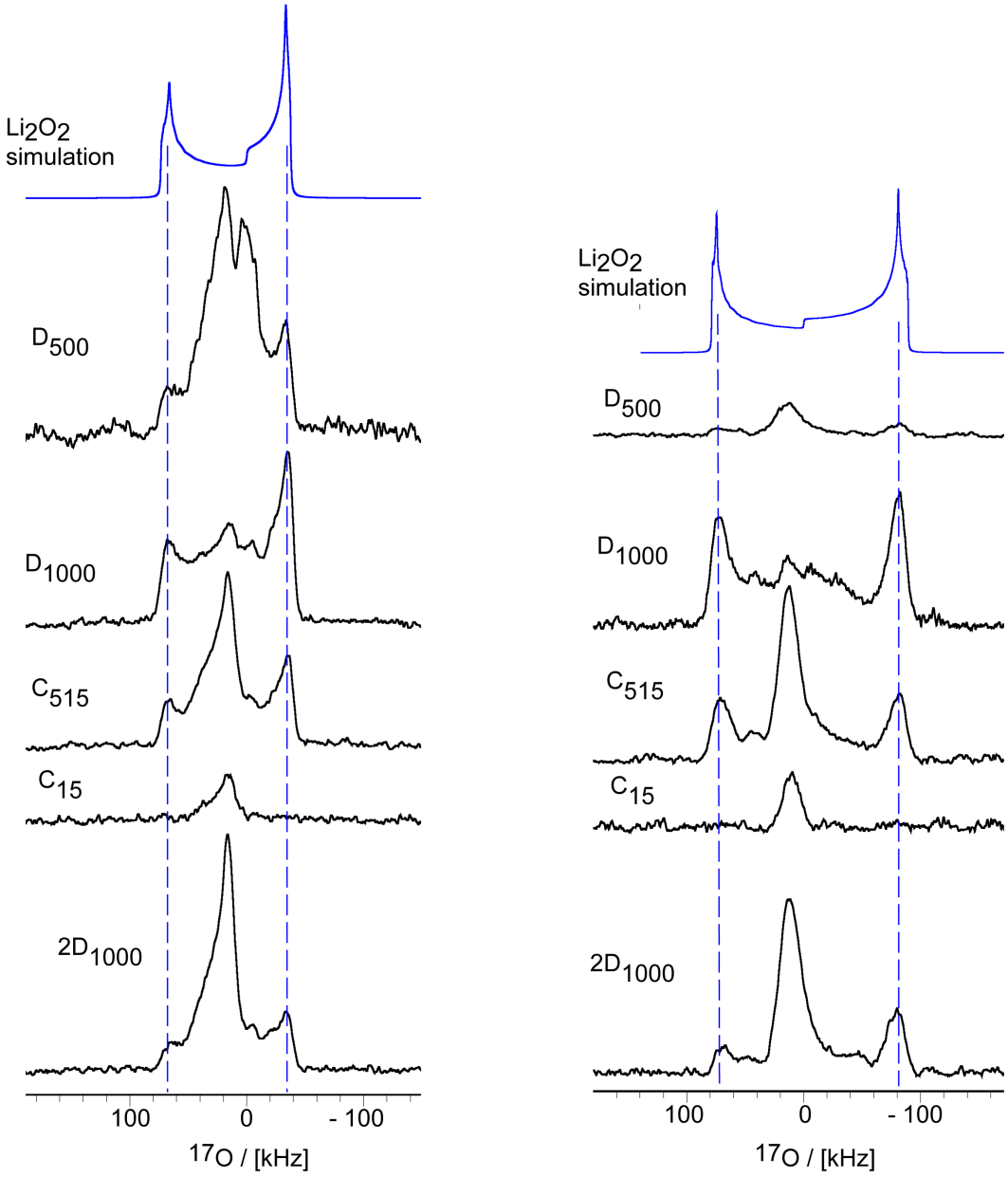

Figure 5-5 The normalized static ^{17}O NMR spectra of the cycled electrodes collected at (left) 21.1 T and (right) 11.7 T, where the Li_2O_2 lineshape is modeled using the ^{17}O NMR parameters reported in Table 5-1

Furthermore **Figure 5-5** demonstrates that the electrochemically produced Li_2O_2 is fully reversible. Li_2O_2 is observed in the cathode samples during discharge (D_{500} and D_{1000}) and for a portion of the charging process (C_{515}). However, by the end of the charging profile (C_{15}), Li_2O_2 is not present in a measurable quantity. This indicates that Li_2O_2 has fully decomposed upon charging. At $2D_{1000}$ Li_2O_2 is once again found in the ^{17}O NMR spectrum, demonstrating the reformation of Li_2O_2.

Residual signal intensity centered at 0 kHz, is observed in the ^{17}O NMR spectra of the C_{15} electrode. This indicates that degradation products are present in a measureable quantity at the end of charging process. This could result from the incomplete decomposition of the reaction products during charging or from further parasitic side reactions. Regardless of the source, the species are predicted to continue accumulating on the electrode with subsequent cycling. These species block the surface, preventing the redox processes from occurring at the electrode, which in turn inhibits cell cycling.[13] The long-term cycling behavior of the Li-O_2 cell is further explored in section 5.3.4.

As outlined above, the Li_2O_2 ^{17}O NMR parameters are well known (**Table 5-1**). Thus we can accurately model the component of the experimental ^{17}O spectrum that corresponds to Li_2O_2. Based on the modeling, the integrated area, which corresponds to the amount of Li_2O_2 present, may be determined with the TopSpin 2.1 software. To determine the relative amount of Li_2O_2 at a given capacity, the integrated value of Li_2O_2 was divided by the total integration value for the entire lineshape. From this, the percentage of Li_2O_2 was calculated. With this approach the relative amounts of Li_2O_2 at the different capacities, can be compared in **Table 5-2**. The low field data set typically

provides a higher estimation for the relative amount of Li_2O_2. This is attributed to the fact that the low field datasets correspond to a broader Li_2O_2 spectrum, where a small error in the intensity could result in a significant accumulated error for the total Li_2O_2 intensity.

Table 5-2 Comparison of the Relative Amounts of Li_2O_2 formed at Different Discharge Capacities

	Based on 11.7 T spectra		Based on 21.1 T spectra	
Discharge capacity	% of lineshape corresponding to Li_2O_2	% of lineshape corresponding to breakdown species	% of lineshape corresponding to Li_2O_2	% of lineshape corresponding to breakdown species
D_{500}	30	70	33	69
D_{1000}	65	35	59	41
C_{515}	45	55	38	62
C_{15}	0	100	0	100
$2D_{1000}$	51	49	37	63

As expected, **Table 5-2** confirms that the amount of Li_2O_2 decreases during the charging process. Although Li_2O_2 is reformed on the second discharge, as evident in **Figure 5-5**, 18 % less Li_2O_2 was observed at $2D_{1000}$ compared to D_{1000} based on the integrated amount of Li_2O_2. The sudden decrease in the amount of Li_2O_2 over the second discharge, highlights a challenge associated with the long-term cycling of the TEGDME electrolyte.

5.3.2.2 Influence of the Charging Voltage on Li_2O_2 Production at $2D_{1000}$

The reformation of Li_2O_2 on the second discharge was found to be sensitive to the charging potential voltage. When the charging cut off voltage was set to 4.8 V (**Figure 5-6**), Li_2O_2 was not observed in that static ^{17}O NMR spectrum (**Figure 5-6**) at $2D_{1000}$. In that case, only electrolyte breakdown products were found. However when the charging cut off voltage was lower to 4.6 V, Li_2O_2 was once again observed on the second

discharge, as illustrated in **Figure 5-5**. Limiting the charging voltage is one way to promote the desired electrochemistry to occur. [5]

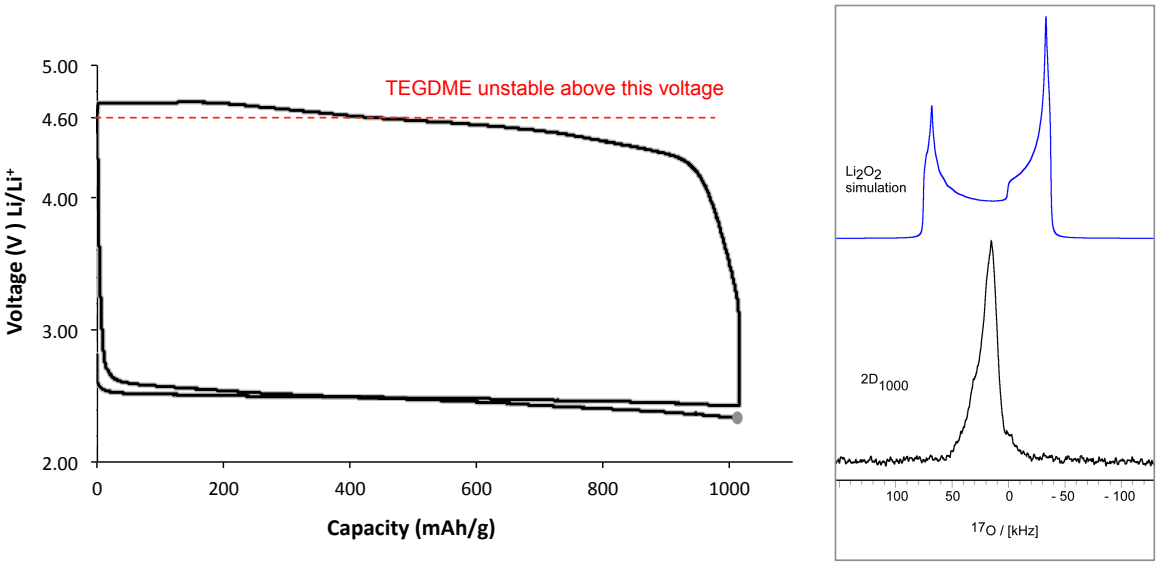

Figure 5-6 (left) Representative Li-O_2 curve where the charging cut off voltage was 4.8 V and (right) the static ^{17}O NMR spectrum of $2D_{1000}$, collected at 21.1 T

5.3.2.3 Identification of the Li-O_2 Degradation Products via Ultrafast MAS at a Ultrahigh Magnetic Field

As discussed above, there is evidence of electrolyte breakdown species in all of the static ^{17}O NMR spectra of the cycled electrodes (**Figure 5-5**). The undesirable reaction products have unique isotropic ^{17}O chemical shifts[7-8] that allow the species to be readily identified, if spectral resolution is achieved (**Figure 5-3**).

Initial identification attempts were made by collecting the cathode NMR spectra at 21.1 T, with a with a moderate MAS rate of 31.25 kHz (see *appendix A8*). This spinning

speed was originally used, as the 2.5 mm rotors (which support MAS rates of ~ 35 kHz) allow for the entire ^{17}O-enriched electrode to be measured. As illustrated in **Figures 5-3** the ^{17}O MAS spectra of the cathodes, appears complex when a considerable amount of Li_2O_2 is present and the spectrum is collected a moderate MAS speed. This is a result of the large CSA contribution to the Li_2O_2 lineshape. As discussed in section 5.3.3.1, a simpler spectrum with superior resolution is achievable, by moving to 1.3 mm rotors. The smaller diameter rotors support ultrafast MAS speed, at the expensive of a decreased sample volume.

Figure 5-7 is the 62.5 kHz ^{17}O MAS NMR spectrum of D_{1000}. A deconvolution has been performed on the experimental spectrum using the previously reported ^{17}O NMR parameters[8] that are provided below in **Tables 5-1** and **5-3**. The deconvolution of the cathode spectrum reveals that Li_2CO_3, LiOH and H_2CO_2Li / CH_3CO_2Li are present at D_{1000} in addition to Li_2O_2.

Table 5-3 Summary of ^{17}O NMR Parameters for the Li-O_2 Degradation Products[8]

	Li_2CO_3 O1	Li_2CO_3 O2	LiOH	Acetate / formate
δ_{iso}	154	166	-12	265
δ_{aniso}	90	150	-30	-25
η_{aniso}	0.8	0	0.1	0.05
C_Q (MHz)	7.22	7.4	7050	7800
η_Q	0.9	0.8	0.1	0.6
α	-	-	-	-
B	-	-	-	-
γ	-	-	-	-

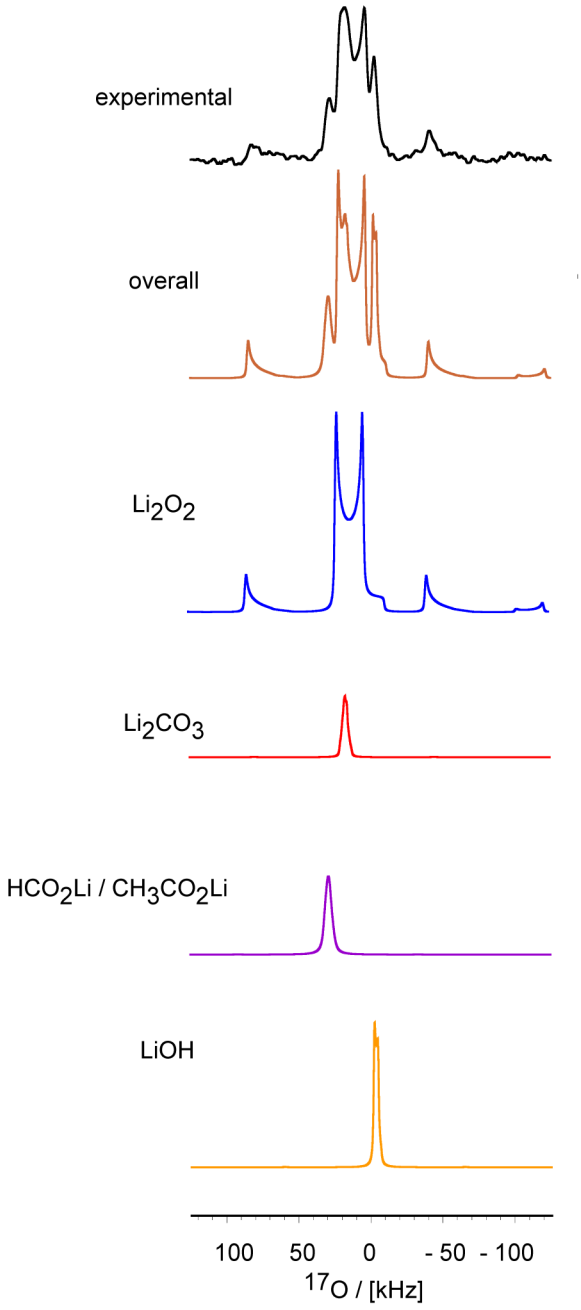

Figure 5-7 A 62.5 kHz ^{17}O MAS NMR spectrum of D_{1000}, where a deconvolution is provided revealing the reaction products present at this discharge capacity

All of the breakdown species are produced from undesirable chemical side reactions between the cell components.[3-4, 14] It is widely accepted that LiOH results form a reaction between lithium peroxide and H_2O[15] and is chemically formed via **equation 5.1**:[8]

$$Li_2O_2 + H_2O \rightarrow 2LiOH + ½\ O_2 \qquad (5.1)$$

Lithium carbonate, lithium acetate and lithium formate all result from the degradation of the TEGDME electrolyte solvent. *Freunberger et al.*[3] has proposed a potential reaction mechanism for gylme based electrolytes, where the breakdown process is initiated by a proton abstraction from the ether structure by the superoxide. This is illustrated in **equations 5.2**[3] using DME (H_3C-O-CH_2-CH_2-O-CH_3) as the ether electrolyte. DME and TEGDME are both ethers, with DME being the simplest gylme structure. In **equation 5.2**, after the proton is removed, molecular oxygen is proposed to undergo oxidative decomposition reactions with the alkyl radical, producing H_2O, CO_2, HCO_2Li and CH_3CO_2Li.[3]

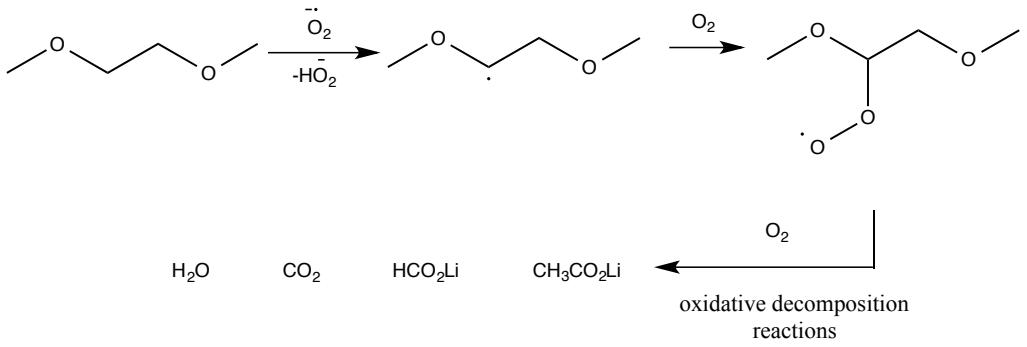

Li_2CO_3 is also be generated during the charging process through the oxidization of the carbon electrode by Li_2O_2 as outlined in **equation 5.3**.[8, 13]

$$3Li_2O_2 + 2C + \rightarrow 2Li_2CO_3 + 2e^- + 2Li^+ \qquad (5.3)$$

This solid-state reaction has been confirmed to occur with ^{13}C enriched electrodes, which allows the formation of $Li_2{}^{13}CO_3$ to be correlated with the cycling conditions. [8, 13] The ^{13}C study demonstrated that the carbon source was in fact the electrode and that **equation 5.3** occurred when the cell voltage was above 3.5 V. [13] One approach to minimize the carbonate formation is to limit the charging potential. However, this is not a practical solution as voltages greater than 3.5 V are required to oxidize the insulating Li_2O_2.[4, 16]

Ultrafast MAS ^{17}O NMR spectra were collected for each electrode sample, thereby revealing the parasitic species produced during the first and second discharge. Individual deconvolutions were performed for each spectrum and have been combined into a single stackplot shown in **Figure 5-8**. The spectra in **Figure 5-8** have been normalized to account for the cathode's mass and the number of scans collected in the acquisition. Using the integrated intensity approach, outlined in section 5.3.3.1, the relative amounts of each reaction product as a function of discharge capacity was determined and is illustrated in **Figure 5-9.**

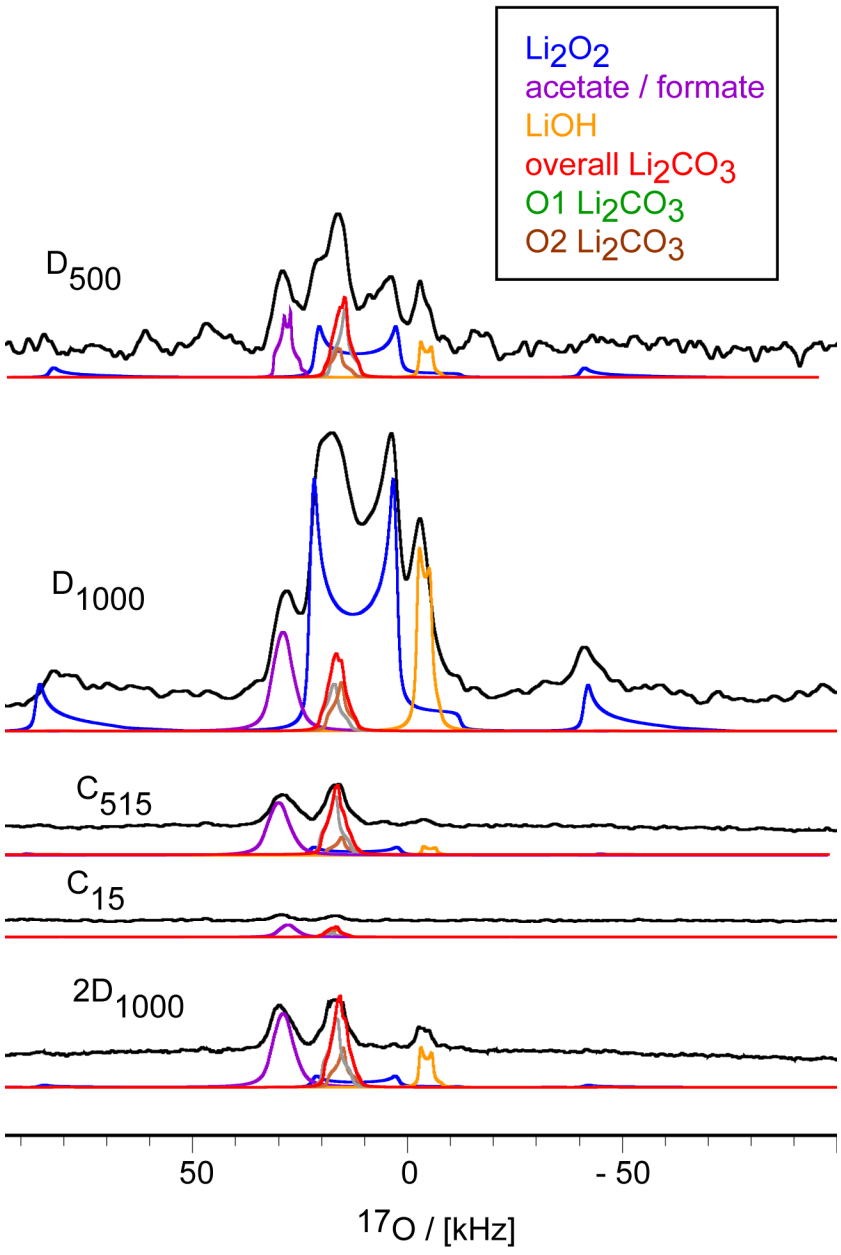

Figure 5-8 62.5 kHz MAS ^{17}O NMR spectra of the cycled electrodes, where the individual deconvolutions are included for the normalized spectra, allowing the discharge products to be monitored as a function of capacity

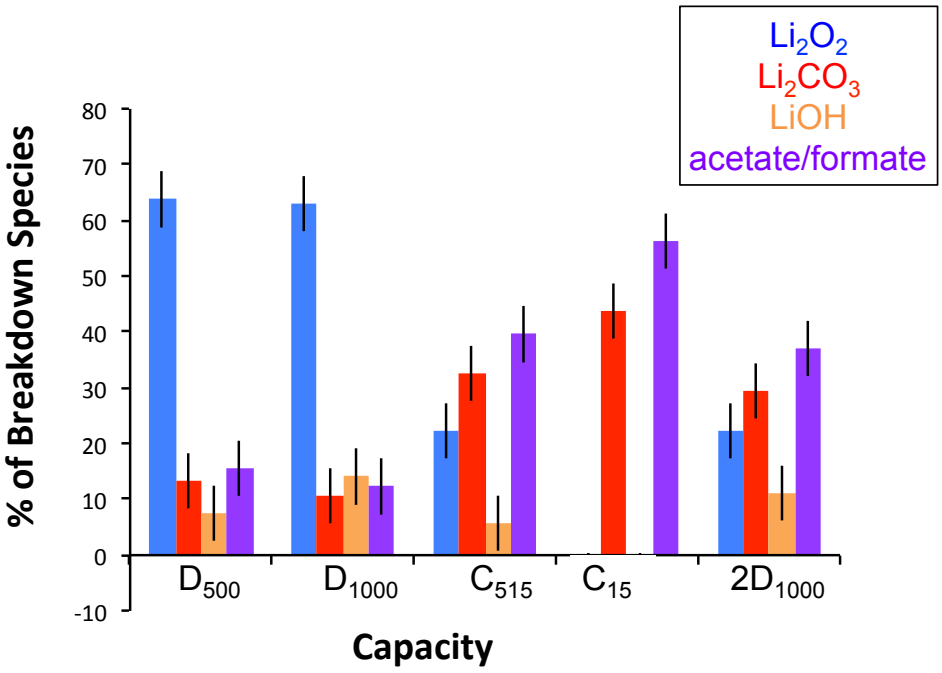

Figure 5-9 A plot illustrating the relative amounts each reaction product (based on the ^{17}O integrated values) as a function of discharge capacity, which demonstrates the reversible formation of Li_2O_2 and LiOH

Figures 5-8 and **5-9** confirm that Li_2O_2 is reversible formed on the second discharge. Based on the analysis of the MAS spectra (**Figure 5-9**) 40 % less Li_2O_2 is detected at $2D_{1000}$ compared to D_{1000}. This is consistent with the trend observed in the static ^{17}O spectra of the cathodes (**Figure 5-5**). However in the static NMR data 18 % less Li_2O_2 was observed at $2D_{1000}$ compared to D_{1000}. This discrepancy is attributed to sample ageing effects. The static measurements were performed within a week of the cycling, whereas the ultrafast MAS experiment (at 21.1 T) occurred 3.5 weeks later. During the intervening time Li_2O_2 may have degraded despite the sample being stored under inert conditions. This could result in the decreased amount of Li_2O_2 detected in the

MAS data. The high field MAS experiment did not occur immediately after cycling due to scheduling conflicts at the National Ultrahigh-Field NMR Facility for Solids, at the National Research Council in Ottawa. Future studies will explore aging effects, with a particular interest in the long-term stability of electrochemically generated Li_2O_2.

It should be noted that a higher amount of Li_2O_2 is reported for D_{500} in **Figure 5-9** than in **Table 5-2**. This is because two different electrode samples, each (cycled to a capacity of 500 mAh/g) were measured in the static and MAS ^{17}O NMR experiments. The variation in the amount of Li_2O_2 as a function of the electrode sample highlights a challenge in quantifying the reaction products. The amount of electrochemical reaction product appears to be dependent on the cycling conditions. To obtain more accurate values in future studies; an average relative amount should be determined. This would require the ^{17}O NMR spectrum to be collected multiple times for each capacity of interest, but that is beyond the scope of the current study. Also, data collected at earlier depth of discharge, for example D_{100}, could be use to further probe hypothesis A.

A closer inspection of **Figures 5-8** and **5-9** reveal that LiOH is also reversibly produced in the Li-O_2 cell. The Li_2CO_3 and CH_3CO_2Li/HCO_2Li phases show partial reversibility (decomposition) throughout the charge process as the overall signal intensity in the NMR spectra decreases from C_{515} to C_{15} (**Figure 5-8**). However, these reaction products indicate loss of liquid electrolyte, and are detrimental irrespective of their reversibility. The MAS spectrum of C_{15} reveals that lithium carbonate and lithium acetate / lithium formate are the species which remain on the electrode at the end of the charging process. From **Figure 5-8**, it is unclear as to whether lithium acetate, lithium formate or

both phases are present in the electrode samples. This is rectified in section 5.3.4 where ^{1}H NMR spectroscopy if performed on the cycled electrodes.

5.3.3 ^{1}H NMR of Cycled Electrodes

^{1}H NMR was performed to determine which protonated reaction products were formed on the first (D_{500} and D_{1000}), second ($2D_{1000}$) and seventeenth ($17D_{400}$) discharge. The ^{1}H NMR spectra of the discharged electrodes (**Figure 5-10**) are scaled to the intensity of the PVDF binder resonance, observed at 2.5 ppm.[2] PVDF was used as an internal standard for normalizing the signal intensity, as the amount of PVDF was expected to be constant for all of the electrodes. Here we assume negligible breakdown of the PVDF binder following the first and second electrochemical cycles.[15] However, this is not an appropriate assumption for the seventeenth cycle, as some degradation is expected to occur during extended cycling. This highlights a limitation of using the PVDF binder. Future studies that explore the long-term cycling should use alternative binders and electrode materials. Nevertheless, despite PVDF not being an ideal reference for the $17D_{400}$ cathode, it is still possible to elucidate valuable information regarding which protonated species are present after extended cycling.

In **Figure 5-10** the signal intensity observed in the 3.5 ppm to 4.0 ppm chemical shift range was attributed to residual TEGDME that remained on the electrode, after the cell were washed with pure TEGDME to remove the residual conducting salt. The ^{1}H chemical shifts of TEGDME are known from the solution state ^{1}H NMR spectrum corresponding to pure TEGDME, provided in *appendix A9*.

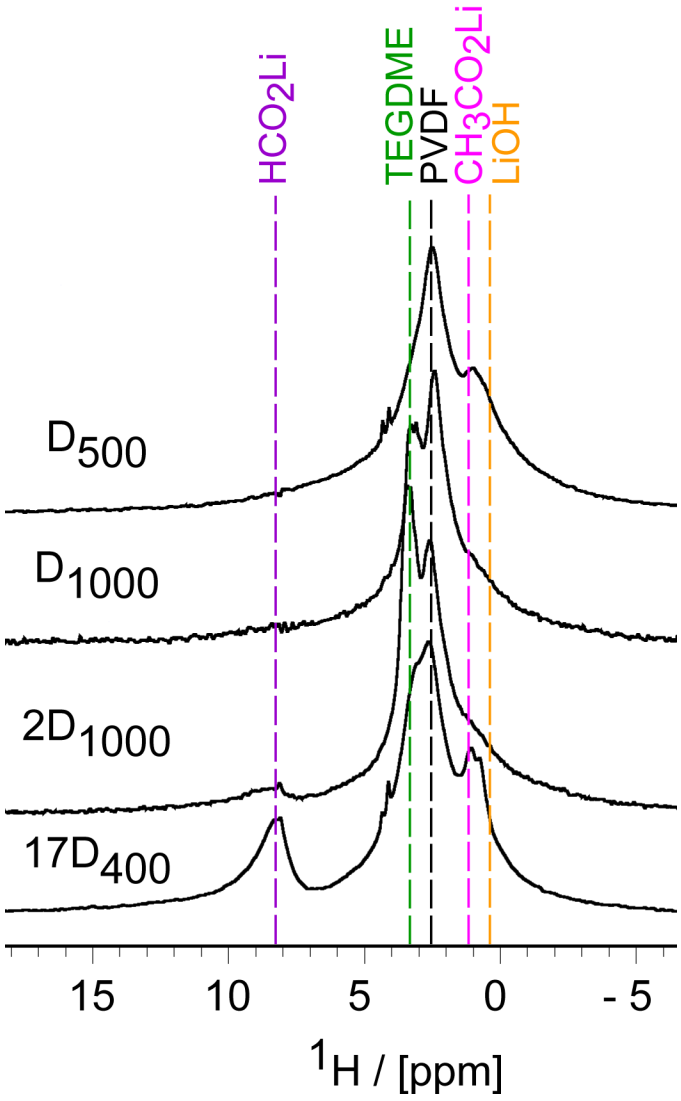

Figure 5-10 ^{1}H NMR spectra of the cycled electrodes, where the discharge products produced over the first, second and seventeenth discharge are compared

The ultrafast MAS ^{17}O NMR spectra (**Figure 5-8**) of the cycled cathodes, provides convincing evidence that the protonated reaction products are lithium acetate/formate phase and lithium hydroxide. The solution state ^{1}H NMR spectra of the cathode washing solution (from a discharged electrode, provided in *appendix A9*) does not display evidence of additional species, suggesting that the ssNMR spectra are representative of all the reaction products.

The absence of a strong resonance at 8 ppm, (the expected ^{1}H chemical shift of lithium formate) in the D_{500} or D_{1000} ^{1}H NMR spectra, demonstrates that lithium formate is not a main reaction species during the initial discharge. Thus the signal intensity corresponding to the reaction products, observed in the -0.5 to 2 ppm region is attributed to lithium acetate and lithium hydroxide. This is consistent with the previously reported ^{1}H chemical shifts for lithium acetate and lithium hydroxide.[8]

It is interesting to note that there is a weak signal at 8 ppm in the ^{1}H NMR spectrum of $2D_{1000,}$ suggesting that lithium formate is a minor product at $2D_{1000}$. A much more intense resonance is observed at 8 ppm in the $17D_{400}$ spectrum, indicating that a significant amount of lithium formate that is present on the seventeenth discharge. Additionally at $17D_{400,}$ there is signal intensity in the -0.5 to 2 ppm region, suggesting that lithium hydroxide and lithium acetate are also present.

5.3.4.1 Comments on the Long-Term Instability of TEGDME

When the ^{1}H NMR spectra of the discharged electrodes are compared, the greatest amount of electrolyte breakdown is observed for the cathode that under went the highest

number of discharge cycles ($17D_{400}$), thus strongly suggesting that the parasitic species accumulate on the electrode, and play a role in the capacity fade, observed in **Figure 5-2**. Additionally the amount of lithium formate is observed to grow with increasing the number of cycles. One explanation for this trend may be that lithium formate is produced from a reaction between lithium acetate and molecular oxygen, as suggested by *Leskes et al.*[8] in **equation 5-4**:

$$CH_3CO_2Li + ½\ O_2 \rightarrow HCO_2Li + H_2O \qquad \textbf{(5-4)}$$

The ^1H NMR spectra of D_{500} and D_{1000} demonstrate that lithium acetate is initially produced. It is speculated that when a large quantity of lithium acetate accumulates, it may begin reacting with the oxygen environment producing lithium formate. Alternatively, lithium formate may simply be the product of oxidative decomposition of TEGDME (**equation 5-2**). Regardless, the ^1H NMR spectra of the cycled electrodes suggest that lithium acetate is a symptom of parasitic reactions that occur during the initial discharge cycles, while lithium formate is associated with the long-term instability of the TEGDME electrolyte.

5.3.4 SEM Images of Cycled Electrode

Scanning electron microscopy (SEM) is performed on a partially charged electrode, to observe the surface structures present on the cathode substrate (**Figure 5-11**). Through previous SEM and transmission electron microscopy studies, crystalline Li_2O_2 is known to have a toroidal structure.[17-18] The crystallization of Li_2O_2 into the

toroidal structure is promoted through the use of high-donor-number electrolyte solvents.[19] The donor number may be thought of as a measure of how well the solvent will solvate a cation[20], such as Li^+. Therefore a high donor number solvents, will strongly solvate Li^+/Li^+-containing species.[19] Thus the discharge process is able to continue without clogging the electrode's pores. With this approach it should be possible to achieve large discharge capacities.[19]

The SEM micrograph of the cycled electrode reveals that toroidal structures are present and distinct from the carbon substrate (which appears as coral) in **Figure 5-11**. Additionally there is also a film that partially coats the electrode. Observation of the toroidal structures confirms that Li_2O_2 is present and suggests that it was formed via the solution-mediated mechanism outlined above. This was expected as TEGDME has an intermediate donor number and the solution-mediated Li_2O_2 mechanism is predicted to account for a portion of the electrochemically created Li_2O_2 product.[19] While Li_2O_2 is identified through the SEM imaging, **Figure 5-11** does not provide chemical information about the electrolyte breakdown species, which are readily observed with ssNMR.

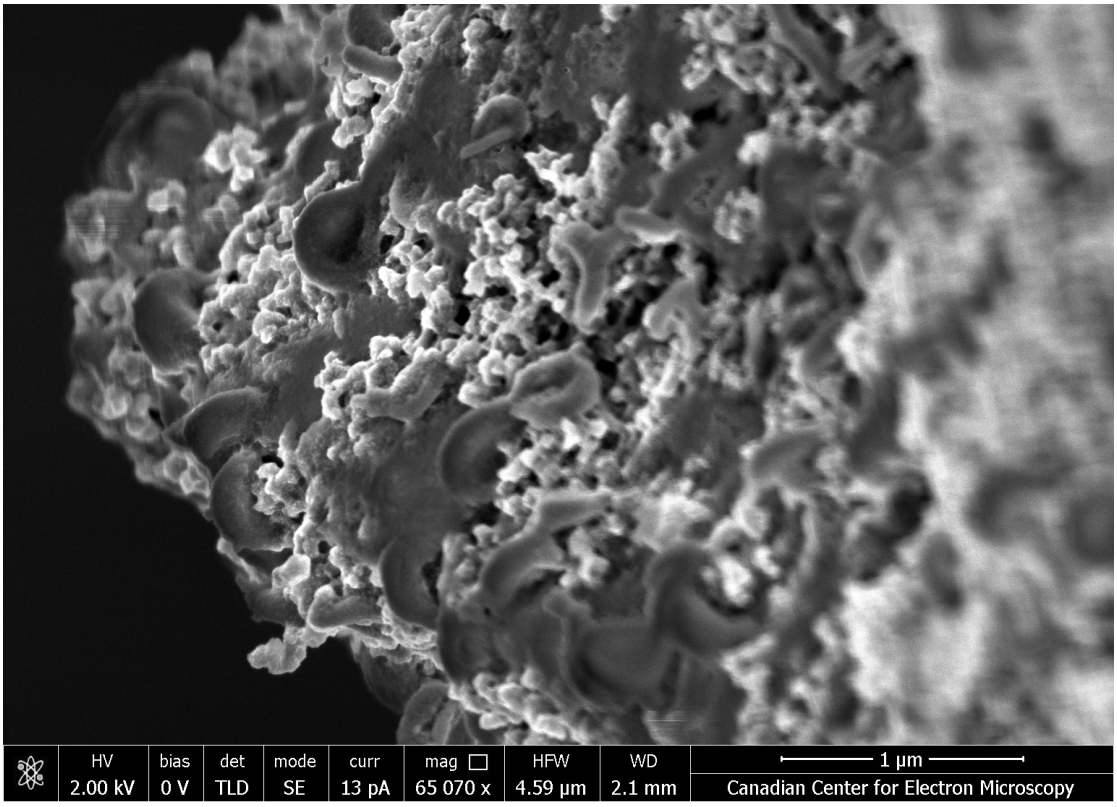

Figure 5-11 SEM micrograph of a partially charged electrode, illustrating that the toroisdal structures (Li_2O_2) are clearly observed and distinct from the carbon support (coral like structure)

5.4 Summary

Together ^{1}H and ^{17}O NMR provide a complete picture of the electrochemical Li-O_2 reaction products produced in the presence of the TEGDME electrolyte. The ^{17}O NMR spectra of the cycled electrodes demonstrated the reversible formation of Li_2O_2 over the first and second discharge cycles, with less Li_2O_2 observed on the second discharge. Using ultrafast MAS at an ultrahigh magnetic field strength, the undesirable degradation products, produced over the first and second discharge, were determined to be Li_2CO_3, LiOH and CH_3CO_2Li. Moreover, LiOH demonstrated reversible formation on the second discharge, whereas Li_2CO_3 and CH_3CO_2Li were found to only partially decomposed upon

charging. With ^{1}H NMR the degradation products were shown to accumulate over multiple cycling events, where lithium formate was found to be a major species on the seventeenth discharge cycle.

Overall the NMR results demonstrate that the nature of the Li-O_2 reaction product changes as the number of discharge cycles increases. This implies that the electrochemical and chemical side reactions evolve throughout the course of a cell's lifetime. Solid-state NMR spectroscopy is expected to continue being an important spectroscopic tool for understanding the alkali metal-oxygen battery chemistry.

5.5 References

[1] Reeve Z. E. M.;Goward G. R.;Bain A. D., *Can. J. Chem.* **2015**, 1.

[2] Reeve Z. E. M.;Pauric A. D.;Harris K. J.;Goward G. R., *J. Phys. Chem. C* **2015**, *119*, 26840.

[3] Freunberger S. A.;Chen Y.;Drewett N. E.;Hardwick L. J.;Bardé F.;Bruce P. G., *Angew. Chem. Int. Ed.* **2011**, *50*, 8609.

[4] McCloskey B. D.;Garcia J. M.;Luntz A. C., *J. Phys. Chem. Lett.* **2014**, *5*, 1230.

[5] Freunberger S. A.;Chen Y.;Drewett N. E.;ardwick L. J.;Bard F.;Bruce P. G., *Angewandte Chemie* **2011**, *50*, 8609.

[6] Lim H.-D.;Park K.-Y.;Gwon H.;Hong J.;Kim H.;Kang K., *Chem. Commun.* **2012**, *48*, 8374.

[7] Leskes M.;Drewett N. E.;Hardwick L. J.;Bruce P. G.;Goward G. R.;Grey C. P., *Angew. Chem. Int. Ed.* **2012**, *51*, 8560.

[8] Leskes M.;Moore A. J.;Goward G. R.;Grey C. P., *J. Phys. Chem. C* **2013**, *117*, 26929.

[9] Bak M.;Rasmussen J. T.;Nielsen N. C., *J. Magn. Reson.* **2000**, *147*, 296.

[10] Adiga S.;Aebi D.;Bryce D. L., *Can. J. Chem.* **2007**, *85*, 496.

[11] Clark S. J.;Segall M. D.;Pickard C. J.;Hasnip P. J.;Probert M. I.;Refson K.;Payne M. C., *Z. Kristallogr.* **2005**, *220*, 567.

[12] Segall M. D.;Lindan P. J. D.;Probert M. I. J.;Pickard C.;Hasnip P. J.;Clark S. J.;Payne M. C., *J. Phys. Condens. Matter* **2002**, *14*, 2717.

[13] Ottakam Thotiyl M. M.;Freunberger S. A.;Peng Z.;Bruce P. G., *J. Am. Chem. Soc.* **2013**, *135*, 494.

[14] Abraham K., *J. Electrochem. Soc.* **2015**, *162*, A3021.

[15] Black R.;Oh S. H.;Lee J.-H.;Yim T.;Adams B.;Nazar L. F., *J. Am. Chem. Soc.* **2012**, *134*, 2902.

[16] McCloskey B. D.;Valery A.;Luntz A. C.;Gowda S. R.;Wallraff G. M.;Garcia J. M.;Mori T.;Krupp L. E., *J. Phys. Chem. Lett.* **2013**, *4*, 2989.

[17] Mitchell R. R.;Gallant B. M.;Shao-Horn Y.;Thompson C. V., *J. Phys. Chem. Lett.* **2013**, *4*, 1060.

[18] Lu Y.-C.;Gallant B. M.;Kwabi D. G.;Harding J. R.;Mitchell R. R.;Whittingham M. S.;Shao-Horn Y., *Energy Environ. Sci.* **2013**, *6*, 750.

[19] Johnson L.;Li C.;Liu Z.;Chen Y.;Freunberger S. A.;Ashok P. C.;Praveen B. B.;Dholakia K.;Tarascon J.-M.;Bruce P. G., *Nat. Chem.* **2014**, *6*, 1091.

[20] Gutmann V., *Coord. Chem. Rev.* **1976**, *18*, 225.

Chapter 6 : Use of Solid-State ^{23}Na NMR Spectroscopy to Evaluate the Expected Sodium-Oxygen Battery Reaction Products

6.1 Introduction

NMR spectroscopy is a powerful tool for studying electrochemical materials. There are many NMR techniques, and the choice of method is governed by the materials' characteristics. Chapters 3, 4 and 5 of this thesis, have outlined the use of multinuclear solid-state NMR to characterize the Li-O_2 battery.[1-2] Here and in Chapter 7 the sodium-oxygen (Na-O_2) battery, is explored with ssNMR. To the best of our knowledge, this is the first time that ^{23}Na NMR has been applied to investigate the Na-O_2 battery chemistry.

The Na-O_2 battery is an emerging metal-oxygen battery technology, which is attracting increasing attention due to its large theoretical energy density coupled with the low cost and high abundance of sodium in nature.[3-5] However, the factors that influence the Na-O_2 electrochemistry are currently under debate, but can be revealed through careful characterization of electrochemically-cycled electrodes. Before solid-state NMR is applied to analyze the electrochemical reaction products, it is important to first establish that the pristine materials themselves have unique, resolvable NMR signatures, even in mixed composition samples.

This chapter assesses the suitability of ^{23}Na NMR spectroscopy to differentiate the expected Na-O_2 reaction products. The reference materials examined in this chapter include; sodium superoxide (NaO_2), sodium peroxide (Na_2O_2), and sodium carbonate (Na_2CO_3). Sodium peroxide and sodium superoxide are the desired discharge products, with sodium superoxide being the preferred phase.[6] Sodium superoxide is proposed to be the most electrochemically reversible component and would provide the advantage of a

low overpotential of < 200 mV, if it could be exclusively formed.[6-7] However, NaO_2 has proven to be elusive and potentially unstable,[8] as the electrochemical production of pure NaO_2 has not been unequivocally confirmed.[8-12] Instead Na_2O_2[13], sodium peroxide dihydrate ($Na_2O_2 \cdot 2H_2O$)[14], sodium carbonate (a main electrolyte degradation species)[8, 11] and a mixture there of[8-9, 11] have been reported as constituent discharge products by; PXRD[9, 11, 14], Raman[9, 11], IR[11], TEM[8, 13], SEM[8-9, 11] X-Ray absorption near edge structure (XANES)[8] and X-Ray photoelectron spectroscopy (XPS)[11].

The findings presented in this chapter demonstrate that the expected reaction products have unique ^{23}Na NMR signatures, thus allowing Na_2O_2, NaO_2 and Na_2CO_3 to be readily differentiated with ^{23}Na NMR spectroscopy. Therefore, it is predicted that the electrochemical reaction products will be identified in the ^{23}Na NMR investigation of cycled Na-O_2 electrodes, which is discussed in Chapter 7.

Here, a combination of NMR techniques including; 3QMAS,[15-16] variable temperature (VT) NMR and T_1 filtering experiments are used to fully characterize the pristine phases. A variety of NMR methods are required due to differences in local symmetry and in electron configurations among the reference materials.

This work was adapted from a manuscript, which was published in *the Journal of the American Chemical Society*. Initial drafts of the manuscript were prepared by the current author, Z. E. M. Reeve. The content was reproduced with the permissions of: *The Journal of the American Chemical Society (DOI: 10.1021/jacs.6b11333) with co-authors C. J. Franko, K. J. Harris, H. Yadegari, X. Sun and G. R. Goward. © 2017 American Chemical Society.* NaO_2 was synthesized by Chris Franko at McMaster University as an

undergraduate thesis student, under the supervision of Zoe Reeve. All NMR spectra were collected and processes at McMaster University with the supervision of Prof. Gillian Goward. The powder X-Ray diffraction experiment was performed by Victoria Jarvis at the McMaster University with the Analytical X-Ray Diffraction Facility.

6.1.1 Selecting ^{23}Na NMR Methods to Characterize the Expected Na-O_2 Reaction Products

When selecting an appropriate ^{23}Na NMR analysis method, the electronic configuration and the magnitude of the ^{23}Na quadrupolar coupling constant (^{23}Na I = 3/2), must be considered simultaneously. In the case of the Na-O_2 battery, the expected reaction products vary in their electron configurations. Na_2O_2 and Na_2CO_3 are diamagnetic compounds, whereas NaO_2 is paramagnetic.

6.1.2 Pristine Reference Materials: Diamagnetic Na_2O_2 and Na_2CO_3

The diamagnetic species Na_2O_2 and Na_2CO_3 are strongly influenced by the quadrupole interaction. Additionally, each material has multiple Na sites as Na_2O_2 is composed of two crystallographic sodium sites[17] and Na_2CO_3 contains three crystallographic sodium sites[18]. Through the application of 2D ^{23}Na-3QMAS, each of the Na sites in Na_2O_2 and Na_2CO_3 is resolved and the quadrupole parameters may be extracted. Importantly, when ^{23}Na-3QMAS spectroscopy is applied to a mixed sample (Na_2O_2 and Na_2CO_3 are ground together), the Na_2O_2 and Na_2CO_3 NMR signals are separated from each other, allowing in both components of the mixture to be identified.

6.1.3 Pristine Reference Material: Paramagnetic NaO_2

Sodium superoxide is paramagnetic, owing to the unpaired electron found within the superoxide anion. The paramagnetism introduces the paramagnetic interaction (a nuclear – electron interaction) to the spin system, which strongly influences the NMR spectrum. The unpaired electron density is transferred from the paramagnet to the spins of the nucleus under observation either directly via a through bonds (Fermi-contact) interaction or indirectly by a through space (dipolar) interaction.[19]

The unpaired electrons in the paramagnet have an electronic spin state (S), which possess a magnetic moment μ_e, which aligns in the presence of a static B_0 field. The lifetime of the electronic spin state (T_{1e}), is extremely short on the NMR timescale. Thus the NMR spins cannot couple with S_z but instead couple to the time averaged local electronic field $<S_z>$ (**equation 6.1**), where μ_0 is permeability of space, g is the electron g-factor, μ_B is the Bohr magneton, N_0 is Avogadro's number and χ_M is the magnetic molar susceptibility in m^3mol^{-1}.[20]

$$< S_z > = -\frac{B_0}{\mu_0 g N_0 \mu_B} \chi_M \qquad (6.1)$$

The rapid electronic relaxation times causes extremely fast nuclear relaxation.[19] In addition to short T_1 values, the paramagnetic resonance also displays a temperature dependent chemical shift.[19]

Given that the crystallographic symmetry at the Na site in NaO_2 is cubic,[21] the NaO_2 signal will be invisible to the 3Q filter (as discussed in Chapter 2, section 2.3.4). Thus the paramagnetic NaO_2 must be detected using alternative methods such as VT NMR or variable delay (T_1 filtering) experiments.

6.2 Experimental

6.2.1 NaO_2 Synthesis

Sodium superoxide was chemically synthesized under an argon atmosphere following a previously published procedure.[22] Oxygen gas was rapidly bubbled through liquid NH_3 and then individual pieces of sodium metal were added to the solution. As each sodium metal piece was solvated, a blue colour appeared and subsequently dissipated as the reduced O_2 reacted with the solvated Na^+ ions. Once the desired amount of sodium metal fully reacted, the liquid ammonia was boiled off. The final product was dried under vacuum for several hours and stored in an argon glovebox. The product was composed of two phases, a yellow and white phase. The yellow phase was confirmed to be the to be the disordered pyrite NaO_2 structure ($Fm\bar{3}m$, ICSC 87176) with powder X-Ray diffraction (PXRD). Variable temperature ^{23}Na NMR was applied to confirm that NaO_2 is paramagnetic. The white phase was determined to primarily be composed of NaOH (Bmmb, ICSD 26831) with PXRD. Both PXRD experiments were performed under inert conditions, described below in section 6.2.4.

6.2.2 Sample Handling and Preparation

Na_2O_2 (Alfa Aesar) was used without further purification and Na_2CO_3 (Sigma Aldrich, purity) was dried at 120 ^{0}C for several hours prior to use. Both materials were stored and packed in a NMR rotor inside an argon glovebox. The mixed samples were fabricated by grinding Na_2O_2 and Na_2CO_3 and Na_2O_2 and NaO_2 together under an argon atmosphere.

6.2.3 Solid-State ^{23}Na NMR Spectroscopy

^{23}Na NMR spectra were acquired on a Bruker Avance I spectrometer (B_0 = 11.7 T, $\nu_0(^{23}Na)$ = 132.294 MHz) using a custom-built double-resonance probe supporting 1.8 mm rotors capable of magic angle spinning (MAS) frequencies from 20 kHz up to 45 kHz. The spectra were referenced to a 1 M NaCl solution at 0 ppm. All 1D spectra were collected via single pulse experiments using a hard 90 pulse at an RF field of 125 kHz, and signal averaged over eight scans. The delay times used for the synthesized NaO_2, pristine Na_2O_2, pristine Na_2CO_3, The Na_2O_2/NaO_2 mixture and the Na_2O_2/Na_2CO_3 mixture were 1 s, 30 s, 5 s, 60 s and 30 s respectively. Variable temperature ^{23}Na MAS experiments were performed on the synthetic NaO_2 sample for the temperature range of 300 K to 350 K. T_1 measurements were performed with a standard inversion-recovery sequence where twelve relaxation times were used for each T_1 determination.

The multiple quantum magic angle spinning (MQMAS)[15-16] pulse sequence used in all experiments was the three pulse, z-filtered sequence. All 2D ^{23}Na triple quantum magic angle spinning (3QMAS) spectra were acquired with 64 t_1 increments at 100 μs in the F1 dimension with 64 scans per t_1 increment at a MAS rate of 20 kHz. The RF field used in the excitation (excitation of the triple quantum coherence (3QC)) and conversion (conversion of the 3QC to single quantum coherence (SQC)) pulses was 125 kHz and a 20 kHz RF field was applied for the selective CT pulse. The respective pulse lengths for the excitation, conversion and selective CT pulses were 4.7 us, 1.7 us and 11.5 us.

6.2.4 Powder X-Ray Diffraction of Synthesized NaO_2

The PXRD samples were prepared under inert conditions inside an argon glovebox. The NaO_2 and NaOH powders were each mounted into a 0.5 mm diameter capillary and sealed with grease inside an argon glovebox. The X-ray diffraction characterization was performed on a Bruker 3-circle D8 goniometer system equipped with a Bruker SMART 6000 CCD area detector, Rigaku RU-200 rotating anode Cu $\bar{K}\alpha$ generator, and cross-coupled parallel focusing optics. An exposure time of 300s/frame was used. Integrated diffractograms were obtained with a 2θ range of 5-95°.

6.3 Results and Discussion

6.3.1 1D ^{23}Na NMR of the Expected Na-O_2 Reaction Products

The ^{23}Na MAS NMR spectra of Na_2O_2, NaO_2 and Na_2CO_3 (**Figure 6-1**) demonstrate that the expected Na-O_2 reaction products have distinct ^{23}Na NMR signatures, which are in agreement with previous reports of these phases.[23-24] Excerpts from the relevant crystal structures, highlighting the local coordination environments of the Na atoms, are shown together with each spectrum. The oxygen atoms are shown in grey, carbon atoms are shown in black and the Na sites are shown in various colours corresponding to the colour scheme illustrated in the NMR spectra (**Figure 6-1**).

For simplicity, the ^{23}Na resonances from compounds with multiple crystallographic sites are labelled from high- to low-frequency as $Na_{(comp\text{-}\#),}$ where "comp" indicates the sodium compound to which it was assigned and # denotes the crystallographic position. For example, $Na_{(per\text{-}1)}$, shows that the labelled NMR resonance in **Figure 6-1** was assigned to the crystallographic site Na1 of Na_2O_2. The assignment of

the ^{23}Na NMR resonances to the crystallographic sites for sodium peroxide, sodium superoxide and sodium carbonate is outlined in **Table 6-1**.

Table 6-1 Assignment of the NMR Resonances to the Crystallographic Sites for the Potential Na-O2 Reaction Products, where the NMR spectra were all collected at 11.7 T

Material/ Crystallographic Site	Assignment Label	^{23}Na Resonance Centered at (ppm)
Na_2O_2 / Na1	$Na_{(per-1)}$	12
Na_2O_2 / Na2	$Na_{(per-2)}$	7
NaO_2 / Na1	$Na_{(sup-1)}$	-23
Na_2CO_3 / Na1 & Na2	$Na_{(carb-1, 2)}$	5
Na_2CO_3 / Na3	$Na_{(carb-3)}$	-15

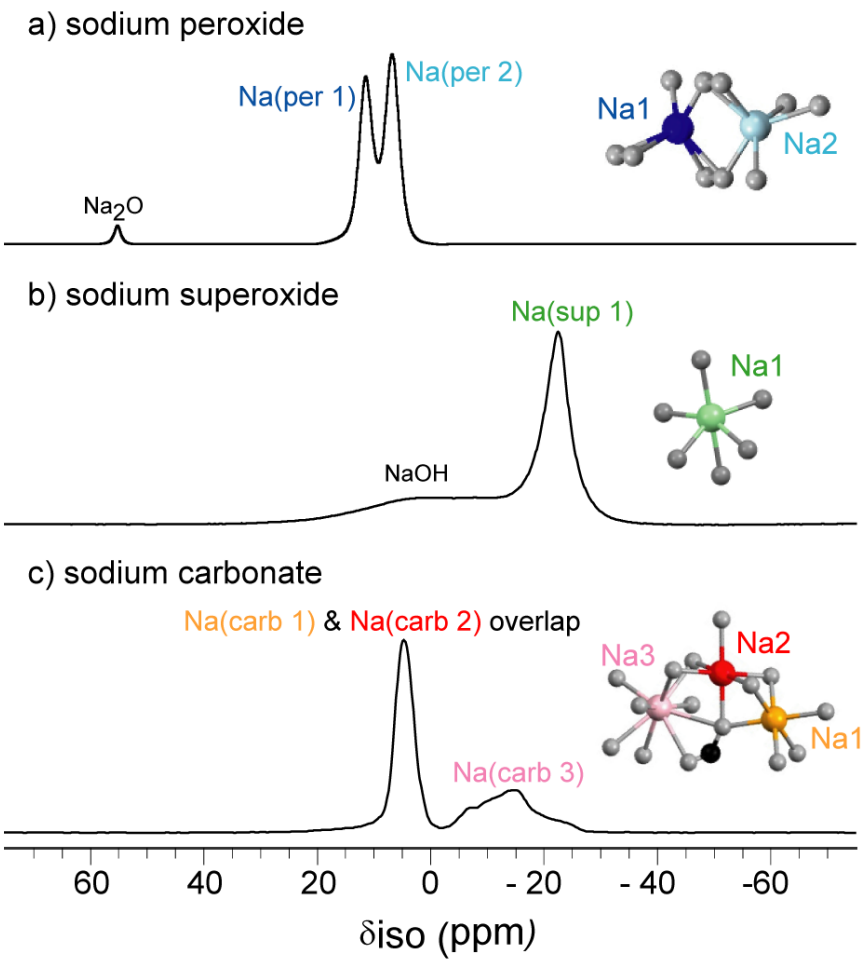

Figure 6-1 1D ^{23}Na NMR spectra of (a) sodium peroxide, with a small sodium oxide impurity (b) sodium superoxide, with residual NaOH and (c) sodium carbonate. All spectra were collected at room temperature under a MAS frequency of 20 kHz, and at 11.7 T applied field. Oxygen atoms are shown in grey, carbon in black, and Na sites in various colors labeled in accordance with Table 6-1

In sodium peroxide, the two unique crystallographic Na positions have extremely similar environments, as reflected by their similar NMR parameters (**Table 6-2**), discussed in section 6.3.3. Previously the ^{23}Na NMR data of Na_2O_2 reported a single Na

resonance.[24] Here the presented 1D and 2D ^{23}Na-3QMAS spectra (**Figure 6-1** and **Figure 6-6** respectively), of Na_2O_2 provide spectral resolution of the two sites. (Application of 2D ^{23}Na-3QMAS spectroscopy to the Na-O_2 species is discussed in section 6.3.2.) The integrated intensity of the 1D NMR resonances; $Na_{(per\text{-}1)}$: $Na_{(per\text{-}2)}$ is 1.0 : 1.0, consistent with the population ratio of the crystallographic sites Na1 : Na2, from the X-ray refinement results.[17] However the sites are not definitively assigned, due to the similarity of the crystallographic environments. Additionally, a small sodium oxide (Na_2O) impurity is observed in the NMR spectrum of sodium peroxide (**Figure 6-1a**), at a chemical shift of 55 ppm. Na_2O has a single crystallographic site and a C_q of 0 MHz due to its cubic symmetry.[23, 25]

The sodium superoxide, NaO_2, is not commercially available and is challenging to synthesize as a pure phase.[6] There are three stable sodium superoxide phases, which exist over different temperature ranges.[26-27] The high temperature phase, disorder pyrite ($Fm\bar{3}m$), is stable at temperatures above 223 K[26-27] and is reported to be the structure of electrochemically generated NaO_2.[6, 28] The NaO_2 sample investigated here, was synthetically-prepared in liquid ammonia following a previously published procedure,[22] and confirmed to be the disordered pyrite structure ($Fm\bar{3}m$, ICSC 87176) with PXRD (**Figure 6-2**).

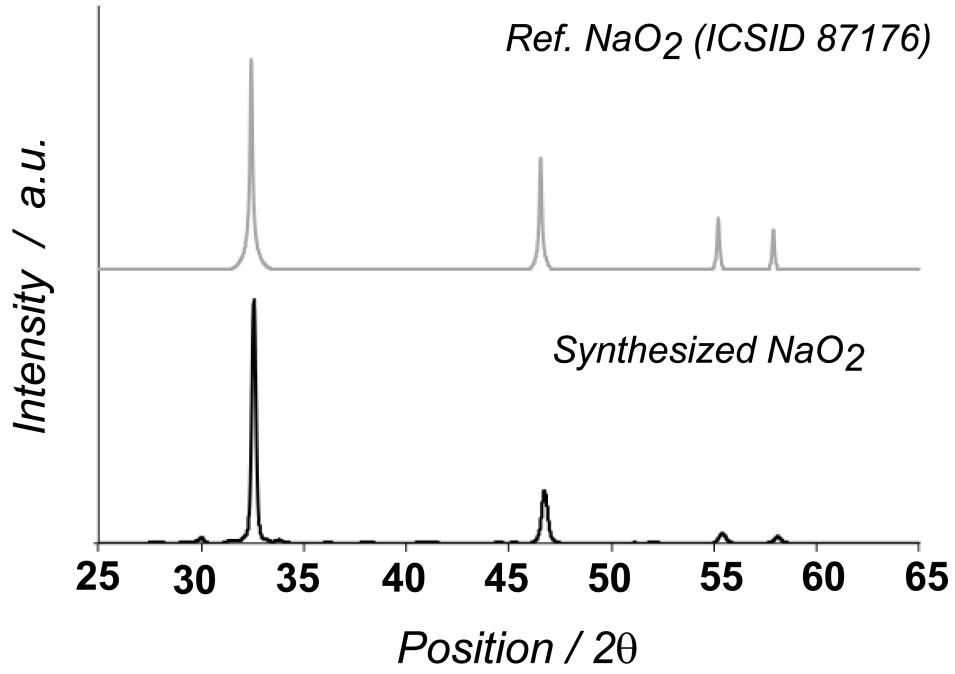

Figure 6-2 Comparison of the chemically synthesized NaO_2 and reference NaO_2 powder X-ray diffraction patterns, confirming that the synthesized NaO_2 has a disordered pyrite structure

The main ^{23}Na peak observed at -23 ppm, in the room temperature NMR spectrum of the synthetic NaO_2 sample (**Figure 6-1b**) is attributed to NaO_2.[23] The resonance is denoted $Na_{(sup\text{-}1)}$, as NaO_2 has a single crystallographic site[21] (**Figure 6-1b**). The remaining spectral features are attributed to NaOH, which is a by-product, of the synthesis. NaOH was identified with PXRD in **Figure 6-3.**

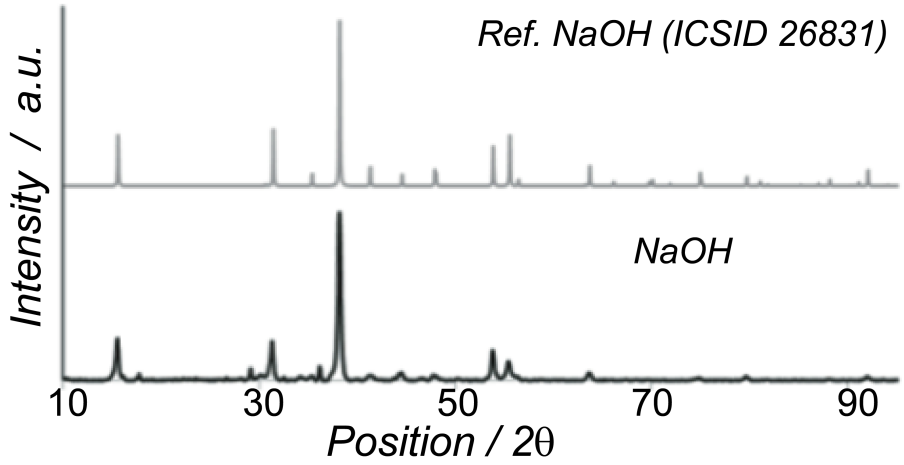

Figure 6-3 Comparison of the NaOH by-product and reference NaOH powder X-ray diffraction patterns

The chemically synthesized NaO_2 is confirmed to be paramagnetic with VT ^{23}Na NMR and T_1 relaxation studies. The chemical shift of the NaO_2 resonance ($Na_{(sup\text{-}1)}$) displays a temperature dependent behaviour in **Figure 6-4**, consistent with a previous VT NMR study of NaO_2.[23] Additionally NaO_2 has a very rapid ^{23}Na T_1 relaxation time of 7 ms, further demonstrating the paramagnetic nature of this material. The relaxation properties of the expected Na-O_2 species are compared in section 6.3.4.

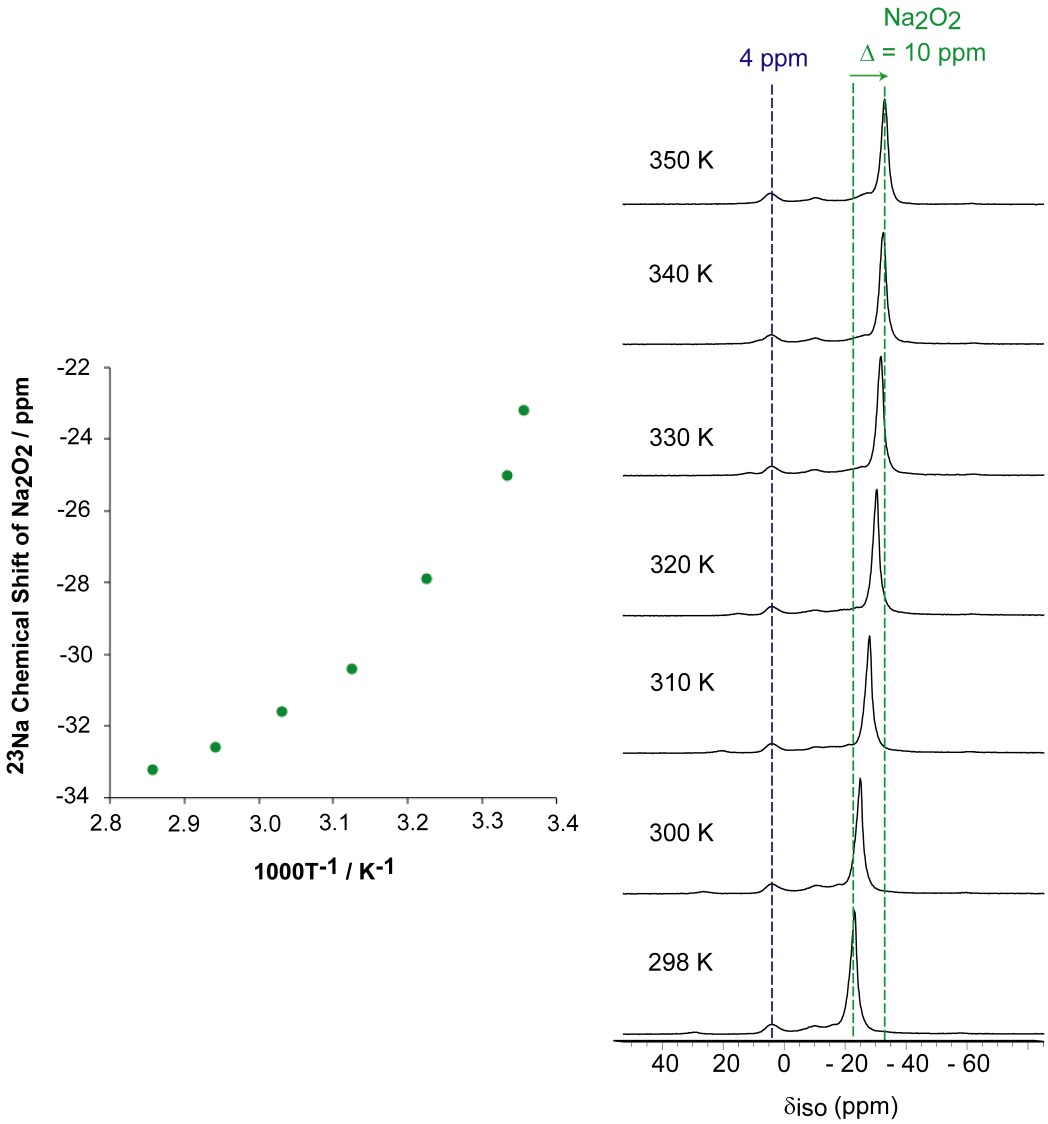

Figure 6-4 (Left) Plot of the NaO_2 ($Na_{(sup\text{-}1)}$) ^{23}Na chemical shift vs. 1000/T and (Right) the experimental ^{23}Na NMR spectra of the synthesized sodium superoxide, where the NaO_2 ($Na_{(sup\text{-}1)}$) resonance moves to lower frequencies as the sample temperature is increased compared to the diamagnetic impurity which remains at a constant chemical shift with temperature. All measurements were made at a MAS speed of 20 kHz at a magnetic field of 11.7 T

Sodium carbonate has three unique crystallographic Na sites[18], yet only two NMR resonances are observed in the 1D ^{23}Na NMR spectrum (**Figure 6-1c**). The $Na_{(carb\text{-}}$

$_{1,2)}$ and $Na_{(carb-3)}$ resonances are centred at 5 ppm and – 15 ppm respectively. The crystallographic sites are populated in a ratio of 1.0 : 1.0 : 2.0 for the crystallographic sites Na1 : Na2 : Na3 based on the X-ray refinement results.[18] The integrated intensity of the NMR resonances is 1.2 : 1.0 for $Na_{(carb-1,2)}$: $Na_{(carb-3)}$, indicating that one of the NMR resonances is composed of two crystallographic sites and the other corresponds to a single (doubly populated) site. The spectral overlap of Na_2CO_3 has not previously been investigated, and is elucidated in the following section using triple-quantum magic angle spinning (3QMAS).[15-16]

6.3.2 2D ^{23}Na-3QMAS Results of the Expected Na-O_2 Reaction Products

^{23}Na-3QMAS provides spectral resolution of the individual chemical shifts in the indirect (isotopic) dimension, and separates the quadrupole lineshapes of each, in the direct (isotropic + quadrupolar) dimension (labelled as $\delta_{iso + aniso}$)[15-16] shown in **Figures 6-5, 6-6,** and **6-8**. We note that the sodium sites in both sodium oxide and sodium superoxide have a C_q of 0 MHz,[23] and therefore neither species is detectable through a 3Q filter.

The 2D ^{23}Na-3QMAS spectrum of Na_2CO_3 (**Figure 6-5**) reveals three Na sites. The $Na_{(carb-3)}$ resonance at low frequency has by far the largest C_q, and is therefore assigned to the crystallographic site Na3, as it has by the lowest symmetry in the structure.[18] The other two crystallographic sites are assigned to two overlapping NMR resonances observed at higher frequency: $Na_{(carb-1)}$ and $Na_{(carb-2)}$. These two similar sites, which are not resolved in the 1D spectrum (**Figure 6-1b**), are separated as two distinct resonances in the indirect dimension of the 2D spectrum (**Figure 6-5**). This demonstrates

the value of applying 2D 3QMAS to materials, which contain sodium sites of similar symmetry and chemical shifts. The NMR parameters, reported in **Table 6-2** (section 6.3.3), for the three Na_2CO_3 sites were determined by simulating the extracted 1D slices for each site, as shown in **Figure 6-5**.

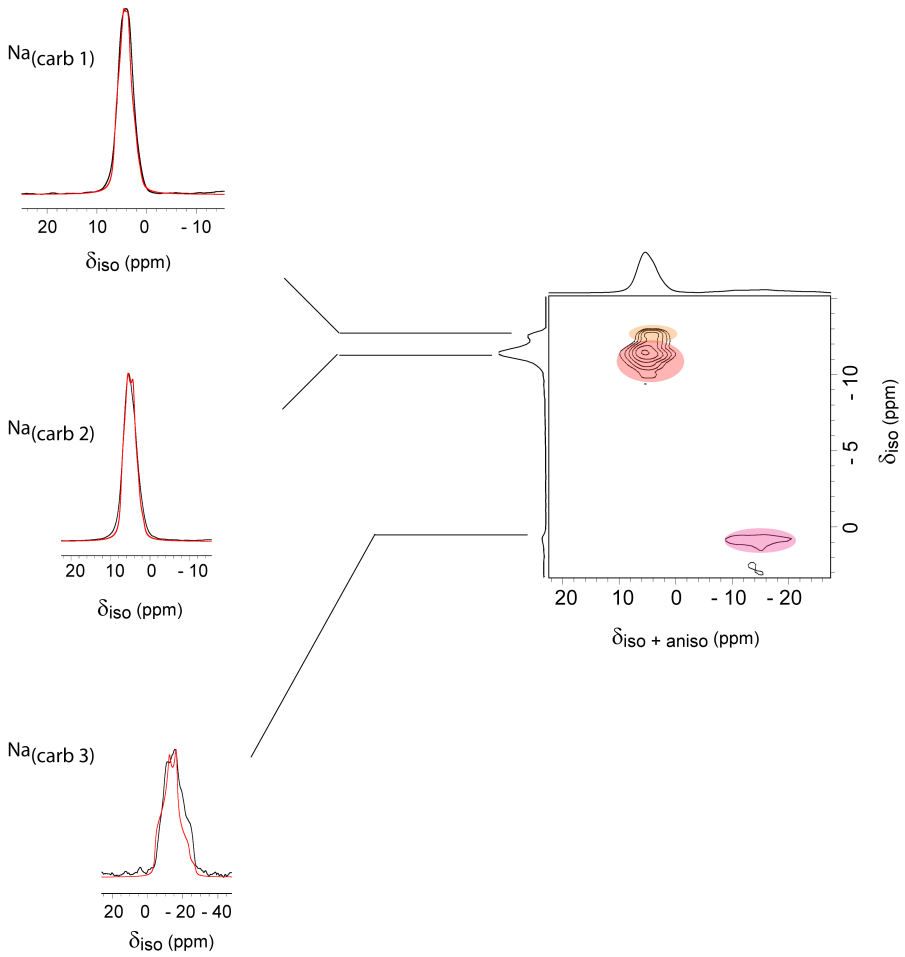

Figure 6-5 2D ^{23}Na-3QMAS spectrum of Na_2CO_3, illustrating good site resolution for the three Na sites, where the 1D extracted slices for each site is shown, simulated using the parameters reported in Table 6-2

The ^{23}Na-3QMAS spectrum of Na_2O_2 **Figure 6-6**, illustrates that $Na_{(per-1)}$ and $Na_{(per-2)}$ are clearly resolved. In the 2D spectrum neither the $Na_{(per-1)}$ or $Na_{(per-2)}$ resonances are parallel to the direct dimension. Instead both resonances are observed to be at an angle with respect to the direct dimension, which indicates that the resonances correspond to a distribution of isotropic chemical shifts. This suggests that Na_2O_2 is disordered or amorphous. This trend is also observed in **Figure 6-8**, the 2D ^{23}Na-3QMAS spectrum of the Na_2O_2 and Na_2CO_3 mixture. A similar behaviour has been observed in the 2D 3QMAS NMR spectra of other amorphous materials.[29]

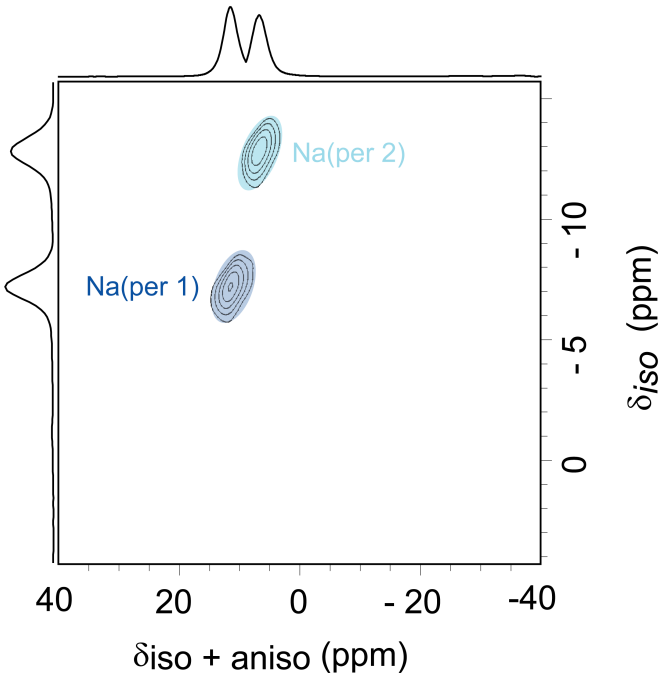

Figure 6-6 2D ^{23}Na-3QMAS NMR spectrum of pure sodium peroxide collected at a MAS frequency of 20 kHz and a 11.7 T magnetic field

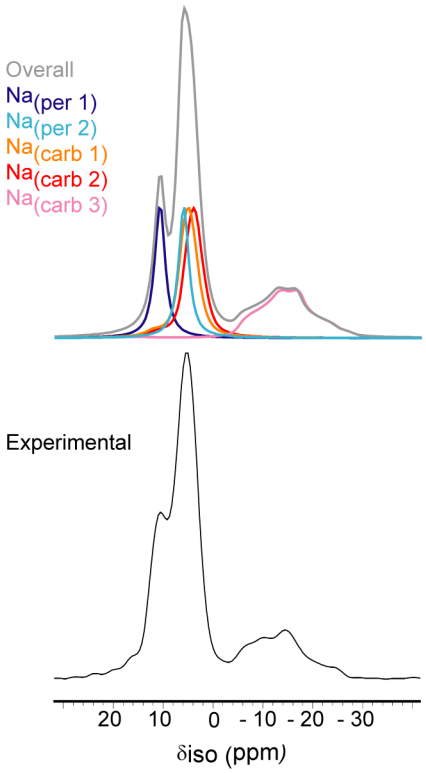

Figure 6-7 A comparison of the experimental (lower) and simulated (upper) ^{23}Na NMR spectrum of the Na_2O_2 and Na_2CO_3 physical mixture, where the experimental data was fit to the two Na_2O_2 resonances ($Na_{(per-1)}$ and $Na_{(per-2)}$) and the three Na_2CO_3 resonances ($Na_{(carb-1)}$, $Na_{(carb-2)}$ and $Na_{(carb-3)}$) in accordance with Table 6-2. The experimental spectrum was collected at a 11.7 T magnetic field at a MAS rate of 20 kHz.

In order to demonstrate that the diamagnetic species can be distinguished from each other in a multi-component sample, a physical mixture of Na_2O_2 and Na_2CO_3 was fabricated. From the 1D spectrum of the mixture (**Figure 6-7**), Na_2O_2 and Na_2CO_3 are identified through the observation of $Na_{(per-1)}$ and $Na_{(carb-3)}$ respectively. Thus 1D ^{23}Na NMR of the cycled Na-O_2 electrodes, is expected to be a valuable screening tool for determining if Na_2O_2 or Na_2CO_3 are electrochemically formed. However the $Na_{(per-2)}$,

$Na_{(carb-1)}$ and $Na_{(carb-2)}$ resonances overlap. This is overcome through the application of 2D ^{23}Na-3QMAS (**Figure 6-8**).

2D ^{23}Na-3QMAS (**Figure 6-8**) of the physical mixture successfully separates the two Na_2O_2 signals from the three Na_2CO_3 resonances. The diagnostic sites; $Na_{(per-1)}$ (Na_2O_2) and $Na_{(carb-3)}$ (Na_2CO_3) are still well separated in **Figure 6-8**. Moreover, the NMR resonances that overlapped in the 1D spectrum are now well resolved in the 2D spectrum.

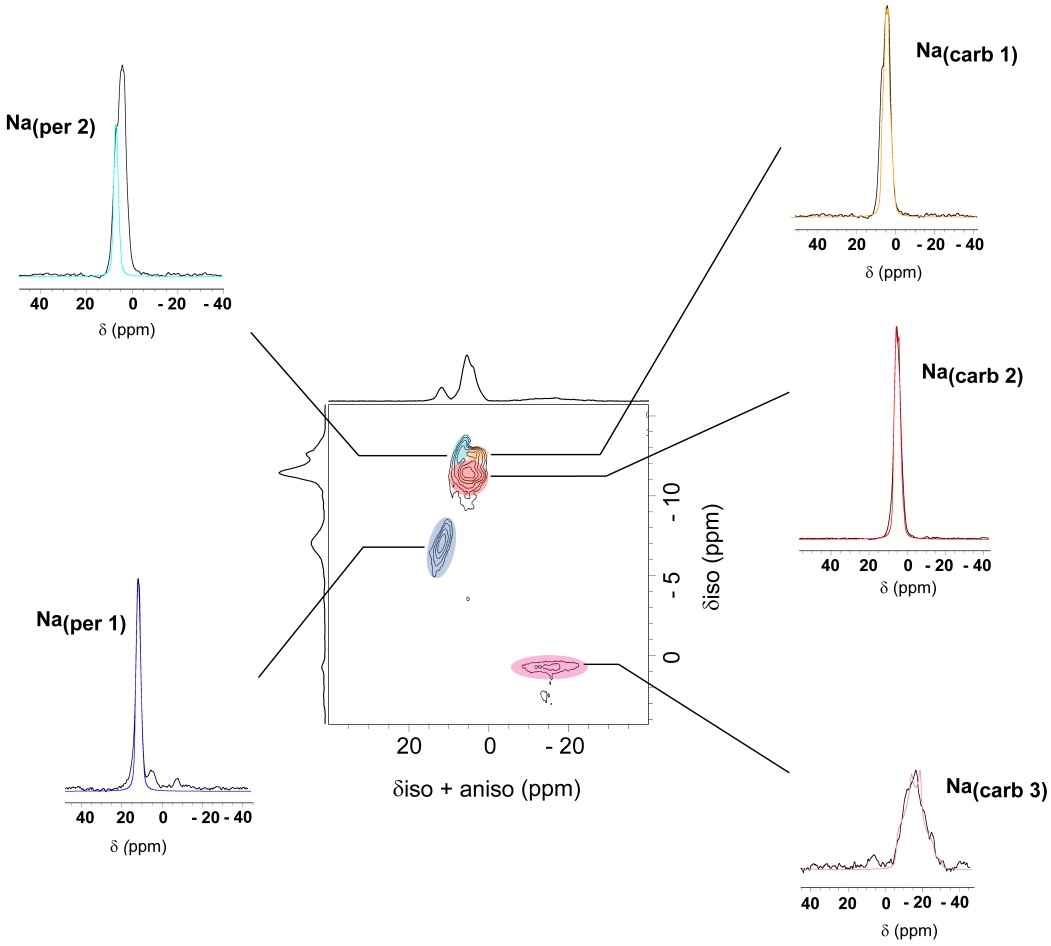

Figure 6-8 2D ^{23}Na-3QMAS spectrum of the Na_2O_2 and Na_2CO_3 physical mixture, where the 1D extracted slides for each site in shown and simulated using the parameters outlined in Table 6-2

Figure 6-8 demonstrates the utility of applying 3QMAS to analyze multi-component mixtures. It is expected that ^{23}Na-3QMAS will be invaluable in confirming the formation of electrochemically-produced sodium peroxide and sodium carbonate in Chapter 7.

6.3.3 ^{23}Na NMR Parameters for the Expected Na-O_2 Reaction Products

The experimentally determined ^{23}Na NMR parameters for the expected Na-O_2 reaction products, are reported in **Table 6-2** and compared to existing literature values where available. The NMR spectra were simulated using the TopSpin 3.2 software.

Table 6-2 Comparison of the Experimental and Literature ^{23}Na NMR Parameters at Room Temperature for the Relevant Na-O_2 Species

Compound / Assigned NMR Resonance		δ_{iso} (ppm)	C_q (MHz) ± 0.05	$\eta_q \pm 0.1$
Na_2O_2	Lit.[24]	6.9	0.47	-
Na_2O_2 / $Na_{(per-1)}$	Expt.	7.0	0.47	0.1
Na_2O_2 / $Na_{(per-2)}$	Expt.	11.8	0.47	0.1
Na_2O	Lit [23]	48.0	-	-
	Expt.	55.0	0.00	0.00
NaO_2 / $Na_{(sup-1)}$	Lit.[23]	-28	-	-
	Expt.	-23	0.00	0.00
Na_2CO_3 / $Na_{(carb-1)}$	Expt.	7	1.20	0.60
Na_2CO_3 / $Na_{(carb-2)}$	Expt.	7.5	1.28	0.50
Na_2CO_3 / $Na_{(carb-3)}$	Expt.	-4	2.48	0.65

The quadrupole coupling constant (C_q) is an important parameter, which is used to differentiate between the various Na-O_2 reaction products. For the species of interest, the magnitude of C_q ranges from 0 MHz to 2.48 MHz, where only the $Na_{(carb-3)}$) site displays in a characteristic second-order quadrupolar lineshape. As noted above in section 6.3.2, the NMR parameters reported in **Table 6-2** for Na_2CO_3, were determined by simulated the extracted 1D slice for each of the three sodium carbonate sites shown in **Figure 6-5**.

The ^{23}Na NMR parameters for Na_2O_2 were determined by evaluating the spinning side band manifolds, which is reflective of the first order quadrupole powder pattern (**Figure 6-9**). With 2D ^{23}Na-3QMAS, Na_2O_2 is confirmed have two Na sites (**Figure 6-6**)

in accordance with the reported crystal structure.[17] The two Na sites of sodium peroxide, were found to have the same quadrupole coupling constant, in accordance with ^{23}Na C_q value previously reported by *Bastow et al.*[24]. However *Bastow et al.* modeled the spectrum as a single site[24], where the data sets were collected at a magnetic field of 9.4 T and at a MAS frequency ranging from 12 and 16 kHz. The 1D ^{23}Na and 2D ^{23}Na-3QMAS spectra (**Figure 6-1** and **6-6** respectively) presented here, were collected at a higher magnetic field of 11.7 T and at a faster MAS frequency of 20 kHz, demonstrating that Na_2O_2 has two distinct Na sites.

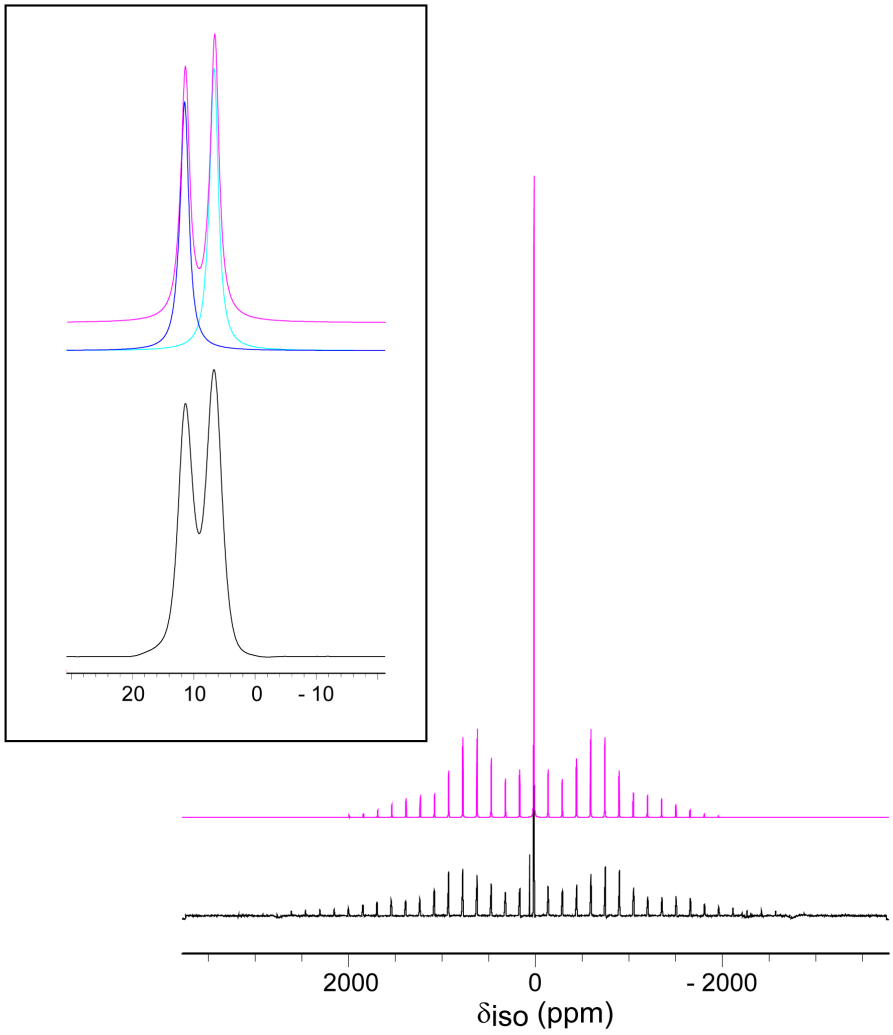

Figure 6-9 (Pink) simulated and (black) experimental ^{23}Na NMR spectra of Na_2O_2 collected at 11.7 T with a MAS rate of 20 kHz, where an evaluation of the central transition illustrates that the two Na sites; $Na_{(per\ 1)}$ (dark blue) and $Na_{(per\ 2)}$ (light blue) are resolved.

6.3.4 ^{23}Na Relaxation Study of the Expected Na-O_2 Reaction Products

Sodium superoxide and sodium peroxide are readily differentiated with ^{23}Na NMR based on their significantly different chemical shifts (**Figure 6-1**) and moreover,

their distinct relaxation properties. The T_1 relaxation times were determined using inversion recovery and are outlined in **Table 6-3**. NaO_2 has the shortest T_1 value due to the paramagnetic interactions of this open-shell compound, thus NaO_2 is easily identified via T_1 filtering experiments. **Figure 6-10** illustrates the influence that T_1 has on the signal intensity, where the diamagnetic Na_2O_2 resonances ($Na_{(per-1)}$ and $Na_{(per-2)}$ resonances) relax at a much slower rate compared to the signal from the paramagnetic NaO_2 ($Na_{(sup-1)}$). This is a valuable, yet simple tool for comparing electrochemical reaction products, and thereby following the roles of paramagnetic centers, which are of key importance to the proposed free-radical mechanisms of the sodium-oxygen batteries.

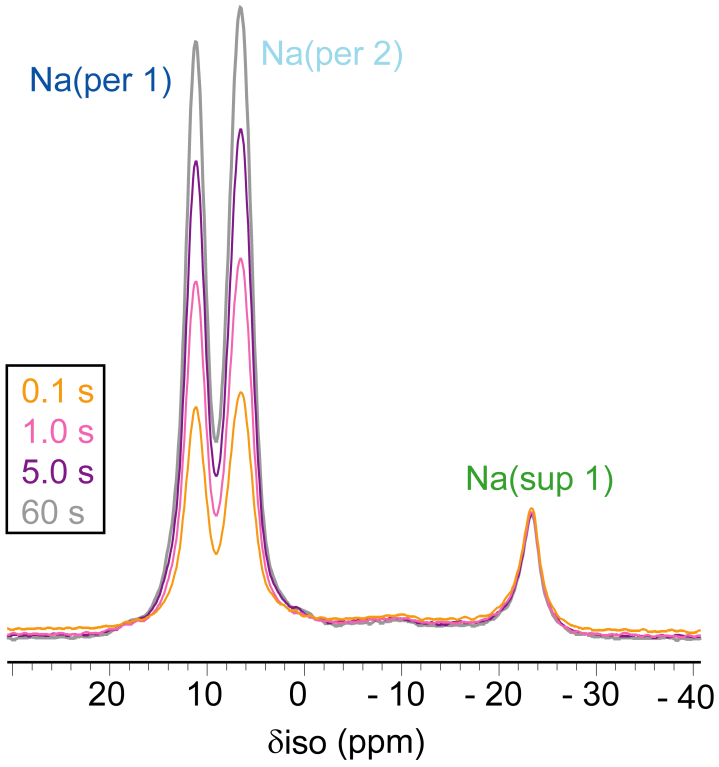

Figure 6-10 Results from a T_1 filtering experiment where the delay was varied from 0.1 s to 60 s, for a sodium superoxide and sodium peroxide mixture. The 1D ^{23}Na NMR spectra were collected at a MAS frequency of 20 kHz and at a magnetic field of 11.7 T

Table 6-3 ^{23}Na Spin-Lattice (T_1) Relaxation Times for Na-O_2 Reaction Species collected at 11.7 T

NMR Resonance	T_1 value (s)
$Na_{(per-1)}$ & $Na_{(per-2)}$	14.0 ± (0.1)
$Na_{(sup-1)}$	$7.0 \times 10^{-3} \pm (5.0 \times 10^{-3})$
Na_2CO_3 / $Na_{(carb-1,2)}$	$9.0 \times 10^{-1} \pm (3.0 \times 10^{-2})$
$Na_{(carb-3)}$	1.5 ± (0.1)

6.4 Summary and Outlook

The ^{23}Na NMR study outlined in this chapter demonstrates that the expected reactions products; NaO_2, Na_2O_2 and Na_2CO_3, have unique ^{23}Na NMR signatures. Thus, allowing the pristine reference materials to be readily differentiated with solid-state ^{23}Na

NMR. This is particularly true for sodium superoxide and sodium peroxide, which have dissimilar ^{23}Na chemical shifts and relaxation properties.

A variety of NMR methods are employed in this work, due to the differences in the local symmetry and in electronic configurations among the species of interest. The paramagnetic NaO_2 is characterized by rapid T_1 relaxation times and a temperature dependent ^{23}Na chemical shift. The diamagnetic Na_2O_2 and Na_2CO_3 species, display much slower T_1 relaxation times and their NMR spectra are heavily influenced by the quadrupole interaction. Additionally, the application of 2D ^{23}Na-3QMAS allows the Na_2O_2 lineshape to be separated from the Na_2CO_3 lineshape in a mixed sample.

Given the relative ease with which, the ^{23}Na NMR spectra of the expected Na-O_2 reaction products were acquired, it is predicted that ^{23}Na NMR will be a valuable characterization tool for uncovering the Na-O_2 electrochemistry. The ssNMR investigation of electrochemically-cycled Na-O_2 electrodes is discussed in the next chapter.

6.5 References

[1] Z. E. M. Reeve;G. R. Goward;A. D. Bain, *Can. J. Chem.* **2015**, 1.
[2] Z. E. M. Reeve;A. D. Pauric;K. J. Harris;G. R. Goward, *J. Phys. Chem. C* **2015**, *119*, 26840.
[3] S. K. Das;S. Lau;L. A. Archer, *J. Mater. Chem. A* **2014**, *2*, 12623.
[4] B. L. Ellis;L. F. Nazar, *Curr. Opin. Solid State Mater. Sci.* **2012**, *16*, 168.
[5] E. Peled;D. Golodnitsky;R. Hadar;H. Mazor;M. Goor;L. Burstein, *J. Power Sources* **2013**, *244*, 771.
[6] P. Hartmann;C. L. Bender;M. Vračar;A. K. Dürr;A. Garsuch;J. Janek;P. Adelhelm, *Nat. Mater.* **2013**, *12*, 228.
[7] C. L. Bender;P. Hartmann;M. Vračar;P. Adelhelm;J. Janek, *Adv. Energy. Mater.* **2014**, *4*, 1301863.
[8] H. Yadegari;M. N. Banis;B. Xiao;Q. Sun;X. Li;A. Lushington;B. Wang;R. Li;T.-K. Sham;X. Cui;X. Sun, *Chem. Mater.* **2015**, *27*, 3040.
[9] J. Kim;H. Park;B. Lee;W. M. Seong;H.-D. Lim;Y. Bae;H. Kim;W. K. Kim;K. H. Ryu;K. Kang, *Nat. Commun.* **2016**, *7*.
[10] H. Yadegari;Q. Sun;X. Sun, *Adv. Mater.* **2016**, *28*, 7065.
[11] H. Yadegari;Y. Li;M. N. Banis;X. Li;B. Wang;Q. Sun;R. Li;T.-K. Sham;X. Cui;X. Sun, *Energy Environ. Sci.* **2014**, *7*, 3747.
[12] N. Ortiz-Vitoriano;T. P. Batcho;D. G. Kwabi;B. Han;N. Pour;K. P. C. Yao;C. V. Thompson;Y. Shao-Horn, *J. Phys. Chem. Lett.* **2015**, *6*, 2636.
[13] W. Liu;Q. Sun;Y. Yang;J.-Y. Xie;Z.-W. Fu, *Chem. Commun.* **2013**, *49*, 1951.
[14] J. Kim;H.-D. Lim;H. Gwon;K. Kang, *Phys. Chem. Chem. Phys.* **2013**, *15*, 3623.
[15] A. Medek;J. S. Harwood;L. Frydman, *J. Am. Chem. Soc.* **1995**, *117*, 12779.
[16] L. Frydman;J. S. Harwood, *J. Am. Chem. Soc.* **1995**, *117*, 5367.
[17] R. L. Tallman;J. L. Margrave;S. W. Bailey, *J. Am. Chem. Soc.* **1957**, *79*, 2979.
[18] M. Dusek;G. Chapuis;M. Meyer;V. Petricek, *Acta Crystallogr., Sect. B: Struct. Sci* **2003**, *59*, 337.
[19] C. P. G. a. N. Dupre, *Chem. Rev.* **2004**, *104*, 4493.
[20] C. Kittel, *Introduction to solid state*, John Wiley & Sons, **1966**.
[21] M. Ziegler;M. Rosenfeld;W. Kaenzig;P. Fischer, *Helv. Phys. Acta* **1976**, *49*, 57.
[22] W. H. Schechter;H. H. Sisler;J. Kleinberg, *Journal of the American Chemical Society* **1948**, *70*, 267.
[23] T. R. Krawietz;D. K. Murray;J. F. Haw, *J. Phys. Chem. A* **1998**, *102*, 8779.
[24] T. Bastow, *Z. Naturforsch., A: Phys. Sci.* **1994**, *49*, 320.
[25] E. Zintl;A. Harder;B. Dauth, *Z. Elektrochem. Angew. Phys. Chem* **1934**, *40*, 588.
[26] G. F. Carter;D. Templeton, *Journal of the American Chemical Society* **1953**, *75*, 5247.
[27] D. H. Templeton;C. H. Dauben, *J. Am. Chem. Soc.* **1950**, *72*, 2251.
[28] B. Lee;D.-H. Seo;H.-D. Lim;I. Park;K.-Y. Park;J. Kim;K. Kang, *Chem. Mater.* **2014**, *26*, 1048.
[29] A. P. M. Kentgens, *Geoderma* **1997**, *80*, 271.

Chapter 7 : Detection of Electrochemical Reaction Products from the Sodium-Oxygen Battery with Solid-State ^{23}Na NMR Spectroscopy

7.1 Introduction

This chapter describes the uses of ^{23}Na NMR, to investigate the electrochemical reaction products produced in the Na-O_2 battery. Chapter 6 demonstrated that Na_2O_2, NaO_2 and Na_2CO_3, are distinguishable with 1D and 2D ^{23}Na NMR techniques. Here ^{23}Na NMR of electrochemically-cycled electrodes reveals a combination of degradation species; newly observed sodium fluoride (NaF) and the expected Na_2CO_3, as well as the desired reaction product Na_2O_2. The initial reaction product, NaO_2, is not present in a measurable quantity in the ^{23}Na NMR spectra of the cycled electrodes. This suggests that NaO_2 may have undergone further reactions with the battery components. The reactivity of NaO_2 and Na_2O_2 with the carbon electrode (carbon C65 + PVDF) was further investigated with ^{23}Na NMR and PXRD, which revealed that the electrode degraded in the presence of the sodium oxides species. NaF and Na_2CO_3 were observed in the NMR spectrum and the PXRD diffraction pattern, whereas NaO_2 was no longer present.

This work was adapted from a manuscript that was published in *the Journal of the American Chemical Society*. Initial drafts of the manuscript were prepared by the current author, Z. E. M. Reeve. The content was reproduced with the permissions of: *The Journal of the American Chemical Society (DOI: 10.1021/jacs.6b11333) with co-authors C. J. Franko, K. J. Harris, H. Yadegari, X. Sun and G. R. Goward. © 2017 American Chemical Society*. All NMR spectra were collected and processes at McMaster University with the supervision of Prof. Gillian Goward. The powder X-Ray diffraction experiment was

performed by Victoria Jarvis at the McMaster University with the Analytical X-Ray Diffraction Facility.

7.2 Experimental

7.2.1 Sample Handling and Preparation

All materials were purchased from Sigma Aldrich. Sodium bicarbonate, sodium tartrate dehydrate and anhydrous sodium acetate were used without further purification. Sodium bicarbonate and anhydrous sodium acetate were stored under inert conditions. Dehydrated sodium tartrate, sodium hydroxide, sodium formate, sodium oxalate and sodium triflate were dried at 120 ^{0}C for several hours under active vacuum prior to use.

The NaO_2 synthesis and characterization was discussed in Chapter 6, section 6.2.1. The Na_2O_2 / NaO_2 mixture and the mock cathode (Na_2O_2 / NaO_2 mixture + carbon PVDF electrode and Na_2O_2 + carbon PVDF electrode) were fabricated by grinding the required components together under an argon atmosphere.

7.2.2 Na-O_2 Electrochemistry

The Na-O_2 cells were constructed following previously published methods.[1] Gas diffusion electrodes were prepared by casting a mixture of commercial carbon black and Polyvinylidene fluoride (PVDF, Alfa Aesar) with a weight ratio of 9:1 on a separator (Celgard 3500). The electrodes were 3/8 inch in diameter with a loading of ~0.25 mg. Swagelok type cells comprised of sodium foil anode, Celgard 3500 separator, gas diffusion electrode and a stainless steel mesh as current collector were used to prepare the discharge product. A fresh sodium foil was prepared with the aid of a homemade press machine using sodium metal blocks (Sigma Aldrich), inside the argon-filled glove box.

The electrolyte was a 0.5 M solution of sodium triflate ($NaSO_3CF_3$ 98%, Aldrich) dissolved in diethylene glycol dimethyl ether (DEGDME reagent grade ≥ 98%, Aldrich). The sodium triflate electrolyte salt was dried at 80 ˚C under vacuum for 48 hours and the water content of diethylene glycol dimethyl ether solvent was removed using molecular sieves for at least 10 days. The assembled Na-O_2 cells were sealed into a specially designed testing chamber and then taken out of the glove box. A moderate vacuum was applied to remove the argon, and subsequently the chamber was back-filled with pure oxygen (purity 99.993%). The oxygen pressure was brought to 1.0 atm and maintained under static conditions throughout the discharge cycle. The Na-O_2 cells were discharged at a current density of 75 mA g^{-1} and stopped at the specific capacities of interest along the discharge curve. Following electrochemical cycling the Na-O_2 cells were disassembled in the glovebox and packed in an NMR rotor without further modification.

7.2.3 Solid-State ^{23}Na NMR Spectroscopy

The ^{23}Na NMR spectra of the electrochemically cycled electrodes were acquired on a Bruker Avance I spectrometer (B_0 = 11.7 T, $\nu_0(^{23}Na)$ = 132.294 MHz) using a custom-built double-resonance probe supporting 1.8 mm rotors capable of magic angle spinning (MAS) frequencies from 20 kHz up to 45 kHz. The spectra were referenced to a 1 M NaCl solution at 0 ppm. The 1D spectra of the cycled electrodes were collected via single pulse experiments using a hard 90 pulse at an RF field of 125 kHz, signal averaged over 8 scans with a delay time of 1 s.

The MQMAS[2-3] pulse sequence applied to the cycled cathode D_{750} was the three pulse, z-filtered sequence. The 2D ^{23}Na-3QMAS spectrum was acquired with 64 t_1

increments at 100 μs in the F1 dimension with 192 scans per t_1 increment at a MAS rate of 20 kHz. The RF field used in the excitation and conversion pulses was 125 kHz and a 20 kHz RF field was used for the selective pulse. The respective pulse lengths for the excitation, conversion and selective pulses were 4.7 μs, 1.7 μs and 11.5 μs.

The ^{23}Na NMR spectra of the NaO_2/Na_2O_2 mixture, the NaO_2/Na_2O_2 mock cathode, Na_2O_2, the Na_2O_2 mock cathode and the potential Na-O_2 degradation products (sodium acetate, sodium formate, sodium bicarbonate, sodium oxalate, sodium tartrate, sodium tartrate dihydrate, sodium hydroxide and sodium fluoride) were acquired on a Bruker Avance III 850HD spectrometer (B_0 = 19.9 T, $\nu_0(^{23}Na)$ = 224.876 MHz) using a Bruker 1.9 mm probe with a MAS frequency of 30 kHz. All spectra were referenced to a 1 M NaCl solution at 0 ppm and collected with a soft 90 degree pulse at a RF field of 20 kHz. The spectra of Na_2O_2, the Na_2O_2 mock cathode, the NaO_2/Na_2O_2 mixture and the NaO_2/Na_2O_2 mock cathode were collected with a 45 s delay time in 16 scans. The spectra of sodium tartrate dihydrate, sodium fluoride and sodium bicarbonate were collected with a 60 s delay time in 8 scans. The spectra of sodium oxalate and sodium formate were collected with a delay time of 30 s in 8 scans. The spectra of sodium acetate and sodium hydroxide were collected with a delay time of 10 s in 8 scans. The spectrum of the dried sodium tartrate sample was collected with a 5 s delay time in 8 scans.

7.2.4 Powder X-Ray Diffraction of Mock Electrode

The mock cathode was prepared for PXRD under inert conditions, inside an argon glovebox. The sample was mounted into a 0.7 mm diameter capillary, which was sealed with grease inside the glovebox. The X-ray diffraction characterization was performed on

a Bruker 3-circle D8 goniometer system equipped with a Bruker SMART 6000 CCD area detector, Rigaku RU-200 rotating anode Cu $\bar{K}\alpha$ generator, and cross-coupled parallel focusing optics. An exposure time of 300s/frame was used. Integrated diffractograms were obtained with a 2θ range of 5-95°.

7.3 Results and Discussion

7.3.1 Na-O_2 Electrochemistry

A representative Na-O_2 electrochemical curve illustrating the first discharge is shown in **Figure 7-1**. The electrolyte system investigated here is a 0.5 M solution of sodium triflate, in one of the standard ether electrolytes; diethylene glycol dimethyl ether (DEGDME). This electrolyte was selected as pure NaO_2 was previously detected when DEGDME was employed.[4] Here, the electrochemical reaction products are identified with 1D and 2D solid-state ^{23}Na NMR of cycled Na-O_2 electrodes. Two samples were selected for the ^{23}Na NMR study; one early and one later in the discharge process, where the specific capacities were limited to either 100 mAh/g (D_{100}) or 750 mAh/g (D_{750}).

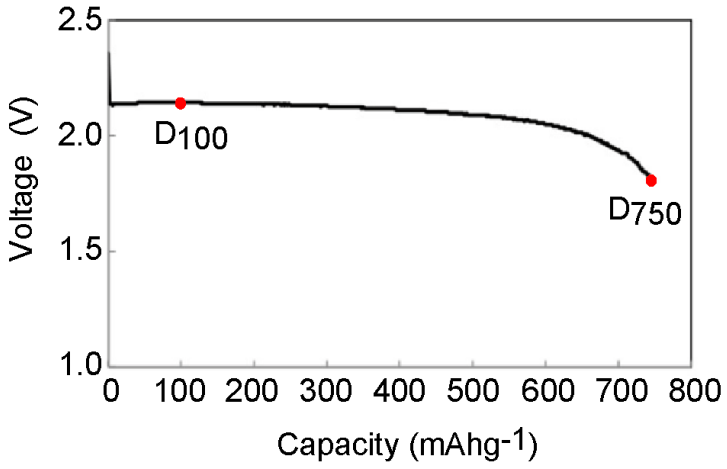

Figure 7-1Representative Electrochemical discharge profile of the first discharge for a Na-O_2 cell with a 0.5 M electrolyte solution of sodium triflate in diethylene glycol dimethyl ether, specifying the specific capacities D_{100} and D_{750} that correspond to the two extracted cells

The conducting salt sodium triflate, has five crystallographic Na sites with a population ratio of 1:1:1:1: 0.5 for Na1 : Na2 : Na3 : Na4 : Na5.[5] This accounts for the complex ^{23}Na NMR spectrum of sodium triflate shown in **Figure 7-2**. When the spectra of Na_2CO_3 and sodium triflate are compared (**Figure 7-2**), it becomes evident that the sodium triflate and $Na_{(carb\ 3)}$ resonances overlap. Additionally a minor amount of NaF is present in the sodium triflate sample. It has previously been suggested that NaF may be generated from sodium triflate.[6] To better understand the source of the NaF in the cell, the reactivity of the sodium oxide species with the carbon electrode, in the absence of the electrolyte was further studied in section 7.3.4. Future studies will focus on alternative electrolyte systems with simpler and more stable conducting salts. Nevertheless it was possible to analysis the 1D and 2D ^{23}Na NMR spectra of the cycled cathodes (**Figures 7-3** and **7-4**), as significant amounts of sodium triflate were not present.

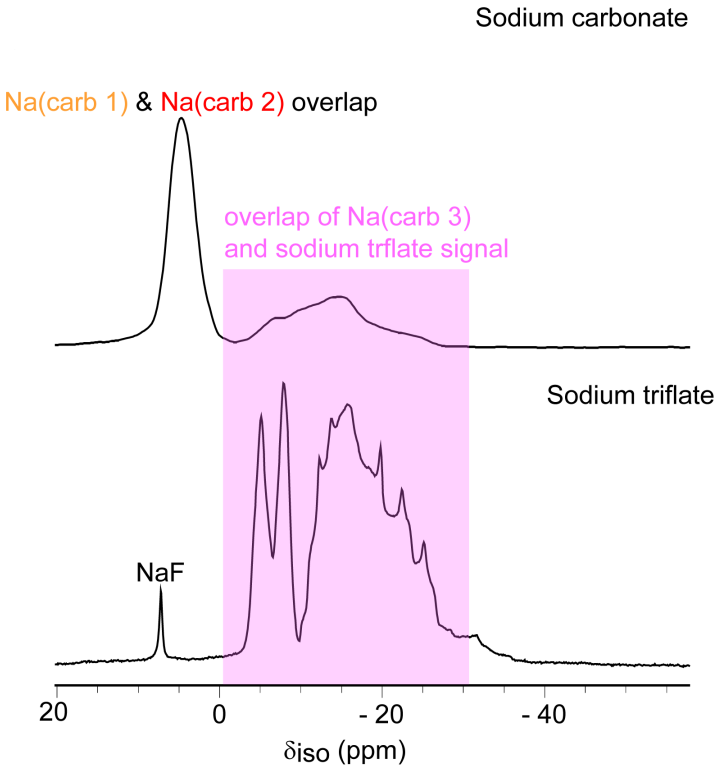

Figure 7-2 Comparison of the sodium carbonate and sodium triflate ^{23}Na MAS NMR spectra collected at 11.7 T with a MAS rate of 20 kHz, highlighting the overlap between the sodium triflate and sodium carbonate ($Na_{(carb\ 3)}$) NMR signals, where sodium triflate has five unique crystallographic sites.[5]

7.3.2 ^{23}Na NMR of Cycled Electrodes

The resonances observed in the ^{23}Na NMR spectra of the cycled electrodes (**Figure 7-3**) are labelled in accordance with the notation outlined in Chapter 6 (**Table 6-1**), were the spectroscopic properties of the expected Na-O_2 reaction products (Na_2O_2, NaO_2 and Na_2CO_3) were examined in detail. **Figure 7-3** illustrates that there is no signal in the sodium superoxide ($Na_{(sup-1)}$) region at –23 ppm, for either discharge capacity. This signifies that NaO_2 is not produced in an appreciable quantity, or, more likely, that NaO_2

is unstable and has been consumed by subsequent reactions. The absence of NaO_2 was confirmed with T_1 filtering experiments, where no evidence of the NaO_2 species was detected, even with many scans at short recycle delays (conditions which enhance the NaO_2 signal while suppressing those of the other species). Rather, one of the sodium peroxide resonances, ($Na_{(per-1)}$) and one of the sodium carbonate resonances, ($Na_{(carb-3)}$) are resolved in the 1D NMR spectrum of D_{100} and D_{750}. The remaining Na_2O_2 and Na_2CO_3 sites ($Na_{(per\ 2)}$, $Na_{(carb\ 1)}$ and $Na_{(carb\ 2)}$) overlap in **Figure 7-3**.

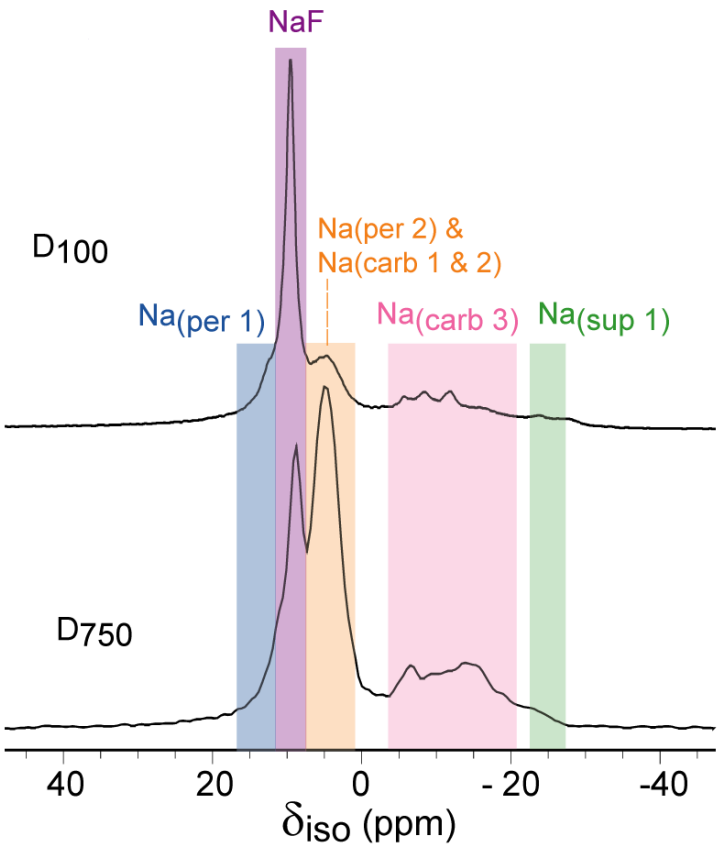

Figure 7-3 1D ^{23}Na NMR spectra of cycled electrodes collected at an MAS frequency of 20 kHz at 11.7 T, labeled in accordance with Table 6-1

Spectral overlap in the multi-component electrochemical samples can be rectified through the application of 2D ^{23}Na-3QMAS spectroscopy. The 2D ^{23}Na-3QMAS spectrum of D_{750} (**Figure 7-4)** shows clear resolution of five crystallographic Na sites corresponding to Na_2O_2 ($Na_{(per\ 1)}$, $Na_{(per\ 2)}$) and Na_2CO_3 ($Na_{(carb\ 1)}$, $Na_{(carb\ 2)}$, $Na_{(carb\ 3)}$). The 2D 3QMAS spectrum demonstrates that we will be able to successfully separate and identify the electrochemical reaction products in future studies, and track their presence and quantity as we iterate cell designs.

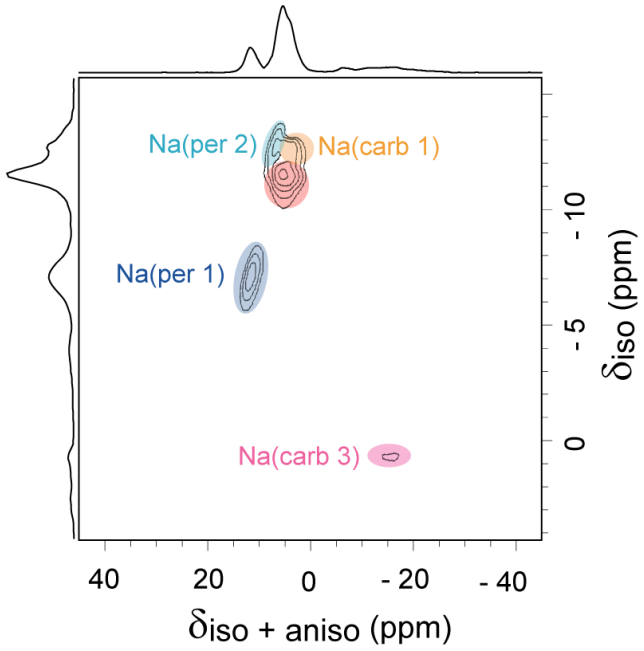

Figure 7-4 2D ^{23}Na-3QMAS NMR spectrum of the D_{750} extracted cathode at 11.7 T under 20 kHz MAS

An unanticipated species, which we have identified as NaF, is observed at 9 ppm in the 1D ^{23}Na NMR spectra of the cycled electrodes (**Figure 7-3**). The unexpected phase is assigned to NaF owing to the similarity of its ^{23}Na chemical shift to that of pristine NaF

(7.4 ppm). Additionally the NaF assignment is supported by filtering out of this new signal in the 3QMAS experiment, as would only be expected for a very high symmetry Na environment such as the cubic salt NaF.[7] The process involved in identifying the new degradation species is further discussed in the next section.

7.3.3 ^{23}Na NMR of Potential Na-O_2 Degradation Species

The unexpected appearance of the new degradation species indicates that the electrochemical reaction products include a material that is distinct from the pristine phases analyzed in Chapter 6. The origin of the new sodium-containing breakdown species is hypothesized to result from a secondary reaction between the electrochemical products (NaO_2, Na_2O_2 or the superoxide radical) and the cell components (i.e. carbon support and electrolyte).

In order to assign the new breakdown species, a wide range of oxygen- and carbon-containing sodium salts were investigated. The experimental ^{23}Na NMR spectra of the potential degradation products are provided in **Figure 7-5**, while the ^{23}Na NMR parameters (determined via lineshape simulation with TopSpin 3.2 software) are reported in **Table 7-1**.

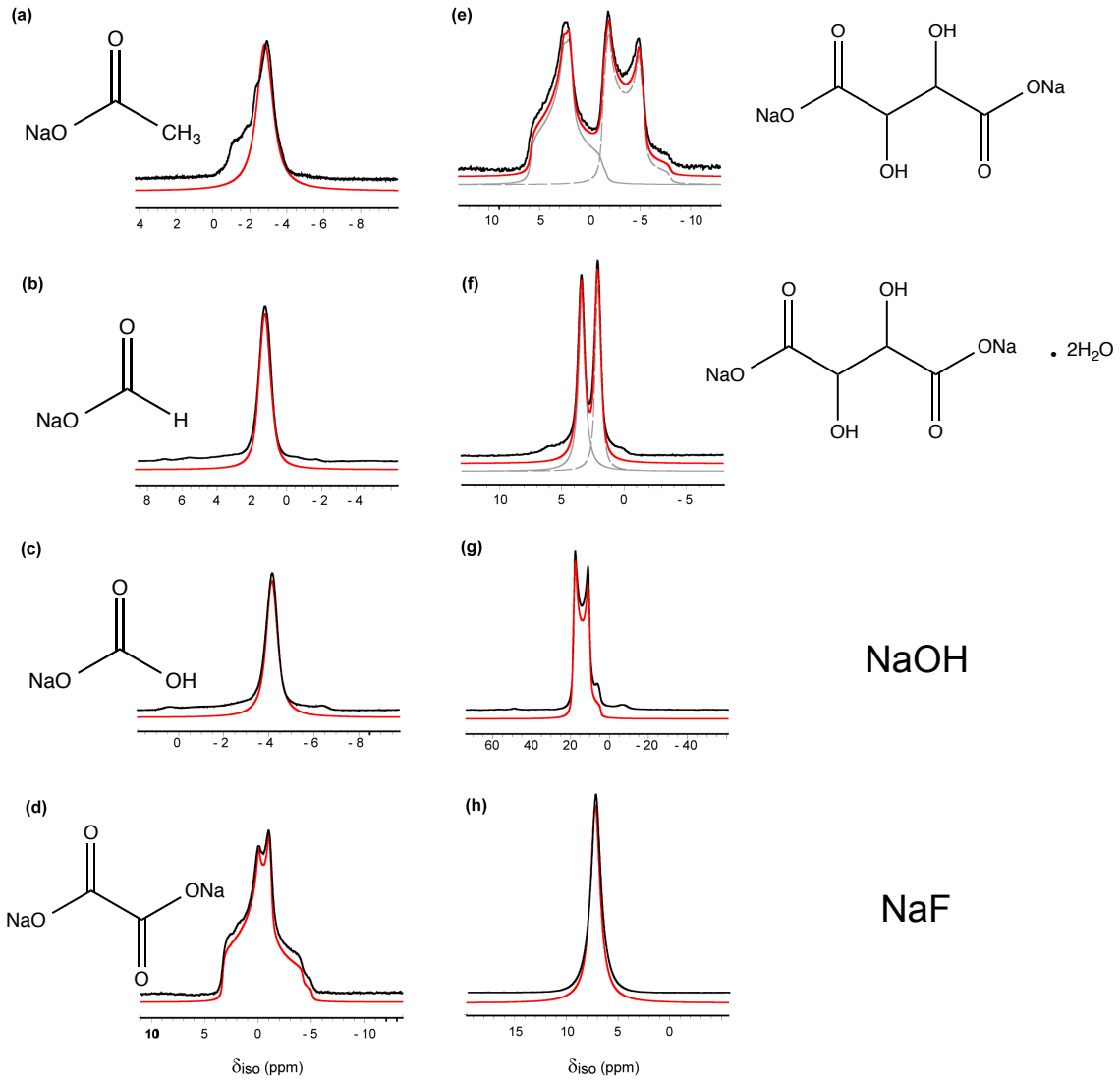

Figure 7-5 ^{23}Na MAS NMR spectral library of potential Na-O_2 degeneration products with the molecular structures, comparing the experimental spectra (black) and simulated best fits (red) collected at MAS rate of 30 kHz at a 19.9 T magnetic field of (a) sodium acetate, (b) sodium formate, (c) sodium bicarbonate, (d) sodium oxalate, (e) dehydrated sodium tartrate, (f) sodium tartrate dihydrate, (g) sodium hydroxide and (h) sodium fluoride

Table 7-1 Experimental ^{23}Na NMR Parameters of Potential Na-O_2 Degradation Species

Compound	δ_{iso} (ppm)	C_q (MHz) ± 0.05	η_q ± 0.05
Sodium acetate	-2.5	0.70	1
Sodium formate	1.6	0.85	0.75
Sodium bicarbonate	-4.0	0.60	1.00
Sodium oxalate	3.0	2.49	0.76
dehydrated Sodium tartrate (Na1)	7.9	2.34	0.85
dehydrated Sodium tartrate (Na2)	1.5	2.46	0.15
Sodium tartrate dihydrate (Na1)	3.4	0.71	0.5
Sodium tartrate dihydrate (Na2)	2.3	0.22	1
Sodium hydroxide	20.5	3.60	0.15
Sodium fluoride	7.4	0	0

As discussed in Chapter 2, for half-integer quadrupolar nuclei when the $C_q >> \gamma B_1$ field, the nutation frequency is compressed by a factor of I + ½. The experimental implication is that the maximum signal intensity is obtained by dividing the 90^0 pulse length (which is typically calibrated on a solution standard) by I + ½. For a I = 3/2 spin system such as ^{23}Na, the maximum signal intensity then corresponds to a nominal 45^0 pulse, when the sodium material contains a non-zero quadrupole moment. If the material's quadrupole moment is zero, than the maximum signal intensity is obtained with a 90^0 pulse. This is a simple and effective approach to screen for the presence of a C_q.

The pulse response of the potential degradation products was reported in **Table 7-2,** where two pulse lengths were tested; a 45^0 pulse and 90^0 pulse. The applied flip angles were calibrated on a 1M NaCl solution. **Table 7-2** confirmed that NaF has C_q of 0 MHz, which is intriguing as the new degradation species also has a C_q of 0 MHz.

Table 7-2 Pulse Response of the Potential Na-O_2 Degradation Species

Compound	Pulse Length which Produced Maximum Signal
Sodium acetate	45^0
Sodium formate	45^0
Sodium bicarbonate	45^0
Sodium oxalate	45^0
dehydrated Sodium tartrate (Na1)	45^0
dehydrated Sodium tartrate (Na2)	45^0
Sodium tartrate dihydrate (Na1)	45^0
Sodium tartrate dihydrate (Na2)	45^0
Sodium hydroxide	45^0
Sodium fluoride	90^0

After reviewing the NMR parameters for the potential Na-O_2 degradation products, NaF was found to best match the spectroscopic characteristic associated of the new phase observed in **Figure 7-3**. Thus the new phase is identified as NaF.

7.3.4 ^{23}Na NMR and PXRD Study of NaO_2 / Na_2O_2 Mock Electrodes

To evaluate the stability of the Na-O_2 reaction products, a NaO_2 / Na_2O_2 mixture was created and a portion of the NaO_2 / Na_2O_2 mixture was ground with a carbon electrode (carbon C65 + PVDF), generating a NaO_2 / Na_2O_2 mock electrode. Both the mixture and the mock cathode were stored under inert conditions for approximately a week prior to analysis with ^{23}Na NMR and PXRD.

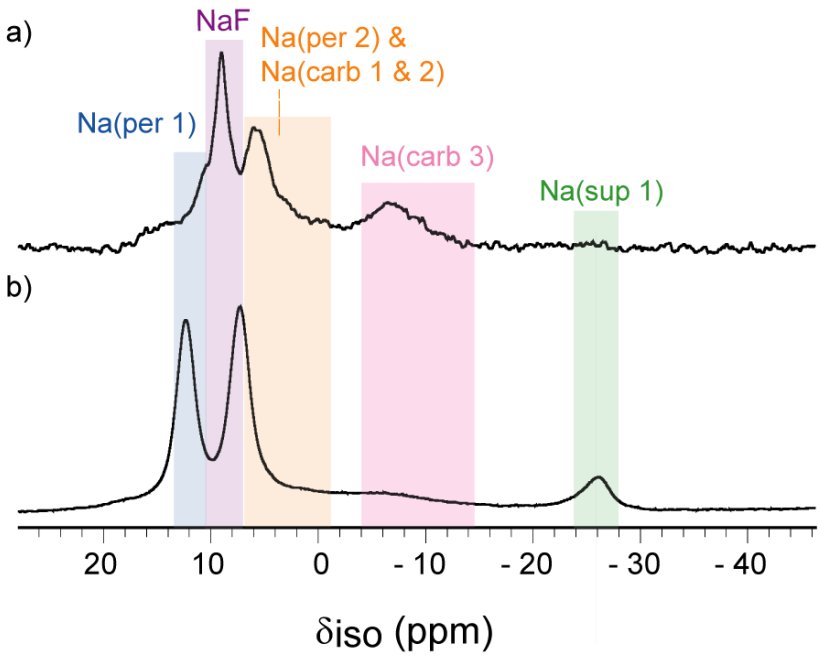

Figure 7-6 1D ^{23}Na NMR spectra of (a) a mock cathode where Na_2O_2 and NaO_2 were ground with a carbon + PVDF electrode, (b) a Na_2O_2 and NaO_2 mixture. NMR spectra were collected at 19.9 T under 30 kHz MAS

The ^{23}Na NMR spectrum of the aged mock cathode **Figure 7-6a**, reveals that Na_2CO_3 ($Na_{(carb\ 3)}$) and NaF are produced, while all of the NaO_2 ($Na_{(sup\ 1)}$) and nearly all of the Na_2O_2 ($Na_{(per\ 1)}$, $Na_{(per\ 2)}$) are gone. Na_2CO_3 and NaF formation is confirmed with powder X-ray diffraction in **Figure 7-7**. We also note that **Figure 7-6b** shows no sign of a reaction between sodium peroxide and sodium superoxide as ($Na_{(per\text{-}1)}$, $Na_{(per\text{-}2)}$ and $Na_{(sup\text{-}1)}$ remain the dominant resonances, with no visible change in intensity or position. This indicates that peroxide and superoxide phases are compatible with each other but that the sodium oxide phases are not stable in presence with the carbon electrode.

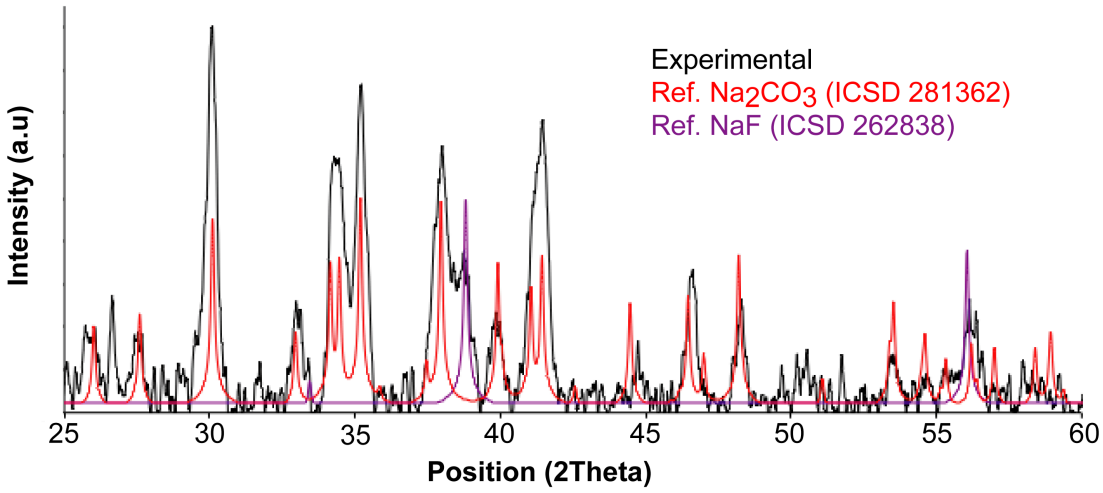

Figure 7-7 Experimental PXRD diffraction pattern of the mock cathode (black) overlaid with the reference PXRD patterns for Na_2CO_3 (red) and NaF (purple) which was collected under inert conditions

Figures 7-6 and **7-7** demonstrate that NaF and Na_2CO_3 are generated from a reaction between Na_2O_2, NaO_2 and the electrode itself. Interestingly, Na_2CO_3 was created in this electrolyte-free reaction, indicating that the carbonate source in the electrochemical cells need not be the organic electrolyte, as traditionally assumed,[8-9] but may in fact be the conductive carbon support itself.[8-9] It was unexpected that the NaO_2 would react with the electrode in this case, as the stability of NaO_2 is generally accepted as being greater than that of LiO_2[4, 8, 10-11] with pure NaO_2 reported as the Na-O_2 discharge product.[4] However, the greater stability of NaO_2 is in fact called into question by the present results.

7.3.5 Summary of Observed Na-O_2 Degradation Reactions

The degradation products; NaF and Na_2CO_3, are found to originate from the breakdown of the carbon electrode by the electrochemical Na-O_2 discharge products. Reactions between electrochemical components and the carbon support are not unprecedented in M-O_2 systems.[12] Analogous reactions are observed in the Li-O_2 literature, where Li_2O_2 reacts with the carbon electrode producing Li_2CO_3[13-14] and the superoxide species attacks the PVDF binder producing LiF.[12] Based on our initial mock cathode investigation, it is unclear as to which species degrades what electrode component. Thus the reactivity of Na_2O_2 and NaO_2 in the presence of the carbon electrode were individually explored.

The Na_2O_2 reactivity was investigated by grinding Na_2O_2 with a carbon electrode under inert conditions. The Na_2O_2 mock cathode then rested in an argon glovebox for approximately a week prior to analysis. The ^{23}Na NMR spectrum of the aged Na_2O_2 mock cathode (**Figure 7-8**), does not display any evidence of NaF or Na_2CO_3. Instead Na_2O_2 (Na(per 1) and Na(per 2)) is observed to be the main components, suggesting that Na_2O_2 displays minimal reactivity towards the carbon electrode. This is consistent with observations from the NMR spectra of the cycled electrodes (**Figure 7-3**), where Na_2O_2 was observed at both discharge capacities. Thus it is hypothesized that NaO_2 is responsible for the electrode breakdown reactions.

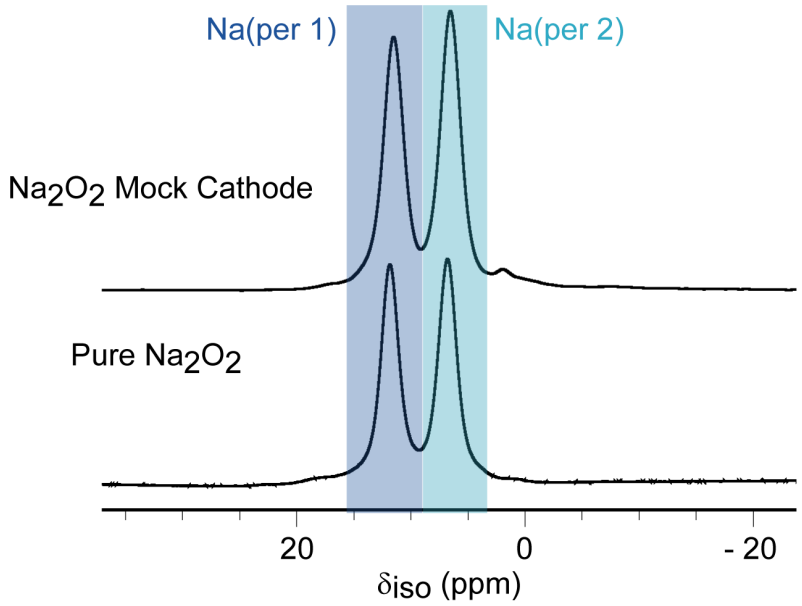

Figure 7-8 ^{23}Na NMR spectra of the Na_2O_2 mock cathode (upper) and pure Na_2O_2 (lower) illustrating that NaF and Na_2CO_3 are not produced when Na_2O_2 is ground with a carbon C65 + PVDF electrode, where the spectra were collected at magnetic field of 19.9 T and at a MAS rate of 30 kHz

The reactivity of NaO_2 with the cell components was also explored, as part of the future work for this project. In the NaO_2 reactivity study three mixtures were fabricated under inert conditions; NaO_2 + C65 carbon black, NaO_2 + PVDF and NaO_2 + carbon PVDF electrode. Using ^{23}Na and ^{19}F NMR, NaF was observed when NaO_2 was combined with both pure PVDF and the carbon electrode, whereas Na_2CO_3 was observed in all three mixtures. The NaO_2 reactivity with the electrode materials is summarized in the schematic diagram provided in **Figure 7-9**.

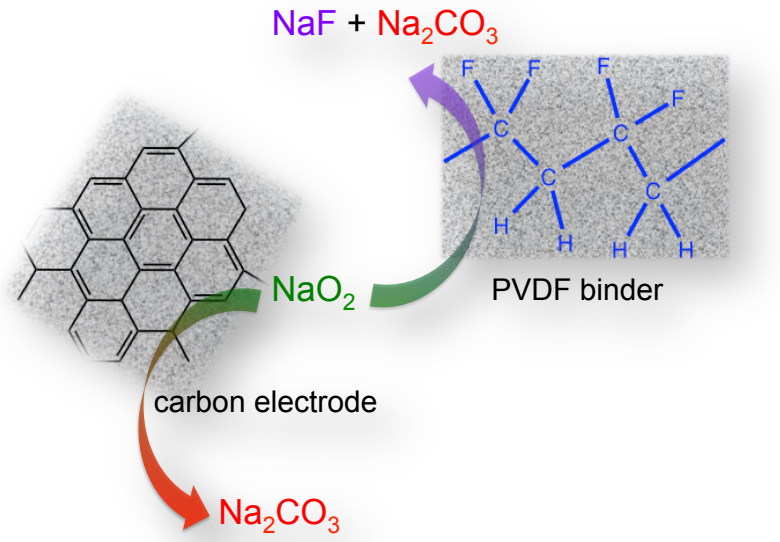

Figure 7-9 Schematic diagram illustrating the degradation of the carbon PVDF electrode by NaO_2

7.5 Conclusion

In conclusion, we have shown that ^{23}Na ssNMR is a sensitive probe for unveiling the complex Na-O_2 electrochemistry. With 1D and 2D ^{23}Na NMR of Na-O_2 electrodes, the expected reaction products Na_2O_2 and Na_2CO_3 are observed in addition to an unanticipated phase, NaF. Both NaF and Na_2CO_3 are observed to result from parasitic reactions involving the carbon electrode and a Na_2O_2 / NaO_2 mixture. This demonstrates the reactivity of the Na-O_2 reaction products with the cell components and highlights that Na_2CO_3 may be produced from alternative process other than degradation of the organic electrolyte.

7.6 References

[1] H. Yadegari;Y. Li;M. N. Banis;X. Li;B. Wang;Q. Sun;R. Li;T.-K. Sham;X. Cui;X. Sun, *Energy Environ. Sci.* **2014**, *7*, 3747.

[2] A. Medek;J. S. Harwood;L. Frydman, *J. Am. Chem. Soc.* **1995**, *117*, 12779.

[3] L. Frydman;J. S. Harwood, *J. Am. Chem. Soc.* **1995**, *117*, 5367.

[4] P. Hartmann;C. L. Bender;M. Vračar;A. K. Dürr;A. Garsuch;J. Janek;P. Adelhelm, *Nat. Mater.* **2013**, *12*, 228.

[5] N. Sofina;E. M. Peters;M. Jansen, *Z. Anorg. Allg. Chem.* **2003**, *629*, 1431.

[6] P. Hartmann;C. L. Bender;J. Sann;A. K. Durr;M. Jansen;J. Janek;P. Adelhelm, *Phys. Chem. Chem. Phys.* **2013**, *15*, 11661.

[7] P. J. Dirken;J. B. H. Jansen;R. D. Schuiling, *Am. Mineral.* **1992**, *77*, 718.

[8] B. D. McCloskey;J. M. Garcia;A. C. Luntz, *J. Phys. Chem. Lett.* **2014**, *5*, 1230.

[9] B. D. McCloskey;A. Valery;A. C. Luntz;S. R. Gowda;G. M. Wallraff;J. M. Garcia;T. Mori;L. E. Krupp, *J. Phys. Chem. Lett.* **2013**, *4*, 2989.

[10] S. Kang;Y. Mo;S. P. Ong;G. Ceder, *Nano letters* **2014**, *14*, 1016.

[11] B. Lee;D.-H. Seo;H.-D. Lim;I. Park;K.-Y. Park;J. Kim;K. Kang, *Chem. Mater.* **2014**, *26*, 1048.

[12] R. Black;S. H. Oh;J.-H. Lee;T. Yim;B. Adams;L. F. Nazar, *J. Am. Chem. Soc.* **2012**, *134*, 2902.

[13] M. Leskes;A. J. Moore;G. R. Goward;C. P. Grey, *J. Phys. Chem. C* **2013**, *117*, 26929.

[14] M. M. Ottakam Thotiyl;S. A. Freunberger;Z. Peng;P. G. Bruce, *J. Am. Chem. Soc.* **2013**, *135*, 494.

Chapter 8 : Concluding Remarks and Outlook

8.1 Summary

This thesis describes the use of multinuclear solid-state NMR to investigate alkali metal-oxygen batteries. The Li-O_2 and Na-O_2 cells have extremely large theoretical energy densities, making the metal-oxygen battery technology a competitive energy storage device for electric vehicles.[1-2] In order for Li-O_2 and Na-O_2 cells to become commercially feasible, a fundamental understanding of the electrochemistry is required for both systems.[3]

This thesis sought to evaluate the stability of Li-O_2 electrolytes and explore the viability of using solid-state ^{23}Na NMR to correlate the cycling conditions to the electrochemical Na-O_2 reaction products. NMR spectroscopy of cycled M-O_2 electrodes is non-trivial to acquire due to small sample sizes and the air sensitive nature of the cycled materials. The Li-O_2 battery system has the additional challenge that, direct 1D ^{6,7}Li NMR is not informative[4-6] because diamagnetic lithium materials have a small ^{6,7}Li chemical shift range of $\pm$ 5 ppm.[4] Alternative approaches such as ^{7}Li nutation spectroscopy[7] and ^{17}O NMR[8-9] were employed to characterize the Li-O_2 reaction products.^{17}O NMR is a highly sensitive probe of the Li-O_2 system.[8-9] However ^{17}O is a challenging NMR nucleus due to the extremely low natural abundance (0.04 %) and the low Larmor frequency. To overcome these sensitivity issues ^{17}O-enrichment and signal enhancement techniques were applied. The following section describes the key findings from each chapter and suggestions for future work are proposed in section 8.3.

8.2 Summary of Key Findings from Each Chapter

Chapters 3 and 4 describe the multinuclear NMR investigation of TMP, where the suitability of TMP as potential Li-O_2 electrolyte was explored. The cyclic voltammetry experiment and electrochemical cycling studies suggested that TMP would be a stable electrolyte solvent. The reaction products are carefully characterized with ^{7}Li nutation spectroscopy and direct 1D ^{1}H, ^{7}Li, ^{17}O and ^{31}P NMR of cycled electrodes.

Chapter 3 discusses the use of ^{7}Li nutation spectroscopy to identify the reaction product formed in the TMP electrolyte. Before ^{7}Li nutation spectroscopy was applied to the unknown electrochemical system, it was first demonstrated that the pristine phases (Li_2O_2 and Li_2CO_3) are differentiated through a comparison of their pseudo ^{7}Li nutation frequencies. The pseudo ^{7}Li nutation frequencies of pristine Li_2O_2 (33 kHz) and pristine Li_2CO_3 (40 kHz) were found to be distinct, thus confirming the diagnostic power of nutation spectroscopy.

The next step in this method development study was to confirm that electrochemically generated Li_2O_2 can be separated from Li_2CO_3 via the pseudo ^{7}Li nutation frequencies. The Li-O_2 electrolyte systems selected were PC/DMC and TEGDME. Li_2CO_3 is the main product in the PC/DMC in the electrolyte[10] whereas both Li_2O_2 and Li_2CO_3 are produced in TEGDME cells[11]. The pseudo nutation frequency of the PC/DMC cathode (41 kHz) was almost identical to that of pristine Li_2CO_3 (40 kHz). This confirmed that Li_2CO_3 is the main product in the PC/DMC electrode. The pseudo ^{7}Li nutation frequency of the TEGDME cathode (38 kHz) was an intermediate value between pristine Li_2O_2 (33 kHz) and pristine Li_2CO_3 (40 kHz). It was concluded that both Li_2O_2 and Li_2CO_3 were present.

The pseudo ^{7}Li nutation frequency of the TMP cathode was found to be 45 kHz. Because of the fast pseudo nutation frequency it is unlikely that Li_2O_2 was produced in the TMP cathode. Thus indicating that TMP is an unsuitable Li-O_2 electrolyte. This was confirmed with ^{17}O NMR of a cycled electrode.

^{7}Li nutation spectroscopy was shown to be an effective method for distinguishing lithium materials that have similar ^{7}Li chemical shifts but distinct ^{7}Li quadrupole coupling constants. This technique was demonstrated to be a diagnostic tool for determining the Li-O_2 reaction products without the need for isotropic enrichment.

In Chapter 4 ^{1}H, ^{7}Li, ^{17}O and ^{31}P solid-state NMR spectroscopy provided a complete description of the electrochemical reactions that occurred with the TMP electrolyte. Based on the NMR spectra of the cycled electrodes the main discharge products were determined to be; Li_2CO_3, CH_3CO_2Li, LiOMe and the TMP derivate species ($^{-}$OP=O$(OMe)_2$). A decomposition mechanism for TMP was developed that accounts for the formation of the observed discharge species.

From the ^{31}P NMR spectra of the uncycled and cycled electrodes, it was concluded that the central phosphorus atom of TMP was not affected during discharge. Instead the methoxy group was determined to be the most probable site of attack by the superoxide. Accordingly, the TMP decomposition was predicted to begin from a proton abstraction (from the methoxy group) and ultimately produce a lithium formate intermediate. The lithium formate is predicted to further react with either peroxide ions producing Li_2CO_3 or with another intermediate species (from the proton abstraction step) resulting in lithium acetate and the TMP derivate.

Despite the promising electrochemistry TMP was shown to be an unsuitable Li-O_2 electrolyte with multinuclear ssNMR. The studies outlined in Chapters 3 and 4 highlight the importance of careful characterization in electrolyte stability studies. Future investigations of new materials, for metal-oxygen batteries are expected to include analysis by multinuclear ssNMR.

Chapter 5 describes a detailed ^{1}H and ^{17}O NMR study of the TEGDME electrolyte. The ^{17}O NMR spectrum of a discharged TEGDME electrode, shown in Chapter 4, revealed evidence of Li_2O_2, Li_2CO_3 and potentially other breakdown species. Under static conditions at 11.7 T it is not possible to identify all of the reaction products. Spectral resolution was achieved in Chapter 5 when the ^{17}O NMR spectra were collected at an ultrahigh magnetic field with ultrafast MAS. Through a combination of ^{1}H and ^{17}O NMR the reaction products produced over the first and second discharge, were observed to be; Li_2O_2, LiOH, CH_3CO_2Li and Li_2CO_3.

^{17}O NMR spectra of the cycled electrodes illustrated that the quasi stability of TEGDME. Li_2O_2 demonstrated reversible formation. However, less Li_2O_2 was observed at $2D_{1000}$ compared to D_{1000}. During the charging process Li_2CO_3 and CH_3CO_2Li only partially decomposed, suggesting that the breakdown products will accumulate over extended cycling. Overall the NMR investigation highlighted that TEGDME is not an ideal electrolyte for long-term cycling.

To the best of our knowledge, this thesis is the first time that ^{23}Na NMR spectroscopy is applied to investigate the Na-O_2 battery chemistry. Prior to this work, it was unclear as to whether ^{23}Na NMR would be informative, given how insensitive $^{6,7}Li$

NMR is for the Li-O_2 system.[5-6] Prior to examining cycled Na-O_2 cells, it was first established that the pristine phases themselves were differentiated with solid-state ^{23}Na NMR. Chapter 6 describes the initial NMR study of the expected pristine materials and Chapter 7 outlines the ^{23}Na NMR investigation of electrochemically-cycled electrodes.

In chapter 6 a variety of NMR methods are applied including; direct 1D, 2D ^{23}Na-3QMAS[12-13], VT NMR and T_1 filtering experiments, as the materials of interest differ in their electronic configurations and local symmetry. With these ssNMR techniques, the expected Na-O_2 electrochemical products are readily differentiated. This is especially true for sodium superoxide and sodium peroxide. Theses materials have distinct ^{23}Na chemical shifts and T_1 relaxation properties. Not only does the paramagnetic NaO_2 displays rapid T_1 relaxation, the ^{23}Na NMR resonance also displays a temperature dependence, providing another spectroscopic handle for detecting NaO_2 in electrochemical cells.

The diamagnetic materials (Na_2O_2 and Na_2CO_3) both contain multiple Na sites and are strongly influenced by the quadrupole interaction. When combined, the Na resonances overlapped in the 1D NMR spectrum. The spectral overlap is rectified with 2D ^{23}Na-3QMAS[12-13], providing spectral resolution of all five sites. Given the rapid acquisition times associated with collecting the ^{23}Na NMR spectra of the pristine phases, ^{23}Na NMR was expected to elucidate the Na-O_2 electrochemistry.

In Chapter 7 the desired product, Na_2O_2, and the expected breakdown species, Na_2CO_3, were detected in the 1D ^{23}Na NMR spectra. Additionally, NaF was unequivocally observed in the cathode NMR spectra. This is unlike a previous study where the NaF was difficult to definitively measure due to low resolution in the F XPS

data, where the NaF signal may have originated from decomposition of the sample in the presence of the X-ray beam.[14] With 2D ^{23}Na-3QMAS of the D_{750} cathode, good site resolution was obtained, allowing the Na_2O_2 ($Na_{(per\ 1)}$ and $Na_{(per\ 2)}$) sites and Na_2CO_3 ($Na_{(carb\ 1)}$, $Na_{(carb\ 2)}$ and $Na_{(carb\ 3)}$) sites to be well resolved. Moreover, NaF was not observed in the 2D ^{23}Na-3QMAS spectrum of the cycled electrode. This further supports the assignment of NaF as the new electrochemical phase. The Na site in NaF has cubic symmetry[15] and therefore is not expected to be observed via the 3Q filter.

The absence of NaO_2 in the 1D cathode NMR spectra suggests that sodium superoxide was either not electrochemically produced or that it further reacted with the cell components, prior to the NMR measurement. This led to questions about the relative stability of the sodium oxides specie with the battery materials. ^{23}Na NMR and PXRD demonstrated that NaO_2 and Na_2O_2 are unstable in in the presence of the carbon electrode (carbon C65 + PVDF). In the absence of the electrolyte, NaO_2 and Na_2O_2 degrade the carbon electrode resulting in NaF and Na_2CO_3. The brings into question the stability of the NaO_2 and the claims that Na-O_2 cells operate as cleaner devices wither fewer side reactions.[14, 16-19]

The findings presented in Chapters 6 and 7 demonstrate that ^{23}Na NMR spectroscopy is a powerful technique, which is well suited to characterize the Na-O_2 electrochemistry. Furthermore, the ^{23}Na NMR investigation of the cycled cathodes illustrates that alternative electrode materials need to be considered. Suggestions for furthers studies are provided in the following section.

8.3 Future Studies

Despite the extensive study of the Li-O_2 batteries over the past decade, practical Li-O_2 cells are still plagued with many fundamental challenges such as the limited cycle life[20] and a high charge overpotential[21]. Comparatively, research on the Na-O_2 battery chemistry is still in its infancy.[2] Chapters 6 and 7 demonstrate that ^{23}Na NMR is a sensitive characterization tool, for analysing the electrochemical species. Thus the future work suggested by the thesis will focus primary on expanding the use ssNMR to study the Na-O_2 battery, while simultaneously working to improve electrochemical performance.

A key finding from Chapter 7 was the unexpected instability of the NaO_2 in the presence of electrode (Super C65 carbon black + PVDF binder). This suggests that new electrode materials need to be explored, and the possibility of moving to a binder-free electrode should be considered. As part of the on going work within the Goward Group, the reactivity of NaO_2 with disorder carbons is currently being explored with ^{23}Na NMR by Chris Franko, in collaboration with Dr. Andy Sun at Western University. Future studies will continue to investigate the reactivity of NaO_2 and Na_2O_2 with different types of carbon. Additionally the stability of different binders will also be examined with ^{1}H, ^{19}F and ^{23}Na NMR. In combination to the stability tests, the electrochemical performance of the new electrode compositions will be examined using electrochemical techniques such as cyclic voltammetry.

Given that the popular ether-based electrolytes are also susceptible to degradation in Na-O_2 cells[22], alternative electrolytes need to be invested. Future studies will focus on evaluating both the electrochemical and chemical stability. The fate of the electrolyte materials will be monitored with ^{1}H, ^{17}O ^{19}F and ^{23}Na NMR. The electrolyte solvents

selected for future studies will have a high donor number (measure of Lewis basicity). As higher donor number solvents are thought to better solvate the superoxide radical,[23] leading to higher cell capacities with few side reactions.

Additionally the role of H_2O and other weak acids, which act as proton phase-transfer agents (PPTA), will be explored with ^{1}H, ^{2}H and ^{23}Na. The PPTA is proposed to facilitate the formation and oxidation of NaO_2 in solution.[24] The exact nature of the reaction products, the reversibility of this electrochemistry and the long-term stability of the PPTA are unclear. With the aim of understanding the influence of PPTA, first anhydrous electrolyte will be investigated with ^{1}H and ^{23}Na NMR, before the electrolyte is spiked with a weak acid. By using deuterated weak acids (i.e. D_2O), it becomes possible to easily monitor the fate of the weak acid with ^{2}H NMR. ^{1}H-^{23}Na and ^{2}H-^{23}Na correlation studies are expected to provide valuable insight into the chemistry involving PPTA.

Lastly, the use of alternative conducting salts should be considered. Sodium triflate (the conducting salt used in Chapter 7) is believed to decompose to NaF over extended cycling.[14] Moreover, sodium trifltate has a very complex ^{23}Na NMR spectrum (from the multiple Na sites[25]), which overlaps with the ^{23}Na NMR spectrum of Na_2CO_3. This makes it challenging to interpret the cathode spectra if a significant amount of sodium triflate and sodium carbonate are present. In future studies, conducting salts that display increased stability and have a simpler chemical structure, will be used. The stability of the conducting salts may be monitored through ^{1}H, ^{19}F and ^{23}Na NMR.

8.4 Concluding Remarks

Solid-state multinuclear NMR is expected to continue being a valuable tool for characterizing the Li-O_2 and Na-O_2 batteries. This thesis focused on expanding the number of ssNMR techniques available for studying metal-oxygen systems, explored the Li-O_2 electrolyte stability and investigated the Na-O_2 electrode stability. This information is expected to aid in the selection of new materials for Li-O_2 and Na-O_2 cells, which should improve the electrochemical performance of these energy storage devices.

8.5 References

[1] Girishkumar G., McCloskey, B., Luntz, C., Swanson, S. and Wilcke, W. , *J. Phys. Chem. Lett.* **2010**, *1*, 2193.

[2] Yadegari H.;Sun Q.;Sun X., *Adv. Mater.* **2016**, *28*, 7065.

[3] Landa-Medrano I.;Li C.;Ortiz-Vitoriano N.;Ruiz de Larramendi I.;Carrasco J.;Rojo T., *J. Phys. Chem. Lett.* **2016**, *7*, 1161.

[4] Xu Z.;Stebbins J. F., *Solid State Nuclear Magnetic Resonance* **1995**, *5*, 103.

[5] Xiao J.;Hu J.;Wang D.;Hu D.;Xu W.;Graff G. L.;Nie Z.;Liu J.;Zhang J.-G., *J. Power Sources* **2011**, *196*, 5674.

[6] Huff L. A.;Rapp J. L.;Zhu L.;Gewirth A. A., *J. Power Sources* **2013**, *235*, 87.

[7] Reeve Z. E. M.;Goward G. R.;Bain A. D., *Can. J. Chem.* **2015**, 1.

[8] Leskes M.;Moore A. J.;Goward G. R.;Grey C. P., *J. Phys. Chem. C* **2013**, *117*, 26929.

[9] Leskes M.;Drewett N. E.;Hardwick L. J.;Bruce P. G.;Goward G. R.;Grey C. P., *Angew. Chem. Int. Ed.* **2012**, *51*, 8560.

[10] Freunberger S. A.;Chen Y.;Peng Z.;Griffin J. M.;Hardwick L. J.;Barde F.;Novak P.;Bruce P. G., *J. Am. Chem. Soc.* **2011**, *133*, 8040.

[11] Freunberger S. A.;Chen Y.;Drewett N. E.;Hardwick L. J.;Bardé F.;Bruce P. G., *Angew. Chem. Int. Ed.* **2011**, *50*, 8609.

[12] Medek A.;Harwood J. S.;Frydman L., *J. Am. Chem. Soc.* **1995**, *117*, 12779.

[13] Frydman L.;Harwood J. S., *J. Am. Chem. Soc.* **1995**, *117*, 5367.

[14] Hartmann P.;Bender C. L.;Sann J.;Durr A. K.;Jansen M.;Janek J.;Adelhelm P., *Phys. Chem. Chem. Phys.* **2013**, *15*, 11661.

[15] Dirken P. J.;Jansen J. B. H.;Schuiling R. D., *Am. Mineral.* **1992**, *77*, 718.

[16] Hartmann P.;Bender C. L.;Vračar M.;Dürr A. K.;Garsuch A.;Janek J.;Adelhelm P., *Nat. Mater.* **2013**, *12*, 228.

[17] Lee B.;Seo D.-H.;Lim H.-D.;Park I.;Park K.-Y.;Kim J.;Kang K., *Chem. Mater.* **2014**, *26*, 1048.

[18] Kang S.;Mo Y.;Ong S. P.;Ceder G., *Nano Lett.* **2014**, *14*, 1016.

[19] McCloskey B. D.;Garcia J. M.;Luntz A. C., *J. Phys. Chem. Lett.* **2014**, *5*, 1230.

[20] Balaish M.;Kraytsberg A.;Ein-Eli Y., *Phys. Chem. Chem. Phys.* **2014**, *16*, 2801.

[21] Jung H.-G.;Jeong Y. S.;Park J.-B.;Sun Y.-K.;Scrosati B.;Lee Y. J., *Acs Nano* **2013**, *7*, 3532.

[22] Black R.;Shyamsunder A.;Adeli P.;Kundu D.;Murphy G. K.;Nazar L. F., *ChemSusChem* **2016**.

[23] Johnson L.;Li C.;Liu Z.;Chen Y.;Freunberger S. A.;Ashok P. C.;Praveen B. B.;Dholakia K.;Tarascon J.-M.;Bruce P. G., *Nat. Chem.* **2014**, *6*, 1091.

[24] Xia C.;Black R.;Fernandes R.;Adams B.;Nazar L. F., *Nat Chem* **2015**, *7*, 496.

[25] Sofina N.;Peters E. M.;Jansen M., *Z. Anorg. Allg. Chem.* **2003**, *629*, 1431.

Appendix A1: ^{23}Na Simulations of the Relevant Na-O_2 Species

^{23}Na and ^{17}O (A2) Simpson simulations were not performed for NaO_2, as it is a paramagnetic and CASTEP cannot accurately predict chemical shift interactions when the structure includes unpaired electrons.

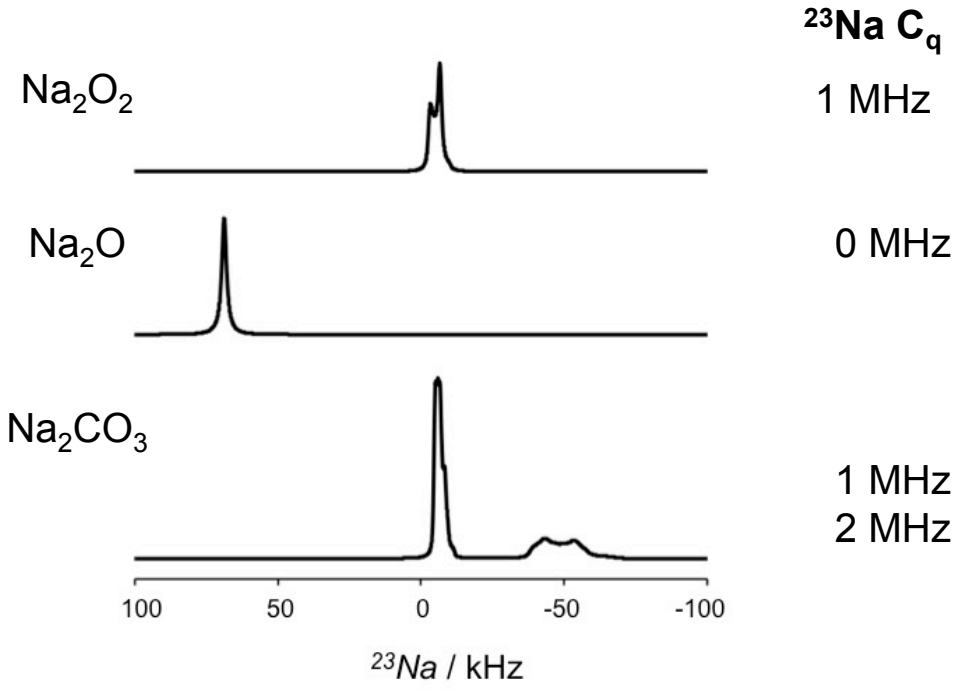

Figure A1.1 Simulations of the ^{23}Na central transition lineshapes of sodium peroxide, sodium oxide and sodium carbonate at 11.7 T under 30 kHz MAS, using the ^{23}Na C_Q calculated by CASTEP, where the calculated values are reported on the right

Appendix A2: ^{17}O Simulations of the Relevant Na-O_2 Species

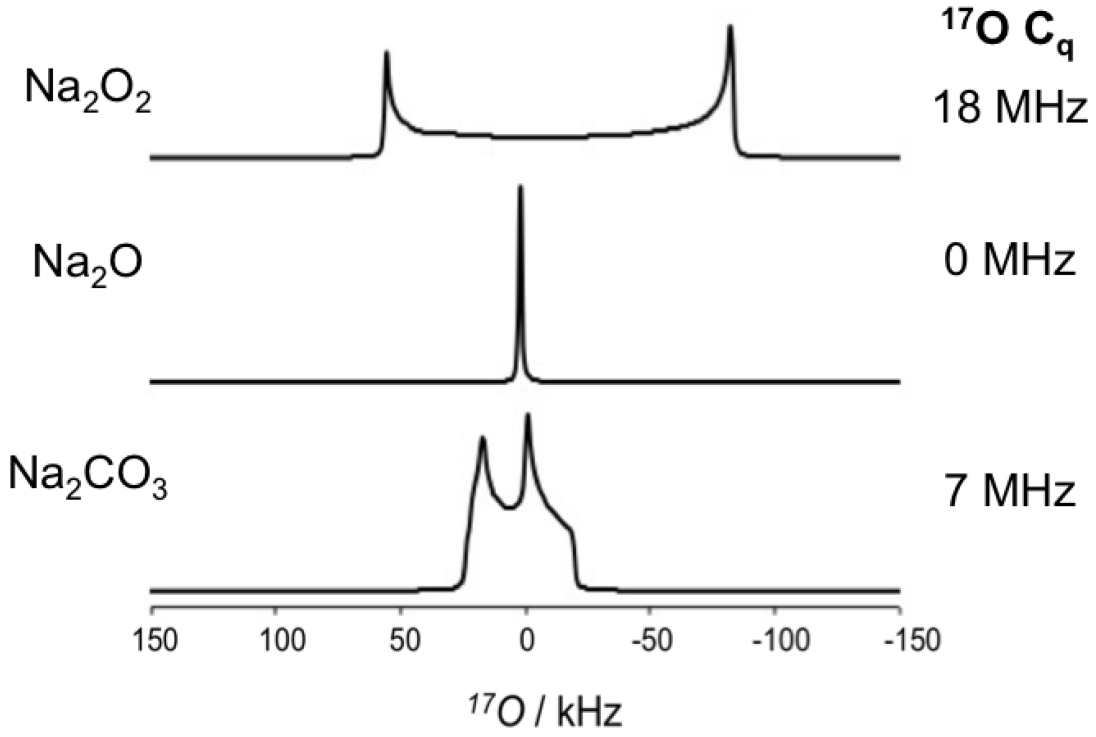

Figure A2.1 Simulations of the ^{17}O central transition lineshapes of sodium peroxide, sodium oxide and sodium carbonate at 19.9 T under 40 kHz MAS, using the ^{17}O C_Q calculated by CASTEP, where the calculated values are reported on the right

Appendix A3: Sample Simpson Input Files

A3.1 Simpson input file modeling the Li_2O_2 lineshape at 21.1 T under 60 kHz MAS

```
spinsys {
  channels     17O
  nuclei       17O
  shift        1 225p -235p 0 0 0 0
  quadrupole   1 2 18.05e6 0 30 0 0
}

par {
  method              gcompute
  gamma_angles        9
  spin_rate           60000
  sw                  spin_rate*gamma_angles
  np                  1024
  proton_frequency    900.0e6
  crystal_file        zcw28656
  start_operator      I1x
  detect_operator     I1c
  verbose             1111
}

proc pulseq {} {
  global par
set dw [expr 1.0e6/$par(sw)]

  reset
acq_block {
  delay $dw
}

}
proc main {} {
  global par
  set f [fsimpson]
  fzerofill $f 16384
  faddlb $f 2500 0
  fft $f
  fsave $f $par(name).spec  -xreim
  funload $f
}
```

A3.2 Simpson input file modeling the Li_2O_2 lineshape under static conditions at 21.1 T

```
spinsys {
  channels     17O
  nuclei       17O
  shift        1 225p -235p 0 0 0 0
  quadrupole   1 2 18.05e6 0 30 0 0
}

par {
  method              direct
  spin_rate           0
  sw                  1e6
  np                  1024
  proton_frequency    900.0e6
  crystal_file        zcw986
  start_operator      I1x
  detect_operator     I1c
  verbose             1111
}

proc pulseq {} {
  global par
set dw [expr 1.0e6/$par(sw)]
  for {set i 1} {$i <= $par(np)} {incr i} {
  acq
  delay $dw
}

}

proc main {} {
  global par
  set f [fsimpson]
  faddlb $f 2500 0
  fft $f
  fsave $f $par(name).spec  -xreim
  funload $f
}
```

Appendix A4: Details of the ^{17}O-Enrichment Gas Line Manifold

All ^{17}O-enrichment was performed utilizing a specially designed gas line manifold. A schematic diagram of the gas line manifold is provided in **Figure A4.1** and a photo of the ^{17}O-enrichment device in use is shown in **Figure A4.2**.

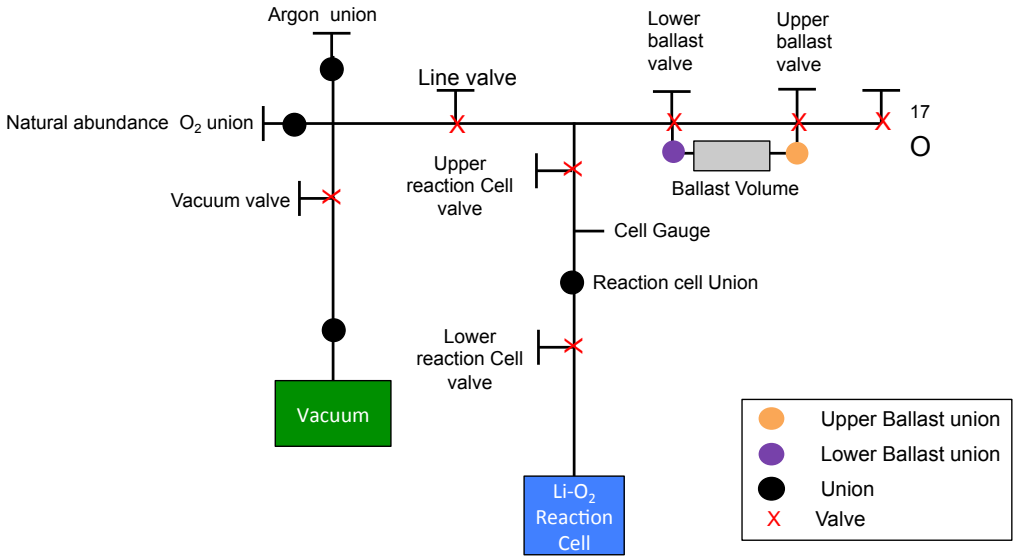

Figure A4.1 Schematic diagram of the ^{17}O-enrichment gas line manifold

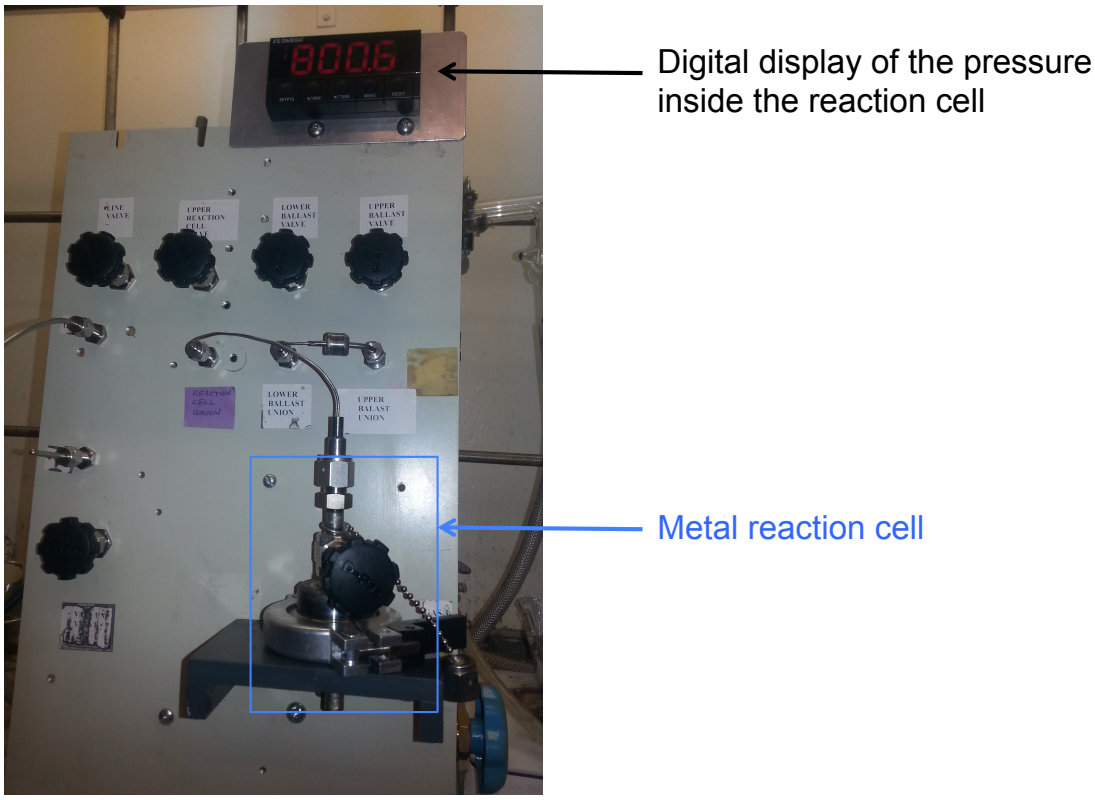

Figure A4.2 Picture of the gas line manifold with a Li-O_2 cell being ^{17}O-eriched prior to electrochemical-cycling

The gas line manifold was designed so that the entire system could be flushed with either argon or natural abundance oxygen gas, before attaching the reaction cell to the manifold. This was done to prevent contaminating the M-O_2 battery with ambient atmosphere. A pressure transducer (purchased from Omega, called the cell gauge in **Figure A4.1**) was included in the manifold's design to monitor the pressure inside the reaction cell during the gas exchange process. The pressure transducer was calibrated in units of mmHg by Zoe Reeve, with the aid of Jim Garrett. Prior to use the gas line manifold was carefully leaked tested. The gas line manifold was designed so that a

minimal volume of ^{17}O-enriched gas would be used in each experiment, while still maintaining an oxygen rich environment for electrochemical reactions to occur under. The SOP for the ^{17}O-enrichment of a Li-O_2 cell is provided in **Appendix A.5**. The same procedure could be used to ^{17}O-enrich a Na-O_2 cell.

Appendix A5: SOP for the ^{17}O-Enrichment of a Li-O_2 Cell

A5.1 Bringing the Li-O_2 Cell Out of the Glovebox

The Li-O_2 cell is assembled and the open circuit voltage (OCV) is tested inside an argon glovebox. The OCV is the difference in electrical potential between the two electrodes in the absence of an applied current. Before the Li-O_2 is removed from the glovebox, the cell is placed inside the metal reaction chamber and the ***cell valve is closed***. The electrical connections to cell should be tested before proceeding to the next step. The SOP assumes that all the valves in the gas line manifold are ***closed*** before the reaction cell is attached. Please see **Figure A4.1** for details about the gas line manifold.

Important Notes:

- Li-O_2 cell volume to flood the cell – 20mL
- Ballast volume - 1mL

A5.2 Testing Li-O_2 OCV under Natural Abundance O_2

1. Attach the reaction cell to the gas line manifold at the reaction cell union. Open the upper reaction cell valve.
2. Open the line valve.
3. Open the vacuum valve.
4. Remove the atmosphere in the manifold by turning on the vacuum and evacuating the manifold.
5. When the pressure transducer reads between 10 – 20 mmHg, ***open the lower reaction cell valve.*** Evacuate until the cell pressure is between 20 – 30 mmHg. Close the the upper cell reaction valve and the vacuum valve.

*Do not evacuate to a lower pressure as this will remove all of the electrolyte, killing the cell.

6. Open the natural abundance O_2 tank valve and close it after 2 seconds. Open the large valve (on the O_2 regulator) until there is approximately 10 psi in the small gage. Close the small valve and open the T valve (at the regulator) to introduce the natural abundance O_2 to the gas line.
7. Open the upper reaction cell valve. Allow the natural abundance oxygen to flow into the reaction cell until a pressure of ~ 760 mmHg is reached.
8. Close the natural abundance O_2 valve/or tank. Close the line valve. Close the upper and lower reaction cell valve. Check the battery OCV. To proceed with the ^{17}O-enrichment, the OCV of the Li-O_2 cell is be >2.8 V (vs. Li/Li^+)

   *For a Na-O_2 cell, the OCV should be >2.1 V (vs. Na/Na^+) to proceed to the ^{17}O-enrichment step

   **If the OCV of the Li-O_2 cell is <2.8 V, the battery may be left under O_2 for up to an hour. If the OCV does not increase to the desired voltage, a new cell should be constructed before continuing for the ^{17}O-enrichment process.

A5.3 ^{17}O-Enrichmnet of a Li-O_2 Cell

At this point the vacuum valve is closed, the ^{17}O-tank has not been opened and the gas line manifold is under natural abundance O_2 gas.

1. Open the vacuum valve, open the line valve and open the upper and lower cell valves. Evacuate the cell until the pressure is ~20 mmHg.
2. Close the vacuum valve and the line valve.
3. Open the ^{17}O cylinder one turn and close it.
4. Open the upper ballast valve, turn the valve once then close the upper ballast vale. This will fill the ballast volume with ^{17}O-enriched O_2 gas.
5. Open the lower ballast valve. The ^{17}O-enriched O_2 gas will now move from the ballast volume into the reaction cell. This is monitored by an increase in the observed pressure (of the reaction cell). Once the pressure stabilizes (i.e. it is not increasing, no more gas is flowing into the reaction cell), close the lower ballast valve.
6. Repeat steps 3, 4 and 5 until the pressure inside the reaction cell is 760 mmHg.
7. Record the pressure of the cell in the log book.
8. Close the line valve, the upper reaction cell valve and lower reaction cell valve.
9. Detach the cell from the gas line manifold and attach the reaction cell to the electrochemical cycler to cycle the cell.
10. Cycle the enriched cell to the desired capacity and extract electrode for NMR analysis.

Appendix A6: ^{7}Li Nutation Frequencies

The ^{7}Li nutation frequencies were calculated by performing a Fourier transformation on the time domain nutation data sets. The Fourier transformations were performed using Mathematic software. A sample Mathematic input file is shown in section A6.1. Sample frequency domain nutation plots, comparing the pristine Li_2O_2 and pristine Li_2CO_3, the PC/DMC cathode and TEGDME cathode and the TMP cathode are provided in sections A6.2, A6.3 and A6.4 respectively. The ^{7}Li nutation frequencies reported in Chapter 3, was taken as the frequency corresponding to the maximum amplitude observed in the frequency domain nutation plots.

A6.1 Mathematic Input File

```
(* raw data t 1st zero crossing , A1 =TMP cathode @ 30 kHz *)

      data1 =

{25.11521,50.17463,75.12259,99.90352,124.46209,148.74328,172.69246,196.25548,219
.37876,242.00938,264.09522,285.58506,306.42865,326.57694,345.98212,364.5978,382.
37912,399.28297,415.26804,430.29505,444.32684,457.32858,469.26785,480.11482,489.
84238,498.42624,505.84509,512.08066,517.11783,520.94471,523.5527,524.93653,525.0
9433,524.02756,521.7411,518.24317,513.54532,507.66236,500.61227,492.41617,483.09
816,472.68525,461.20718,448.69635,435.18762,420.71817,405.32736,389.05653,371.94
889,354.04928,335.40407,316.0097,296.06886,275.47765,};


Transpose[data1]

(* duration of data collection Tf-T0, li2o2 \[Rule] 72us @ 360 degree, li2co3 \[Rule] 72us
@ 360 degree *)
```

```
time1 = 0.05;

(* length of the data array *)

len1 = Length@data1;

 (* Line plot of the data samples *)

td1 =ListLinePlot[data1, PlotRange-> All];

td2 =ListLinePlot[data2, PlotRange -> All, PlotStyle -> Red];

(* Fourier of the data using signal processing convention *)

fd1 = ListLinePlot[ Sqrt[4/len1] Abs@Fourier[data1, FourierParameters -> {1,-1}],

DataRange -> {0, (len1 - 1)/time1}, PlotRange -> {{0,100},{0,9}}, PlotStyle ->

Orange,AxesLabel->{"Nutation Frequency (kHz)","Amplitude"}];

Show[td1]

Show[tdfrq]

Show[fd1]
```

A6.2 Frequency Domain Nutation Plots of Pristine Li_2O_2 and Pristine Li_2CO_3

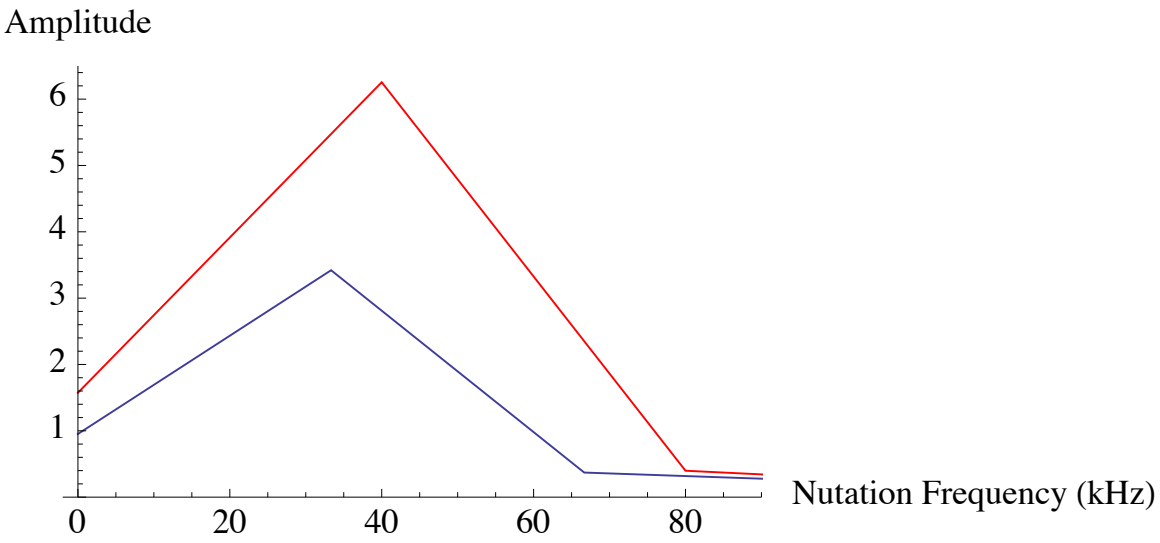

Figure A6.2 The frequency domain nutation plots of pristine Li_2O_2 (blue) and pristine Li_2CO_3 (red) when the applied RF field was 30 kHz

A6.3 Frequency Domain Nutation Plots of TEGDME Cathode and PC/DMC Cathode

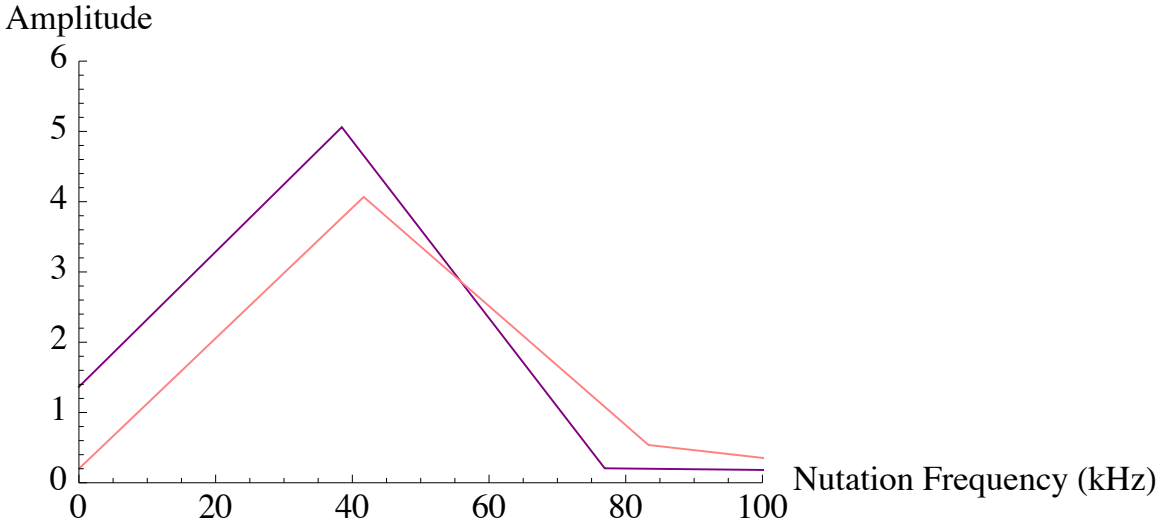

Figure A6.3 The frequency domain nutation plots of TEGDME cathode (purple) and PC/DMC (pink) when the applied RF field was 30 kHz

A6.4 Frequency Domain Nutation Plot of the TMP Cathode

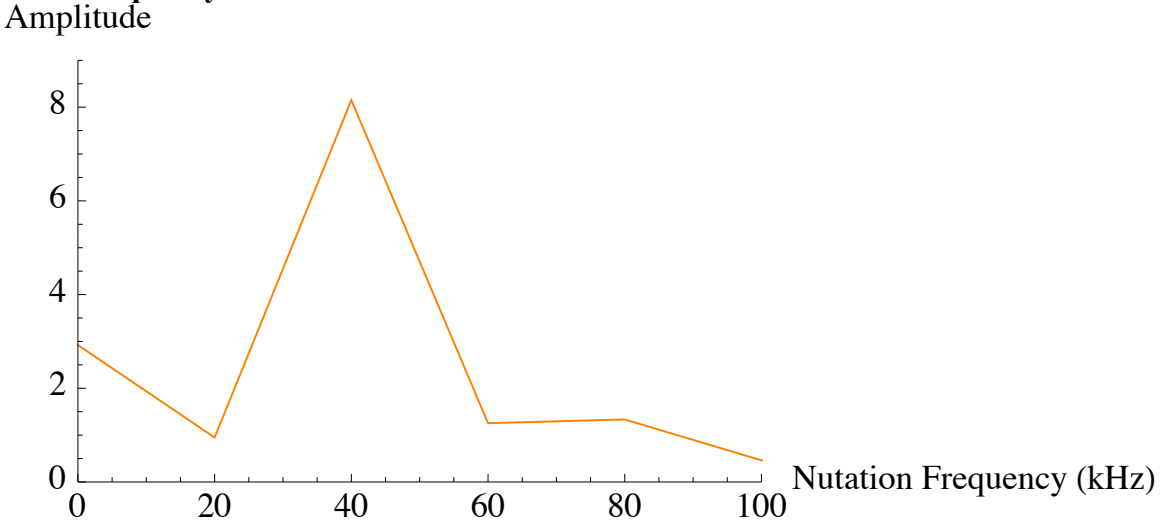

Figure A6.4 The frequency domain nutation plots of the TMP cathode when the applied RF field was 30 kHz

Appendix A7: Solution State NMR Analysis of the Waste Washing Solutions from Cycled TMP Cathodes

A7.1 Introduction

Before ssNMR analysis occurred, the cycled cathodes were washed in dry acetonitrile and then were dried under active vacuum for several hours. This was performed in an argon glovebox. To determine if soluble discharge species were washed away during the preparation process, the washing solution was retained and solution state ^{1}H and ^{31}P NMR spectra were acquired. Below are representative solution state spectra of the D_{800} cathode washing solution.

A7.2 Experimental

The spectra were all collected on a Bruker 500MHz Avance I spectrometer using a BBI solution probe. The ^{1}H NMR spectrum was collected with a 1 s delay time with a 11 kHz RF pulse. The washing solution, acetonitrile, was used as the internal reference at 1. 94 ppm. The neat ^{31}P NMR spectrum was collected with a 2 s delay time with a 7 kHz RF pulse and was referenced to an external standard of 85% H_3PO_4 at 0 ppm.

A7.3 Results and Discussion

A7.3.1 ^{1}H NMR of Waste Washing Solution

In the solution state ^{1}H NMR spectrum, the only species observed in a measurable quantity was the washing solution at 1.94 ppm and methoxy functional group from TMP and the TMP derivate at 3.5 ppm.

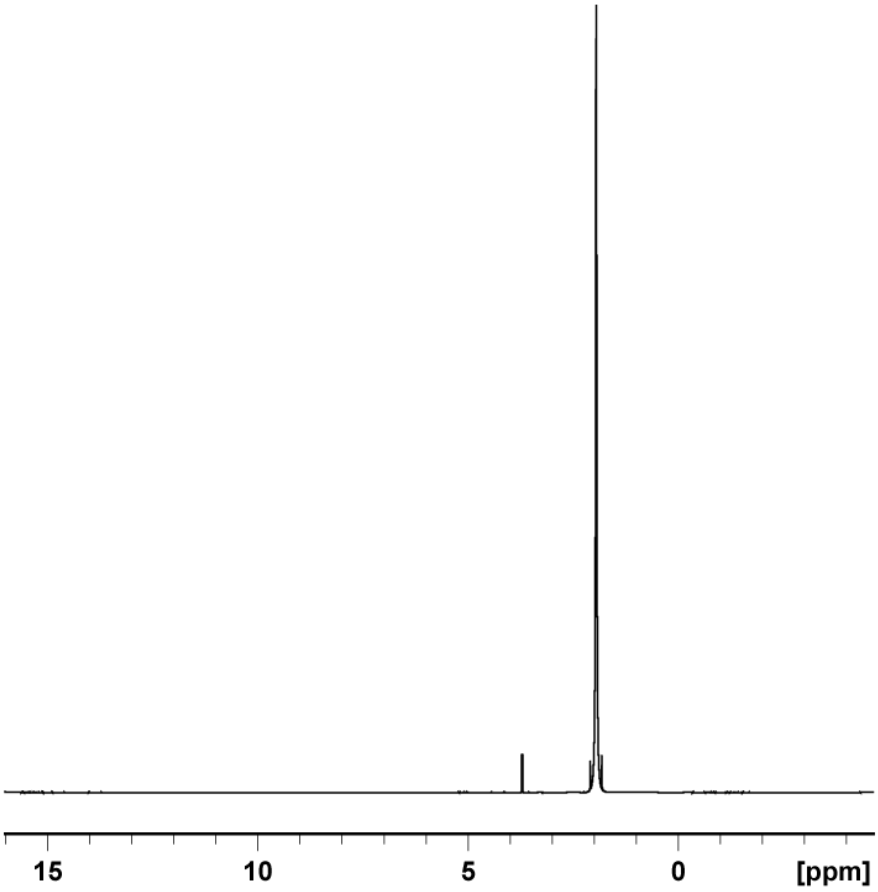

Figure A7.1 Solution state ^{1}H NMR spectrum of washing solution used to prepared D_{800} for ssNMR analysis

A7.3.2 ^{31}P NMR of Waste Washing Solution

In the neat solution state ^{31}P NMR spectrum of the washing solution, a single resonance was observed at 3 ppm. This was attributed to pristine TMP and the TMP derivate, as observed in the ssNMR spectra of the cycled cathodes.

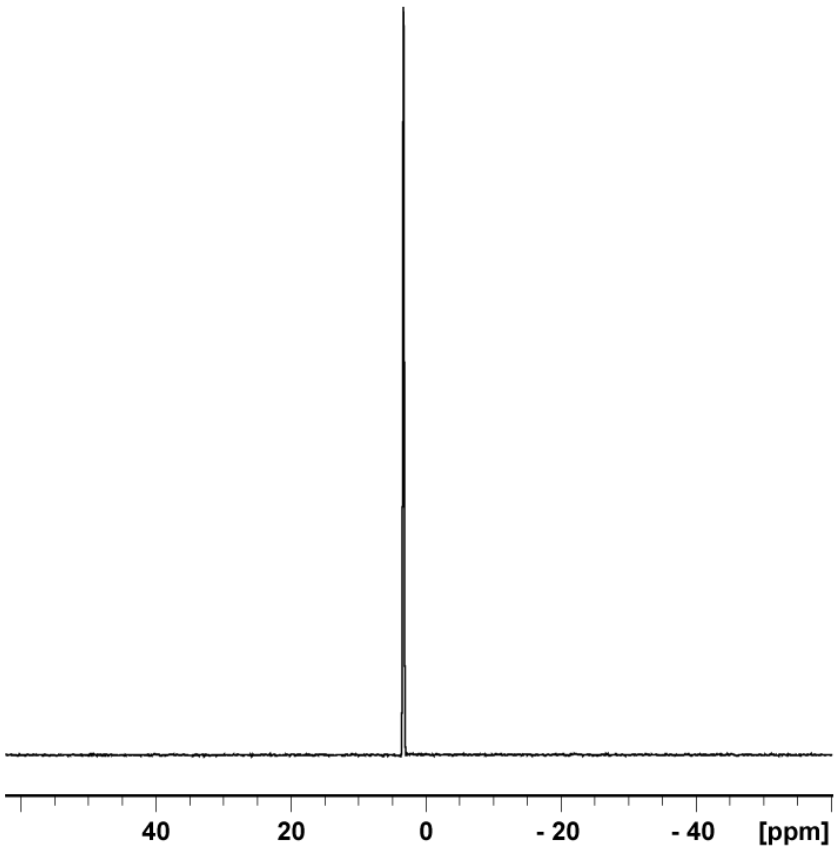

Figure A7.2 Solution state ^{31}P NMR spectrum of washing solution used to prepared D_{800} for ssNMR analysis

A7.4 Summary

The solution state ^{1}H and ^{31}P NMR spectra did not provide evidence of additional soluble species in the retained washing solution. This confirms that the ^{1}H and ^{31}P solid-state NMR spectra of the cycled cathodes are representative of all protonated and phosphorus discharge species formed when the TMP electrolyte, was used in Li-O_2 cells.

Appendix A8: ^{17}O MAS Spectra of ^{17}O-enriched TEGDME Li-O_2 Electrodes

A8.1 ^{17}O NMR Spectra where the Li_2O_2 ^{17}O Signature is Highlighted

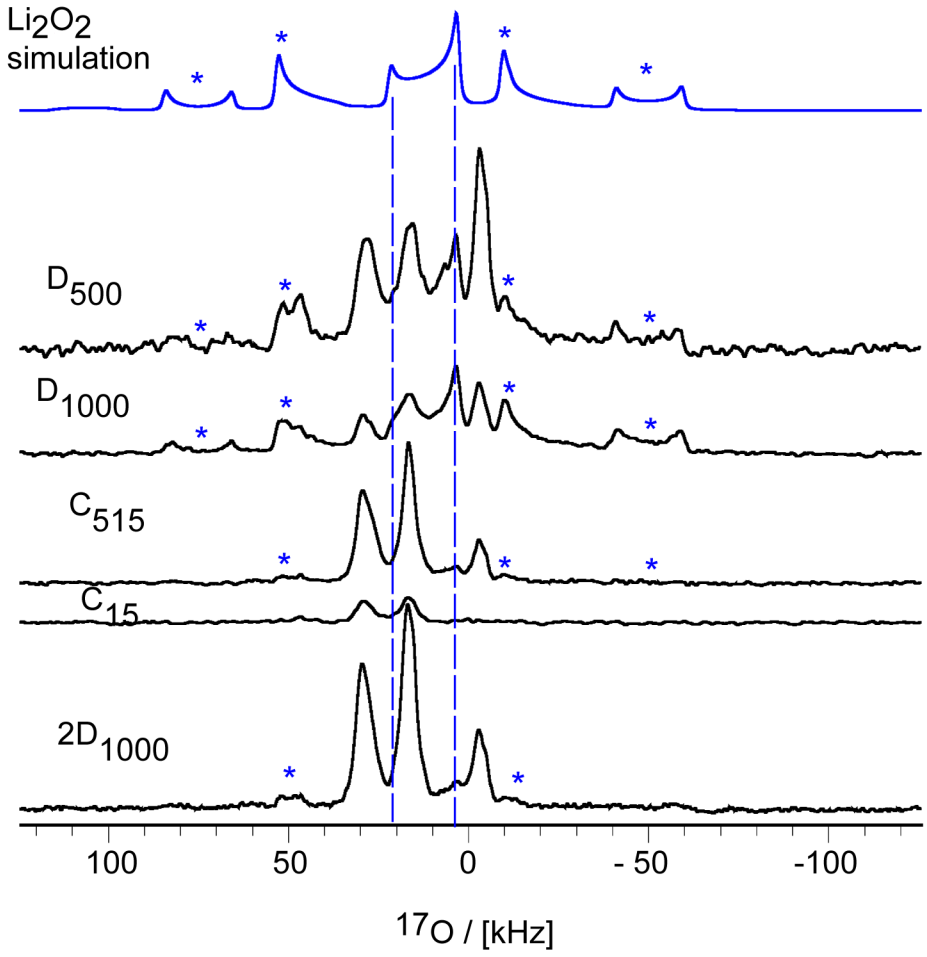

Figure A8.1 ^{17}O NMR spectra of cycled Li-O_2 electrodes collected at a 21.1 T with a 31.25 kHz MAS rate, where the Li_2O_2 NMR features are highlighted in blue

A8.2 ^{17}O NMR Spectra where the Relevant Li-O_2 Reaction Products are Identified

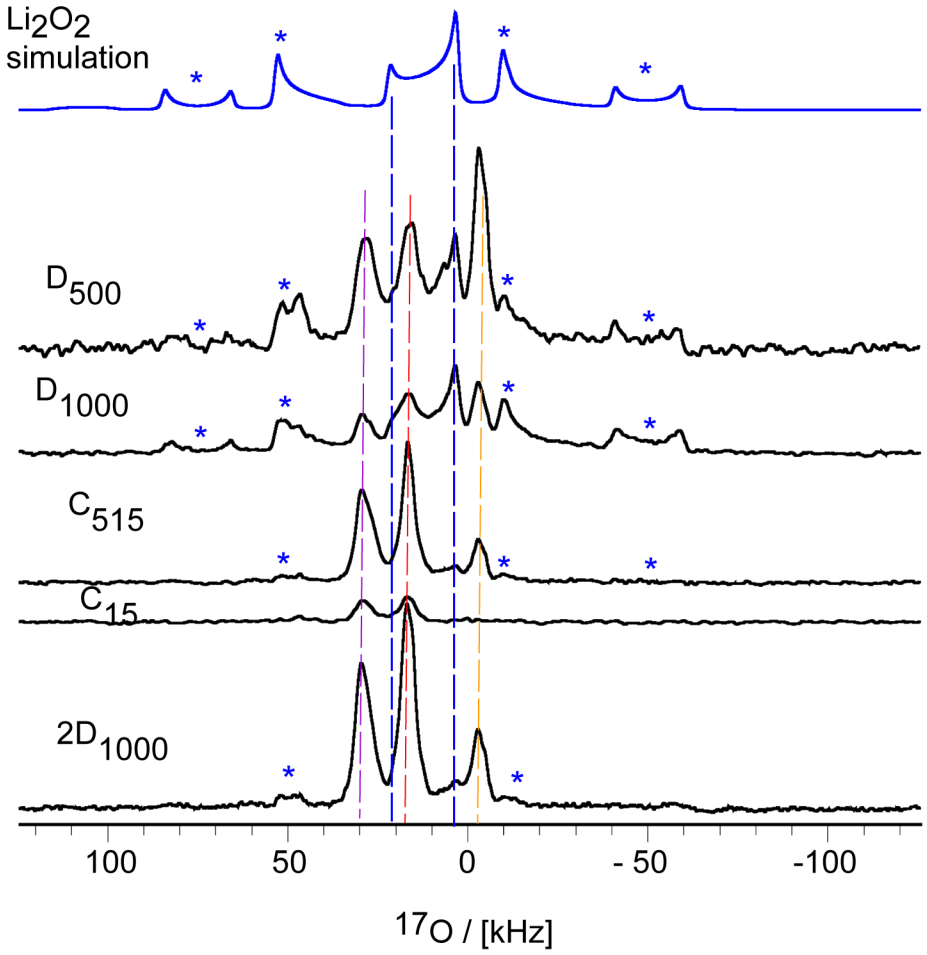

Figure A8.2 ^{17}O NMR spectra of cycled Li-O_2 electrodes collected at a 21.1 T with a 31.25 kHz MAS rate, where the relvant Li-O2 reaction species are identified as Li_2O_2 (blue), LiOH (yellow), Li_2CO_3 (red) and CH_3CO_2Li/HCO_2Li (purple) using the ^{17}O chemical shifts outlined in Table 5.1

Appendix A9: Solution State ^{1}H NMR of Pure TEGDME and Cathode Washing Solution

A9.1 Introduction

As part of the preparation for ssNMR analysis, the TEGDME cathodes were washed with pure TEGDME. As in appendix A7, the washing solution was retained and ^{1}H NMR was performed to determine if soluble species were lost . Here the ^{1}H spectrum of the washing solution was compared to the solution state ^{1}H NMR spectrum of pure TEGME.

A9.2 Experimental

The spectra were all collected on a Bruker 200MHz Avance I spectrometer using a BBI solution probe. The neat ^{1}H NMR spectra were collected with a 2 s delay time with a 30 kHz RF pulse. Both spectra were externally referenced to $CDCl_3$ at 7.2 ppm.

A9.3 Solution State ^{1}H NMR Spectra

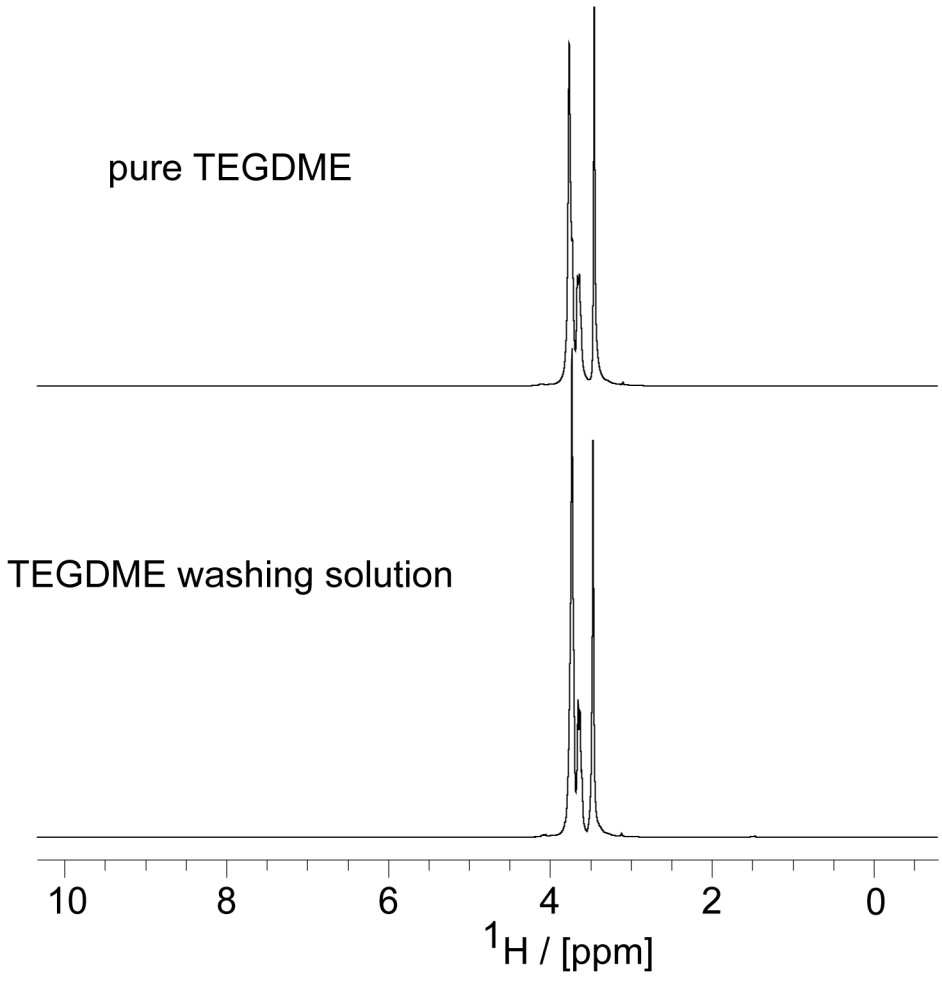

Figure A9.1 Solution State ^{1}H NMR spectra comparing neat TEGDME and the TEGDME washing solution (from a discharged electrode), where no additional protonated species were observed

A9.4 Summary

The solution state ^{1}H spectra did not display additional evidence of additional protonated species in the washing solution. This confirming that the solid-state spectra are representative of the all protonated reaction species.